ALMA Mater Studiorum
Università degli Studi Bologna

SCUOLA DI SCIENZE

Corso di Laurea Magistrale in Astrofisica e Cosmologia

Dipartimento di Fisica e Astronomia

Dynamical properties and mass-luminosity relation of elliptical galaxies

Elaborato finale

Candidato:
Alessandro Savino

Relatore:
Chiar.mo Prof.:
Alberto Buzzoni

Sessione III
Anno Accademico 2012/2013

To my family, who made this journey possible;
to my teachers, who made it instructive;
to my friends, who made it enjoyable.

Contents

List of Tables

List of Figures

Abstract

In this work we analysed a sample of 22 early-type galaxies. Using a cross-correlation technique, we extracted velocity dispersion and rotational velocity radial profiles. These data allowed us to probe many of the galaxies dynamical properties. We found constraints about the orbital anisotropy and evaluate estimates for the masses and the M/L ratios of the sample. Found masses ranges from 10^{10} to $10^{12} M_{\odot}$ and bolometric M/L ratios are of the order of the unit, depending on the luminosity trough $M/L \propto L^{0.28}$. We also investigated the well known scaling laws and used a Lick/IDS indices data set to establish relations between chemical and dynamical properties. In particular, we found correlation between many of the indices tracing the metallicity and both the depth of the potential well and the M/L. Both rotation and shape of the velocity dispersion profile seem to be irrelevant on chemical properties. As a last step, we considered eventual implication of our data upon stellar population and X-ray emission properties of our galaxies. Colour index and M/L seem to indicate that the stellar population of our galaxies is dominated by stars of late-G and early-K spectral class. A correlation seems to be found between X-ray emission and the depth of the potential well among the sample elements.

In questo elaborato abbiamo analizzato un campione di 22 galssie early-type. Utilizzando una tecnica di cross-correlazione, abbiamo ottenuto profili radiali di rotazione e di dispersione di velocitá. Questi dati ci hanno permesso di investigare molte delle proprietá dinamiche delle nostre galassie. Abbiamo ottenuto indizi sull'anisotropia orbitale e stimato le masse e il rapporto M/L del campione. Le masse misurate variano da 10^{10} a $10^{12} M_{\odot}$, mentre i valori degli M/L, per cui abbiamo trovato una dipendenza del tipo $M/L \propto L^{0.28}$, sono dell'ordine dell'unitá. Abbiamo anche riprodotto le famose relazioni di scala e abbiamo utlizzato un set di dati sugli indici di Lick/IDS per ricercare relazioni tra le proprietá chimiche e quelle dinamiche. In particolare, abbiamo riscontrato una correlazione tra molti degli indici dipendenti dalla metallicitá e la profonditá della buca di potenziale. Tali indici sembrano correlare anche con il M/L. La rotazione e la forma del profilo di dispersione di velocitá sembrano essere ininfluenti sulle proprietá chimiche. In ultima analisi, abbiamo considerato le implicazioni delle nostre misure riguardo la natura della popolazione stellare e dell'emissione X delle nostre galassie. L'indice di colore e il M/L sembrano indicare che la popolazione stellare delle nostre galassie é dominata da stelle appartenenti alle classi spettrali late-G e early-K. Sembra inoltre esserci una correlazione tra l'emissione X degli elementi del nostro campione e la profonditá della loro buca di potenziale.

Chapter 1

Introduction

For a long time, the study of elliptical galaxies produced only a limited amount of clues about their internal structure, principally due to the numerous observative difficulties in the characterization of the photometric and dynamical features of these extragalactic objects. The first works by, for instance, Hubble (1930) and Oort (1940) mainly focused on the shape of the light distribution, and many of the properties they inferred were grounded on strong assumptions. The earlier observations, indeed, suggested that this class of galaxies was extremely simple and homogeneous. The accepted model considered elliptical as isothermal oblate spheroids completely supported by rotation compatibly with their degree of flattening. They were also thought to be completely lacking of gas and dust, and devoid of any complex structural feature.

It was in the middle of '70 that the first important data began to be available. This was possible thanks to the improvement of observing conditions and the advent of CCDs and digitalized data, which largely pushed down the magnitude limit in the observation of diffuse "nebulae", compared to the previous photographic techniques. The earliest works on rotation (Bertola & Capaccioli, 1975; Illingworth, 1977; Peterson, 1978; Wilson, 1976) show that most of the ellipticals galaxies rotate much less than was expected. Almost simultaneously, first data on central velocity dispersion were measured (Faber & Jackson, 1976; Sargent et al., 1978; Young et al., 1978). It became clear (Davies, 1981; Kormendy and Illingworth, 1982) that rotation could explain the flattening only in bulges and dwarf galaxies, while the bigger and brighter ones needed to be mainly pressure-supported.

In these same years, scaling relations were discovered among many physical properties of early-type galaxies (also called ETGs). The work of Faber & Jackson (1976) revealed a correlation between the luminosity of ETGs and their central velocity dispersion. Although it seemed that ellipticals could be treated as a one-parameter family, the scatter was high enough such as to cast doubt on the early simplified picture. Kormendy (1977) found then a correlation between the effective radius of the de Vaucouleurs fit and the mean surface brightness within this radius. About ten years later, and almost simultaneously, two independent teams (Dressler et al., 1987; Djorgovski & Davis, 1987) discovered that ETGs populate a two dimensional variety, called "Fundamental plane", that links together effective radius, mean surface brightness and central velocity dispersion, and of which the Faber-Jackson and Kormendy relations are just bi-dimensional "projections".

The discovery of the fundamental plane was a milestone in the study of elliptical galaxies because of the implied regularity in the galactic properties, and because it can be used as a distance estimator (e.g. van Albada, Bertin, & Stiavelli, 1995). However, it opens also new questions on the nature of ETGs. Although the root of this relation seems to be found in the Virial Theorem, if galaxies were an homogeneous family, the predicted slope for the fundamental plane should be different from the observed one. This discrepancy is called "tilt of the fundamental plane" and for its origin it was invoked the non homology of the ETGs family (Graham & Colless, 1997; Trujillo, Burkert, & Bell, 2004) or a variation of the mass-to-light ratio (M/L) with luminosity (Jorgensen, Franx, & Kjaergaard, 1996).

Even the idea that ETGs were lacking any complex feature was, with time, confuted. Improved observations revealed that many ellipticals present a variety of components like shells and ripples (Malin & Carter, 1980), gas and dust lanes (van Gorkom, 1992), embedded stellar rings (Rix & White, 1992), kinematically decoupled cores (Kormendy & Djorgovski, 1989; Illingworth & Franx, 1989) and non ellipticals isophotes (Lauer, 1985; Bender, Doebereiner, & Moellenhoff, 1988). The last ones can be divided into two families, boxy isophotes and disky isophotes, depending on their deviations with respect to the perfect elliptical shape. Isophote shape seems to be of primary importance since these two families of galaxies seem to have completely distinct kinematical and photometric features, such as to lead Kormendy & Bender (1996) to propose a revisited version of the Hubble classification scheme to account for these differences. Nowadays the most detailed data on the ETGs derive from the integral field spectroscopic observation program such as the $SAURON$ project (Emsellem et al., 2004) and the $ATLAS^{3D}$ project (Krajnović et al., 2011) while the statistical properties are probed trough huge sky survey like the Sloan Digital Sky Survey (York et al., 2000).

Given this context, it is clear that ETGs are more complex that was initially thought and need further investigations to clarify the formation and evolution processes that have led these objects to the configuration we observe today. The purpose of this work is the dynamical characterization of a sample of 22 elliptical and lenticular galaxies which observations were carried out in the 1996 and 1997 in the context of a Lick-index study. We used a cross-correlation technique to retrieve rotation and velocity dispersion profiles from which we extracted valuable clues about orbital anisotropy and the mass-to-light ratio. The presence of a dataset of strength index was also exploited to search about relevant relations between dynamical, photometric and chemical features.

The rest of this chapter is dedicated to an introduction to the theory of the stellar systems dynamics, in order to give the basic instruments to the comprehension of this kind of objects. Chapter 2 presents the basic informations about the dataset used in this work, while chapter 3 describes the cross correlation method adopted for the retrieving of the kinematical information. Chapter 4 contains the results of the kinematical analysis and chapter 5 regards the considerations we made about the informations nestled in the profiles, as well as the confrontation with the Lick indexes. Conclusions and recap can be found in chapter 6. This document comprehend three appendices that show, respectively, the code of the principal routines utilized and a series of support diagram for § 4 and § 5.

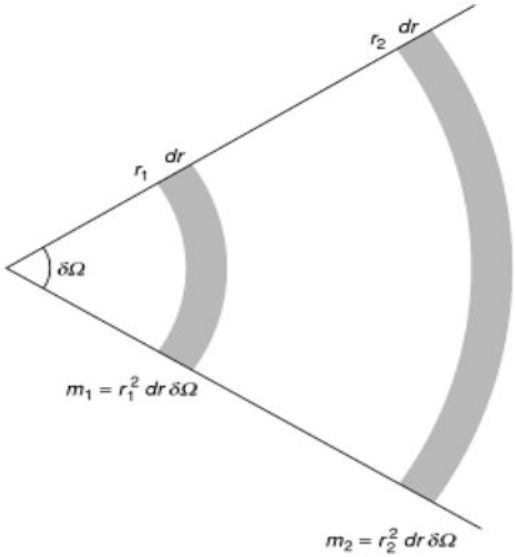

Figure 1.1 *If the stellar density is uniform, the number of stars in the first shaded segment with respect to the second one is* $(\frac{r_1}{r_2})^2$*. The force exercised on the cone apex by a star in the first segment with respect to the force exercised by a star in the second one is* $(\frac{r_1}{r_2})^{-2}$*. So each segment contribute equally to the total force, i.e. a star in the cone apex feel a net acceleration that depends from the global matter distribution.*

1.1 The physicals fundamentals

The dynamics of a stellar system is ruled by the gravitational force acting between the particles that compose the system, i.e. the stars. This force has an inverse dependence with the square of the distance, $F \propto r^{-2}$. If we consider a three dimensional uniform density of stars, the number of stars exercising a gravitational force on a certain point increases as r^2. Thus, any component of the system feels the force of all the distribution of matter (Fig. 1.1). If the matter distribution is spherically symmetric, then one would expect that the total force is null at the centre.

Clearly, this is an idealized case and a star feels a net force that depends on the large scale structure of the density distribution. Furthermore, at sufficient smaller scales, the distribution of stars is unlikely to be homogeneous and close interaction may play a significant role. Thus the dynamic of star of the galaxy is influenced by both the smooth density distribution on the global scale and the stellar encounters. Hereunder we will see the relative importance of the latter ones and their role in the achievement of the equilibrium state.

1.1.1 Relaxation processes

One of the assumptions that lies under most of the galaxies evolution theories is that this stellar systems are relaxed, in other words they have reached an equilibrium configuration

through some certain physical phenomenon. Which is this process that redistributed the energy between the stars is still a hot topic.

Two body relaxation time

The first process we take in consideration is the so called "Two body relaxation". In this process the energy is exchanged by close stellar encounters. After a sufficiently long period of time, the orbit of a generic star of the system is completely changed from the original one and the energy spectrum of the system tends to approach the Gibbs distribution:

$$f(\varepsilon) \propto e^{-\frac{\varepsilon}{k_b T}} = e^{-\frac{m\phi(x)+mv^2/2}{k_b T}}, \tag{1.1}$$

where f is the distribution function and T is defined such as $\frac{1}{2}m\langle v^2\rangle = \frac{3}{2}k_b T$. If the time scale needed to the stellar encounters to achieve relaxation is smaller respect to the other characteristic time scales, the stellar system is called collisional and the encounters play a key role in its evolution. Otherwise the system is called collisionless and relaxation can't be reached by this process.

If we consider a star moving inside the galaxy with a certain velocity v, every interaction change the velocity of the star by a quantity $\delta v_\perp$. Since the perturbations have random orientations, the mean velocity change is zero, but the mean square change, $\langle \delta v_\perp^2 \rangle$, is not. After one crossing time, defined $\tau_{cross} = R/v$, i.e the time needed by the star to go from one side of the galaxy to the other, it can be shown (Binney & Tremaine, 1987, see) that the influence of the perturbations is such that:

$$\frac{\langle \delta v_\perp^2 \rangle}{v^2} \simeq \frac{8}{N} \ln N, \tag{1.2}$$

where N is the number of particle that compose the system. Thus, to achieve relaxation, we expect that the stellar encounters have changed the kinetic energy of the star in a significant way ($\langle \delta v_\perp^2 \rangle \approx v^2$). This happens after a time of the order:

$$\tau_{2B} \simeq \frac{N}{8 \ln N} \cdot \tau_{cross} = \frac{N}{8 \ln N} \cdot \frac{R}{v}. \tag{1.3}$$

It can be seen that for a globular cluster, which is made up of about 10^5 stars, τ_{2B} is of the order of $10^8 yr$. Then, in these systems, collisions are dominant and the relaxation is achieved by two body encounters. *For a typical galaxy, instead, which is several orders of magnitude more massive respect to a globular cluster, the time needed for two body relaxation is greater than* $10^{15} yr$. Since the age of the universe is of about $10^{10} yr$, another process is needed to explain how galaxies have reached relaxation. Furthermore, this result indicate that close encounters are totally unimportant in the internal dynamics of a galaxy and the orbit of the stars that compose it are completely determined by the smooth large scale distribution of matter.

Violent relaxation

We have just seen that the time scale for the two body relaxation is too long to achieve equilibrium in a galactic system. Furthermore, this process tend to lead to energy equipartition between stars of different mass. This would cause a segregation of the more massive stars in the central part of the system, leading to colour gradient that are not observed. Thus, any relaxation process that imply equipartition of energy is not a reasonable choice to explain the equilibrium of galaxies.

Nowadays, the more acclaimed mechanism is the so called "violent relaxation" (Lynden-Bell, 1967). The details of how this process works are quite complicated and we remand to the original work for an in-depth analysis, however we can say that it happens when the gravitational potential of the system is rapidly varying. This is the case of a collapsing protogalaxy or of a merging event. If we consider a star inside a stellar system, we can write its energy per unit of mass as:

$$\varepsilon = \frac{1}{2}v^2 + \Phi. \tag{1.4}$$

If the potential in which the star is embedded is static, ε is an integral of motion and its value is constant, but if the potential has a dependence on time, then ε change according to:

$$\frac{d\varepsilon}{dt} = \left.\frac{\partial \Phi}{\partial t}\right|_{x(t)}. \tag{1.5}$$

Thus, in a system in which the potential is oscillating, the overall effect is to widen the energy spectrum of the stars, in a way that depends on the initial position and velocity of each stars but is independent on their masses. In fact, a star that is the central part of the collapsing structure, as the contraction proceeds, is embedded in a deeper and deeper potential well and ends up with a greater potential energy. Otherwise, a star that is falling from the outer regions, as the centre become more compact, acquire a lot of kinetic energy and, passed the centre, goes away from a shallower potential well, since the core is re-expanding. Then the net kinetic energy of the star is increased. By this process, the central parts of the stellar system become more bounded, transferring energy to the outskirts, that are expelled. *In this way a galaxy can achieve relaxation within a few collapse timescales* ($\tau_{ff} \propto (G\rho)^{-1/2} \approx 10^{8-9} yr$ *for a typical protogalaxy) and at the same tame avoid energy equipartition.* Another strong point of this mechanism is that, although the system has reached equilibrium, it can still admit triaxial shapes and an anisotropic velocity distribution (which we will see are observed in several object).

1.1.2 The collisionless Boltzmann equation and Jeans equations

In the previous section we have seen the scarce importance of collisions in the evolution of a galactic stellar system and the possible explanation for its equilibrium state. Now we focus on the equations that link the various properties of such kind of systems and permit their characterization.

The collisionless Boltzmann equation

At any time, the dynamical state of a stellar system is fully described by the so called "phase space density" or "distribution function" (DF), $f(\vec{x}, \vec{v}, t)$. This is a non negative function that describes the number of stars for each point of the six-dimensional phase space at a given instant. Thus $f(\vec{x}, \vec{v}, t)d^3xd^3v$ is the fraction of stars within the infinitesimal volume d^3x, centred in $\vec{x}$, having velocities included between $\vec{v}$ and $\vec{v} + d\vec{v}$. Integrating f over all the velocities give us $n(x, t)$, the spatial number density of stars. Now, since stars can't be created or destroyed and since, being galaxies collisionless systems, any star can be seen as an isolated system, the DF must satisfy a continuity equation:

$$\frac{\partial f}{\partial t} + \sum_{i=1}^{6} \frac{\partial (f\dot{w}_i)}{\partial \dot{w} i} = 0, \tag{1.6}$$

where $w_i = (x_1, x_2, x_3, v_1, v_2, v_3)$. Since $\dot{x}_j = v_j$, $\dot{v}_j = -\frac{\partial \Phi}{\partial x_j}$ and since:

$$\sum_{i=1}^{6} \frac{\partial (f\dot{w}_i)}{\partial \dot{w} i} = \sum_{i=1}^{6} \frac{\partial \dot{w}_i}{\partial w_i} f + \sum_{i=1}^{6} \dot{w}_i \frac{\partial f}{\partial w_i}, \tag{1.7}$$

we can rewrite the eq.(1.6) as:

$$\frac{\partial f}{\partial t} + f\left[\sum_{i=1}^{3} \frac{\partial v_i}{\partial x_i} + \sum_{i=1}^{3} \frac{\partial}{\partial v_i}\left(-\frac{\partial \Phi}{\partial x_i}\right)\right] + \sum_{i=1}^{3} v_i \frac{\partial f}{\partial x_i} - \sum_{i=1}^{3} \frac{\partial \Phi}{\partial x_i} \cdot \frac{\partial f}{\partial v_i} = 0. \tag{1.8}$$

Because x_j and v_j are independent and because, for gravitational interaction, Φ is independent of v_j, the term in the square brackets is null. Thus the equation becomes:

$$\frac{\partial f}{\partial t} + \sum_{i=1}^{6} \dot{w}_i \frac{\partial f}{\partial w_i} = \frac{\partial f}{\partial t} + \sum_{i=1}^{3} v_i \frac{\partial f}{\partial x_i} - \sum_{i=1}^{3} \frac{\partial \Phi}{\partial x_i} \cdot \frac{\partial f}{\partial v_i} = 0 \tag{1.9}$$

or, in vectorial notation:

$$\frac{\partial f}{\partial t} + \mathbf{v} \cdot \vec{\nabla} f - \vec{\nabla} \Phi \cdot \frac{\partial f}{\partial \mathbf{v}} = 0. \tag{1.10}$$

The last one is called Collisionless Boltzmann Equation (or CBE) and is the basic equation for stellar dynamics theory. This equation is equally valid if we consider the mass density or the number density, furthermore, if several subpopolations of different star species coexist within the galaxy, each of them must separately obey the CBE. Is interesting to note that if we extend the concept of Lagrangian derivative, $\frac{D}{Dt}$, to the six-dimensional phase space, the CBE reduces to:

$$\frac{Df}{Dt} = 0, \tag{1.11}$$

which means that the the flow of the DF in the phase space is that of an incompressible fluid. It has also to be noted that in the case of collisional systems, the right hand term of the eq.(1.9) is not zero but comprehend a term, $\Gamma(f)$, that account for the influence of the collisions on the DF. The CBE with this diffusive term is called Fokker-Planck and is usefully applied in the study of the evolution of globular clusters.

Jeans equations

The direct application of the CBE is often very difficult because of the high number of observable it involve. Even in resolved system we can generally retrieve two spatial pieces of information and a radial velocity. Rarely we can measure proper motions. In unresolved systems things are even more difficult, as we usually gain access only to global quantities such as mean velocities, stellar densities and velocity dispersions (related to the mean square velocity). The comparison of the models with observations is more conveniently done via moments of the DF and of the CBE. We have already seen that integrating the DF over all the velocities allow us to retrieve the spatial density of stars. This quantity is the moment of order zero in v of the DF. Taking the moment of first order in v, this gives us the mean velocity field:

$$n(x) = \int f(\vec{x}, \vec{v})\, d^3v \tag{1.12a}$$

$$, \overline{v}_i = \frac{1}{n} \int v_i f(\vec{x}, \vec{v})\, d^3v. \tag{1.12b}$$

We will now analyse the moments in v of the CBE, that lead to the formulation of a set of equations named Jeans equations. First the 0^{th} order:

$$\int \frac{\partial f}{\partial t}\, d^3v + \int v_i \frac{\partial f}{\partial x_i}\, d^3v - \frac{\partial \Phi}{\partial x_i} \int \frac{\partial f}{\partial v_i}\, d^3v = 0. \tag{1.13}$$

From now on, where the index i appear, it is implied the summation over the three components. Since the velocities are independent of both time and position, we can bring the first two derivative outside of the respective integrals and applying the eq.(1.12) :

$$\frac{\partial n}{\partial t} + \frac{\partial (n\overline{v}_i)}{\partial x_i} - \frac{\partial \Phi}{\partial x_i} \int |f|_{-\infty}^{+\infty}\, d^2v_{\neq i} = 0. \tag{1.14}$$

Since a reasonable DF tends to zero for very high velocities, the last integral vanishes and the relation becomes:

$$\frac{\partial n}{\partial t} + \frac{\partial (n\overline{v}_i)}{\partial x_i} = 0. \tag{1.15}$$

The last one is the first Jeans equation and is also called continuity equation because, in analogy with the hydrodynamics, it states the conservation of the stars and links the local variation of the spatial density with the advective flow of stars.

The first moment of the CBE in v is done multiplying the equation by v_j and integrating over the velocities:

$$\int \frac{\partial f}{\partial t} v_j\, d^3v + \int v_i v_j \frac{\partial f}{\partial x_i}\, d^3v - \frac{\partial \Phi}{\partial x_i} \int v_j \frac{\partial f}{\partial v_i}\, d^3v = 0. \tag{1.16}$$

Eq.(1.16) actually represents three equations, one for each value of j. The last integral of these equations can be transformed by integrating by part and recalling that f vanishes at large v:

$$\int v_j \frac{\partial f}{\partial v_i}\, d^3v = -\int \frac{\partial v_j}{\partial v_i} f\, d^3v = -\int \delta_{ij} f\, d^3v = -\delta_{ij} n. \tag{1.17}$$

At this point we can obtain the second Jeans equation:

$$\frac{\partial(n\overline{v}_j)}{\partial t} + \frac{\partial(n\overline{v_i v_j})}{\partial x_i} + n\frac{\partial \Phi}{\partial x_j} = 0, \tag{1.18}$$

where $\overline{v_i v_j} \equiv \frac{1}{n}\int v_i v_j f\, d^3v$. The last one is called also force equation and if we subtract from it v_j times the eq.(1.15) we obtain:

$$n\frac{\partial \overline{v}_j}{\partial t} - \overline{v}_j\frac{\partial(n\overline{v}_i)}{\partial x_i} + \frac{\partial(n\overline{v_i v_j})}{\partial x_i} + n\frac{\partial \Phi}{\partial x_j} = 0. \tag{1.19}$$

Further rearrangements can be done by splitting $\overline{v_i v_j}$ into a term that concerns the streaming motion, $\overline{v}_i\overline{v}_j$, and a term that accounts for residual velocities with respect to the mean motion:

$$\sigma_{ij}^2 = \overline{(v_i - \overline{v}_i)\cdot(v_j - \overline{v}_j)} = \overline{v_i v_j} - \overline{v}_i\overline{v}_j. \tag{1.20}$$

The quantity σ_{ij}^2 is called velocity dispersion tensor and is symmetric, so we can choose a coordinate system in which it is diagonal. In this system, the eigenvalues $\sigma_{11}, \sigma_{22}, \sigma_{33}$ are the semiaxes of the so called velocity ellipsoid, which describes the local velocity distribution. We can insert the velocity dispersion tensor in eq.(1.19) so that:

$$\frac{\partial \sigma_{ij}^2}{\partial x_i} = \frac{\partial(n\overline{v_i v_j})}{\partial x_i} - \overline{v}_j\frac{\partial(n\overline{v}_i)}{\partial x_i} - n\overline{v}_i\frac{\partial \overline{v}_j}{\partial x_i}. \tag{1.21}$$

In this way we obtain a set of three equations:

$$n\frac{\partial v_j}{\partial t} + n\overline{v}_i\frac{\partial \overline{v}_j}{\partial x_i} = -n\frac{\partial \Phi}{\partial x_j} - \frac{\partial(n\sigma_{ij}^2)}{\partial x_i}. \tag{1.22}$$

This is the third Jeans equation and is very instructive the comparison with the Euler equation of hydrodynamics:

$$\rho\frac{\partial \vec{v}}{\partial t} + \rho(\vec{v}\cdot\nabla)\vec{v} = -\rho\vec{\nabla}\Phi - \vec{\nabla}P. \tag{1.23}$$

We can see that the two equations are practically the same, the only difference lying in the pressure term, that is a tensor in the case of a stellar system while is a scalar in hydrodynamics. This difference is due to the collisional nature of fluids, that are characterized by an isotropic velocity dispersion tensor (i.e. the velocity ellipsoid becomes a sphere). The Jeans equations we have just deduced are of great importance in the characterization of stellar systems, relating several observable quantities. Unfortunately, there isn't an analogous of the fluid state equations to give constrains about the components of the velocity dispersion tensor, thus their primary use is in the construction of theoretical model, making assumption on σ^2, to compare with the observations.

1.1.3 The virial equations

The last tool we analyse in this section is obtained taking the first moment of eq.(1.18) in the spatial coordinates:

$$\int x_k \frac{\partial(\rho\overline{v}_j)}{\partial t}\, d^3x = -\int x_k \frac{\partial(\rho\overline{v_i v_j})}{\partial x_i}\, d^3x - \int x_k \rho \frac{\partial \Phi}{\partial x_j}\, d^3x, \tag{1.24}$$

where we have used the mass density ρ instead of the number density n. This equation can be manipulate to a more useful form. The details can be found in Binney & Tremaine (1987, p. 211) and here we report just the final relation that take the name of Tensor Virial Theorem:

$$\frac{1}{2}\frac{d^2 I_{ik}}{dt^2} = 2T_{ik} + \Pi_{ik} + W_{ik}, \tag{1.25}$$

where:

$$I_{ik} = \int \rho x_i x_k\, d^3x, \tag{1.26a}$$

$$T_{ik} = \int \frac{1}{2}\rho \overline{v}_i \overline{v}_k\, d^3x, \tag{1.26b}$$

$$\Pi_{ik} = \int \rho \sigma_{ik}^2\, d^3x, \tag{1.26c}$$

$$W_{ik} = -\frac{G}{2}\iint \rho(\vec{x})\rho(\vec{x}')\frac{(x_i' - x_i)(x_k' - x_k)}{|\vec{x}' - \vec{x}|^3}\, d^3x'\, d^3x. \tag{1.26d}$$

The quantity I_{ik} is the moment of inertia tensor, while T_{ik} and Π_{ik} are tensors that are linked to the kinetic energy, accounting respectively for the ordered and the chaotic motions, and W_{ik} is the potential energy tensor.

The relation between this quantities is very interesting if the system is in the state of equilibrium. In this case $\frac{d^2 I_{ik}}{dt^2} = 0$ and the trace reduces to:

$$2T + \Pi = 2K = -W. \tag{1.27}$$

This is the famous Scalar Virial Vheorem. The application of the Virial Theorem is very valuable and, under the hypothesis of equilibrium, permits to infer many interesting relation that holds for a stellar system such as the amount of rotation needed by an isotropic oblate spheroid of given shape to sustain its structure.

Chapter 2

Data set

The data set of this work derives from two observational runs carried out in April 1996 and January 1997 with the 2.12 m telescope of the "Guillermo Haro Observatory", built at 2480 m above sea level at north of Cananea, in the state of Sonora, Mexico. The original data consisted of both FITS and pre-reduced BDF format files. For convenience we worked with a unique digital format, converting all the BDF files, which are in the original output format of the MIDAS software, in the more versatile FITS format. Flexible Image Transport System (FITS) is an open standard defining a digital file format useful for storage, transmission and processing of scientific and other images. A major feature of the FITS format is that image metadata is stored in a human-readable ASCII header, so that an interested user can examine the headers to investigate a file of unknown provenance.

Each FITS file consists of one or more headers containing ASCII card images (80 character fixed-length strings) that carry keyword/value pairs, interleaved between data blocks. The keyword/value pairs provide information such as size, origin, coordinates, binary data format, free-form comments, history of the data, and anything else the creator desires. FITS is also often used to store non-image data, such as spectra, data cubes, or even structured data such as multi-table databases. The spectra we worked on were recorded as 3-D images from longslit spectroscopy, sampling a three dimensional spatial-wavelength-flux plane. In this section we present an overview of the observations and of the galaxy sample in order to set a context for the characterization and the critical analysis of the results we have obtained.

2.1 The instrument

The "Guillermo Haro Observatory", where the observations were made, has as a main telescope characterized by an f/12 Ritchey-Chretein design with a 2.12 m primary mirror and a 0.5 m secondary mirror (Fig. 2.1). The Ritchey-Chretein configuration is an evolution of the Cassegrein design conceived mainly to decrease the effect of spherical aberration and coma. While a Cassegrein telescope mounts a parabolic primary mirror and an hyperbolic secondary mirror, in this configuration both the mirrors are hyperbolic. Four different instruments are available to be mounted at the focus. Planning for the telescope began in

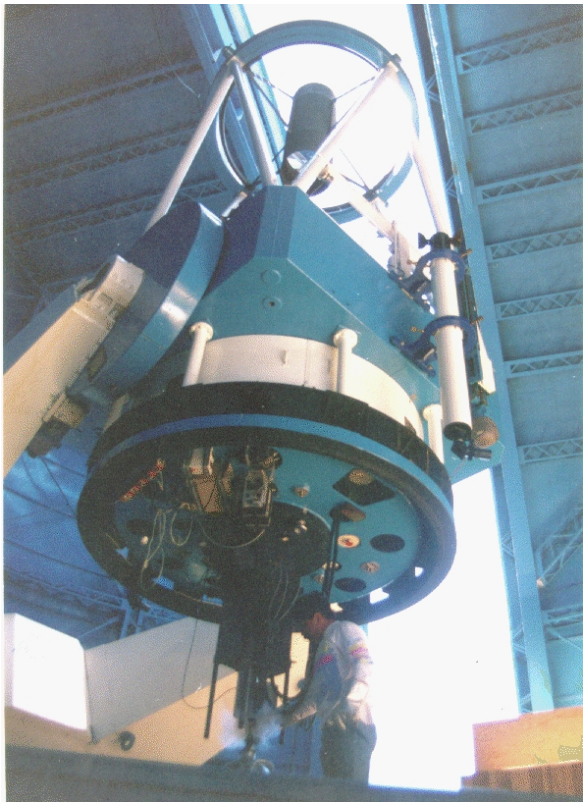

Figure 2.1 *Panoramic view of the 2.12 m telescope of "Guillermo Haro Observatory"*

1972, but it was not dedicated until 1987. Routine operations began in 1992.

The spectrograph used in these observations was a Boller & Chivens longslit spectrograph. A detailed explanation of the functioning of the type of instrument we used can be found in Fig. 2.2. The spectrograph is mounted at the f/12 Cassegrain focus of the telescope, and is equipped with a collimator of focal length 1080 mm and a camera of focal length 465 mm. Slit width can be changed manually at steps of 1 μm all the way up to 1000 μm. A typical slit width of 250 μm (or $2''$) corresponds to 4 detector pixels. Maximum slit length allowed is around $3'$. A 300 line mm^{-1} grism blazed at 5000Å was used, giving a dispersion of about 67 Å mm^{-1}. Tab. 2.1 reports the specifics of the spectra we used.

The detector was a Tektronix TK1024 CCD with 24 μm pixel size. A CCD (Charged Couple Device) is a detector, usually made of silicon, which samples,through a grid of pixels, the light from the focus plane and convert it in a digital signal. The CCD performance is established trough a series of operational characteristic:

Linearity Is the ability to produce digital signal that are directly proportional to the incident photon amount.

Quantum Efficiency The Quantum Efficiency (QE) is the response of the CCD at various wavelengths.

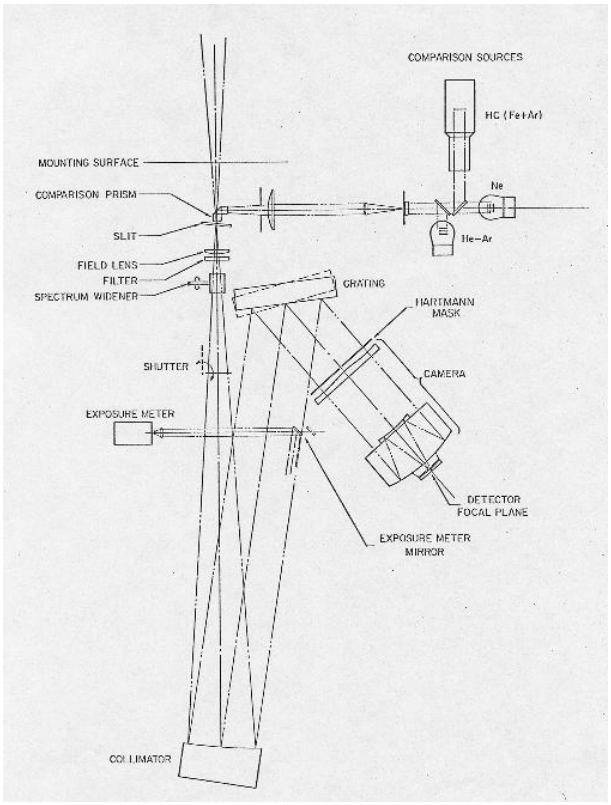

Figure 2.2 *Operation schematic of a Boller&Chivens Spectrograph. After has passed a slit, the light from the source is collimated toward a dispersing element (grism), which splits the photon beam depending on the wavelength. Then the light reaches the camera where, through an optical group, is focused on the detector plane.*

Table 2.1 *Instrumental set-up parameters*

	Apr 1996	Jan 1997
Spatial scale ["/Px]	0.449	0.456
Wavelenght scale [Å/Px]	1.611	1.609
Wavelenght range [Å]	4120-5860	4195-5840
Slit width ["]	1.5	1.3
Resolution FWHM [Å]	5.5	4.7
Instrumental Broadening [Km/s]	163.7	156.1

Table 2.2 *CCD technical features*

Tektronix TK 1024	
Pixel format	1024x446
Pixel size [μm]	24
Dark current [e^-/h]	0.4
Operative temperature[℃]	-111
Full well capacity [e^-]	503000
Response linearity [%]	0.1
Readout rate [kHz]	40
Gain [e^-/ADU]	7.68
Readout Noise [$e^- rms$]	8.4

Gain Is the conversion between the registered electron number and the ADU (Analogic to Digital Unit) number.

Read-out noise Is the noise generated by the electronic itself. It introduces an excess of electrons in the process of reading and conversion of the final signal. It is expressed in unit of electron per pixel.

Full well capacity The maximum recordable signal. Is the maximum number of electrons that can be accumulated in each pixel. It depends on the pixels dimensions.

Dark current Is the amount of electrons generated by the thermal agitation of the material. It can be mitigated using very low operative temperatures

A description of the parameters of the CCD we used is presented in Tab. 2.2 while the QE is shown in Fig. 2.3.

2.2 Observative modalities and reduction

The observations were made over a span of seven nights in 1996 and six nights in 1997. For each object, several frames was taken, generally three, with a typical exposure time of 1200s each. Right before and after each target observation, a sky measure on both galaxy side and a He-Ar lamp reference spectrum, for wavelength calibration, were acquired. Several star spectra were recorded to be used as standard calibrators for flux. For each observing night, six bias frames and two dome flat-fields were measured, typically at the beginning and at the end of the night. Tab. 2.3 report the logbook of the two observing runs. In addition to photometric standard stars for flux calibration, a sample of late G and early K stars spectra were acquired. These stars were originally intended to be a sample of calibrators for Lick indices but, due to their spectral features that, in first approximation, are similar to those of an ETG, many of them were used also as template spectra in the process of cross-correlation (see §3). A summary of template star properties is reported in Tab. 2.4.

Table 2.3. Observing logbook for the Cananea database

Date	Object	no. frames × exp. time	P.A. tel.	Seeing FWHM ″
Apr 17, 1996	N3489	3×1200s	32	1.9
	N5846	4×1200s	45	
Apr 18, 1996	N3607	3×1200s	136	2.2
	N5576	3×1200s	90	
	N5982	3×1200s	90	
Apr 19, 1996	N4125	3×1200s	78	1.7
	N5866	3×1200s	124	
	N6166	4×1200s	45	
Apr 20, 1996	N2764	3×1200s	17	1.2
	N6166	3×1200s	45	
Apr 21, 1996	N4111	3×1200s	150	2.2
	N4742	3×1200s	85	
	N5812	3×1200s	90	
Apr 22, 1996	N3245	3×1200s	0	2.0
	N3489	2×1200s	58	
	N4472	3×1200s	90	
	N4649	3×1200s	101	
Apr 23, 1996	N2685	3×1200S	35	1.6
	N4278	3×1200S	175	
	N4374	3×1200s	129	
Flux standard stars: HD 84971, HD 160233				
Index standard stars: HD 63302, HD 69267, HD 76151, HD 88284, HD 124897, HD 132345, HD 135722, HD 180928, HD 184406, HD 188510, HD 192947				
Jan 10, 1997	N4365	3×1200s	90	1.6
Jan 15, 1997	N1587	3×1200s	81	1.7
	N1588	3×1200s	81	
	N4382	2×1200s	18	
Flux standard stars: SAO 97351, HD 121968, SAO 92336				
Index standard stars: HD 88284, HD 95272, HD 95345, HD 98430, HD 99491				

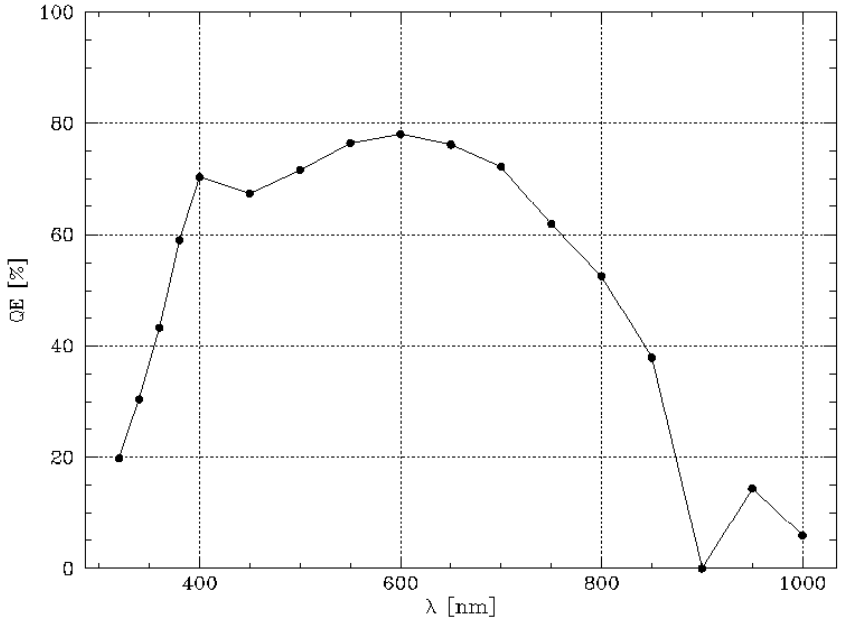

Figure 2.3 *The Quantum Efficiency of the Tektronix TK1024 CCD*

Table 2.4 *Cross-correlation template stars. The upper tab refers to the 1996 run, while the lower one is for the run of 1997. Information taken from the Yale Bright star catalogue (Hoffleit & Jaschek, 1991).*

Star	m_v	Spectral Type	Spectra acquired
HD63302	6.3	K1	2
HD69267	3.5	K4	3
HD88284	3.6	K0	3
HD124897	-0.04	K1	2
HD132345	5.9	K3	2
HD180928	6.1	K4	1
HD184406	4.5	K3	1

Star	m_v	Spectral Type	Spectra acquired
HD88284	3.6	K0	1
HD95272	4.1	K1	1
HD95345	4.9	K1	1
HD98430	3.6	K0	1
HD99491	6.5	K0	1
SA92-336	8.1	G5	1

For this work, the data were supplied already full reduced except for NGC3489, NGC5846 and NGC4365. The two-dimensional spectra of these galaxies were already corrected with bias and flat-field and sky subtracted. We used the MIDAS software to complete the reduction. We used the LONG routine package to perform the wavelength calibration, using the respective reference spectrum and an He-Ar lines list. Then we applied the Beer-Bouguer-Lambert law to correct for atmospheric extinction. Finally, using photometric standards, we built a CCD response curve which was used for flux calibration. The removal of spurious features (cosmic rays, bad pixels etc...) was performed trough a median smoothing algorithm (see §3.3).

2.3 The sample

The sample consisted of 22 bright ETGs in a magnitude range of $9 < m_b < 14$ and in coordinate range of $4h < \alpha < 17h$ and $-11^\circ < \delta < 66^\circ$. The targets mainly belong to group and cluster environments (about 1/3 of the sample consist of Virgo-cluster members), and just few of them are field galaxies. Fig. 2.4 shows some of the sample properties. It can be seen in Fig. 2.4a that the M_b vs. ε plane is well sampled up to $\varepsilon = 0.6$ with the more luminous galaxies that tend to be roundest ones. Fig. 2.4b shows a clear correlation between the integrated colour and the blue magnitude, with the galaxies that occupy the well known "Red sequence". Finally, the last two tabs, show colour and magnitude against the morphological parameter T. It can be seen that the later type galaxies are bluer and fainter with respect to the bulk of the earlier type ones, though a certain amount of spread is noticeable among the latter galaxies due to the presence of either giants and dwarf ellipticals in our sample. *In the following pages we present individual profiles of each galaxy, containing the basic information about position, morphology and photometric structure.* The observed colour indices were corrected for galactic extinction using the dust map from Schlafly & Finkbeiner (2011) and refer to the integrated value inside one effective radius, i.e. the equivalent radius of the isophote containing half of the total galaxy light (hereafter R_e). The imaging of the galaxies was taken from the SDSS (York et al., 2000) while the smaller images represent the direction of the slit in our observations (solid line) superimposed to the major axis of the galaxy (dashed line). A summary of the main properties of the sample is also reported in Tab. 2.5.

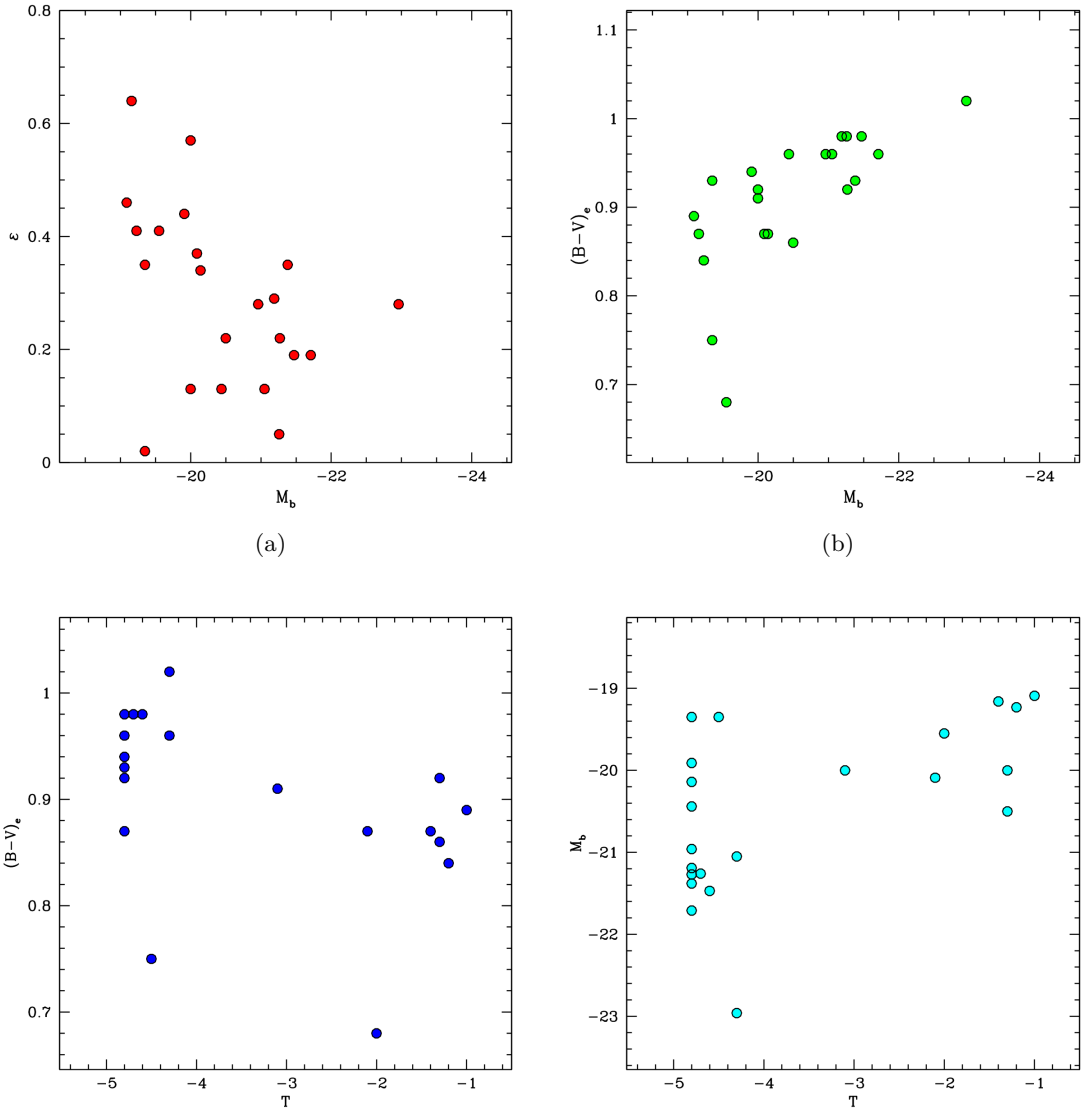

Figure 2.4 *Basic properties of the galaxy sample: a) Absolute blue magnitude vs. ellipticity; b)Absolute blue magnitude vs. colour Index; c) Morphological type vs. colour index; d) Morphological type vs. absolute blue magnitude.*

Table 2.5 *A summary of the main properties of our sample. The columns report respectively: Name; morphological classification; De Vaucouleur parameter T; ellipticity; apparent blue magnitude; absolute blue magnitude; integrated* $(B-V)$ *colour index inside one effective radius, corrected for galactic extinction and peculiarity of each galaxy. The data are taken from de Vaucouleurs et al. (1991) and Paturel et al. (2003).*

Name	Classification	T	ε	m_b	M_b	$(B-V)_e$	Notes*
NGC1587	E1p	-4.8	0.29	12.72	-21.19	0.98	I
NGC1588	E4p	-4.8	0.44	13.89	-19.91	0.94	I
NGC2685	SB0-a	-1.0	0.46	12.16	-19.09	0.89	PR
NGC2764	S0	-2.0	0.41	13.65	-19.55	0.68	···
NGC3245	S0	-2.1	0.37	11.66	-20.09	0.87	CR, NA
NGC3489	SB0-a	-1.2	0.41	11.06	-19.23	0.84	D
NGC3607	S0	-3.1	0.13	10.93	-20.00	0.91	CR, Sy2
NGC4111	S0-a	-1.4	0.64	11.67	-19.16	0.87	CR, NA
NGC4125	E6p	-4.8	0.22	10.64	-21.27	0.92	D, NA
NGC4278	E1	-4.8	0.02	11.04	-19.35	0.93	LI
NGC4365	E3	-4.8	0.28	10.50	-20.96	0.96	BI
NGC4374	E1	-4.3	0.13	10.08	-21.05	0.96	D, Sy2
NGC4382	S0-a	-1.3	0.22	10.02	-20.50	0.86	BI
NGC4472	E2	-4.8	0.19	9.27	-21.71	0.96	Sy2
NGC4649	E2	-4.6	0.19	9.83	-21.47	0.98	···
NGC4742	E4	-4.5	0.35	12.11	-19.35	0.75	···
NGC5576	E3	-4.8	0.34	11.79	-20.14	0.87	BI, TE
NGC5812	E0	-4.8	0.13	12.19	-20.44	0.96	···
NGC5846	E0	-4.7	0.05	11.09	-21-26	0.98	NA
NGC5866	S0-a	-1.3	0.57	10.73	-20.00	0.92	D, NA
NGC5982	E3	-4.8	0.35	11.98	-21.38	0.93	BI, S
NGC6166	cD2p	-4.3	0.28	12.90	-22.96	1.02	MN, SSR

* BI = Boxy isophotes; CR = Circumnuclear ring of dust or stars; D = Strong dust lanes or complex absorption pattern; I = Interacting; LI = LINER activity detected; MN = Multiple nuclei; NA = X-ray or radio nuclear activity detected; PR = Polar ring of gas and stars; Sy2 = Seyfert-2 activity detected; TE = Strongly twisted outer envelope.

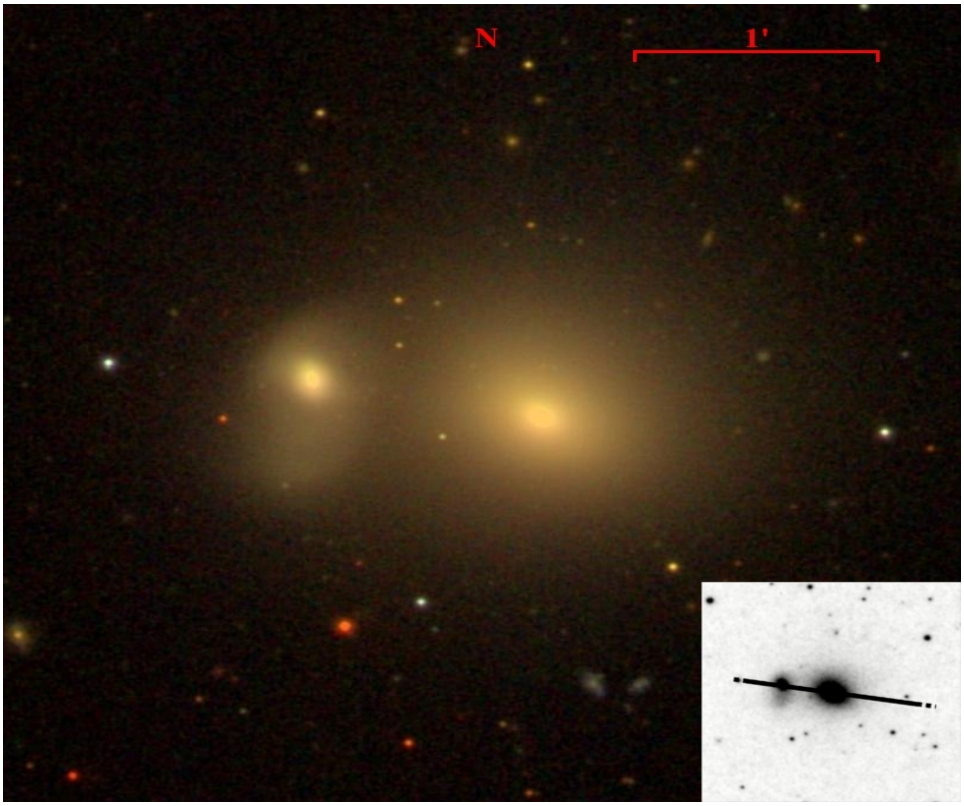

NGC1587

Cross-ID: UGC-03063, PGC015332
Right Ascension(J2000): $04h : 30m : 40s$
Declination(J2000): $+00° : 39' : 42''$
Constellation: Taurus
Apparent blue magnitude m_b: 12.72
Absolute blue magnitude M_b: -21.19
Morphological type: E1p
De Vacouler parameter T: -4.8
Major axis position angle P.A.: 73°
Major axis half-light radius: 27.27″
Minor axis half-light radius: 19.36″
Axial ratio *b/a*: 0.71
Color index inside R_e $(B-V)_e$: 0.98
Environment: In a pair, group

NGC1588

Cross-ID: UGC-03064, PGC015340
Right Ascension(J2000):$04h : 30m : 44s$
Declination(J2000): $+00° : 39' : 53''$
Constellation: Taurus
Apparent blue magnitude m_b: 13.89
Absolute blue magnitude M_b: -19.91
Morphological type: E4p
De Vacouler parameter T: -4.8
Major axis position angle P.A.: 165°
Major axis half-light radius: 16.46″
Minor axis half-light radius: 9.22″
Axial ratio *b/a*: 0.56
Color index inside R_e $(B-V)_e$: 0.94
Environment: In a pair, group

Notes: Interconnected galaxy pair.

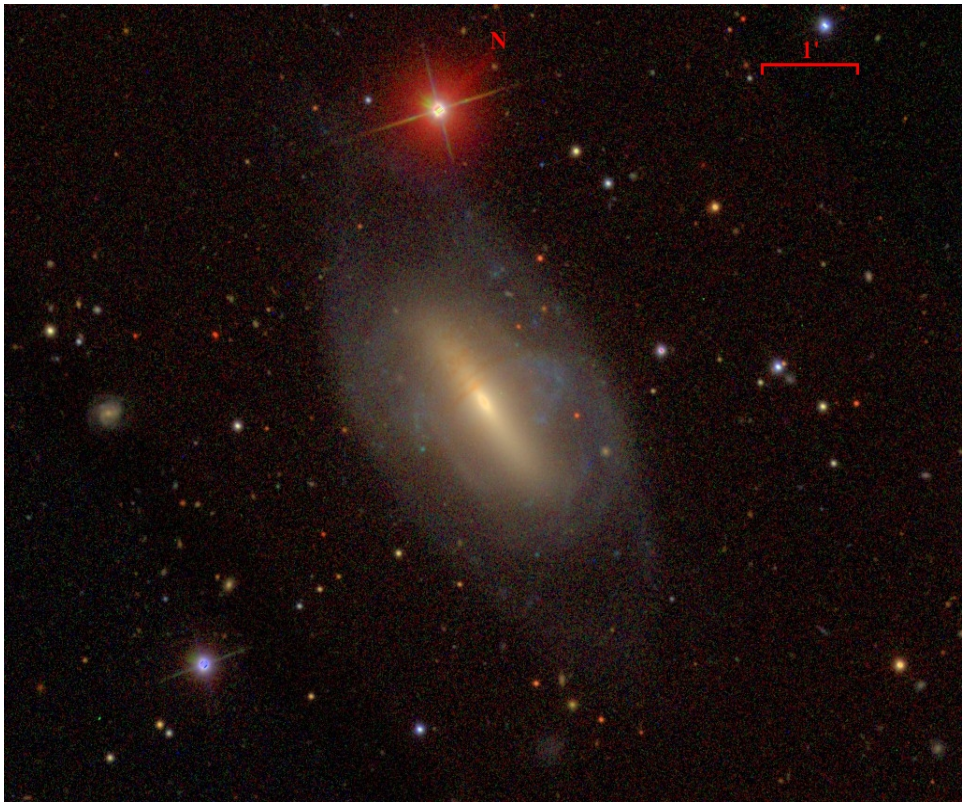

NGC2685

Cross-ID: Helix Galaxy, UGC-0466, ARP336
Right Ascension(J2000): $08h : 55m : 34s$
Declination(J2000): $+58° : 44' : 04''$
Constellation: Ursa Major
Apparent blue magnitude m_b: 12.16
Absolute blue magnitude M_b: -19.09
Morphological type: SB0-a
De Vacouler parameter T: -1.0
Major axis position angle P.A.: 38°
Major axis half-light radius: 41.91″
Minor axis half-light radius: 22.63″
Axial ratio *b/a*: 0.54
Color index inside R_e $(B-V)_e$: 0.89
Radial velocity CZ: 880 Km/s
Environment: Group
Notes: This galaxy presents a polar ring of gas and stars.

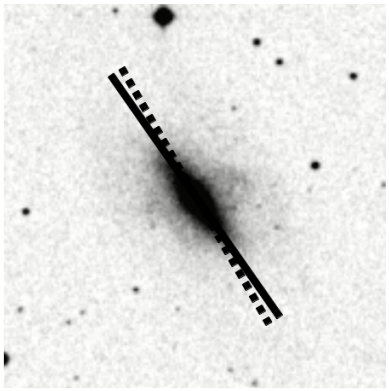

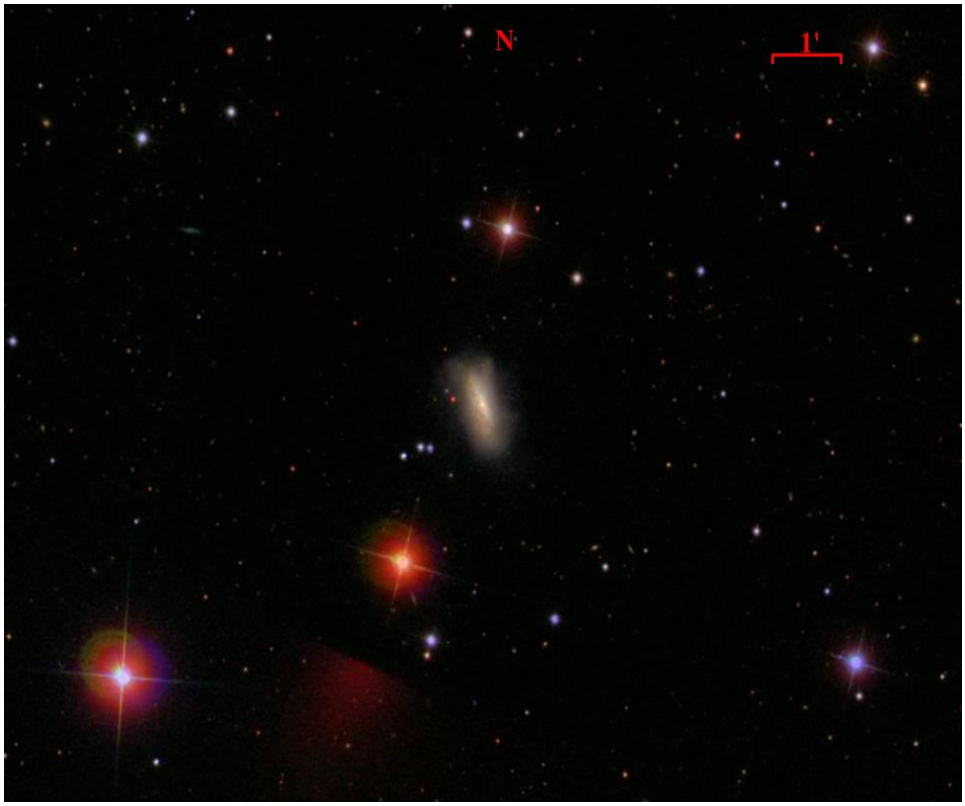

NGC2764

Cross-ID: UGC-04794
Right Ascension(J2000): $08h : 09m : 17s$
Declination(J2000): $+21° : 26' : 36''$
Constellation: Cancer
Apparent blue magnitude m_b: 13.65
Absolute blue magnitude M_b: -19.55
Morphological type: S0
De Vacouler parameter T: -2.0
Major axis position angle P.A.: 19°
Major axis half-light radius: 14.06″
Minor axis half-light radius: 8.30″
Axial ratio *b/a*: 0.59
Color index inside R_e $(B-V)_e$: 0.68
Radial velocity CZ: 2718 Km/s
Environment: In a pair

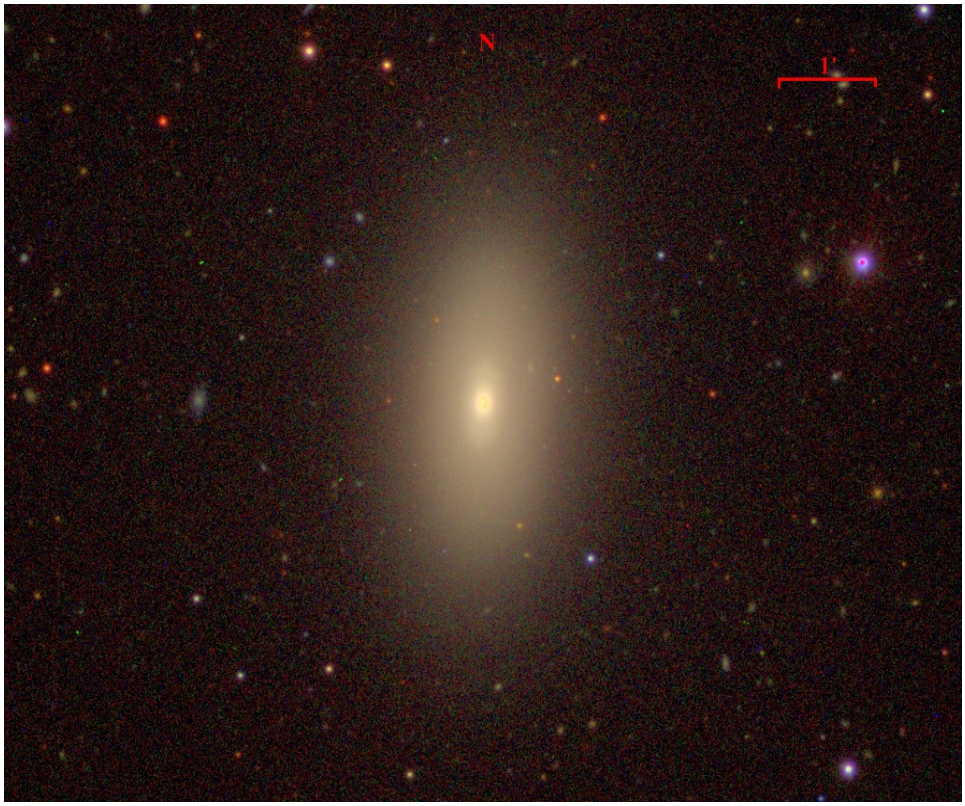

NGC3245

Cross-ID: UGC-05663, PGC-03074
Right Ascension(J2000): $10h : 27m : 18s$
Declination(J2000): $+28° : 30' : 27''$
Constellation: Leo Minor
Apparent blue magnitude m_b: 11.66
Absolute blue magnitude M_b: -20.09
Morphological type: S0
De Vacouler parameter T: -2.1
Major axis position angle P.A.: 176°
Major axis half-light radius: 32.88″
Minor axis half-light radius: 20.72″
Axial ratio *b/a*: 0.63
Color index inside R_e $(B-V)_e$: 0.87
Radial velocity CZ: 1358 Km/s
Environment: Possible field galaxy
Notes: Presence of a stellar ring, X-ray and Radio nuclear activity detected.

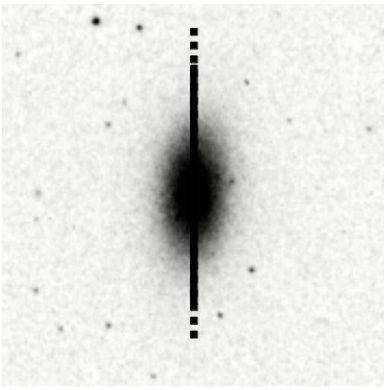

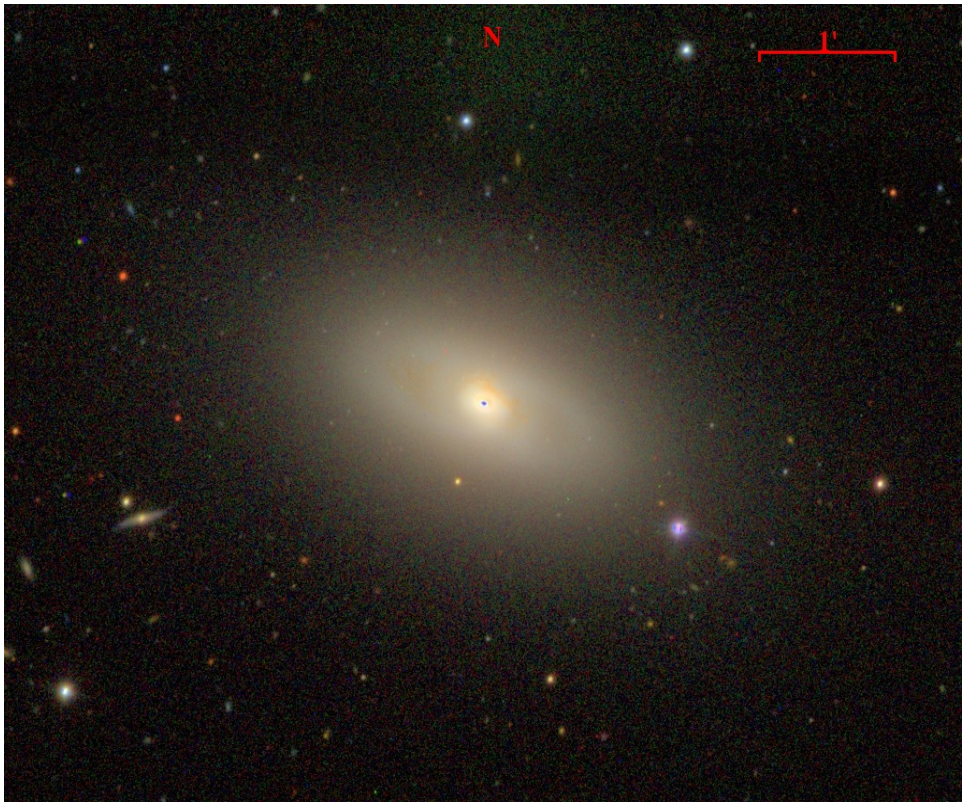

NGC3489

Cross-ID: UGC-06082, PGC-033160
Right Ascension(J2000): $11h : 00m : 18s$
Declination(J2000): $+13° : 54' : 04''$
Constellation: Leo
Apparent blue magnitude m_b: 11.06
Absolute blue magnitude M_b: -19.23
Morphological type: SB0-a
De Vacouler parameter T: -1.2
Major axis position angle P.A.: 70°
Major axis half-light radius: 25.59″
Minor axis half-light radius: 15.10″
Axial ratio *b/a*: 0.59
Color index inside R_e $(B-V)_e$: 0.84
Radial velocity CZ: 688 Km/s
Environment: Possible field galaxy
Notes: Complex absorption pattern.

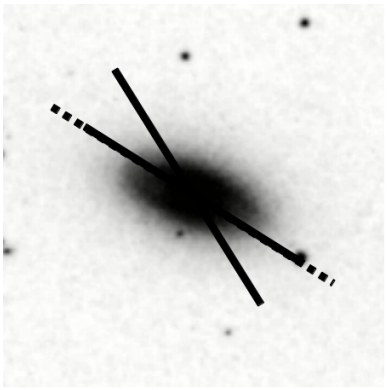

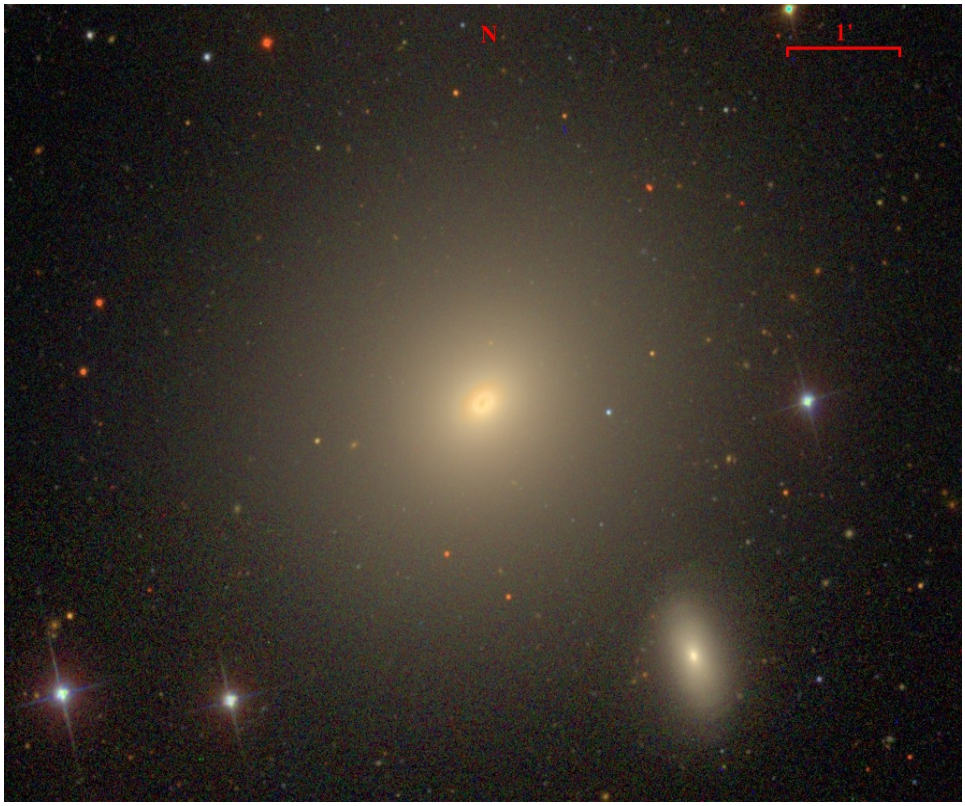

NGC3607

Cross-ID: UGC-06297, PGC-034426
Right Ascension(J2000): $11h : 16m : 54s$
Declination(J2000): $+18° : 03' : 06''$
Constellation: Leo
Apparent blue magnitude m_b: 10.93
Absolute blue magnitude M_b: -20.00
Morphological type: S0
De Vacouler parameter T: -3.1
Major axis position angle P.A.: 120°
Major axis half-light radius: 46.39″
Minor axis half-light radius: 40.36″
Axial ratio *b/a*: 0.87
Color index inside R_e $(B-V)_e$: 0.91
Radial velocity CZ: 935 Km/s
Environment: Group
Notes: Sy2 type nuclear activity, prominent circumnuclear dust ring.

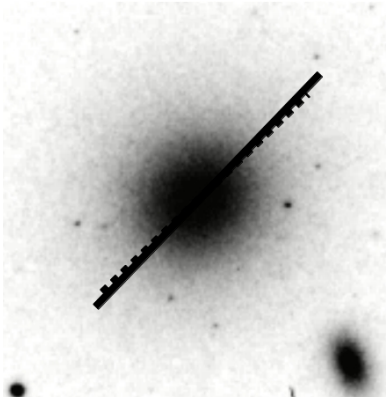

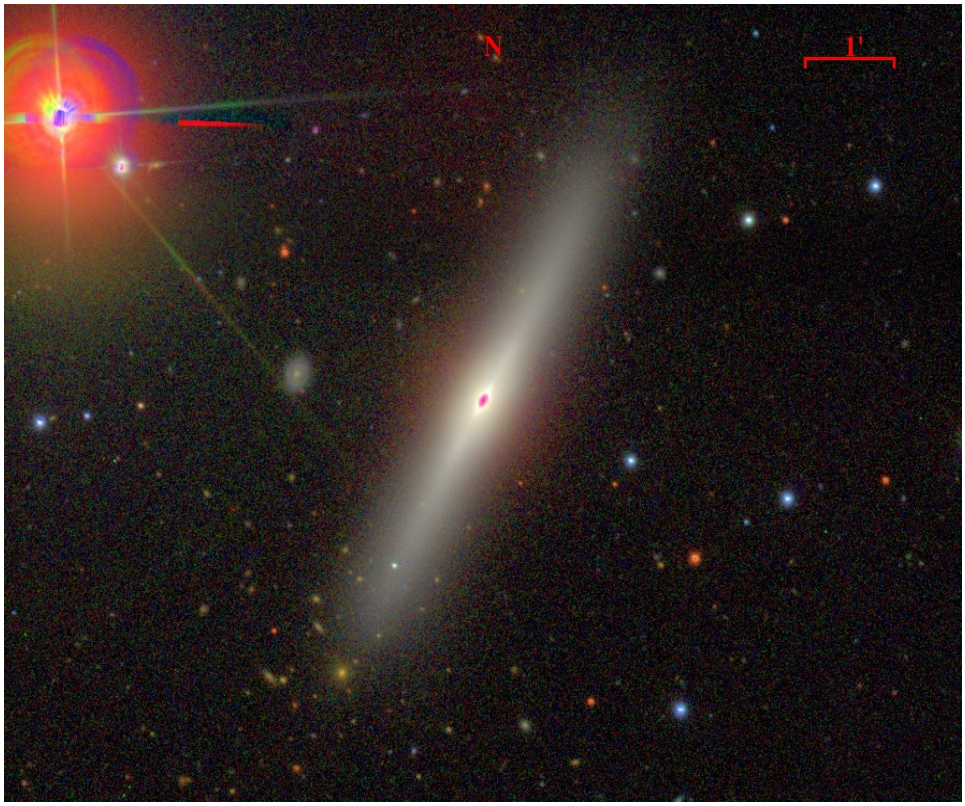

NGC4111

Cross-ID: UGC-07103, PGC-038440
Right Ascension(J2000): $12h : 07m : 03s$
Declination(J2000): $+43° : 03' : 57''$
Constellation: Canes Venatici
Apparent blue magnitude m_b: 11.67
Absolute blue magnitude M_b: -19.16
Morphological type: S0-a
De Vacouler parameter T: -1.4
Major axis position angle P.A.: 153°
Major axis half-light radius: 15.77″
Minor axis half-light radius: 5.677″
Axial ratio *b/a*: 0.36
Color index inside R_e $(B-V)_e$: 0.87
Radial velocity CZ: 779 Km/s
Environment: Group
Notes: Presence of a stellar ring, X-ray and Radio nuclear activity detected.

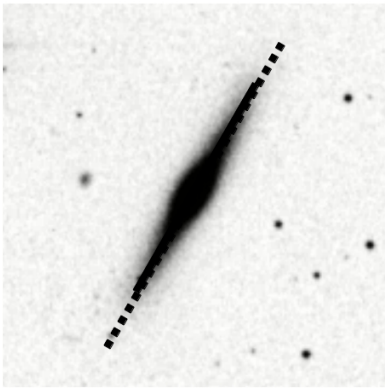

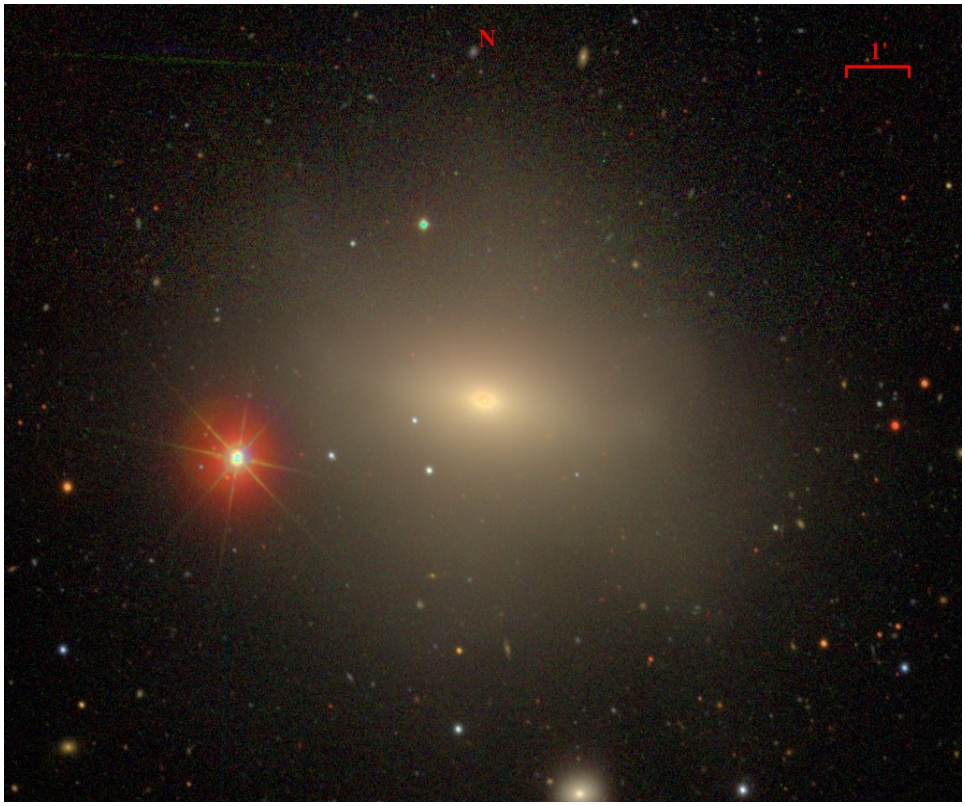

NGC4125

Cross-ID: UGC-07118, PGC-038524
Right Ascension(J2000): $12h : 08m : 06s$
Declination(J2000): $+65° : 10' : 27''$
Constellation: Draco
Apparent blue magnitude m_b: 10.64
Absolute blue magnitude M_b: -21.27
Morphological type: E6p
De Vacouler parameter T: -4.8
Major axis position angle P.A.: 95°
Major axis half-light radius: 65.77″
Minor axis half-light radius: 51.30″
Axial ratio *b/a*: 0.78
Color index inside R_e $(B-V)_e$: 0.92
Radial velocity CZ: 1338 Km/s
Environment: Radial velocity based group
Notes: Presence of a dust lane, X-ray nuclear activity detected.

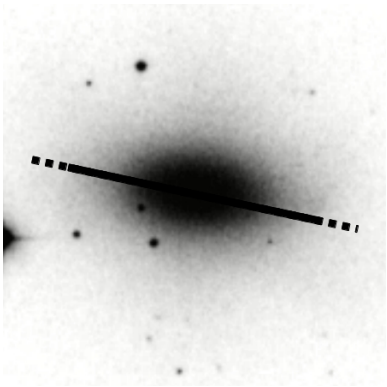

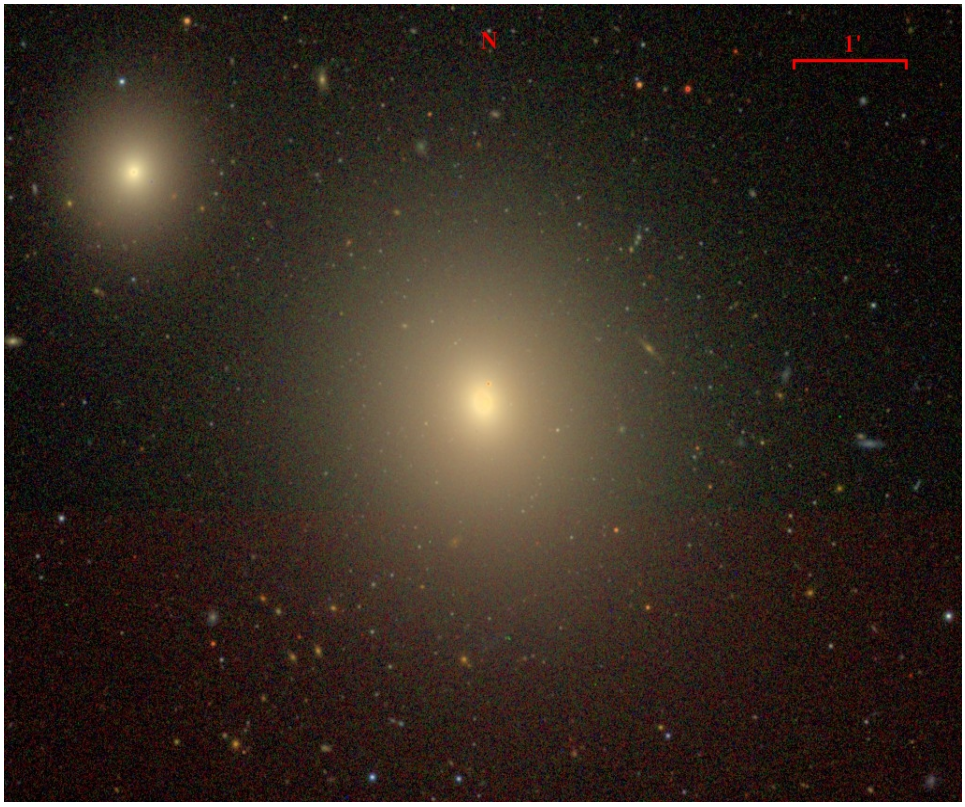

NGC4278

Cross-ID: UGC-07386, PGC-039764
Right Ascension(J2000): $12h : 20m : 07s$
Declination(J2000): $+29° : 16' : 51''$
Constellation: Coma Berenices
Apparent blue magnitude m_b: 11.04
Absolute blue magnitude M_b: -19.35
Morphological type: E1
De Vacouler parameter T: -4.8
Major axis position angle P.A.: 0°
Major axis half-light radius: 34.79″
Minor axis half-light radius: 34.10″
Axial ratio *b/a*: 0.98
Color index inside R_e $(B-V)_e$: 0.93
Radial velocity CZ: 644 Km/s
Environment: Group
Notes: LINER-Sy1 type nuclear activity.

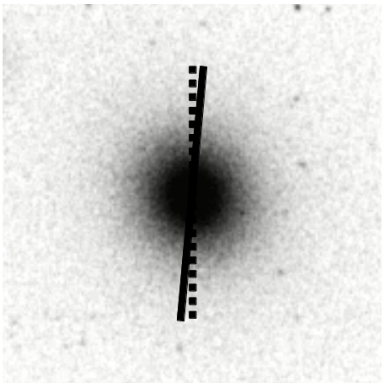

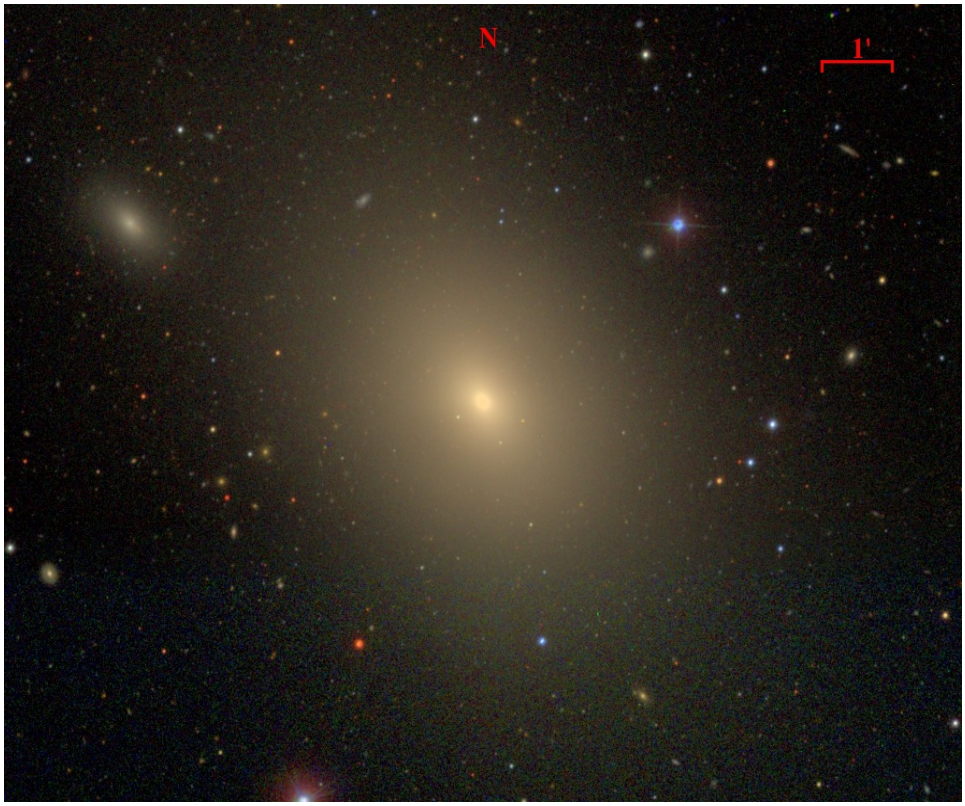

NGC4365

Cross-ID: UGC-07488, PGC-040375
Right Ascension(J2000): $12h : 24m : 28s$
Declination(J2000): $+07° : 19' : 04''$
Constellation: Virgo
Apparent blue magnitude m_b: 10.50
Absolute blue magnitude M_b: -20.96
Morphological type: E3
De Vacouler parameter T: -4.8
Major axis position angle P.A.: 40°
Major axis half-light radius: 57.96″
Minor axis half-light radius: 41.73″
Axial ratio *b/a*: 0.72
Color index inside R_e $(B-V)_e$: 0.96
Radial velocity CZ: 1240 Km/s
Environment: Virgo galaxy cluster
Notes: Very boxy isophotes.

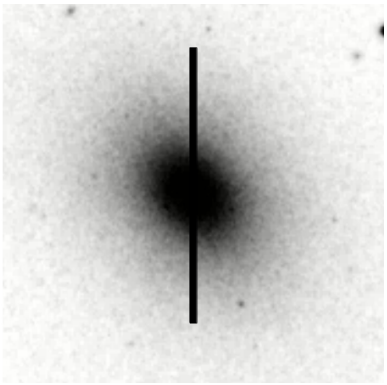

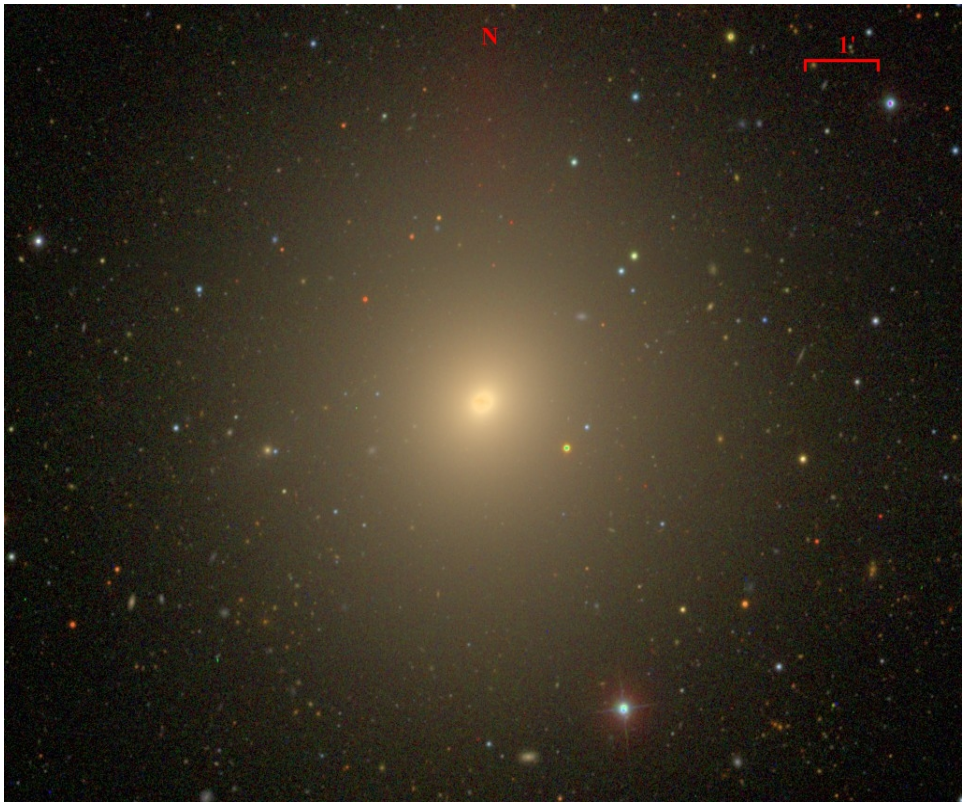

NGC4374

Cross-ID: M84, UGC-07494, PGC-040455
Right Ascension(J2000): $12h : 25m : 04s$
Declination(J2000): $+12° : 53' : 13''$
Constellation: Virgo
Apparent blue magnitude m_b: 10.08
Absolute blue magnitude M_b: -21.05
Morphological type: E1
De Vacouler parameter T: -4.3
Major axis position angle P.A.: 133°
Major axis half-light radius: 54.50″
Minor axis half-light radius: 47.42″
Axial ratio *b/a*: 0.87
Color index inside R_e $(B-V)_e$: 0.96
Radial velocity CZ: 1014 Km/s
Environment: Virgo galaxy cluster
Notes: Sy2 type nuclear activity, presence of two dust lanes.

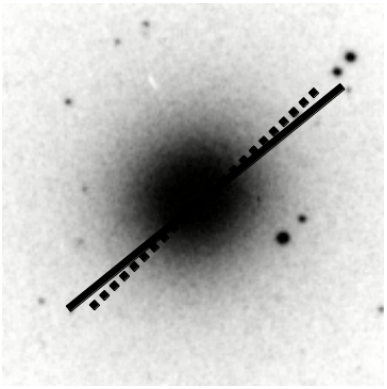

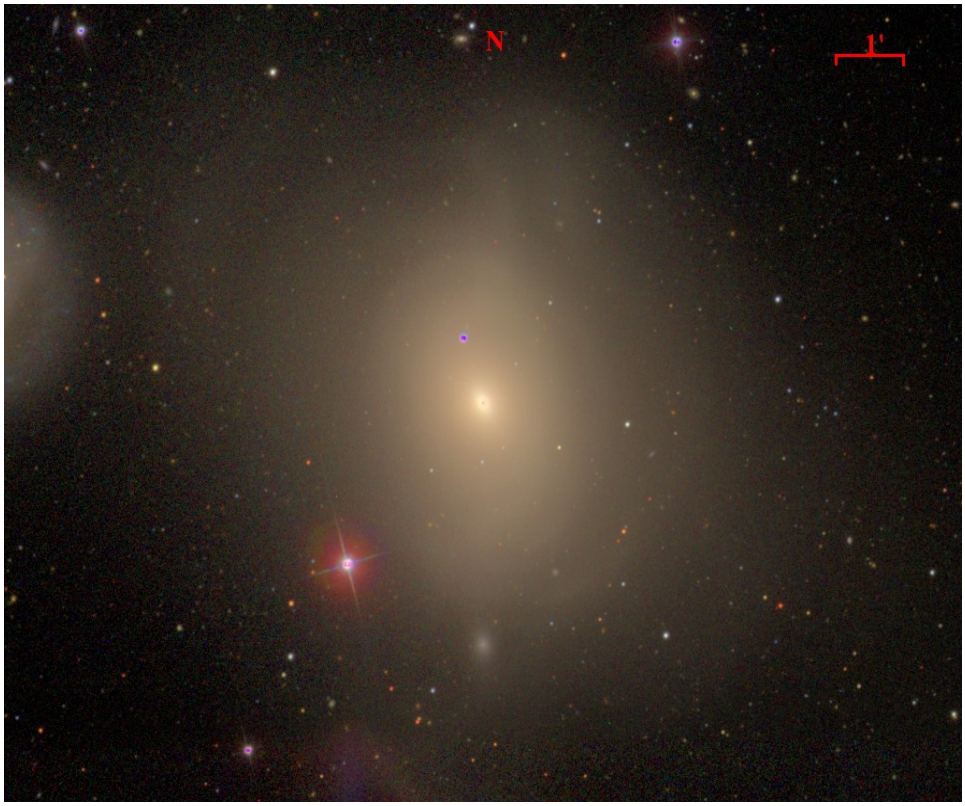

NGC4382

Cross-ID: M85, UGC-07508, PGC-040515
Right Ascension(J2000): $12h : 25m : 24s$
Declination(J2000): $+18° : 11' : 29''$
Constellation: Coma Berenices
Apparent blue magnitude m_b: 10.02
Absolute blue magnitude M_b: -20.50
Morphological type: S0-a
De Vacouler parameter T: -1.3
Major axis position angle P.A.: 0°
Major axis half-light radius: 61.38″
Minor axis half-light radius: 47.88″
Axial ratio *b/a*: 0.78
Color index inside R_e $(B-V)_e$: 0.86
Radial velocity CZ: 718 Km/s
Environment: In a pair, Virgo galaxy cluster
Notes: Very boxy isophotes.

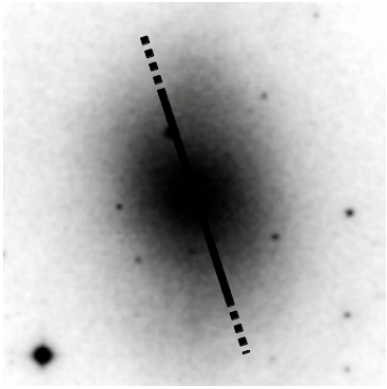

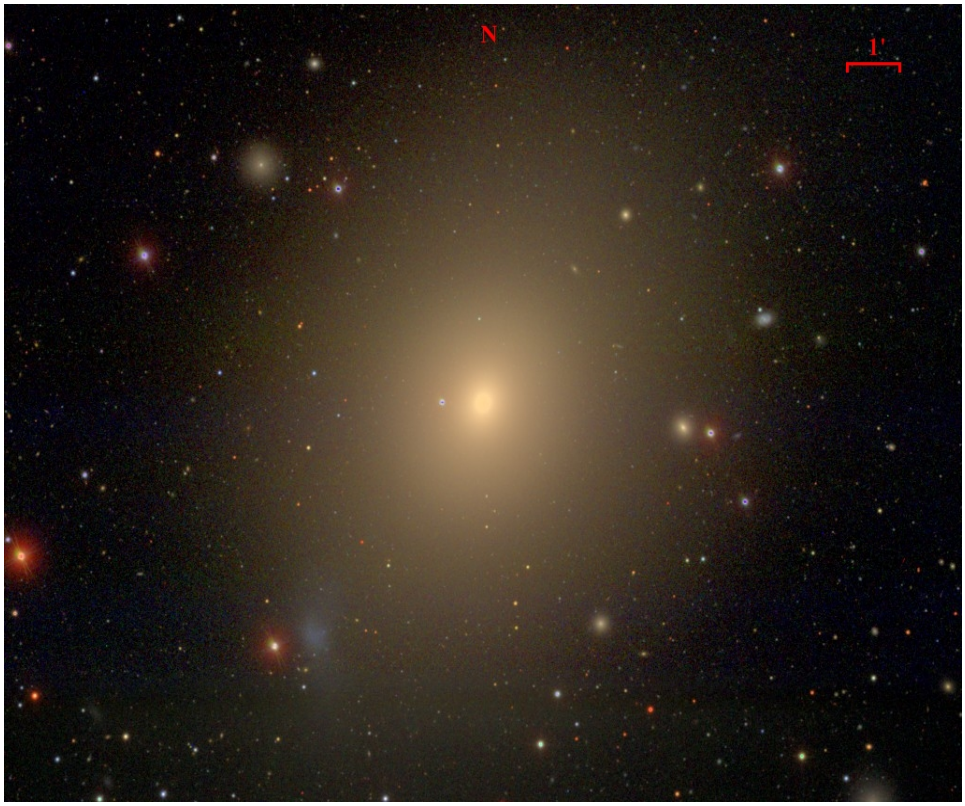

NGC4472

Cross-ID: M49, UGC-07629, PGC-041220
Right Ascension(J2000): $12h : 29m : 50s$
Declination(J2000): $+08° : 00' : 02''$
Constellation: Virgo
Apparent blue magnitude m_b: 9.27
Absolute blue magnitude M_b: -21.71
Morphological type: E2
De Vacouler parameter T: -4.8
Major axis position angle P.A.: 157°
Major axis half-light radius: 115.0″
Minor axis half-light radius: 93.15″
Axial ratio *b/a*: 0.81
Color index inside R_e $(B-V)_e$: 0.96
Radial velocity CZ: 974 Km/s
Environment: Virgo galaxy cluster.
Notes: LINER-Sy2 type nuclear activity.

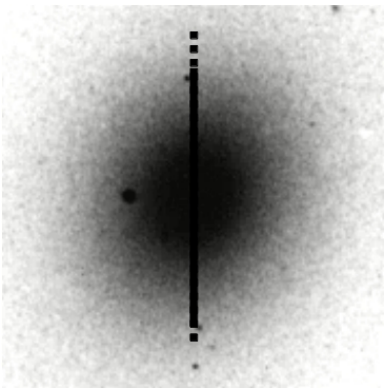

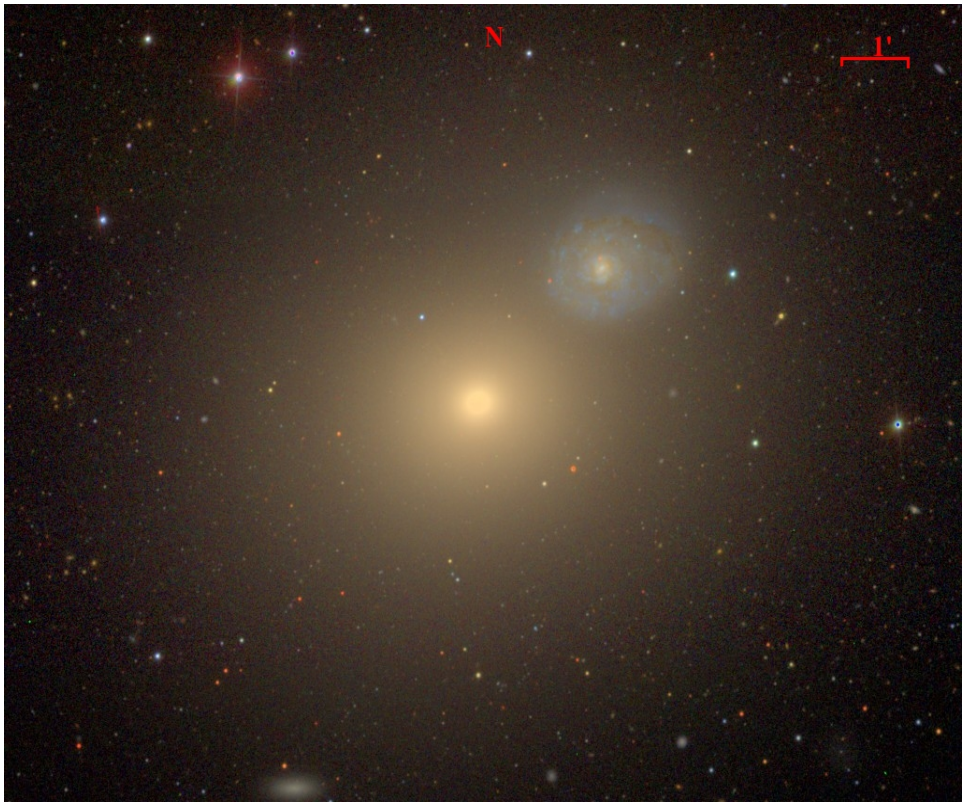

NGC4649

Cross-ID: M60, UGC-07898, PGC-042831
Right Ascension(J2000): $12h : 43m : 40s$
Declination(J2000): $+11° : 33' : 10''$
Constellation: Virgo
Apparent blue magnitude m_b: 9.83
Absolute blue magnitude M_b: -21.47
Morphological type: E2
De Vacouler parameter T: -4.6
Major axis position angle P.A.: 104°
Major axis half-light radius: 75.98″
Minor axis half-light radius: 61.54″
Axial ratio *b/a*: 0.81
Color index inside R_e $(B-V)_e$: 0.98
Radial velocity CZ: 1107 Km/s
Environment: In a pair, Virgo galaxy cluster

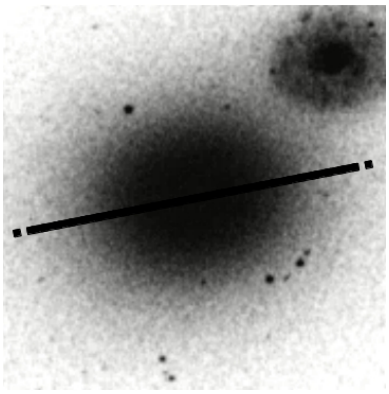

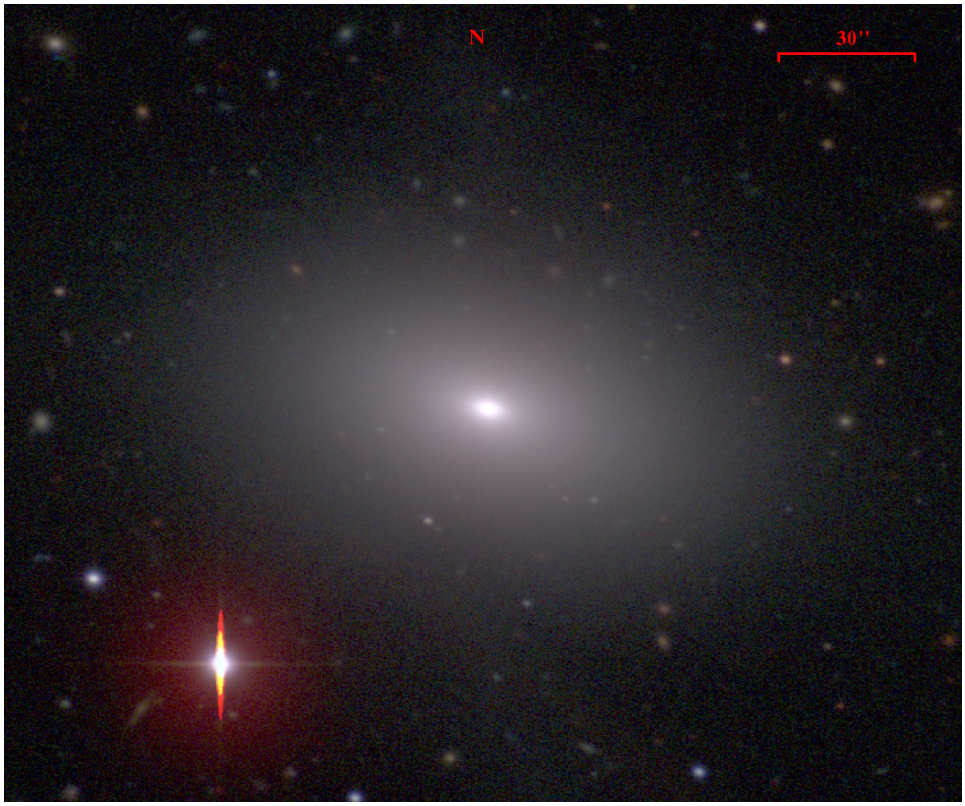

NGC4742

Cross-ID: UGCA-303, PGC-043594
Right Ascension(J2000): $12h : 51m : 48s$
Declination(J2000): $-10° : 27' : 17''$
Constellation: Virgo
Apparent blue magnitude m_b: 12.11
Absolute blue magnitude M_b: -19.35
Morphological type: E4
De Vacouler parameter T: -4.5
Major axis position angle P.A.: 76°
Major axis half-light radius: 14.19″
Minor axis half-light radius: 9.17″
Axial ratio *b/a*: 0.65
Color index inside R_e $(B-V)_e$: 0.75
Radial velocity CZ: 1272 Km/s
Environment: Group

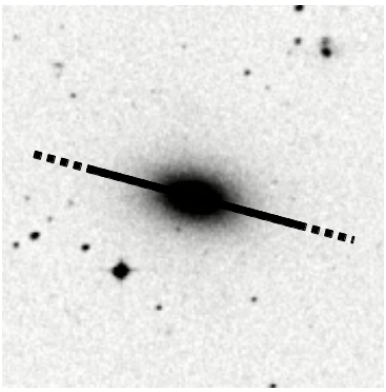

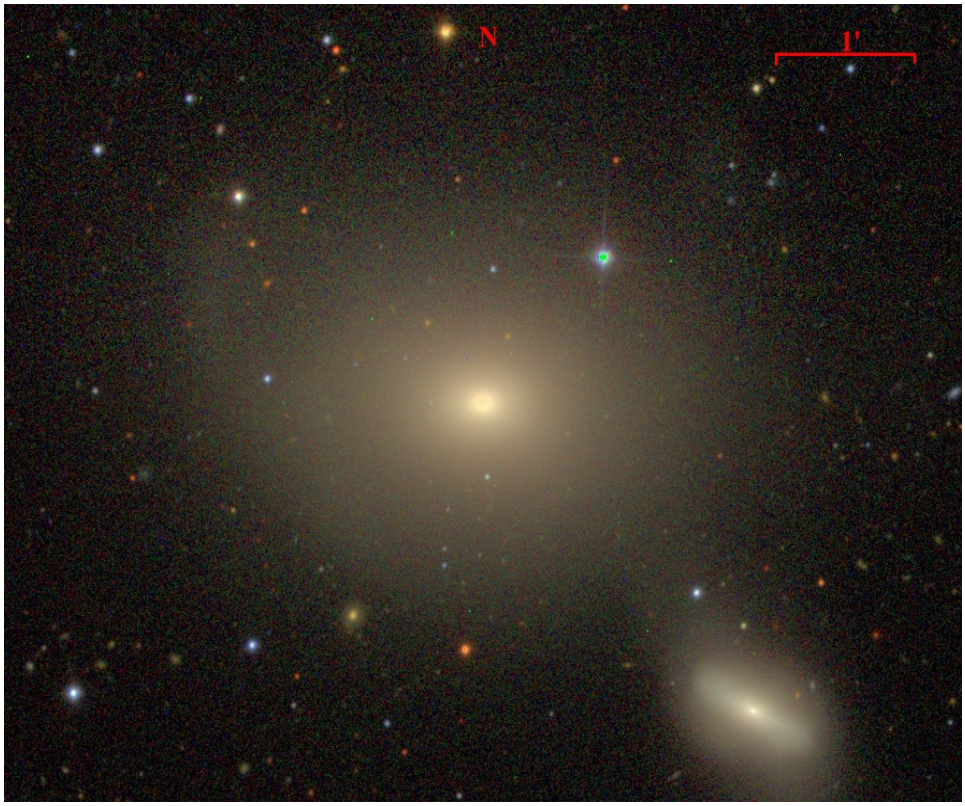

NGC5576

Cross-ID: UGC-09183, PGC-051275
Right Ascension(J2000): $14h : 21m : 04s$
Declination(J2000): $+03° : 16' : 16''$
Constellation: Virgo
Apparent blue magnitude m_b: 11.79
Absolute blue magnitude M_b: -20.14
Morphological type: E3
De Vacouler parameter T: -4.8
Major axis position angle P.A.: 90°
Major axis half-light radius: 21.82″
Minor axis half-light radius: 14.40″
Axial ratio *b/a*: 0.66
Color index inside R_e $(B-V)_e$: 0.87
Radial velocity CZ: 1525 Km/s
Environment: In a triplet
Notes: Very boxy isophotes, strongly twisted envelope.

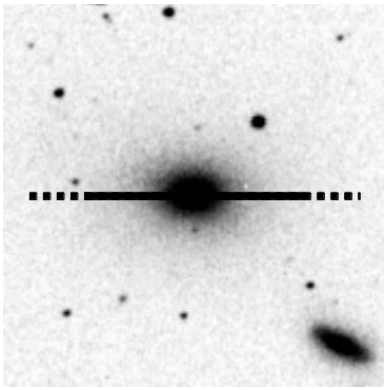

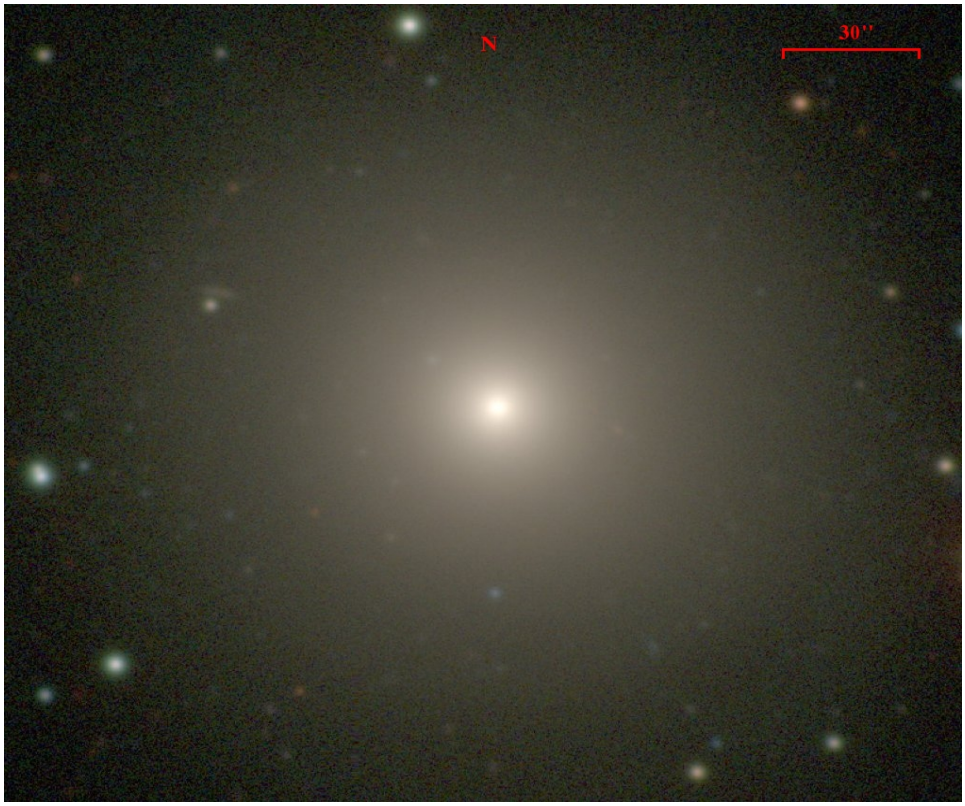

NGC5812

Cross-ID: UGCA-398, PGC-053630
Right Ascension(J2000): $15h : 00m : 56s$
Declination(J2000): $-07° : 27' : 26''$
Constellation: Libra
Apparent blue magnitude m_b: 12.19
Absolute blue magnitude M_b: -20.44
Morphological type: E0
De Vacouler parameter T: -4.8
Major axis position angle P.A.: 73°
Major axis half-light radius: 27.32″
Minor axis half-light radius: 23.76″
Axial ratio *b/a*: 0.87
Color index inside R_e $(B-V)_e$: 0.96
Radial velocity CZ: 1920 Km/s
Environment: In a pair

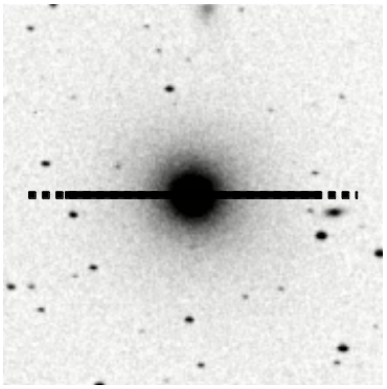

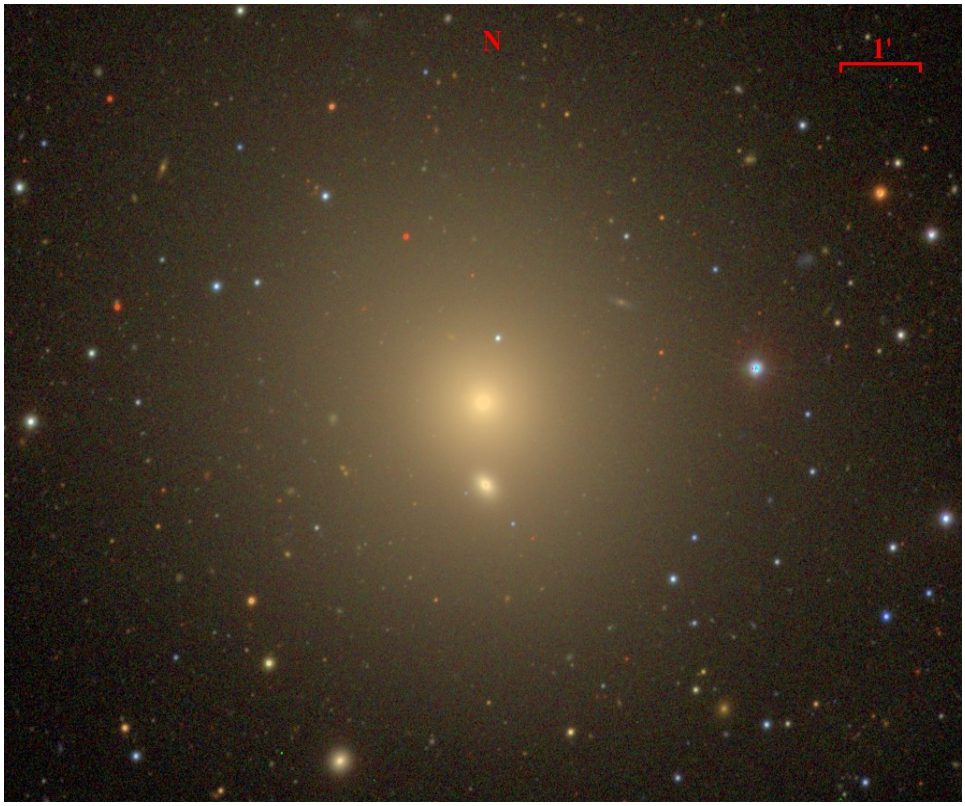

NGC5846

Cross-ID: UGC-09706, PGC-053932
Right Ascension(J2000): $15h : 06m : 29s$
Declination(J2000): $+01° : 36' : 20''$
Constellation: Virgo
Apparent blue magnitude m_b: 11.09
Absolute blue magnitude M_b: -21.26
Morphological type: E0
De Vacouler parameter T: -4.7
Major axis position angle P.A.: 0°
Major axis half-light radius: 64.29″
Minor axis half-light radius: 61.07″
Axial ratio *b/a*: 0.95
Color index inside R_e $(B-V)_e$: 0.98
Radial velocity CZ: 1722 Km/s
Environment: In a pair, group
Notes: Weak nuclear emission.

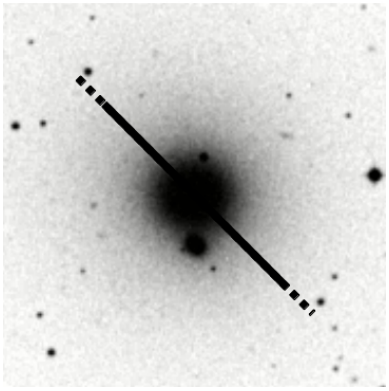

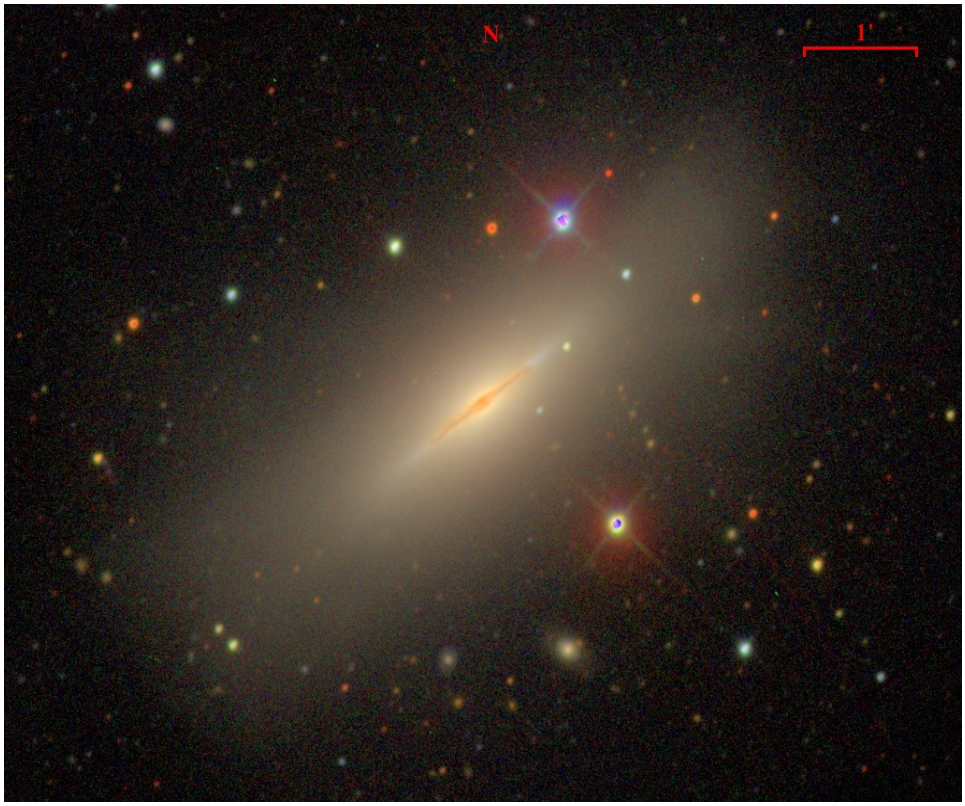

NGC5866

Cross-ID: Spindle Galaxy, M102, UGC-09723, PGC-053933
Right Ascension(J2000): $15h : 06m : 30s$
Declination(J2000): $+55° : 45' : 48''$
Constellation: Draco
Apparent blue magnitude m_b: 10.73
Absolute blue magnitude M_b: -20.00
Morphological type: S0-a
De Vacouler parameter T: -1.3
Major axis position angle P.A.: 128°
Major axis half-light radius: 56.95″
Minor axis half-light radius: 24.49″
Axial ratio *b/a*: 0.43
Color index inside R_e $(B-V)_e$: 0.92
Radial velocity CZ: 674 Km/s
Environment: In a triplet
Notes: AGN activity detected, strong dust lane.

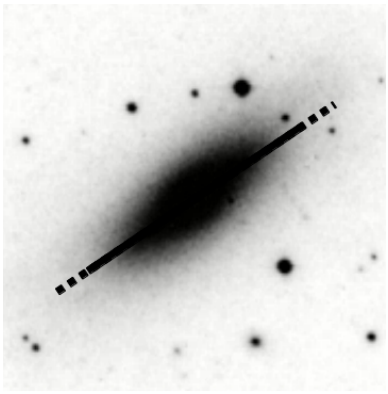

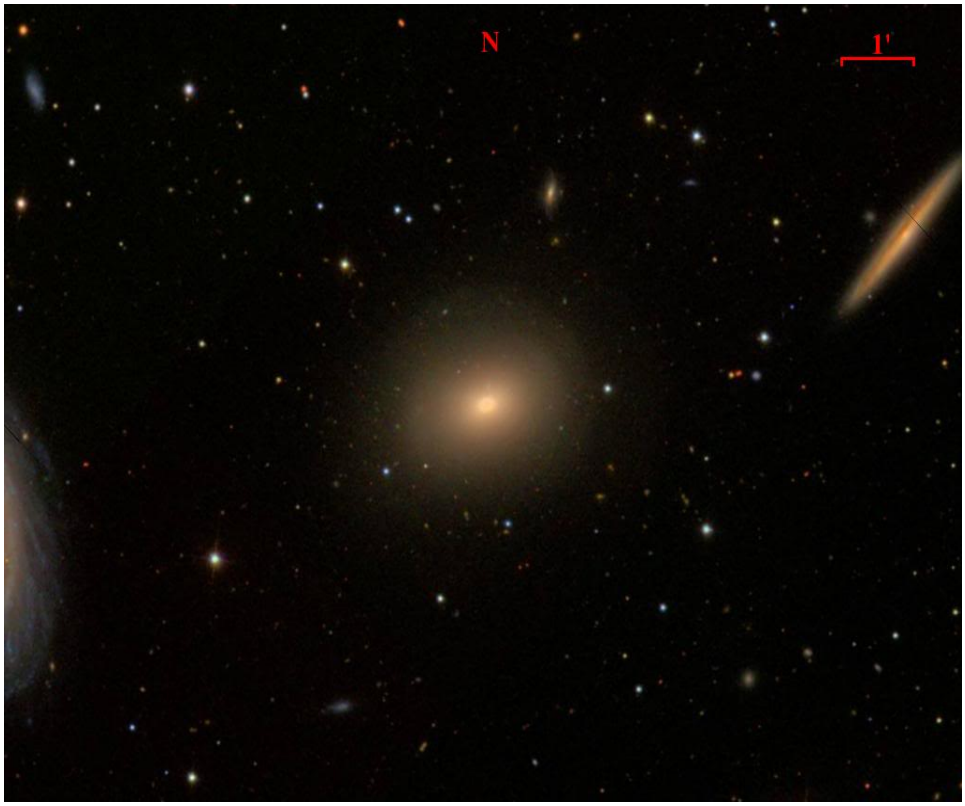

NGC5982

Cross-ID: UGC-09961, PGC-055674
Right Ascension(J2000): $15h : 38m : 40s$
Declination(J2000): $+59° : 21' : 21''$
Constellation: Draco
Apparent blue magnitude m_b: 11.98
Absolute blue magnitude M_b: -21.38
Morphological type: E3
De Vacouler parameter T: -4.8
Major axis position angle P.A.: 110°
Major axis half-light radius: 28.94″
Minor axis half-light radius: 18.81″
Axial ratio *b/a*: 0.65
Color index inside R_e $(B-V)_e$: 0.93
Radial velocity CZ: 2830 Km/s
Environment: In a triplet (Draco Trio)
Notes: Outer boxy isophotes, presence of shells.

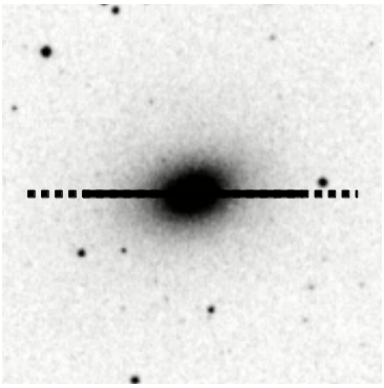

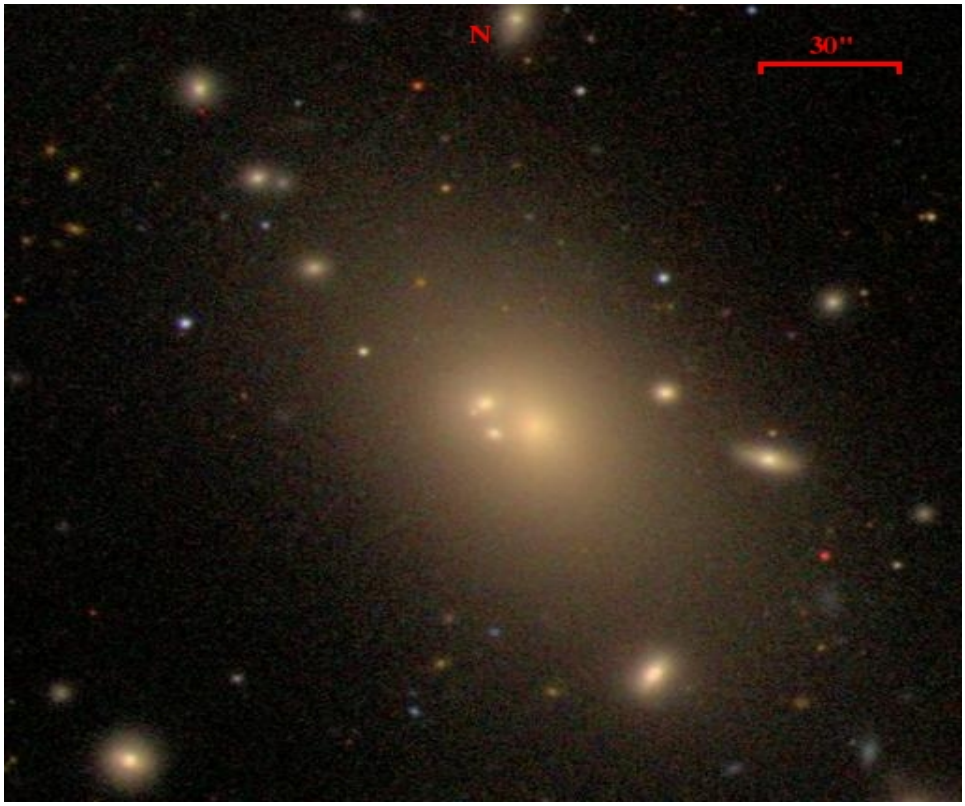

NGC6166

Cross-ID: UGC-10409, PGC-058265
Right Ascension(J2000): $16h : 28m : 39s$
Declination(J2000): $+39° : 33' : 06''$
Constellation: Hercules
Apparent blue magnitude m_b: 12.90
Absolute blue magnitude M_b: -22.96
Morphological type: cD2p
De Vacouler parameter T: -4.3
Major axis position angle P.A.: 35°
Major axis half-light radius: 55.36″
Minor axis half-light radius: 39.86″
Axial ratio *b/a*: 0.72
Color index inside R_e $(B-V)_e$: 1.02
Radial velocity CZ: 9296 Km/s
Environment: Abell 2199 galaxy cluster
Notes: Multiple optical nuclei, very steep spectrum radio source.

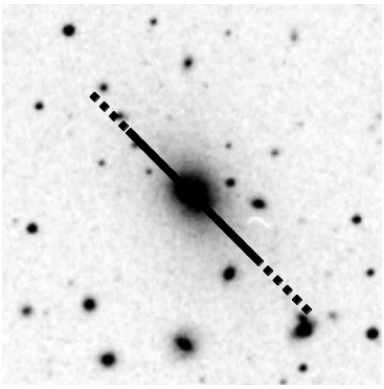

Chapter 3

Theoretical background and analysis tools

In the study of elliptical galaxies, several procedures have been used to retrieve kinematical information. All of them rely on a stellar template spectrum to approximate the unshifted and unbroadened spectrum of the galaxy in order to deduce radial velocity and velocity dispersion. The first developed approaches use a direct fit of a broadened template to the galaxy spectrum (Burbidge et al., 1961; Richstone and Sargent, 1972). Trough the minimization of a χ^2 function, the best parameter set for a given broadening model is chosen. Later devised methods operate in the Fourier space. The most famous of them are the Fourier Quotient method, developed by Sargent et al. (1977), which uses the quotient of template and object Fourier transforms to retrieve the convolution broadening function. Finally, the Cross-Correlation method, suggested by Simkin (1974) and later improved by Tonry and Davis (1979), evaluates redshift and velocity dispersion by the correlation between the two spectra. In this work we used the latter approach, as implemented in the IRAF package XCSAO. We present here a description of the algorithm as well as an overview of the corresponding IRAF package and, in conclusion, we summarize the main steps in the application to our data set.

3.1 Correlation analysis

Let $g(n)$ be the spectrum of a galaxy of unknown redshift and velocity dispersion and let $t(n)$ be a template rest frame spectrum with instrumentally broadened line profiles. The spectra are sampled into N bins, labelled with n such as:

$$n = A \ln \lambda + B. \tag{3.1}$$

This logarithmic binning assure that a velocity redshift causes an uniform linear shift. Then the spectra pass trough a series of operation, in particular:

- continuum removal;
- endmasking to prevent mismatches between the ends of the spectrum;

- Fourier filtering to remove low-frequency continuum variations and high-frequency noise components.

Let $G(k)$ and $T(k)$ be the corresponding discrete Fourier transforms defined in this way:

$$G(k) = \sum_{n=1}^{N-1} g(n) e^{-\frac{2\pi i k n}{N}} \tag{3.2}$$

and let σ_g and σ_t be the rms of the spectra:

$$\sigma_g^2 = \frac{1}{N} \sum_{n}^{N-1} g(n)^2. \tag{3.3}$$

We can now define the normalized cross-correlation function:

$$c(n) \equiv g \times t(n) = \frac{1}{N \sigma_g \sigma_t} \sum_m g(m) t(m-n) \tag{3.4}$$

and the relative Fourier transform:

$$C(k) = \frac{1}{N \sigma_g \sigma_t} G(k) T^*(k) \tag{3.5}$$

In order to find Redshift and Velocity Dispersion suppose that $g(n)$ is a multiple α of $t(n)$, shifted by a quantity δ and broadened by a convolution with a function $b(n)$:

$$g(n) \simeq \alpha t * b(n-\delta). \tag{3.6}$$

An estimate of the parameters α and δ is given by minimizing the expression:

$$\chi^2(\alpha, \delta; b) = \sum_n [\alpha t * b(n-\delta) - g(n)]^2, \tag{3.7}$$

which weights quadratically any deviation from zero so that strong lines are more relevant than weak ones. Accounting that the noise derives mainly from the Poisson fluctuation of the continuum, the error in determining the lines shift depends inversely to the line strength. Thus this weighting scheme seems to be advantageous. Eq.(3.7), in Fourier space, can be written:

$$\chi^2(\alpha, \delta; b) = \sum_k [\alpha T(k) B(k) e^{-\frac{2ik\pi\delta}{N}} - G(k)]^2. \tag{3.8}$$

Rewriting χ^2 as

$$\chi^2(\alpha, \delta; b) = \alpha^2 \sum t*b(n-\delta)^2 - 2\alpha \sum t*b(n-\delta) g(n) + \sum g(n)^2 = \alpha^2 N \sigma_{t*b}^2 - 2\alpha N \sigma_g \sigma_t c*b(\delta) + N\sigma_g^2, \tag{3.9}$$

where σ_{t*b} is:

$$\sigma_{t*b} = \sqrt{\frac{1}{N}\sum (t*b)^2}. \tag{3.10}$$

Minimization with respect to α lead to

$$0 = \frac{\partial \chi^2}{\partial \alpha} = 2N[\alpha\sigma^2_{t*b} - \sigma_t\sigma_g c*b(\delta)] \Rightarrow \alpha_{min} = \frac{\sigma_t\sigma_g}{\sigma^2_{t*b}} c*b(\delta). \tag{3.11}$$

Substituting in 3.9 yields

$$\chi^2(\alpha_{min}, \delta; b) = N\sigma_g^2\left(1 - \frac{\sigma_t^2}{\sigma^2_{t*b}}[c*b(\delta)]^2\right). \tag{3.12}$$

Thus it results that the minimization of the eq.(3.7) requires the maximization of

$$\frac{1}{\sigma_{t*b}} c*b(\delta).$$

3.1.1 Setting redshift

In order to continue and find a value for the shift, we need to make some assumption about t, c and b :

- Let $b(n)$ be a Gaussian of dispersion σ:

$$b(n) = \frac{1}{\sqrt{2\pi\sigma}} e^{-\frac{n^2}{2\sigma^2}}, \tag{3.13}$$

$$B(k) = e^{-\frac{(2\pi\sigma k)^2}{2N^2}}. \tag{3.14}$$

- Assume that the largest peak of $c(n)$ is approximable with a Gaussian centred in δ and with dispersion μ:

$$c(n) \simeq c(\delta) e^{-\frac{(n-\delta)^2}{2\mu^2}}, \tag{3.15}$$

$$C(k) = \sqrt{2\pi}\mu c(\delta) e^{-\frac{(2\pi\mu k)^2}{2N^2}} e^{-\frac{2\pi i\delta k}{N}}. \tag{3.16}$$

- Assume also that $t(n)$ has a Gaussian shaped Fourier transform amplitude, with unconstrained phases and a dispersion related to the width τ of a typical spectral feature:

$$|T(k)| = \sigma_t(2\pi N\tau)^{1/2} e^{-\frac{(2\pi\tau k)^2}{2N^2}}. \tag{3.17}$$

At this point, using the approximate formula

$$\sum_n e^{-n^2/\sigma^2} \simeq \sqrt{\pi}\sigma, \tag{3.18}$$

we can rewrite σ_{t*b} and $c * b(\delta)$:

$$\begin{aligned}\sigma^2_{t*b} &= \frac{1}{N}\sum t * b(n)^2 = \frac{1}{N^2}\sum |T(k)B(k)|^2 \\ &= \frac{1}{N^2}\sigma_t^2 \frac{2\pi N\tau}{\sqrt{\pi}} \sum e^{-\left(\frac{2\pi\tau k}{N}\right)^2} e^{-\left(\frac{2\pi\sigma k}{N}\right)^2} \\ &= \sigma_t^2 \frac{\tau}{\sqrt{\sigma^2+\tau^2}},\end{aligned} \tag{3.19}$$

$$\begin{aligned}c * b(\delta) &= \frac{1}{N}\sum_k C(k)B(k)e^{\frac{2ik\pi\delta}{N}} \\ &= \frac{1}{N}\sqrt{2\pi}\mu c(\delta)\sum e^{-\frac{(2\pi\mu k)^2}{2N^2}} e^{-\frac{(2\pi\sigma k)^2}{2N^2}} \\ &= c(\delta)\frac{\mu}{\sqrt{\mu^2+\sigma^2}},\end{aligned} \tag{3.20}$$

where δ is taken as the centre of the largest peak of $c(n)$.

3.1.2 Setting the velocity dispersion

The estimation of σ can be found by maximizing χ^2:

$$\begin{aligned}0 &= \frac{\partial}{\partial\sigma}\frac{1}{\sigma_{t*b}} c * b(\delta) = 2\sigma\frac{\partial}{\partial\sigma^2}\frac{1}{\sigma_{t*b}} c * b(\delta) \\ &= \frac{\mu\sigma c(\delta)}{2\sigma_t\sqrt{\tau}}(\sigma^2+\tau^2)^{-3/4}(\sigma^2+\mu^2)^{-3/2}[\sigma^2+\mu^2-2(\sigma^2+\tau^2)].\end{aligned} \tag{3.21}$$

This yields to

$$\sigma^2 = \mu^2 - 2\tau^2, \tag{3.22}$$

which accounts for the fact that the width of the correlation peak is a quadratic sum of the velocity broadening width and two, instrumentally broadened, stellar widths. Recapitulating, the cross-correlation peak is fitted by a symmetric function. *Thus, the parameters of the fit, in conjunction with the width of the template, provides values for α, δ and σ.*

3.1.3 Error treatment

The largest peak of $c(n)$ is selected as the redshift peak. Trough fitting a smooth curve we can retrieve estimates for δ, h and w, respectively position, height and FWHM of the peak. These values can deviate from the true ones. Even tough statistical counting errors are present, the major font of uncertainty are the mismatches between the galaxy and the

template spectra. Regardless of the error causes, we can see $c(n)$ as a combination of a perfect correlation function between the spectra, plus a residual function:

$$c(n) = h_0 t * b \times t(n - n_0) + a(n). \tag{3.23}$$

Because the first addend in the right hand term is symmetric around n_0, the antisymmetric part of $c(n)$ is equal to antisymmetric part of $a(n)$. Assuming that the symmetric and antisymmetric part of $a(n)$ have equal rms, we define the parameter

$$R = \frac{h}{\sqrt{2}\sigma_a}, \tag{3.24}$$

where

$$\sigma_a \simeq \frac{1}{2N} \sum [c(\delta + n) - (\delta - n)]^2. \tag{3.25}$$

The parameter R is the ratio between the true peak and the average peak in $a(n)$ and can be shown that the error on the shift:

$$\varepsilon = \frac{N}{8B} \frac{1}{1 + R}, \tag{3.26}$$

where B is the highest wave number where $C(k)$ shows appreciable amplitude. An analogous procedure about w give the expected error on the FWHM of the correlation peak

$$\Delta w \approx \varepsilon.$$

Using eq.3.22 we can derive the error on the velocity dispersion:

$$\Delta\sigma^2 = 2(\mu^2 \Delta\mu^2 + 4\tau^2 \Delta\tau^2 + \sigma^4)^{1/2} - 2\sigma^2. \tag{3.27}$$

3.2 The RVSAO package

RVSAO is an IRAF add-on package developed at the Smithsonian Astrophysical Observatory Telescope Data Center to obtain radial velocities from spectra using cross-correlation and emission line fitting techniques. The package is composed of about a dozen of tasks, many of which play an ancillary role for the two major tasks represented by XCSAO and EMSAO. In detail, the routines implemented are:

XCSAO Extracts redshifts and velocity dispersions using cross correlation methods;

EQWIDTH Computes equivalent widths for rest-wavelength-specified spectral lines;

SUMSPEC Sums spectra to create a composite spectrum (added in 2.0);

LINESPEC Creates an artificial spectrum from a list of spectral lines (added in 2.0);

WL2PIX Return the number of the pixel in a spectrum which corresponds to a specified wavelength;

LISTSPEC List pixel, wavelength, and value of specified piece of a spectrum;

EMSAO Finds redshifts using emission line shifts;

CONTPARS Sets parameters for continuum removal in XCSAO, EMSAO and EQWIDTH;

CONTSUM Sets parameters for continuum removal in SUMSPEC;

BCVCORR Sets barycentric velocity correction for non-standard header parameters;

PIX2WL Return the wavelength of a specified pixel in a spectrum ;

RELEARN Sets values in the parameter file of the new version of a task from the current values.

Hereunder we describe the main features of XCSAO and EMSAO as well as the setting utilized in the extraction of our data.

3.2.1 The XCSAO task

As mentioned, XCSAO is the task deputed to the extraction of kinematical information from the spectrum absorption features. It implements the cross-correlation method seen above and is subdivided in the following operating steps:

- Preprocess Spectra (XCFIT subroutine).
- Set up Template (XCFIT subroutine).
- Compute Velocity Zero Point (XCFIT subroutine).
- Process Spectrum/Template Pair (XCORFIT subroutine).
- Remove Continuum (ICSUBCON subroutine).
- Replace Lines with Continuum (ICSUBCON subroutine).
- Apodize (XCORFIT subroutine).
- Fourier Transform and Filter (XCORFIT subroutine).
- Cross-Correlate (XCORFIT subroutine).
- Report Results (XCFIT subroutine).
- Combine Emission and Cross-Correlation Velocities (VCOMBINE).
- Display Results Graphically (XCPLOT subroutine)(See fig. 3.1).
- Save Results in Image Header (XCFIT subroutine).

Each of these procedures can be personalized by changing a set of operative parameters. A full description of the subroutines and of the related parameters can be found in the online documentation of the task. The parameters set used in our correlations is listed in Tab. 3.1.

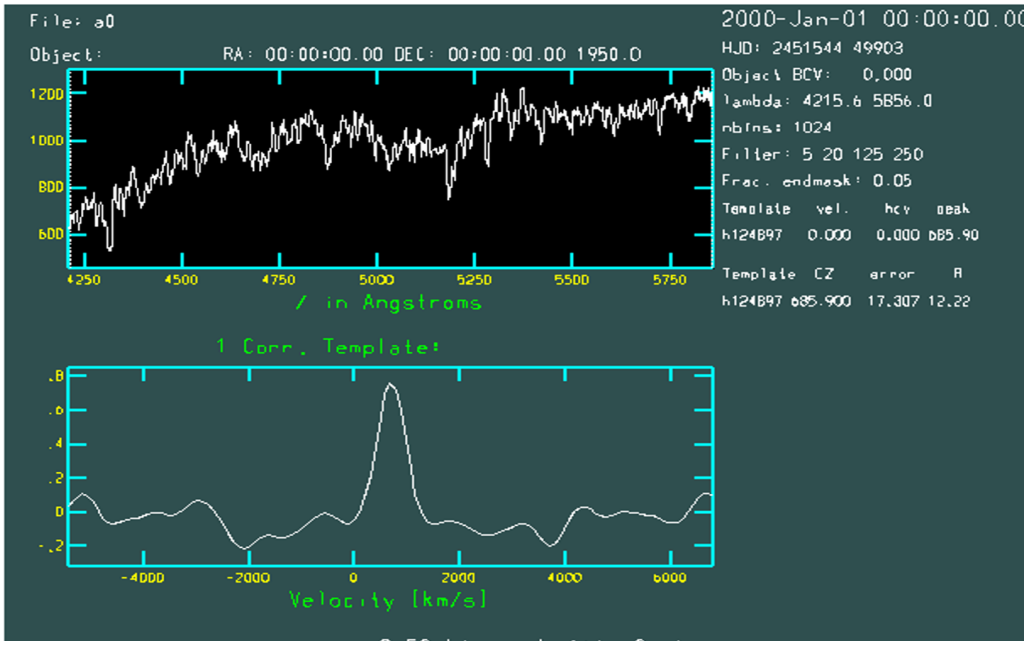

Figure 3.1 *Example of XCSAO output frame. With this graphic mode, the object spectrum is displayed in the upper panel while below is shown the correlation peak. On the right there are basic informations about correlation for each template used.*

Table 3.1: *XCSAO parameters set used*

Parameter	Value
spectra	*<Spectrum name>*
specnum	0
specban	0
specdir	*<Spectrum path>*
correla	velocity
template	*<Template name>*
tempnum	0
tempban	1
tempdir	*<Template path>*
echelle	no
st_lambda	*<Variable (see §3.3.2)>*
end_lambda	INDEF
obj_plot	no
xcor_plot	no
fixbad	no
badline	0

Continues in the next page

Continues from previous page

Parameter	Value
s_emcho	yes
t_emcho	no
s_abs_r	*<Variable (see §3.3.2)>*
s_em_re	*<Variable (see §3.3.2)>*
t_abs_r	0
t_em_re	0
bell_wi	0.05
renorma	no
ncols	1024
interp_	spline3
zeropad	no
low_bin	5
top_low	20
top_nru	125
nrun	250
vel_ini	zero
czguess	0
nzpass	0
tshift	0
svel_co	barycentric
tvel_co	file
pkmode	1
pkfrac	0.5
pksrch	25
minvel	-10000
maxvel	10000
report	2
logfile	STDOUT,xcsao.log
save_ve	no
rvcheck	no
archive	no
nsmooth	0
cvel	INDEF
dvel	INDEF
ablines	ablines.dat
emlines	emlines.dat
linedir	rvsao$lib/
dispmod	1
displot	yes
device	stdgraph

Continues in the next page

Continues from previous page

Parameter	Value
vel_plot	correlation
curmode	no
hardcop	no
plotter	stdplot
temp_pl	no
contsub	no
apodize	no
fft_plo	no
tfft_p	no
uxcor_p	no
nsum	1
debug	no
cursor	
mode	ql

3.2.2 The EMSAO task

EMSAO is an IRAF task in the rvsao package which finds emission lines, computes redshifts for each identified line, and combines them into a single radial velocity. The results may be graphically displayed and/or printed in several formats. As XCSAO, is subdivided in several customizable operative subprocedures, in detail:

- Read Spectrum (EMFIT).
- Sky Spectrum for Noise Calculations (EMFIT).
- Preprocess Spectrum.
- Remove continuum for line search (ICSUBCON).
- Initial Redshift (EMFIT).
- Find Initial Redshift (EMGUESS).
- Find Bright Emission Lines (EMFIND).
- Find All Emission Lines (EMSRCH).
- Find Emission Lines (EMFIND).
- Keep Brightest Emission Lines (EMSRCH).
- Smooth Spectrum for Line Fit (EMFIT).
- Remove Continuum for Line Fit (ICSUBCON).

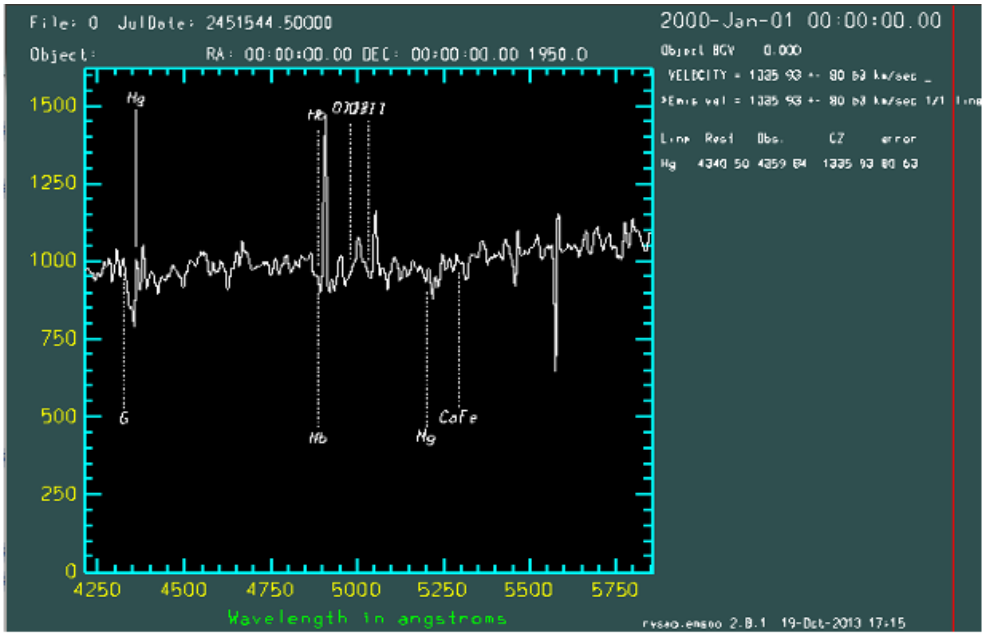

Figure 3.2 *Example of EMSAO output frame. The present displaying modality show object spectrum in the box, along with spectral features recognized. On the right there are informations about velocity for each line used.*

- Fit Emission Lines (EMLFIT).
- Fit Single Velocity (EMVFIT).
- Adjust Combined Velocity and Error (EMFIT).
- Combine Emission and Cross-Correlation Velocities (VCOMBINE).
- Print Results (EMFIT).
- Display Results Graphically (EMPLOT)(See fig. 3.2).
- Save Results in Image Header (EMFIT).

Although we recommend to consult the documentation for further comprehension of this complex algorithm, a clarifier flow chart of how it works can be found in Fig. 3.3. A full description of the operative setting is available in Tab. 3.2

Table 3.2: *EMSAO parameters set used*

Parameter	Value
spectra	*<Spectrum name>*
specnum	0
specban	0
skynum	0
skyband	0
specdir	*<Spectrum path>*
linefit	yes
fixbad	no
badline	badlines.dat
renorma	no
st_lambda	INDEF
end_lambda	INDEF
nsmooth	10
vel_ini	guess
czguess	*<Approximate galaxy cz>*
cortemp	
wspan	12
linesig	1.5
emsearch	emsearch.dat
emlines	emlines.dat
linedir	rvsao$lin/
npfit	2
nlcont	1
esmooth	0
emcombi	emcomb.dat
mincont	0
lwmin	0.4
lwmax	1.7
lsmin	1
sigline	0
disperr	0.01
vel_cor	barycentric
report	1
archive	no
save_ve	no
verbose	yes
logfile	STDOUT,emsao.log
device	stdgraph
hardcop	no

Continues in the next page

Continues from previous page

Parameter	Value
displot	yes
plotter	stdplot
dispmod	2
vel_plo	emission
curmode	yes
dispem	yes
dispabs	yes
ablines	ablines.dat
obj_plo	no
contsub	no
debug	no
nsum	1
cursor	
mode	ql

3.3 Application to the data

In order to effectively apply the cross-correlation method an amount of preliminary work was needed. The quadratic weighting scheme of the cross-correlation algorithm makes the nominal output extremely sensitive to any spurious peak in the spectra. *For this reason, special care must be devised to properly remove cosmic rays, bad pixels and poor-subtracted sky lines (we will shortly refer to all of them as "cosmic rays"), especially in the region with low signal.* To mitigate this problem several measures have been taken. First of all, the two dimensional spectra were smoothed along the spatial axis using a 7-pixels median window. We only operate in the spatial dimension to avoid any loose of information in the wavelength domain. A median smoothing algorithm was chosen instead of a mean one because the former one is more efficient in the removal of cosmic rays.

3.3.1 Sampling the radial profiles

After the smoothing, the spectra were spatially binned in slices of increasing width, moving away from the galaxy photometric centre. The centre was located by looking at the maximum of the light profile of the galaxy in each separate frame. For those spectra with low signal or a clearly distorted light profile, a cumulative profile was computed from all the frames in order to better estimate the galaxy centre. We chose to extract the data from each individual frame to avoid any spatial and spectral broadening while stacking the images. In addition,the individual frames of the same galaxy allowed, in principle, an independent estimate of the internal error of our measures. Only in the cases of NGC2764 and NGC1587/88 the signal was too low to obtain reliable measures and we needed to sum up all the images together. The minimum binning width was set to be greater than the seeing of the respective night. Tough there wasn't used a rigorous method to set the width of each

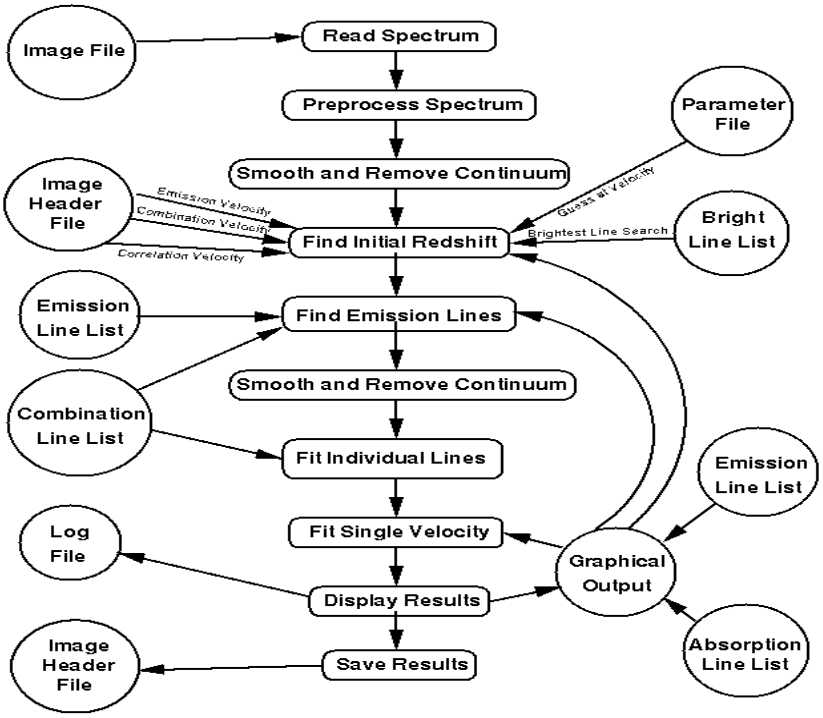

Figure 3.3 *EMSAO algorithm flow chart*

slice, we tried to do a reasonable binning by looking at an estimate of the S/N of the spectra and at the Fourier power parameter R (Tonry and Davis, 1979), obtained by correlating the spectra with a chosen template (HD63302). We aimed at maintaining a roughly constant S/N for all the slices. Clearly, such a performance was difficult to fulfill, especially far away from the galaxy centre, so we had to eventually relax our S/N constraints at large radii. The spatial coordinate assigned to each slice is the flux barycentre computed from the light profile.

3.3.2 Template correlation

Once binned, all the spectra were correlated against all the template of the respective observing run (respectively 14 and 6 for the 1996 and the 1997 runs) and against the central slice of the relative frame. During correlation, where needed, a sigma clipping and a short wavelength cut were applied. Sigma clipping was used to further mitigate cosmic rays influence. Because spectra with higher signal have a smaller Poissonian dispersion, a greater clipping threshold or even no clipping was adopted, generally, for the central regions. Clipping thresholds of 2 or 3 sigma, in both absorption and emission were used. The cut in the blue region of the spectra accounts for the lower sensibility of the CCD in this spectral range, so excluding this part of the spectrum with intrinsic higher Poissonian noise could, in principle, be useful. Short wavelength cuts were made at 4300, 4400 or 4500Å. Each slice was then correlated against the test template to evaluate the necessity and, in case, the

best value for sigma-clipping and wavelength cut.

3.3.3 Results management

After the correlation, the radial velocities obtained were corrected to account for Earth motion. Even after heliocentric correction, residual scatter in radial velocity remained. However, as we were interested in the rotation curve, after we have verified that the scatter was practically constant along all the bins, from all the values was subtracted the radial velocity of the central bin. *In this way we obtained a set of coherent, within statistical scatter, rotation curves.* To obtain velocity dispersion, we used eq.(3.22), where the instrumental broadening was estimated by cross-correlating the template stars against each other and the relative error $\Delta\tau$ was assumed to be the $r.m.s.$ of the values around the mean. Then, the values of radial velocity and velocity dispersion were averaged over all the template. Correlation HWHM were also averaged and the $r.m.s.$ around the mean was taken as $\Delta\mu$.

Where emission lines were detected, we used the IRAF task EMSAO, previously introduced, to estimate a rotation curve for the gas component. Due to the spectral range, the main part of information derived only from O[III] at 5007Å, so a manual check of the results was possible. To compare absorption and emission rotation curves, the velocity obtained with EMSAO were referred to the stellar rest frame averaged over all the absorption velocity profiles. Finally, velocity dispersion profiles and rotation curves obtained from template correlation, core correlation and emission lines were averaged over all the frames. As a last step, a mean stellar rotation curve was obtained averaging template and core data. Note that each time we mention an averaging procedure, the uncertainties of the data are used, where possible, as weights and the error σ_μ on the mean value μ is computed from all the individual uncertainties, according, for instance, to Bevington & Robinson (2003):

$$\mu = \frac{\sum(x_i/\sigma_i^2)}{\sum(1/\sigma_1^2)}, \tag{3.28a}$$

$$\sigma_\mu^2 = \frac{1}{\sum(1/\sigma_i^2)}, \tag{3.28b}$$

where x_i is a sperimental value and σ_i its relative uncertainty. Errors for the radial velocities are supplied by XCSAO and EMSAO tasks. The errors for the velocity dispersions are computed using eq.(3.27).

Chapter 4

Kinematical results

In this section we present the kinematic results we obtained by applying the method previously described. We traced both rotation and velocity dispersion profiles typically out to one R_e, although, in some cases, outer limits can extend rather beyond or within this value. Where detected, gas kinematics was also reconstructed as far as possible. For those galaxies observed in two different nights we preferred to assess the different profiles individually. This decision derives mainly because the position angle sampled was different (NGC3489) or because the spectra were acquired in two different observative runs (NGC4382). Those galaxies, then, will figure two times in all the plot and the tables relative to any physical property inferred from the profiles. For galaxies showing net rotation, the curves were also folded to allow an easier estimate of the mean rotation velocity. Finally, to assess the goodness of our data, an exhaustive bibliographic research was done to compare our results with other studies in the recent literature.

4.1 Stellar component

The first thing to note about our profiles is that, although we computed a nominal error for the velocities (using, as a start point, the internal error of XCSAO for the radial velocities and eq.(3.27) for velocity dispersions, and then computing a new error after each averaging procedure), the data present an amount of scatter that we think is an indicator of a greater "practical" uncertainty. Nevertheless, the kinematic information we retrieved from the analysis of the stellar component light resulted very interesting. Almost all galaxies seem to show a detectable amount of rotation along the sampled direction (in most cases matching the major axis). Only four cases, i.e. NGC4365, NGC4374, NGC5846 and an observation of NGC4382, didn't allow us to detect any appreciable amount of rotation.

Peculiar is the case of NGC3607, for which we detected a clear and definite Kinematically Decoupled Core (hereafter KDC). Another case of interest is that of NGC5866: the photometric profile along the slit showed a secondary peak of light offsetted from the centre by about 32" (Fig. 4.1). A direct inspection with imaging catalogues confirmed this feature to coincide with a bright, compact source. The radial velocities obtained showed that this object is not only tied to the NGC5866 system (probably being a giant globular cluster or

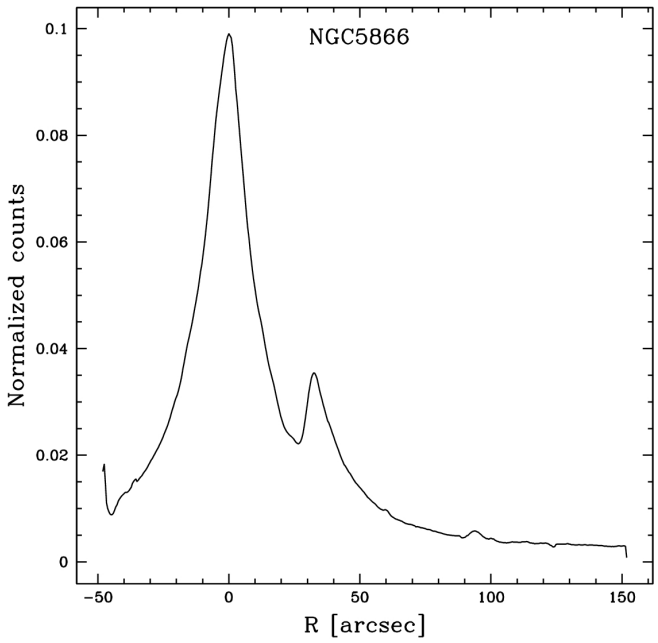

Figure 4.1 *Photometric profile of NGC5866 along the sampled PA (*124°*). The secondary peak of light is evident at about 32" far from the centre.*

a dwarf spheroidal) but its kinematic is also coherent with the large scale rotation of the parent galaxy.

Velocity dispersion profiles show a greater amount of scatter compared with the rotation curves but from the majority of them a trend can nevertheless be inferred. The profiles obtained can be divided into two groups: the ones constant along the radius (e.g. NGC3607, NGC4649 or NGC5846) and the ones that shows a decrease along the radius (this is the case of NGC3245, NGC4111 or NGC4278 for example). Taking into account these profiles, we can attribute a mean scatter to our data, at least in the central regions, not greater than 10%. The profiles are showed in Fig.s 4.2 to 4.25

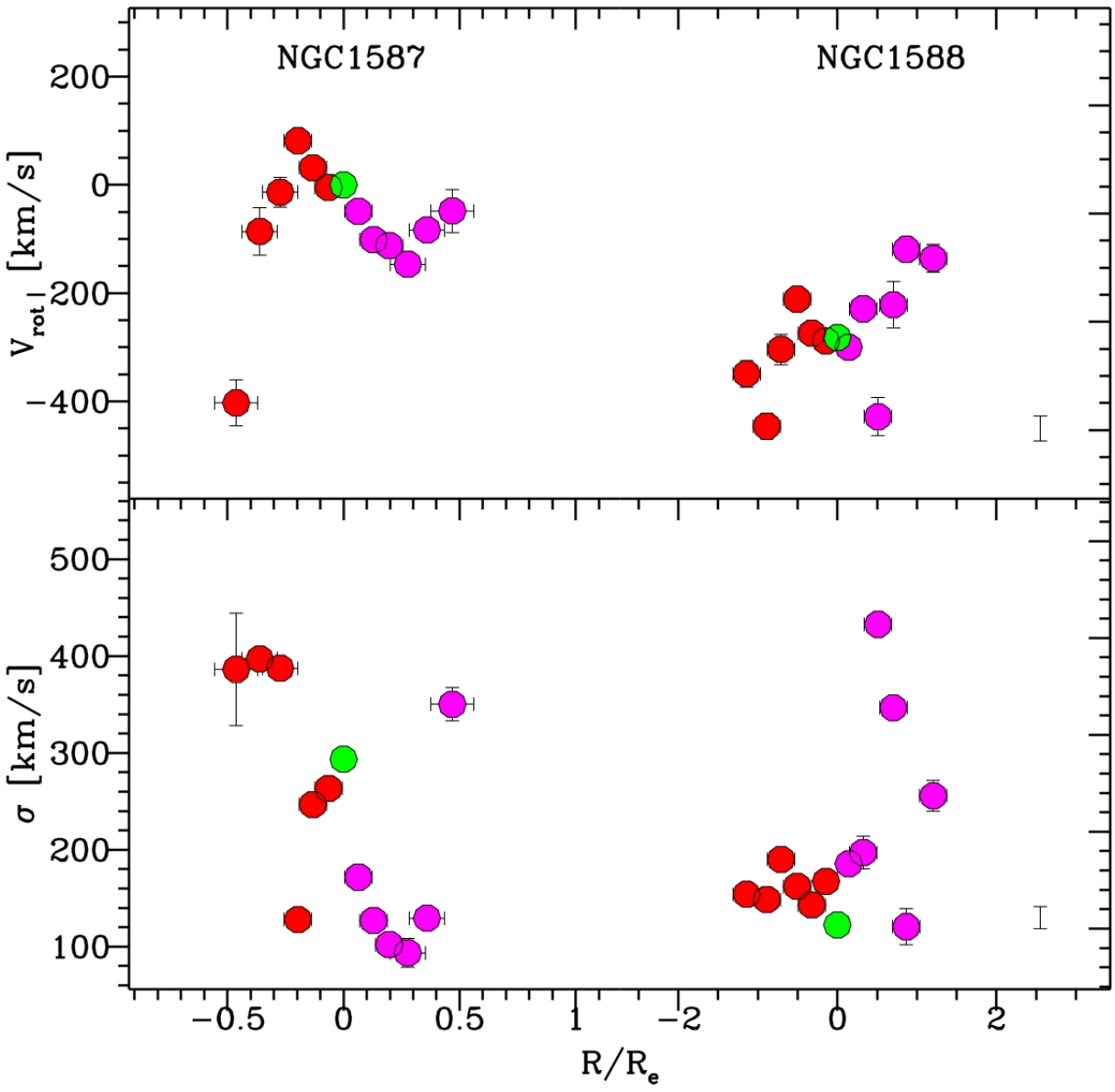

Figure 4.2 *Kinematic profiles of NGC1587 and NGC1588. The upper panel shows the rotation curve while the lower one shows the velocity dispersion profile. The green point represent the photometric centre of the galaxy, the red and the purple ones represent the two sides of the galaxy. Vertical error bars represent the nominal error, computed as explained in § 3, while horizontal error bars represent the width of the bin used for the cross-correlation. Since vertical bars are often too small to be seen, a typical error bar for the stellar component velocity is placed in the lower right corner of each panel.*

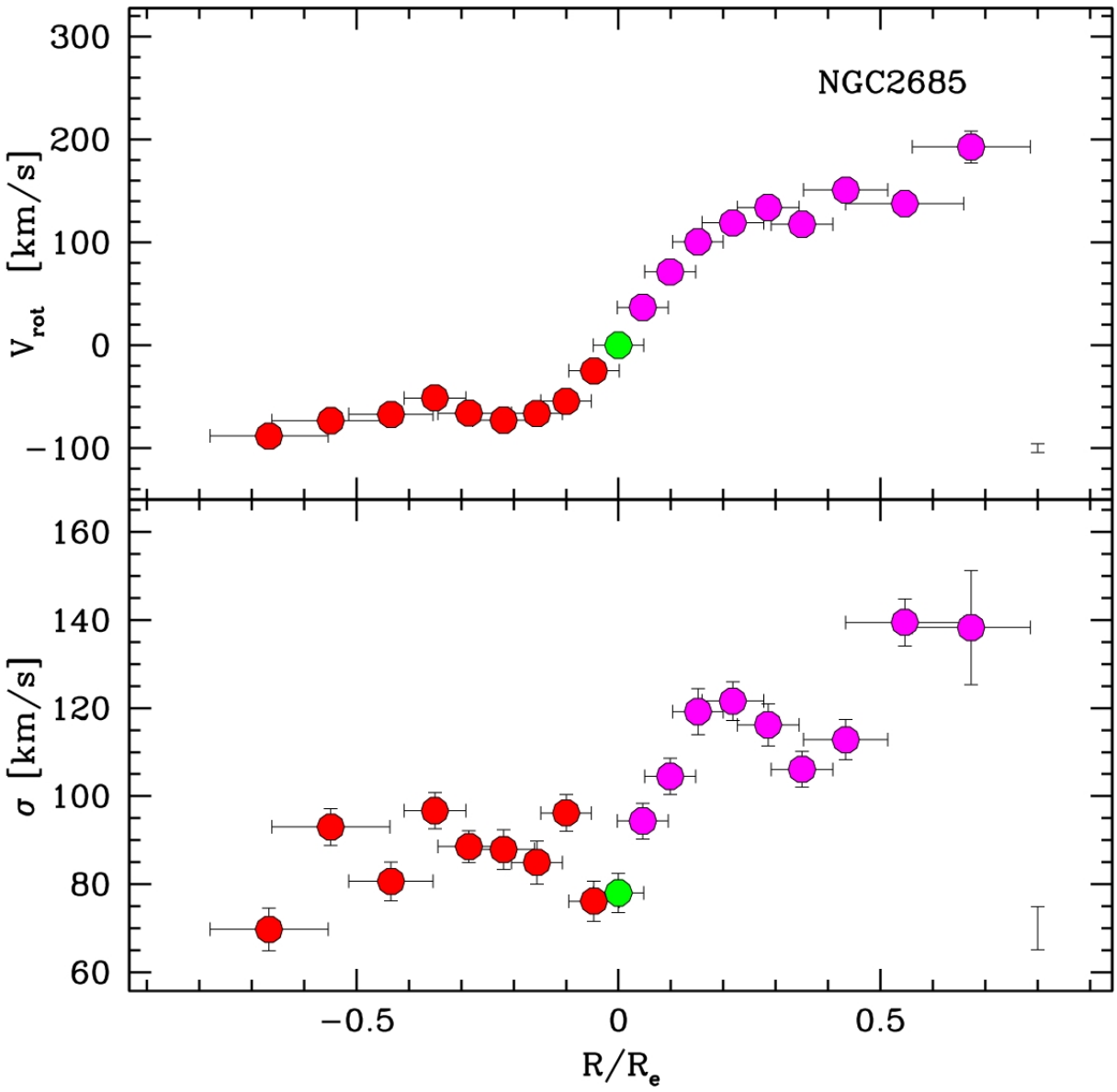

Figure 4.3 *Same of Fig. 4.2 but for NGC2685*

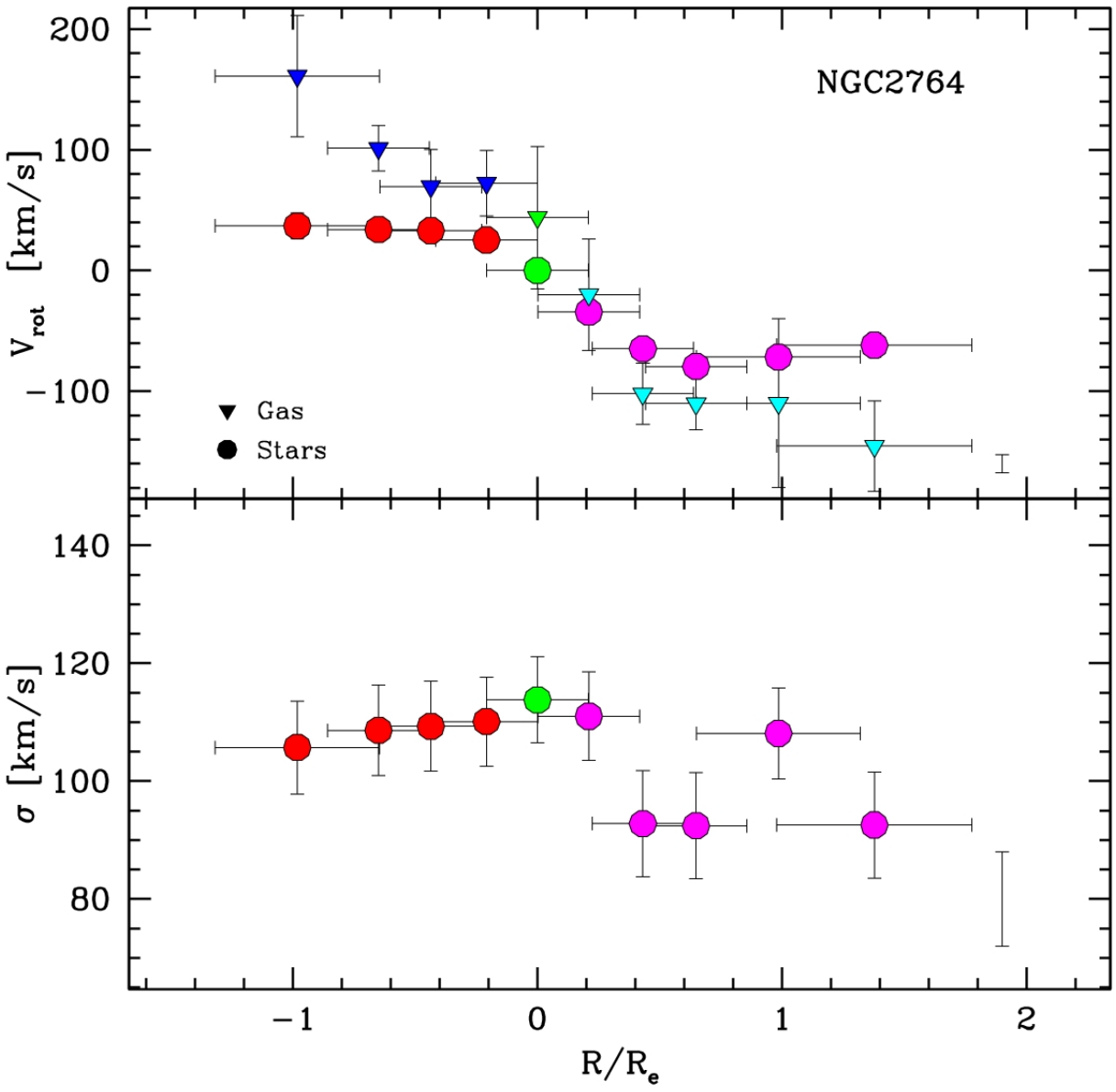

Figure 4.4 *Same of Fig. 4.2 but for NGC2764. The gas kinematic is traced by the triangles where blue and cyan points represent the two sides of the galaxy*

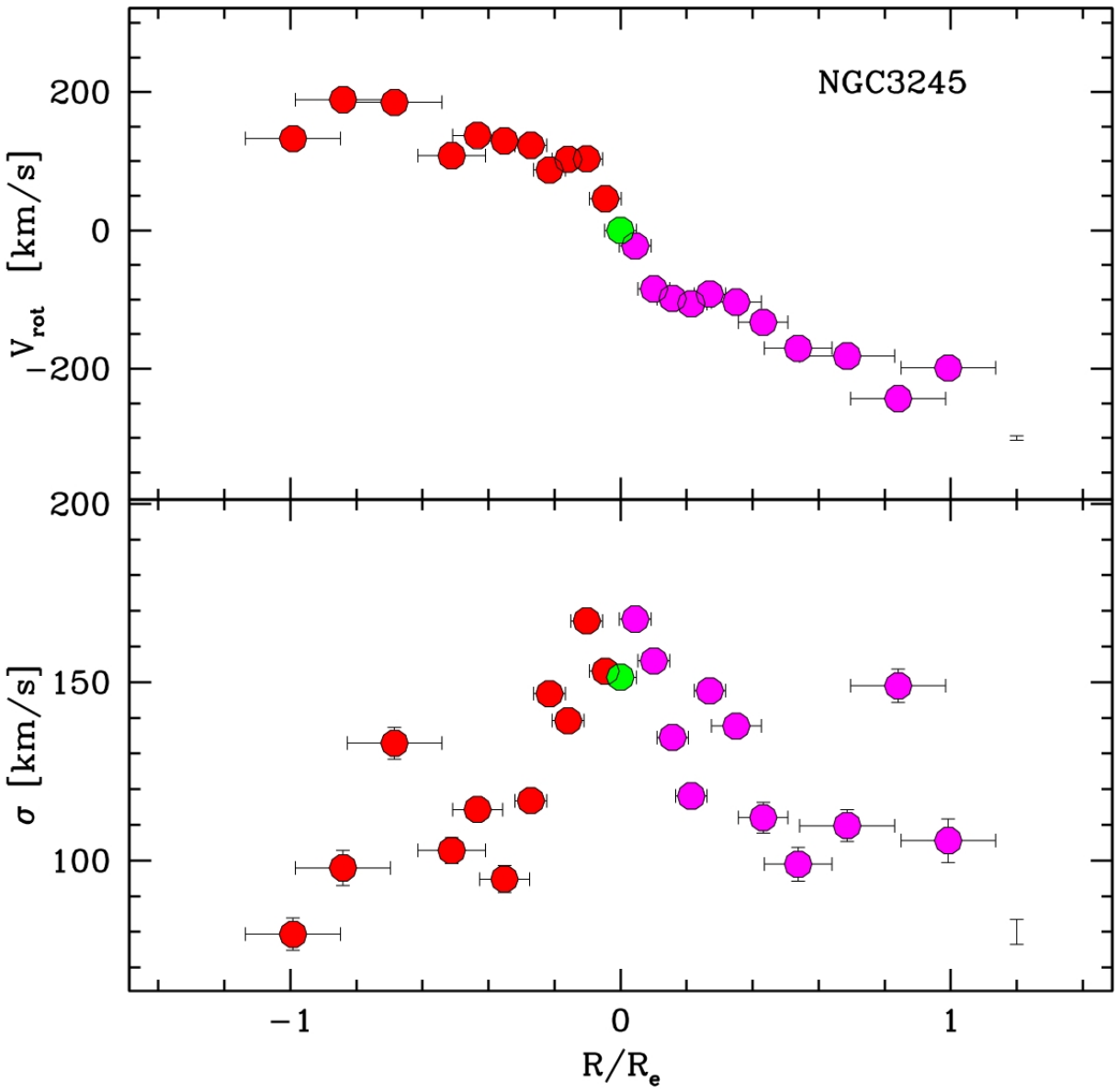

Figure 4.5 *Same of Fig. 4.2 but for NGC3245*

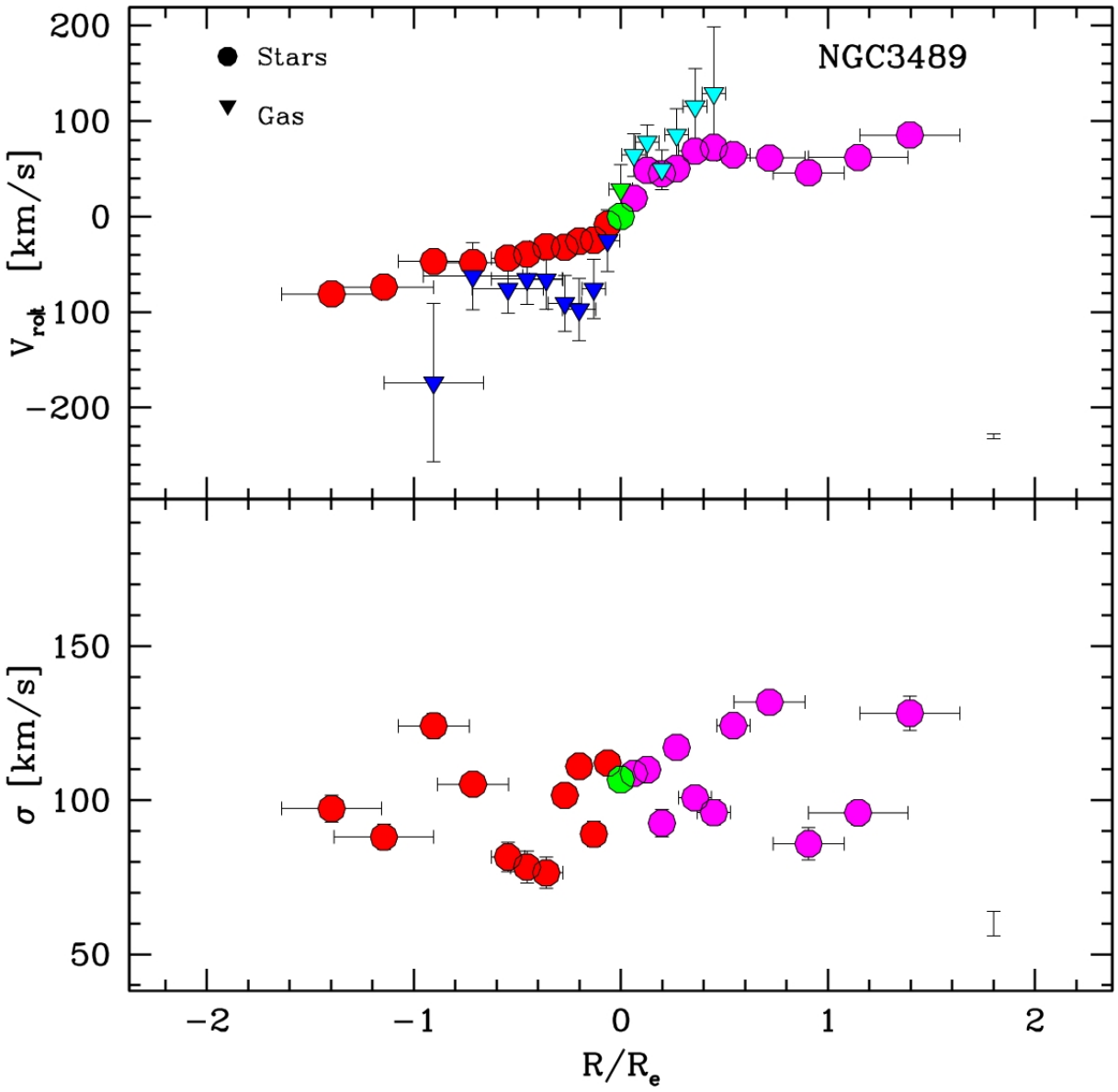

Figure 4.6 *Same of Fig. 4.4 but for NGC3489 (PA=32°)*

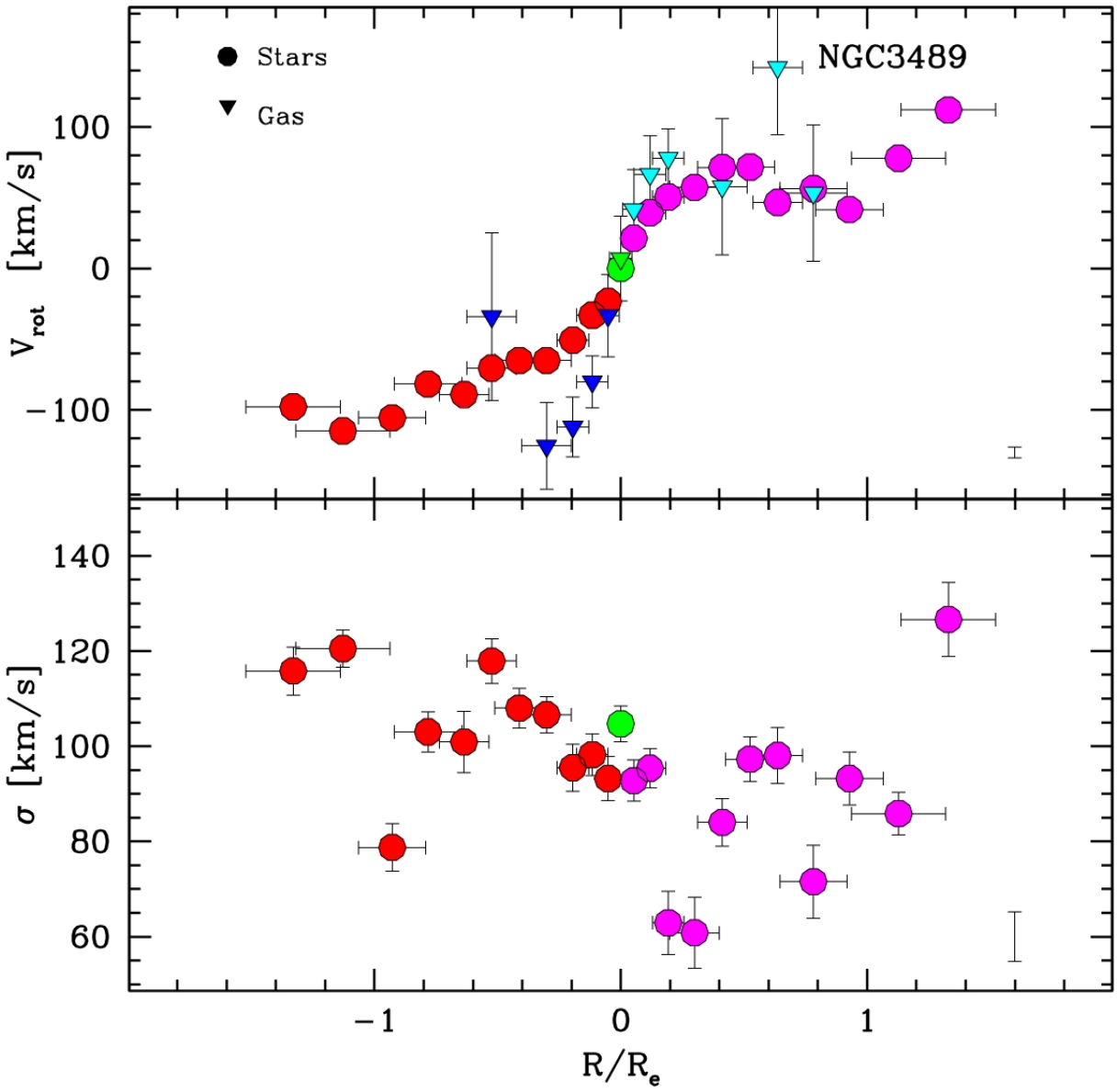

Figure 4.7 *Same of Fig. 4.4 but for NGC3489 (PA=58°)*

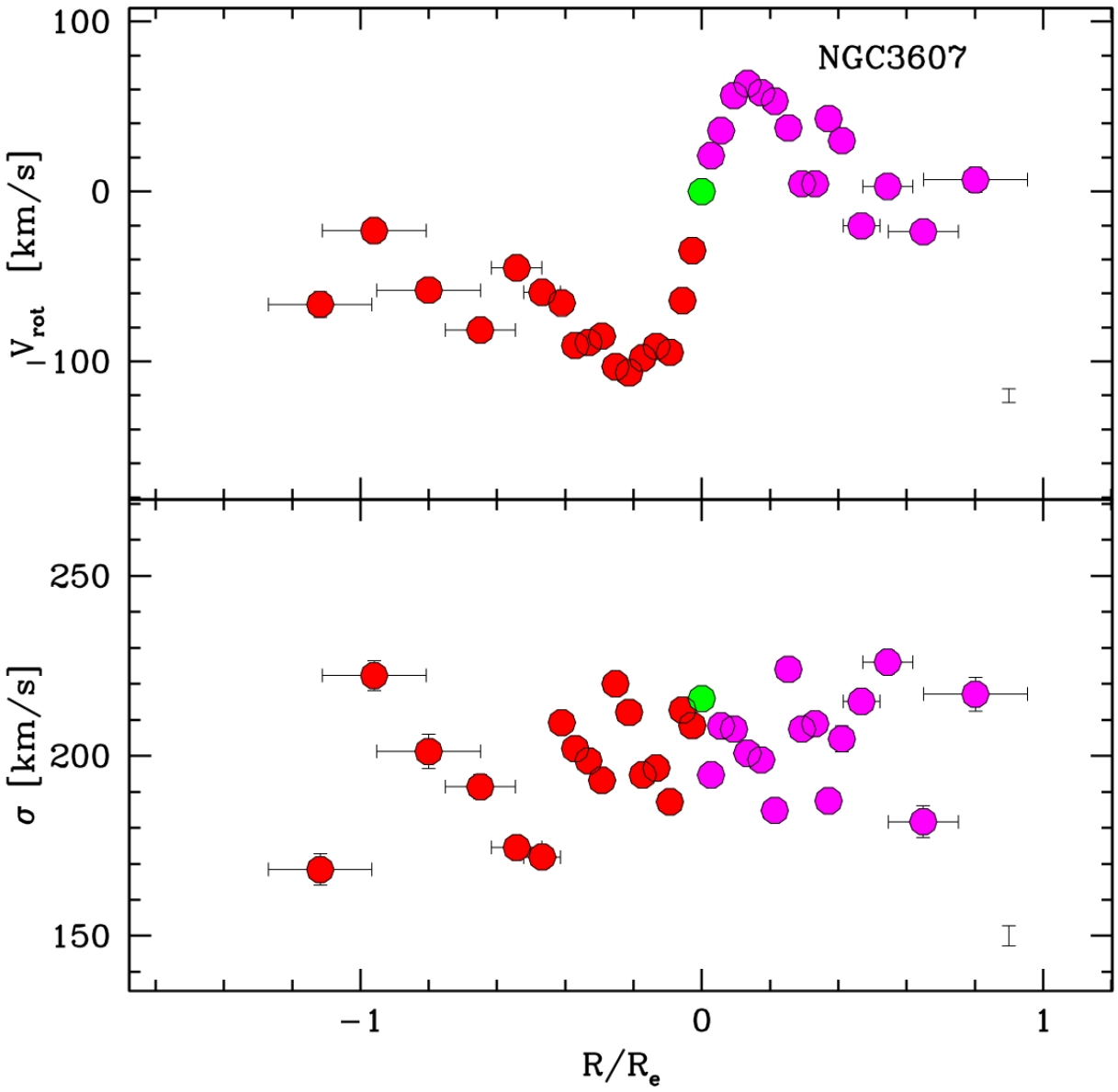

Figure 4.8 *Same of Fig. 4.2 but for NGC3607*

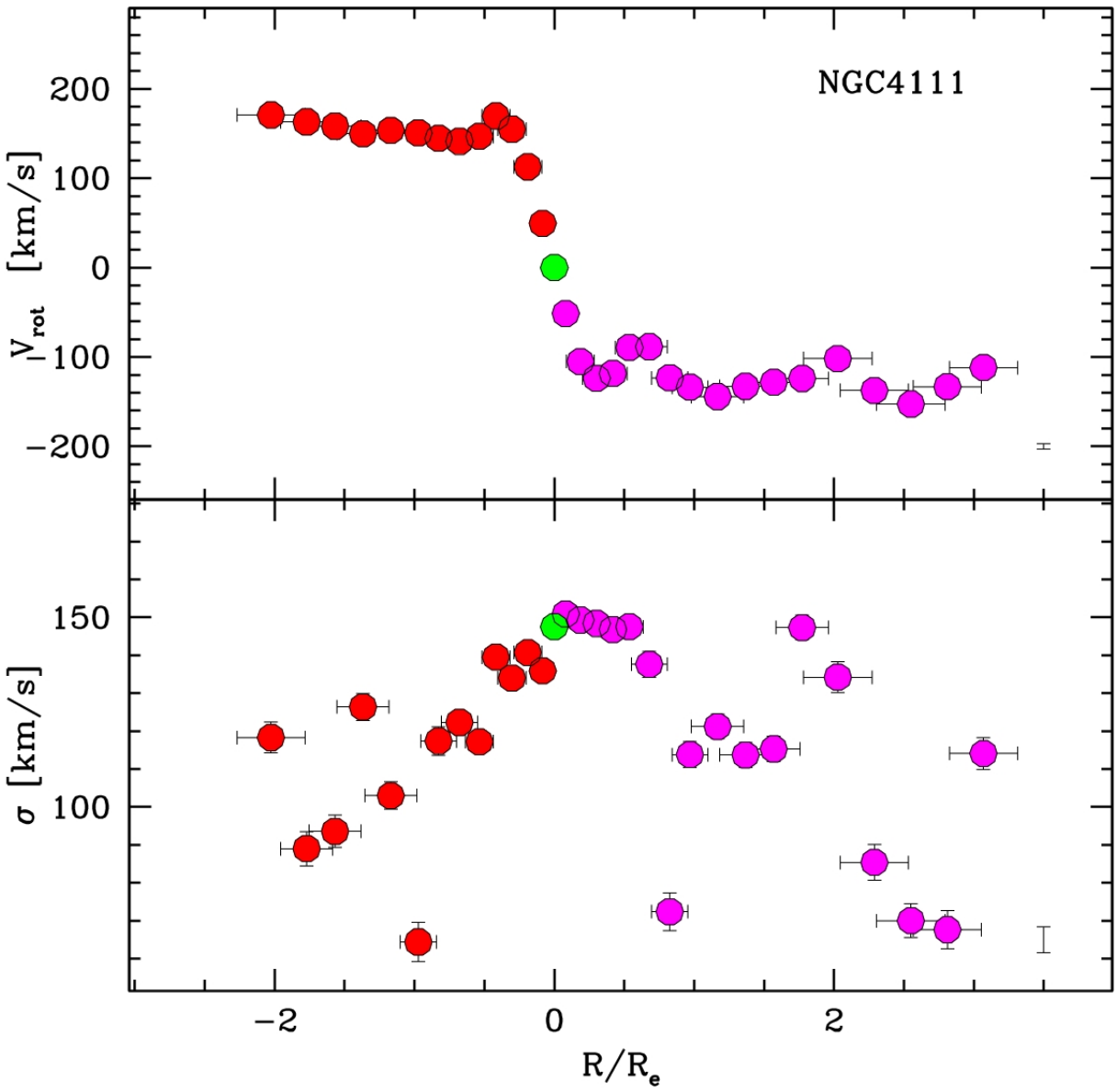

Figure 4.9 *Same of Fig. 4.2 but for NGC4111*

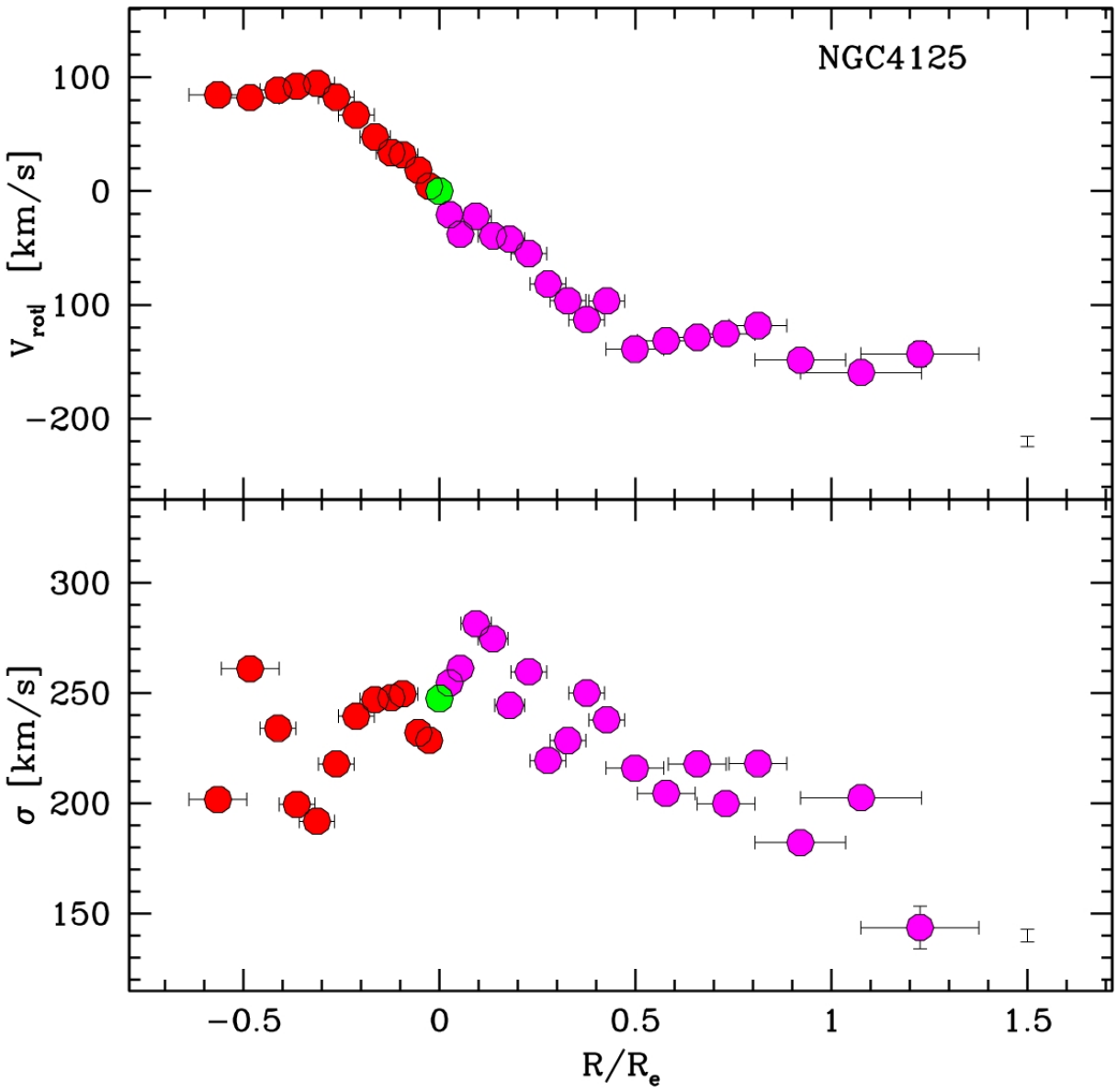

Figure 4.10 *Same of Fig. 4.2 but for NGC4125*

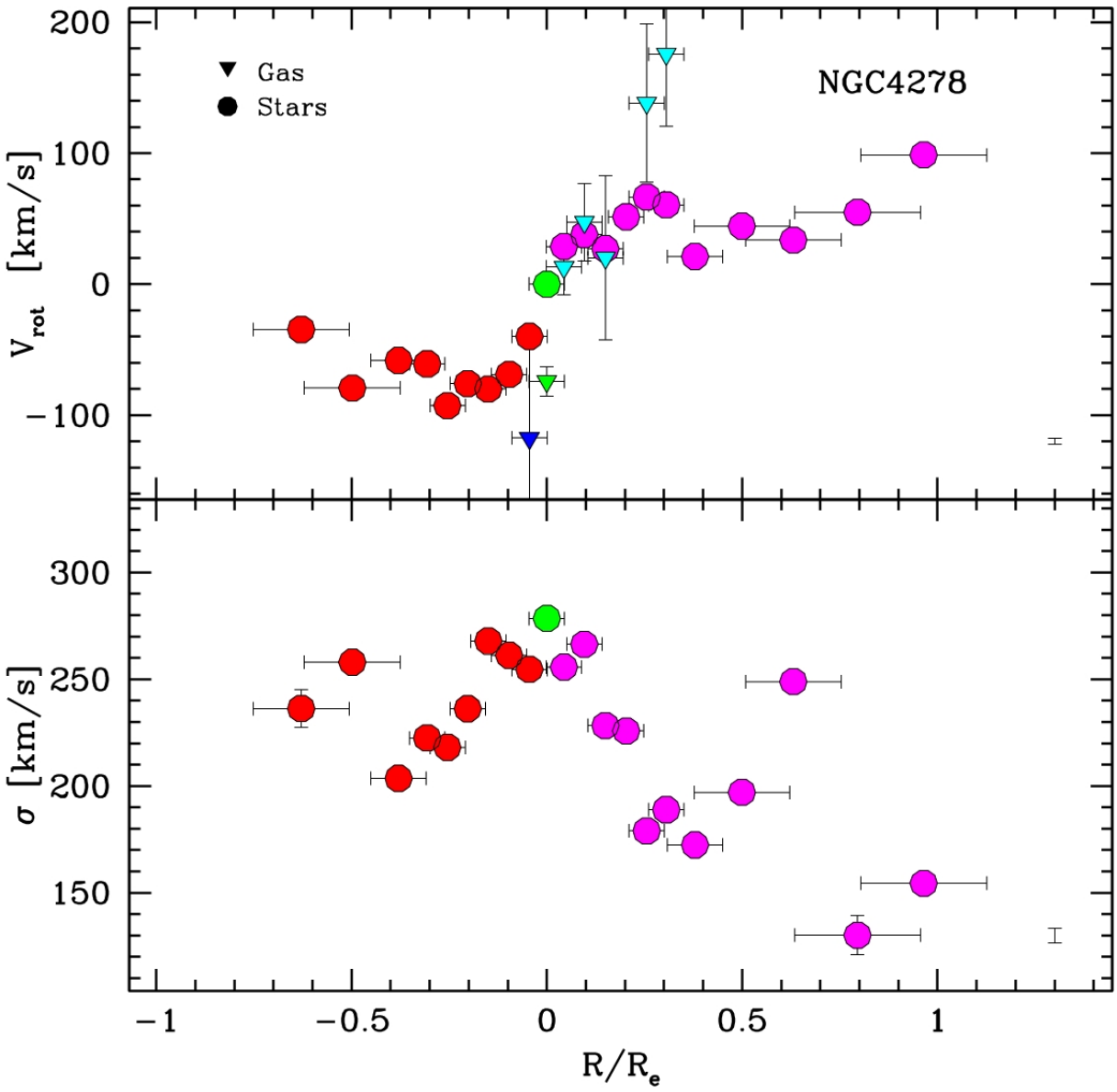

Figure 4.11 *Same of Fig. 4.4 but for NGC4278*

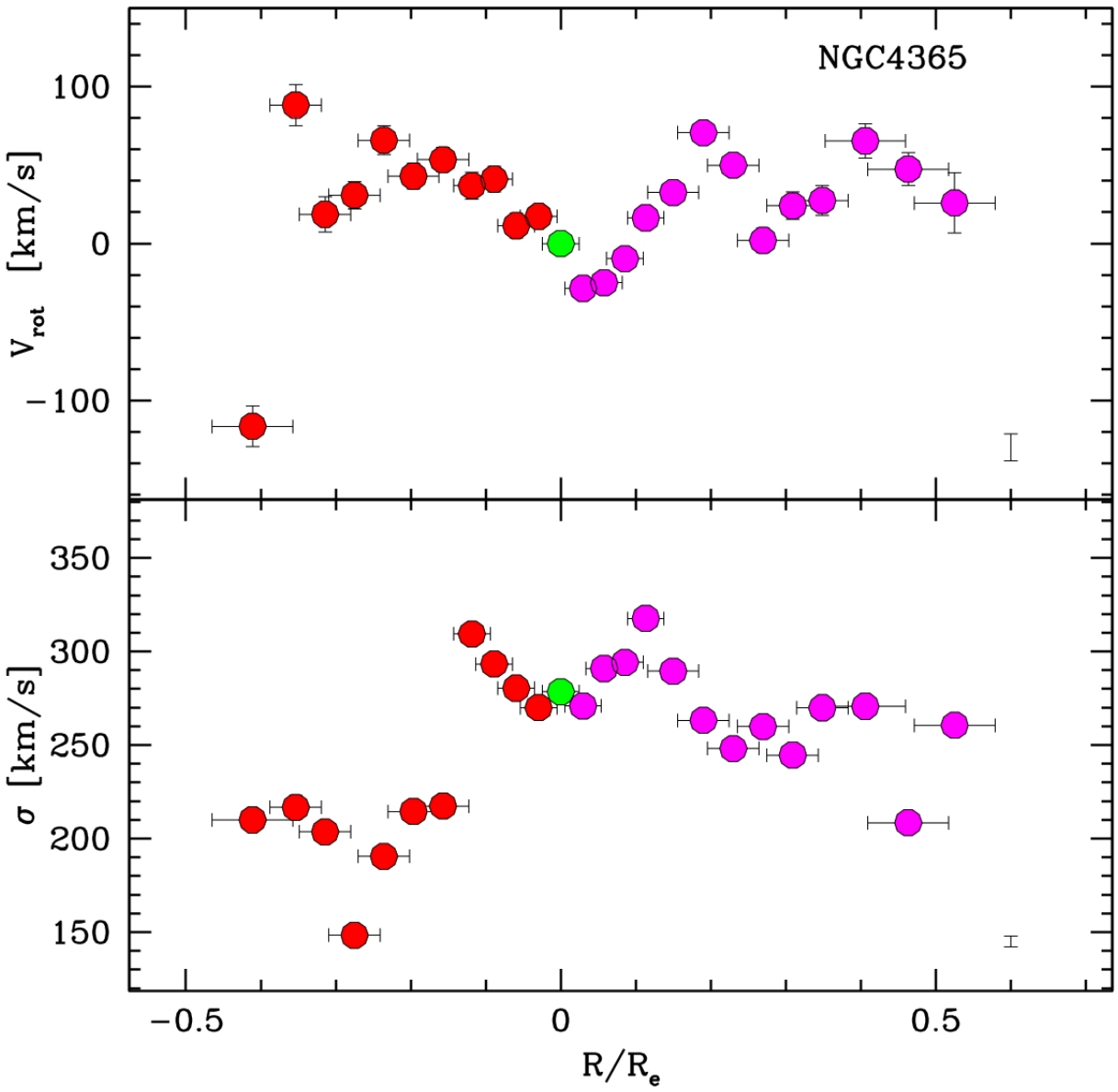

Figure 4.12 *Same of Fig. 4.2 but for NGC4365*

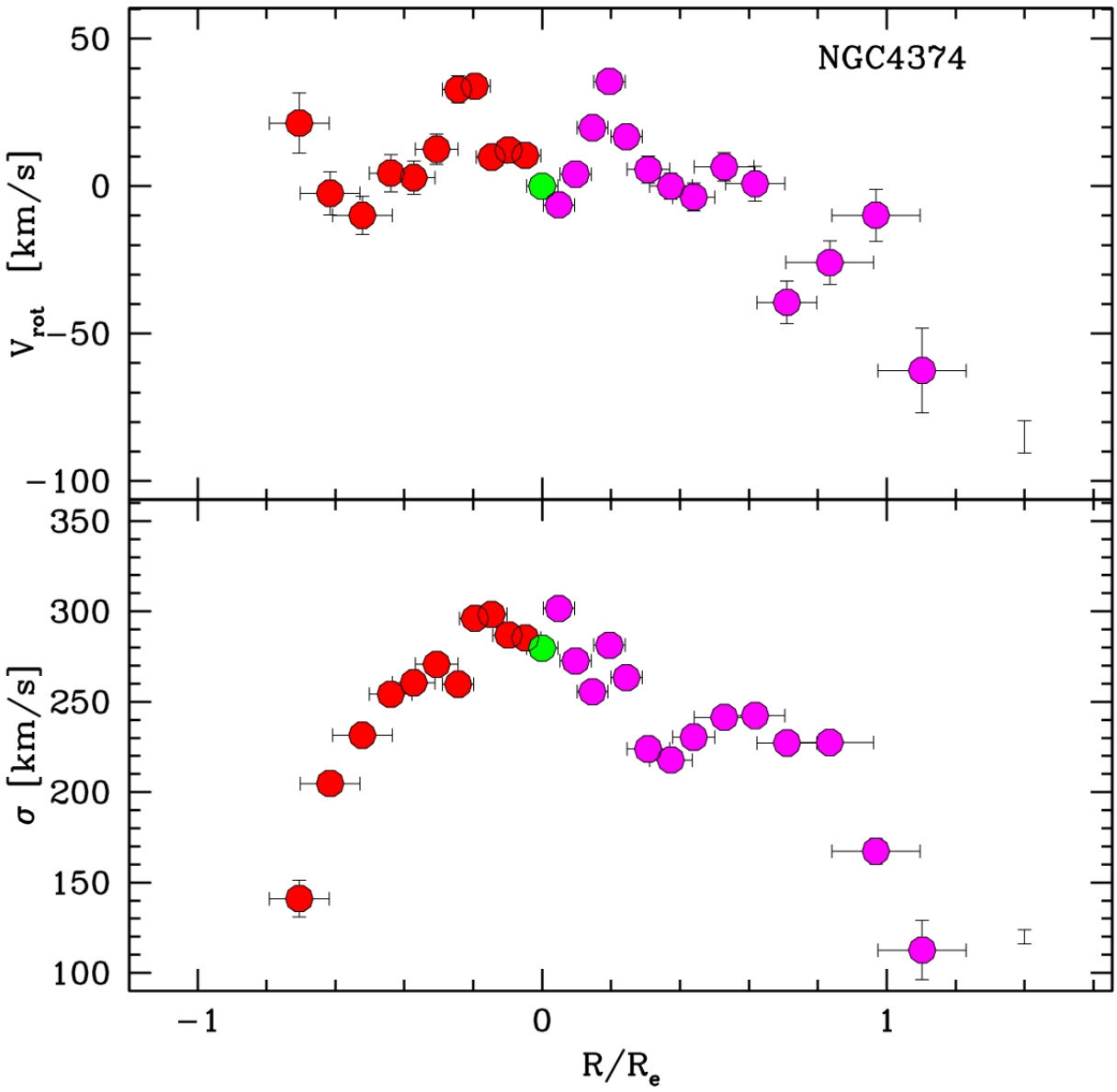

Figure 4.13 *Same of Fig. 4.2 but for NGC4374*

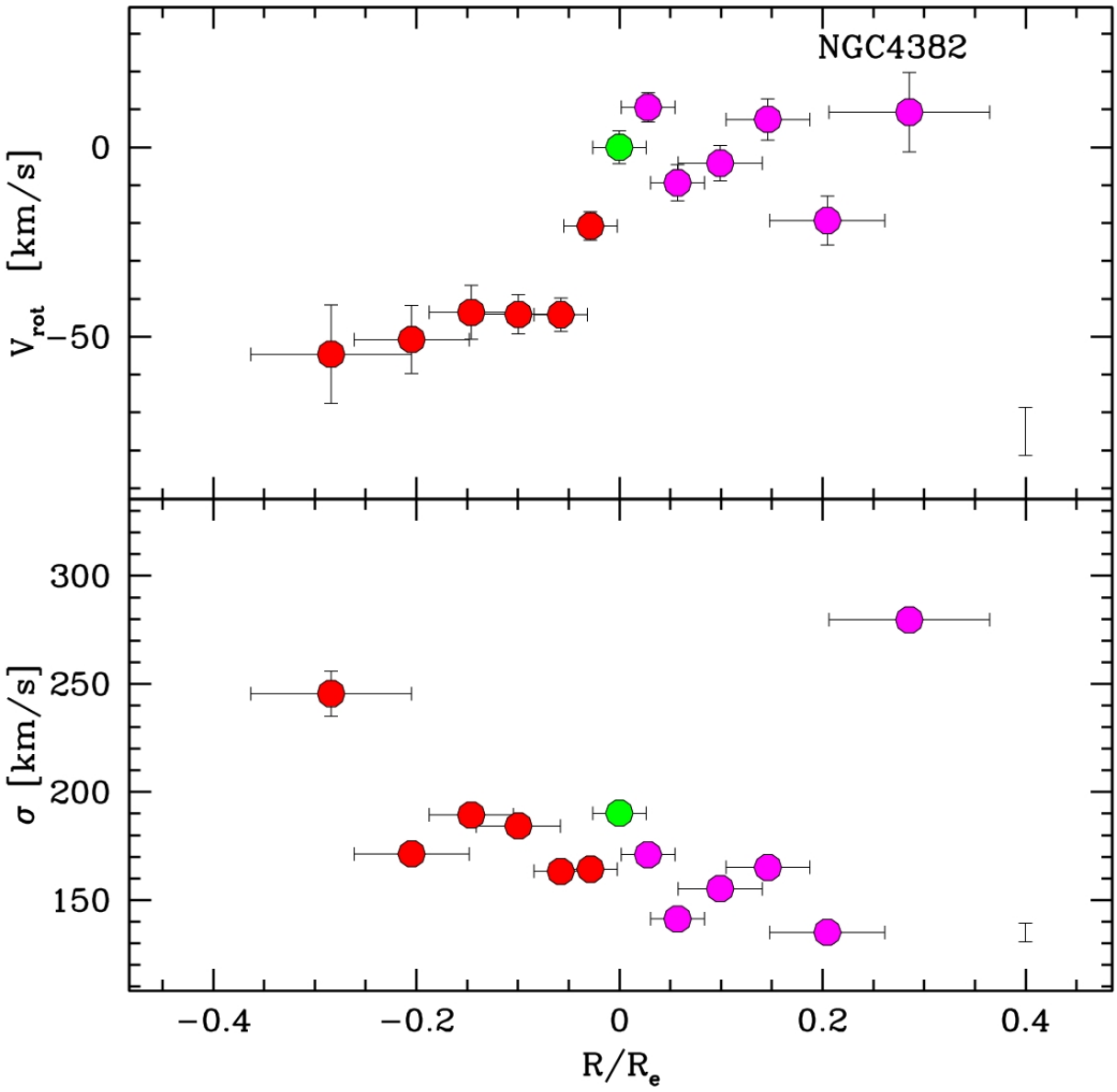

Figure 4.14 *Same of Fig. 4.2 but for NGC4382 (from the run of 1996)*

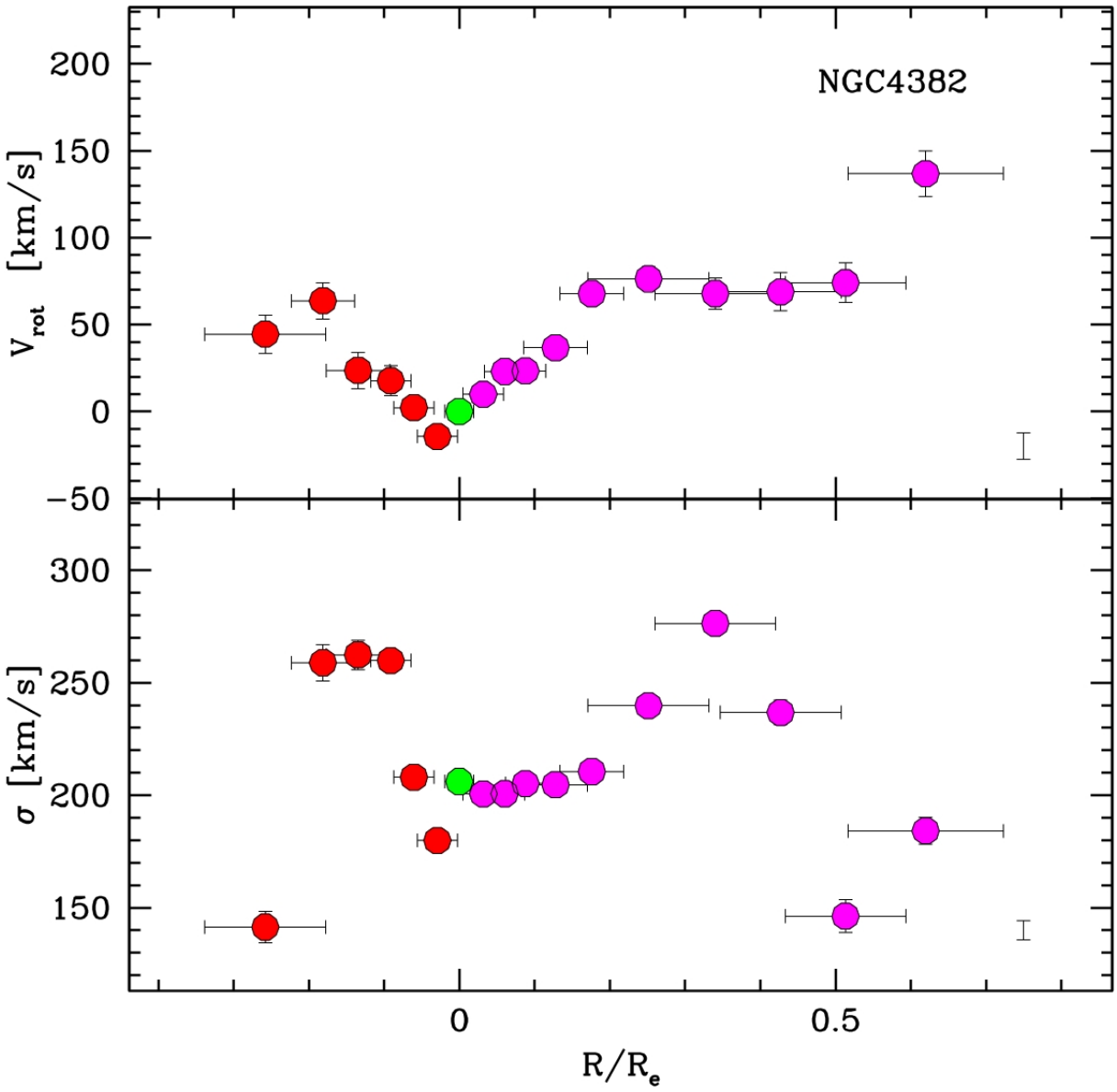

Figure 4.15 *Same of Fig. 4.2 but for NGC4382 (from the run of 1997)*

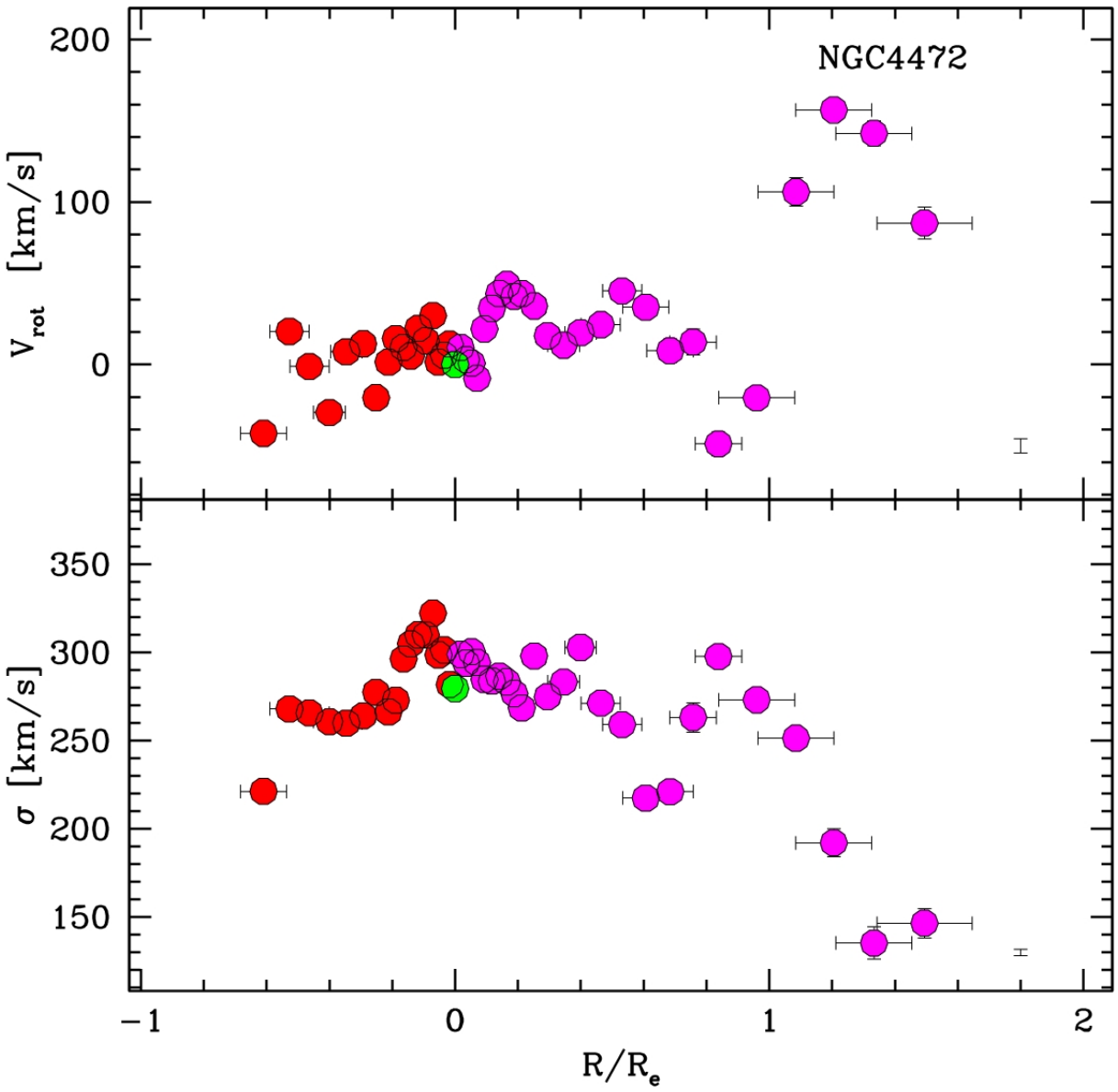

Figure 4.16 *Same of Fig. 4.2 but for NGC4472*

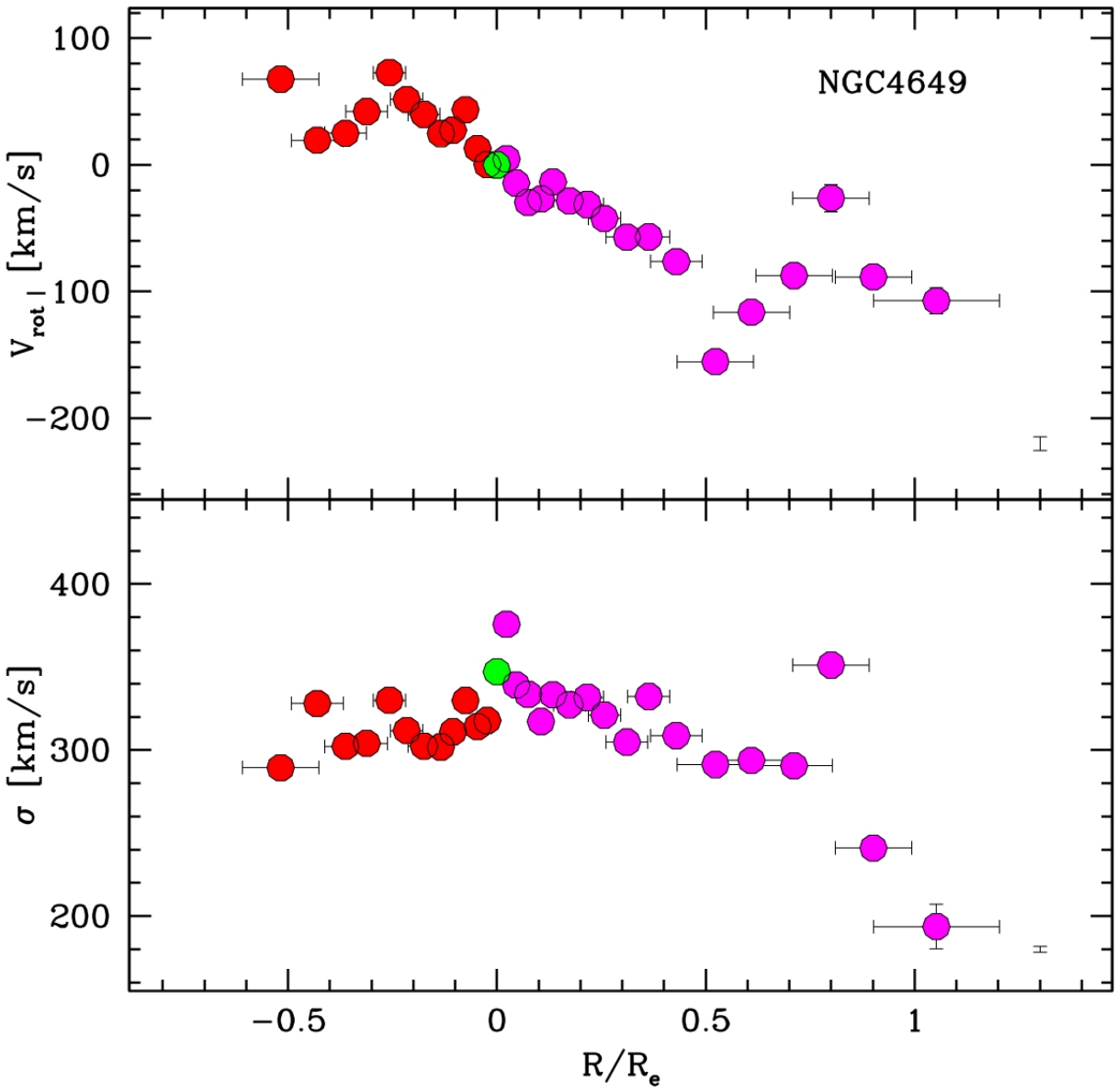

Figure 4.17 *Same of Fig. 4.2 but for NGC4649*

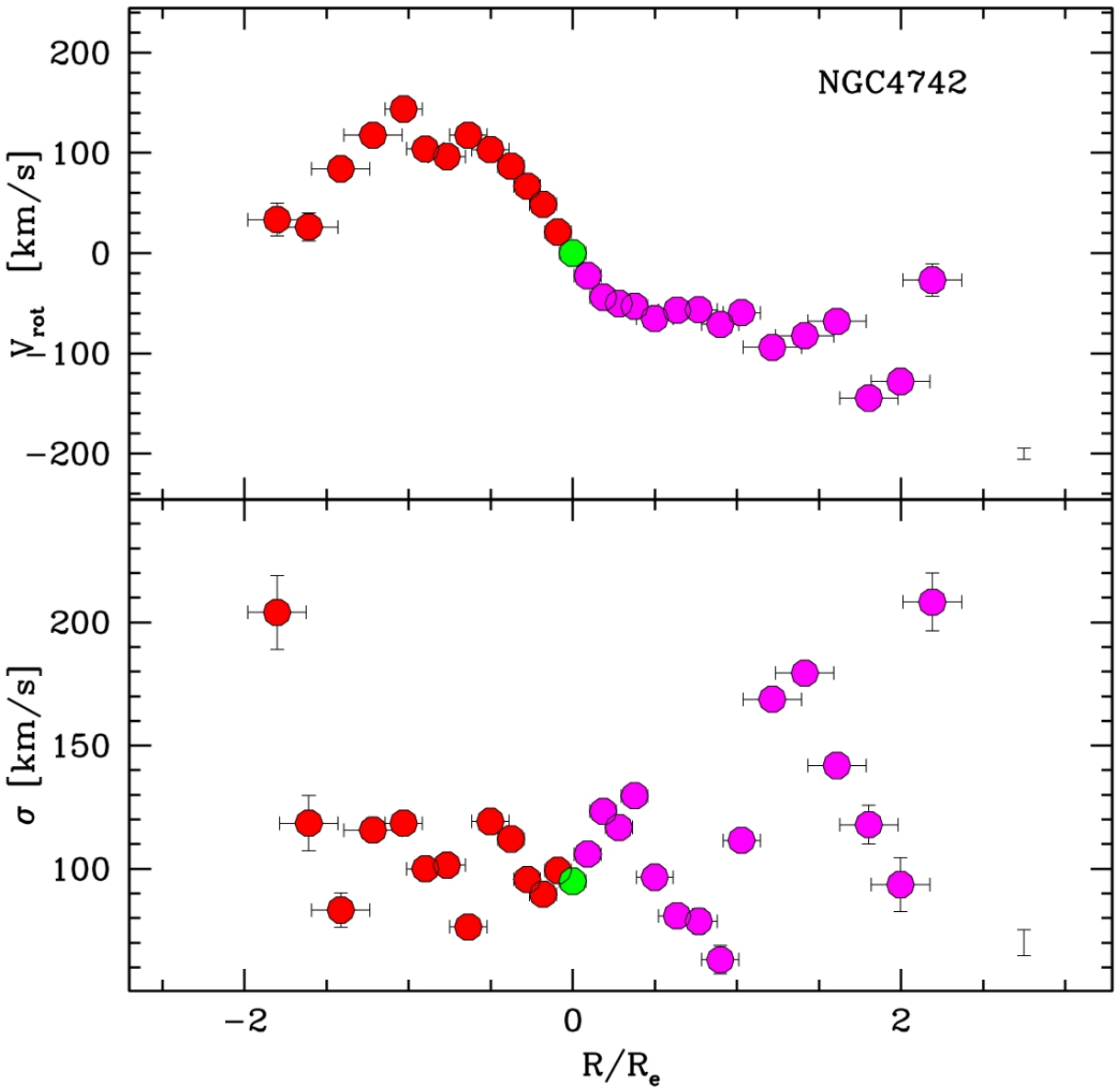

Figure 4.18 *Same of Fig. 4.2 but for NGC4742*

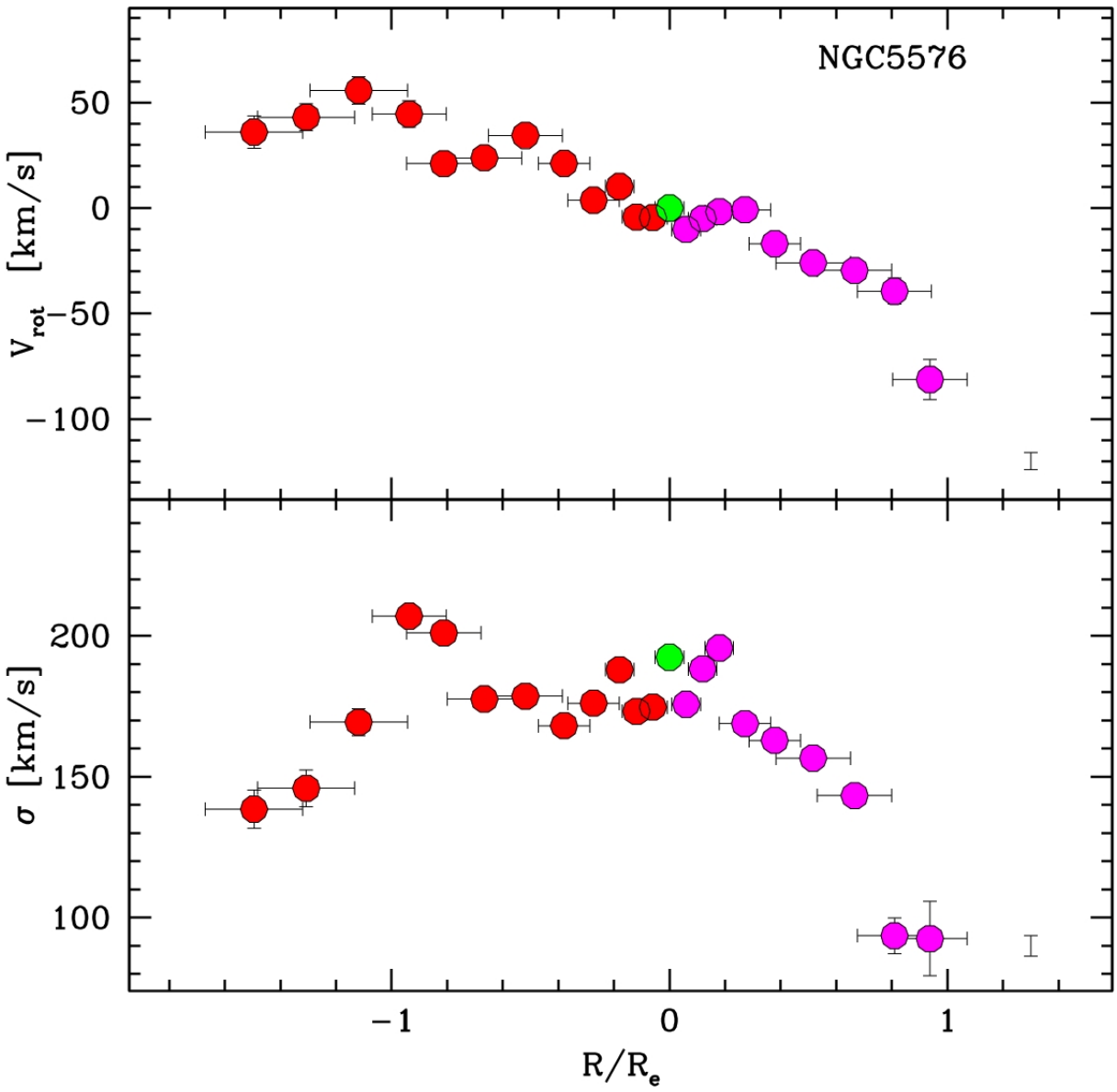

Figure 4.19 *Same of Fig. 4.2 but for NGC5576*

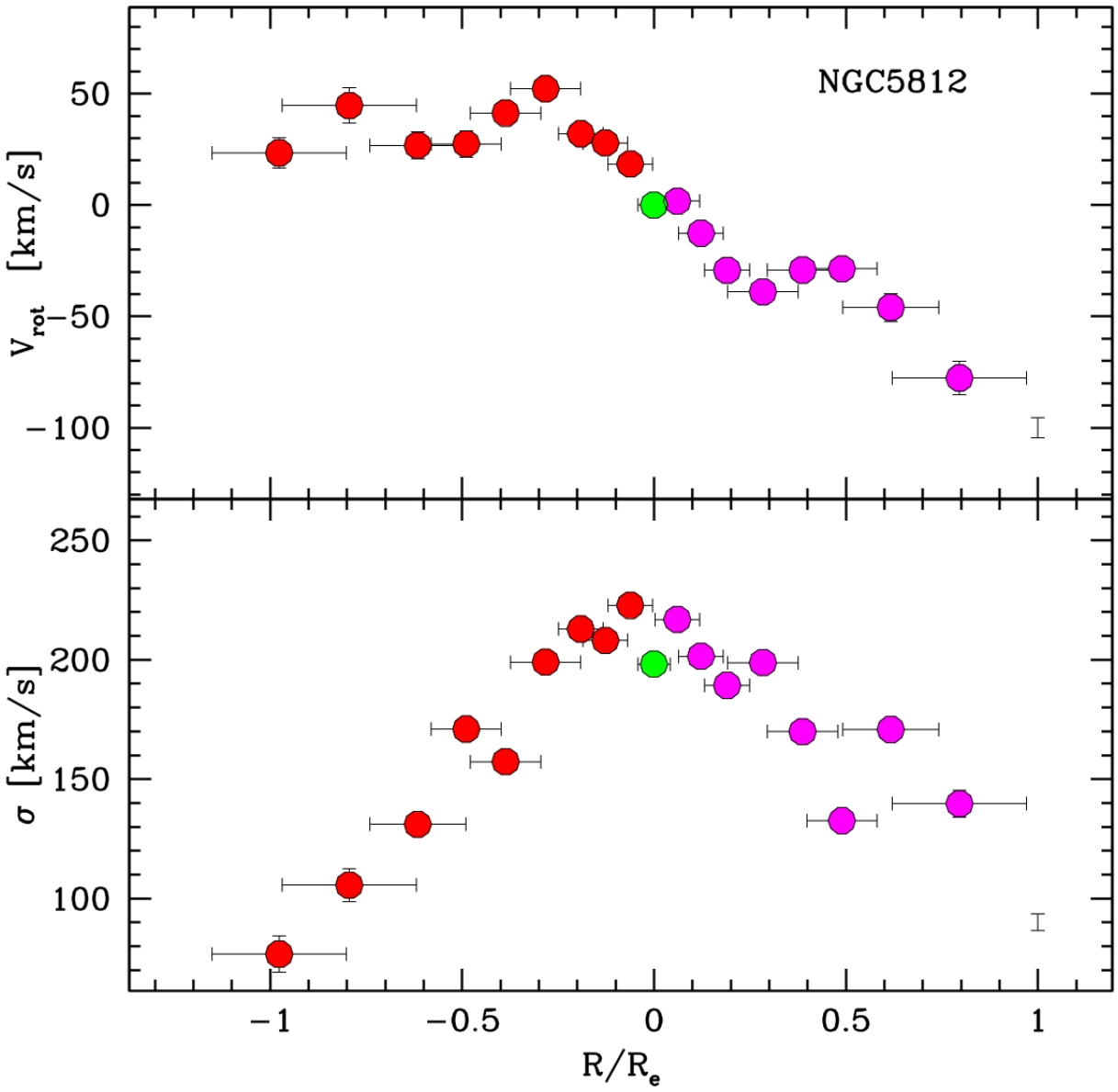

Figure 4.20 *Same of Fig. 4.2 but for NGC5812*
http://www.wordreference.com/iten/esperienza

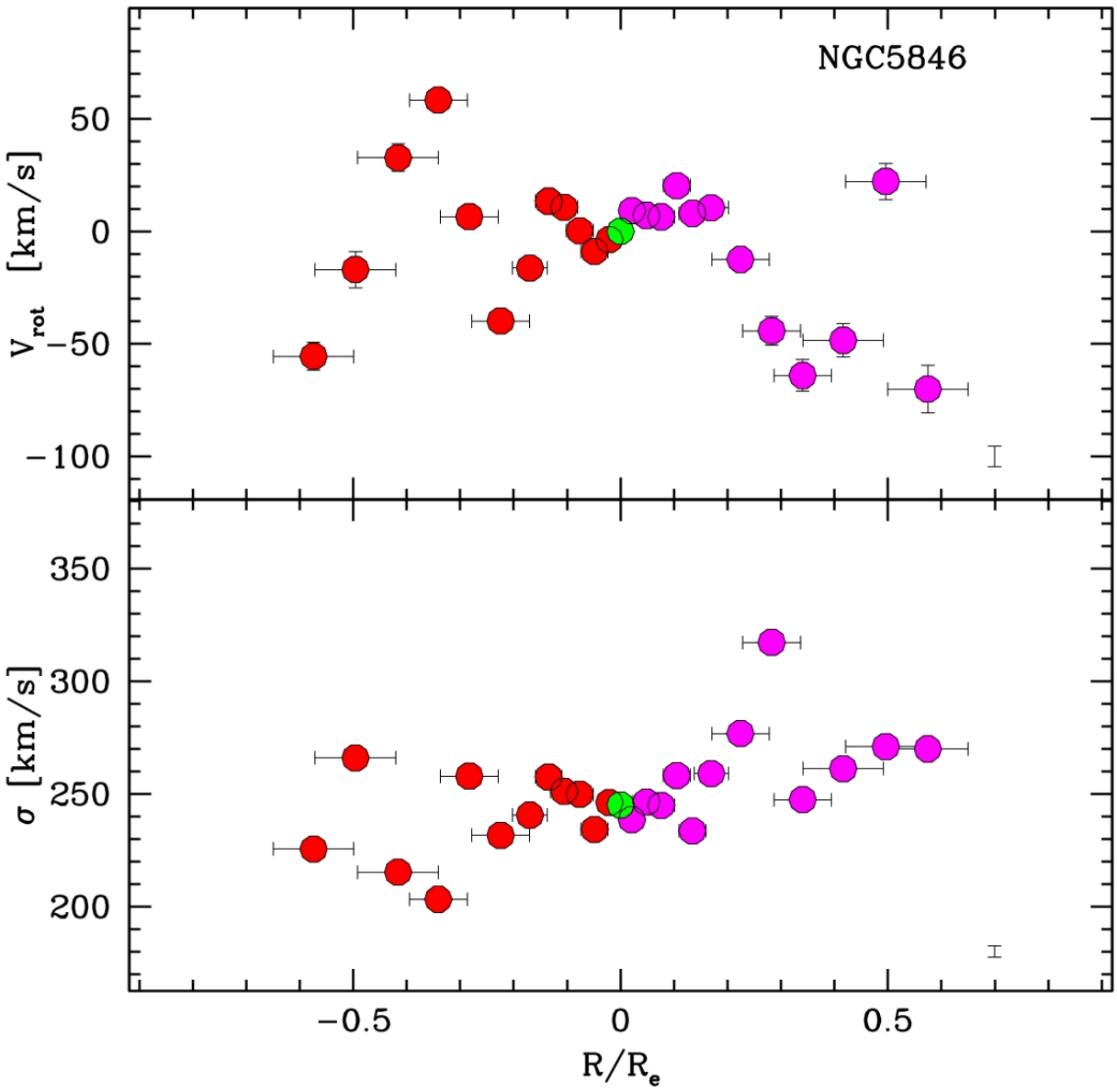

Figure 4.21 *Same of Fig. 4.2 but for NGC5846*

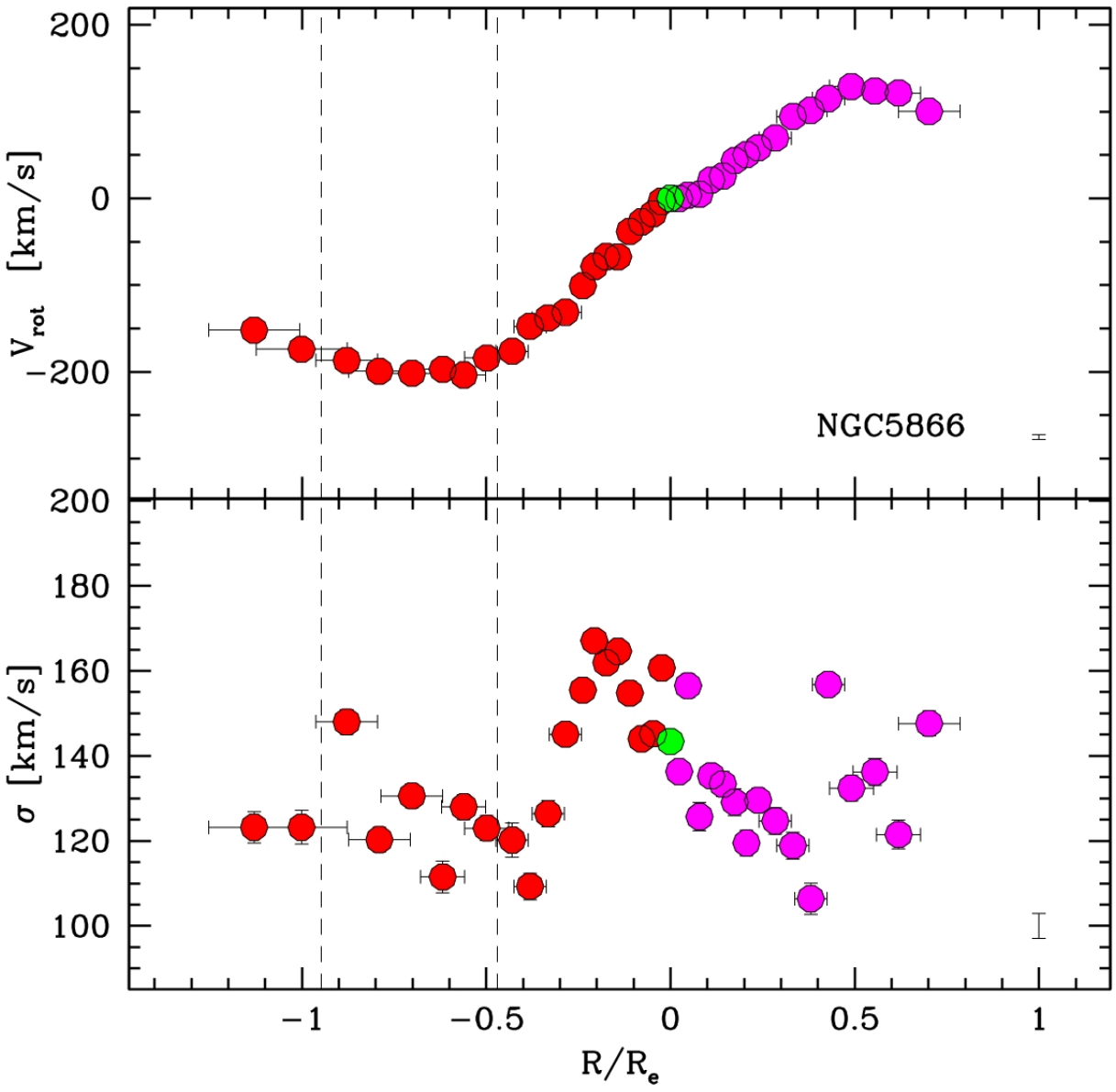

Figure 4.22 *Same of Fig. 4.2 but for NGC5866. The dashed lines enclose the area relative to the secondary peak of light*

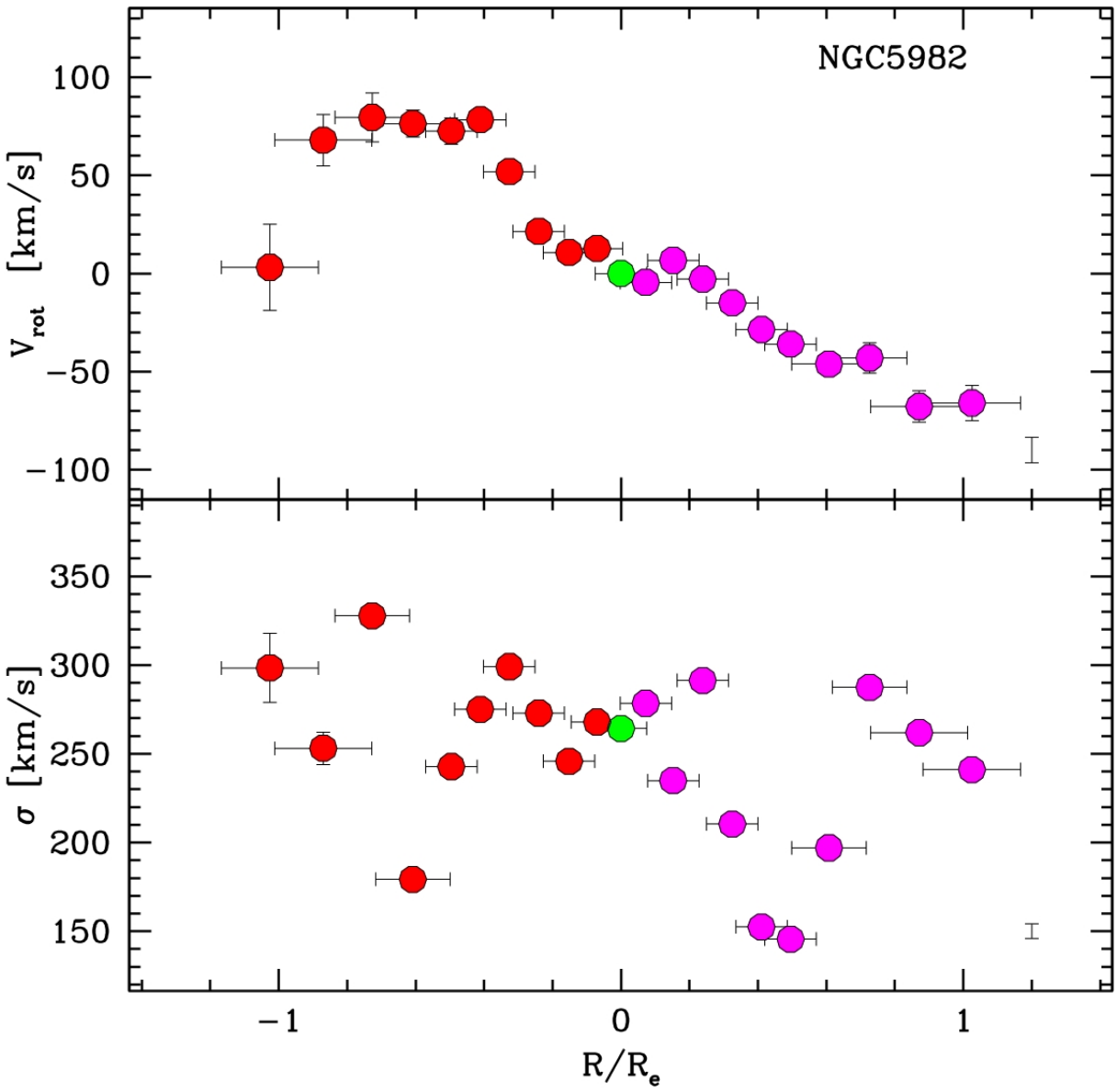

Figure 4.23 *Same of Fig. 4.2 but for NGC5982*

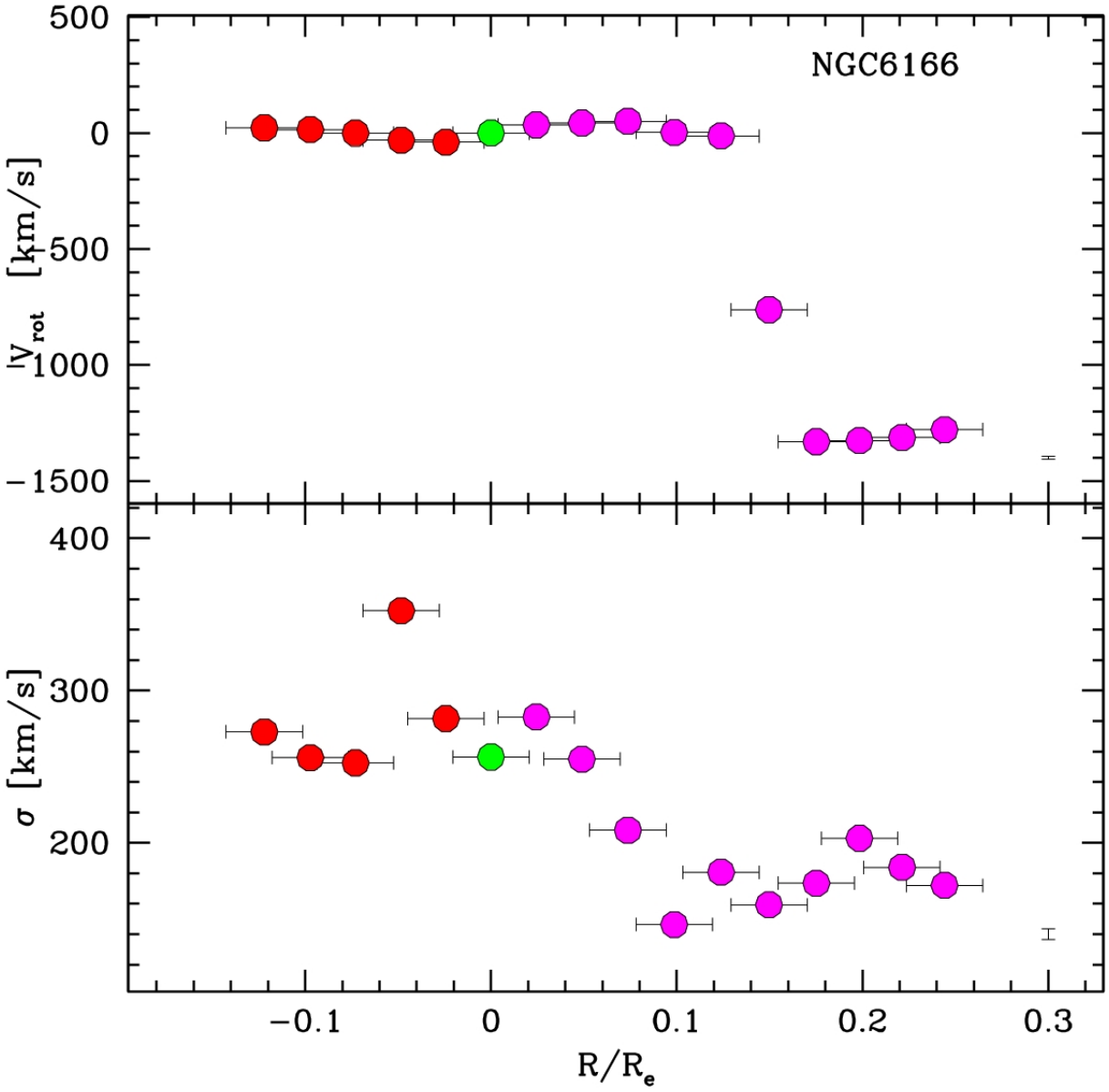

Figure 4.24 *Same of Fig. 4.2 but for NGC6166 (first observation of 1996)*

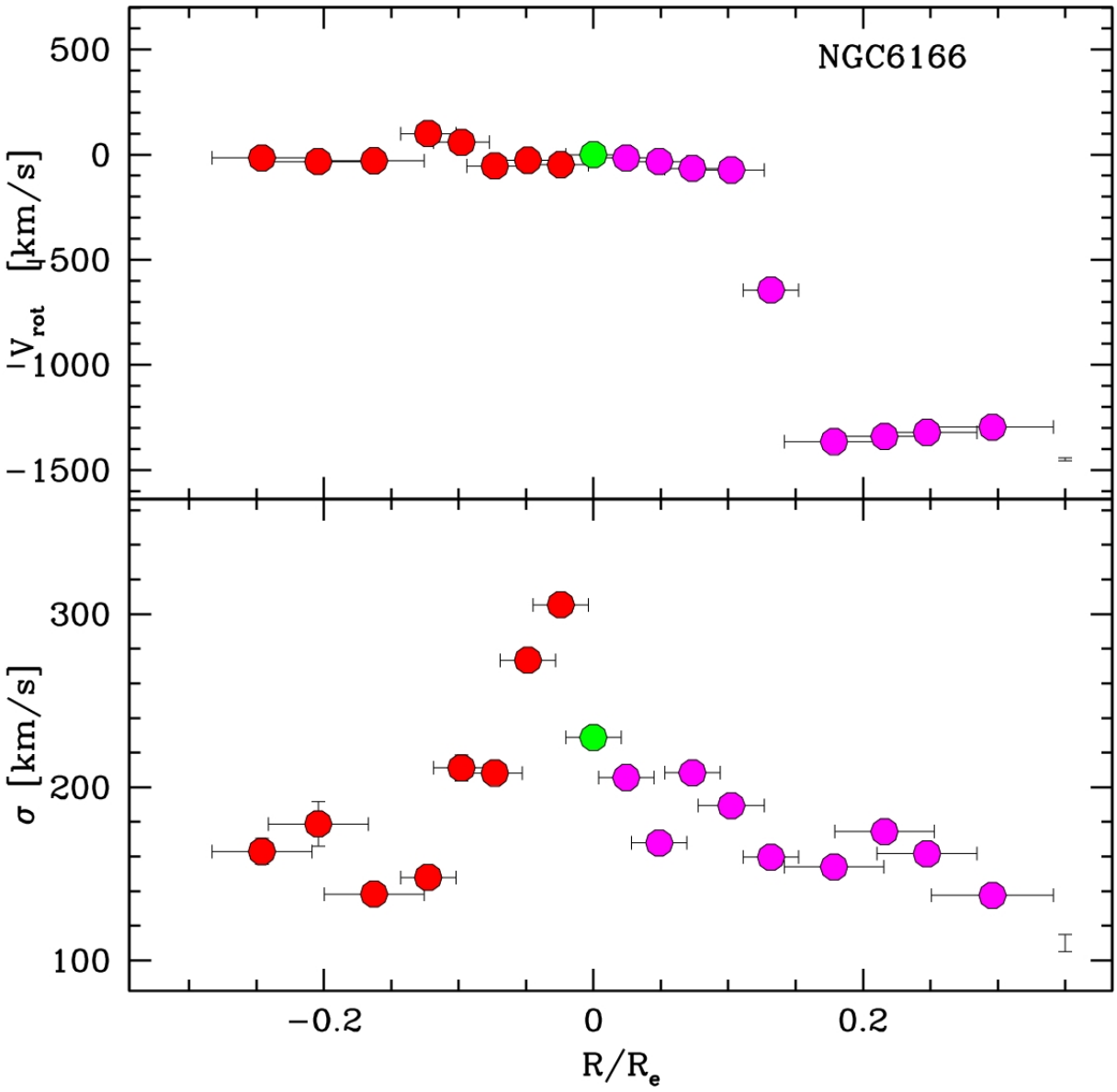

Figure 4.25 *Same of Fig. 4.2 but for NGC6166 (second observation of 1996)*

4.2 The gas component

For NGC2764, NGC3489, and NGC4278 we detected, at least in the central zone, an emission component imputable to the presence of a warm gas medium. As mentioned in § 3 we used only the O[III] emission line at 5007 Å to trace the kinematic of the gas. This because the most relevant emission lines in the spectral range of our observations are the $H\beta$ Balmer line and the O[III] forbidden doublet. Since the $H\beta$ line is mainly seen in absorption, due to the contribution of atmosphere of B to G stars, the detection of the emission component is often very difficult. Thus O[III] doublet is the only emission of interest and because the line at 4959 Å has an intensity of about one third of the one at 5007 Å we used only the latter for our analysis.

For all the galaxies we detected prominent rotation on a concordant direction with the stellar kinematics. The rotation velocities are always found out to be greater with respect to stellar ones. *If we assume that the stars are virialized, this is a strong evidence suggesting that the gas component is receding from the centre of the galaxy toward the outer regions.* However, if the gas isn't in steady state, we may question whether the assumption for the stellar component to be virialized can be reasonable, too. In any case, this indication alone isn't sufficient to move a believable critique to the hypothesis of steady state. Furthermore, any dynamical consideration for a non-virialized system is without doubt very complex. Thus, in the next chapter we make anyway the assumption that the Virial Theorem holds in order to estimate the dynamical masses of our galaxies.

4.3 Folding and interpolation

For many application of the stellar dynamics theory, a reference observable is the maximum rotational velocity (hereafter V_m). To better evaluate this parameter we made the assumption that the properties of our galaxies were axially symmetric. In this way we could fold the rotation curves and retrieve the trend of the rotational velocity with radius. Actually, as we will see in § 5.1, most of the considered sample seems to show a certain amount of anisotropy in the velocity dispersion tensor and, therefore, can admit a triaxial geometry. Anyway, these objects tend to be the roundest ones so axial symmetry is still a reliable approximation. For an optimal folding, a critical step is the location of the true centre of rotation to avoid misalignments between the two sides of the curve. This point can differ from our zero because of an inherent uncertainty in determining the photometric centre within the seeing spot (typically ≈ 2 arcsec) or because of an offset between the photometric maximum and the rotation axis. We implemented a routine for the evaluation of the best folding point. For the full code we refer to appendix A while here we report just the main steps.

First we performed a cubic spline for the interpolation of the data. Then we sampled a range of points around the zero and tested them as turning points. We folded the curve around that point and sorted the sperimental data for increasing absolute value of the radius. Later, we computed a "Merit Factor" as the sum of the squares of the residuals between each point and the previous one. We choose this criterion because, due to the symmetry of the sampling about the centre, this sum accounts for the difference between

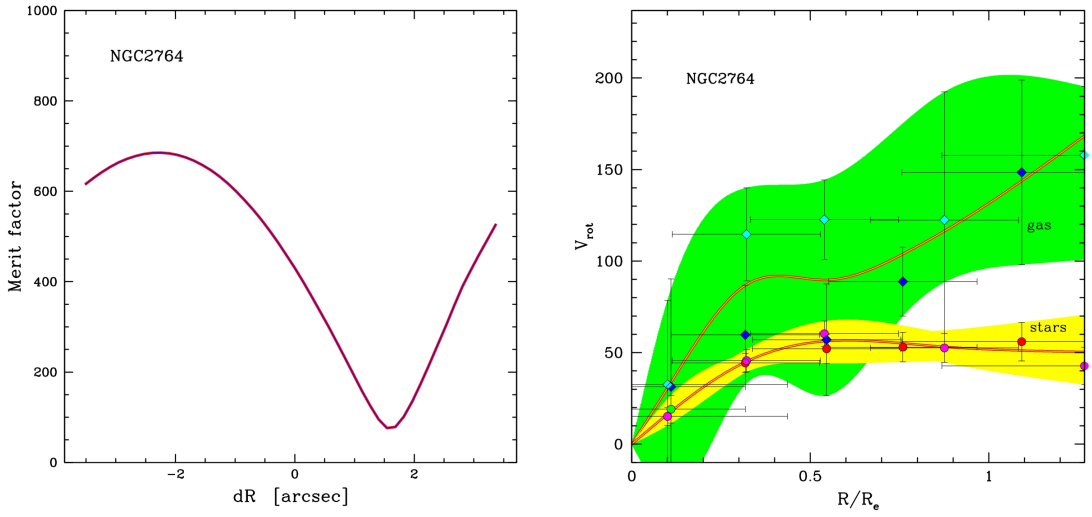

(a) (b)

Figure 4.26 *The folding outcome for NGC2764: a) The Merit Factor along the offset from the centre. b) The folded profile: Circles represent the stellar component while diamonds correspond to the gaseous one. Different colours refer for the two sides of the profile. The solid lines are the mean splines averaged over the two sides. The coloured regions enclose the area delimited by the error bars.*

points of opposite sides lying at similar radii. *The best folding point is chosen as the point corresponding to the minimum of the merit function.* Once folded, we performed a separate spline for each side and then we averaged them to obtain a mean trend of the rotation profile. An example of the outcome of our work is given in Fig. 4.26 while the whole set of folded curves can be found in appendix B.

Typically we chose only offsets smaller than the seeing, yet there were some galaxies for which a greater offset was necessary to produce a well folded rotation curve. This is the case of NGC4125, NGC5866 and NGC5982. Although the merit factor showed a local minimum inside the seeing threshold, in these cases we preferred to adopt a farther turning point apart. A clear example of this situation is reported in Fig. 4.27. Finally, has to be noted that many galaxies showed a well defined minimum in the merit factor trend. Typically, the minimum corresponded to value of the merit factor lower than 500 while, going outside, the merits reached values of the order of 2000. Other galaxies, instead, showed a complex structure of local minimum and maximum around a merit value of few hundreds. For these galaxies we preferentially chose a local minimum lying inside the seeing range while, for those object which didn't show a sufficient defined minimum we set the turning point to zero.

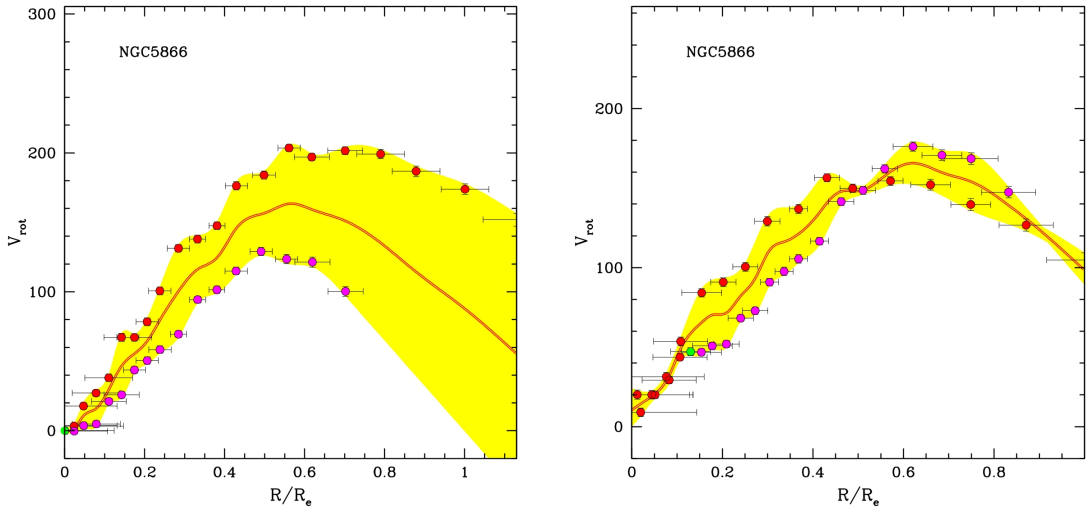

(a) (b)

Figure 4.27 *Comparison between different turning points for NGC5866: a) Rotation curve folded around the zero. b) Rotation curve folded around a centre offsetted by 7.3 ″. The diagrams description is the same as for Fig. 4.26*

4.4 Comparison with earlier works

To test the robustness of our results for each galaxy in our sample, we performed an exhaustive research in literature and plotted our profiles superposed to the curves found by other authors. Currently, the most complete data on Early Type Galaxies kinematics is represented by those acquired by the $ATLAS^{3D}$ (Krajnović et al., 2011) and the $SAURON$ projects (Emsellem et al., 2004). Unfortunately, these works used integral field spectroscopy and, thus, present the data in the form of two-dimensional maps, so a comparison with our work was practically unfeasible. We used all the longslit spectroscopy material available, spanning from the first works (Davies, 1981; Kormendy and Illingworth, 1982) to most recent ones (Caon et al., 2000; Pu et al., 2010). Most of the data derives from few works (Bender et al., 1994; Caon et al., 2000) but, for a more reliable test, we used a total of beyond thirty papers.

We only used the spectra acquired along a Position Angles close to our values $\pm 45°$. To account this difference, we rescaled the spatial axis of the profiles to make them compatible with ours. Knowing the axis dimensions of the galaxy, we computed the effective radius at the Position Angle sampled (this is done through the polar equation of the ellipse). Then we computed the corrective factor as the ratio between the effective radius at our Position Angle and the one at the Position Angle considered by the author.

The comparison show, generally, a good agreement with our data, especially about the rotation curves. Since our velocity dispersion profiles shows a fair amount of scatter, a little discrepancy is sometimes seen, but even this profiles seems to shows a reasonable agreement with the selected works. In a few cases (such as NGC3245 or NGC3489) we

saw an underestimation of the central values of velocity dispersion. This can lead to a poor estimation of the orbital anisotropy and the mass-to-light ratio. The only case that shows a great discrepancy with the literature regards the velocity dispersion of the pair NGC1587/1588. Since these are among the faintest object in our sample (accounting for an apparent blue magnitude of 12.72 and 13.89 respectively), the poor S/N ratio of our spectra led to a greatly uncertain velocity dispersion determination. Few examples of the comparison we made can be found in Fig. 4.28, while the full set of graphs is reported in appendix B.

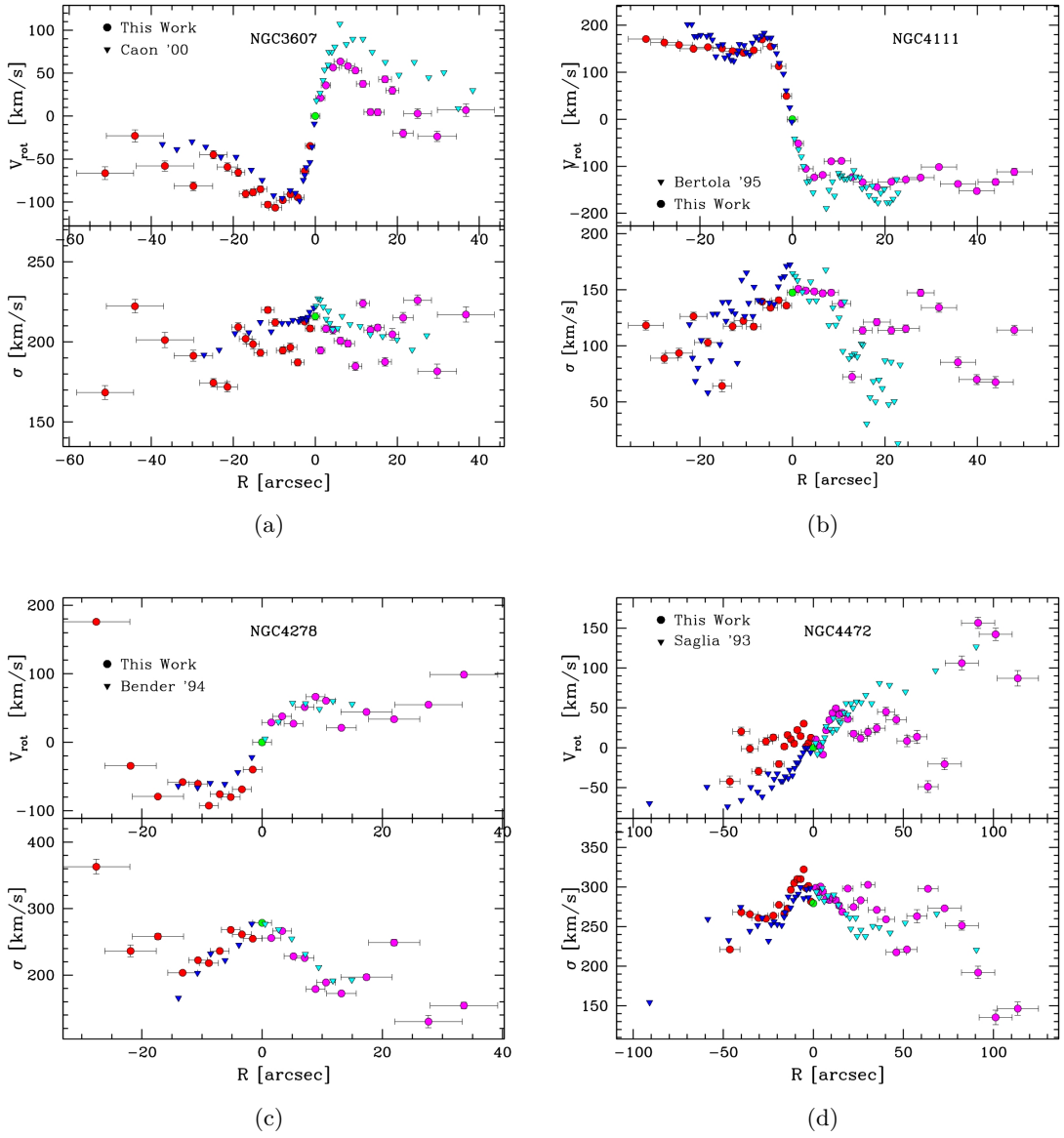

Figure 4.28 *Examples of the comparison work made on the profiles: a) NGC3607, data taken from Caon et al. (2000); b) NGC4111, data taken from Bertola et al. (1995); c) NGC4278, data taken from Bender et al. (1994); d) NGC4472, data taken from Saglia et al. (1993). The upper panel is the rotation curve while the lower one is the velocity dispersion profile. Different colour account for the two side of the galaxy. The centre is the green point.*

Chapter 5

Dynamical interpretation

Since we have obtained the atlas of the kinematical information for our sample, the next step is to consider what we can infer from this data about the dynamical structure of these galaxies. This section summarizes the analysis we carried out and the main points on which we focused our attention. In particular, we tried to retrieve clues on the orbital structure of these stellar systems and to evaluate the masses and the M/L values. Once we have obtained good estimates of these parameters we search for interesting correlations between dynamical, photometric and chemical features.

5.1 The orbital anisotropy

The first point we investigate is whether the flattening of our galaxies is due only to the rotation or a certain amount of orbital anisotropy is needed. Our diagnostic relies on a useful "Anisotropy Diagram" (Binney, 1978; Davies et al., 1983). In few words, one compute the ratio between the ordinate motion (rotation) and the chaotic motion (velocity dispersion) and plot it against the ellipticity. From analytical models and under the hypothesis of virial equilibrium, one can predict the relation that holds for an oblate isotropic rotator (hereafter OIR), i.e. a system in which the rotation accounts for all the observed flattening, and verify if the considered objects satisfy this relation.

In theory, one needs the mass-weighted mean square values of velocity dispersion and rotation velocity in the centre of the galaxy, σ_0 and V_0. Since this parameters are difficult to retrieve, this diagram is usually built up with a typical rotation speed, V_m, and the central velocity dispersion, σ_c, or the mean velocity dispersion within $r_e/2$, $\bar{\sigma}$. With these parameters, the relation for an OIR is (Kormendy, 1982):

$$\left(\frac{V_m}{\bar{\sigma}}\right)_{OIR} \simeq \frac{\pi}{4}\left(\frac{V_0}{\sigma_0}\right)_{OIR} \approx \sqrt{\frac{\varepsilon}{1-\varepsilon}}. \tag{5.1}$$

From our data, we computed $\bar{\sigma}$ as the mean velocity dispersion within $r_e/2$. In theory this value is not very different from the central velocity dispersion but, due to the scatter of our data, $\bar{\sigma}$ is meant, in principle, to be a better indicator of the chaotic motion. Concerning V_m, things are more difficult. An usually preferred value is the maximum measured rotation

Table 5.1 *Values for measured σ_c, $\bar{\sigma}$ and V_m. Ellipticity is also reported.*

Name NGC	σ_c [Km/s]	$\bar{\sigma}$ [Km/s]	V_m [Km/s]	ε
1587	293.5 ± 29.4	236.7 ± 117.6	86.1 ± 17.8	0.29
1588	122.5 ± 12.3	163.1 ± 30.5	78.5 ± 45.5	0.44
2685	78.0 ± 7.8	97.6 ± 15.2	122.4 ± 10.6	0.46
2764	113.8 ± 11.4	107.4 ± 8.3	54.8 ± 1.7	0.41
3245	151.4 ± 15.1	137.2 ± 21.7	197.0 ± 11.2	0.37
3489(32°)	106.7 ± 10.7	100.0 ± 12.9	65.2 ± 4.3	0.41
3489(58°)	104.7 ± 10.5	91.1 ± 16.0	99.4 ± 8.0	0.41
3607	215.9 ± 21.6	202.6 ± 12.1	90.0 ± 3.9	0.13
4111	147.5 ± 14.8	143.7 ± 6.2	153.4 ± 2.3	0.64
4125	247.5 ± 24.8	240.1 ± 22.0	113.7 ± 1.7	0.22
4278	278.5 ± 27.9	230.2 ± 33.3	74.3 ± 3.3	0.02
4365	278.5 ± 27.9	252.5 ± 42.5	0	0.28
4374	279.7 ± 28.0	266.9 ± 25.2	0	0.13
4382('96)	190.2 ± 19.0	181.2 ± 40.2	32.7 ± 2.2	0.22
4382('97)	206.1 ± 20.6	219.4 ± 36.0	0	0.22
4472	279.5 ± 28.0	286.2 ± 16.2	40.0 ± 4.9	0.19
4649	347.1 ± 34.7	322.9 ± 17.5	63.1 ± 5.7	0.19
4742	94.9 ± 9.5	106.4 ± 13.5	108.9 ± 7.2	0.35
5576	192.4 ± 19.2	178.6 ± 10.8	45.8 ± 10.1	0.34
5812	198.2 ± 19.8	190.6 ± 26.0	52.4 ± 7.3	0.13
5846	245.1 ± 24.5	250.1 ± 22.3	0	0.05
5866	143.4 ± 14.3	138.0 ± 17.4	166.8 ± 3.8	0.57
5982	264.2 ± 26.4	244.7 ± 48.7	72.9 ± 1.4	0.35
6166a	256.4 ± 25.6	227.2 ± 57.1	0	0.28
6166b	228.7 ± 23.0	189.6 ± 45.3	0	0.28

velocity. Unfortunately, we know that rotational velocity tends to increase toward external regions, where the statistical uncertainty is higher. The nominally highest measured velocity would led, therefore, to a serious bias. In order to mitigate this overestimation we used a heuristic criterion. Restricting within the distance from the centre where both the sides of the galaxy are sampled (in this way we avoided the noisiest data) we computed V_m as the mean of the five highest measured velocities. The V_m computed in this way are very close to the values of rotation velocity in the region where the profile begins to be shallower and seem to be good approximations of the typical rotational velocity. In the galaxies where we didn't detect any rotation we set $V_m = 0$.

Tab. 5.1 reports the values of σ_c, i.e. the velocity dispersion measure of the central bin, $\bar{\sigma}$ and $V_m$for our sample. The uncertainties of $\bar{\sigma}$ and V_m were evaluated as the standard deviation of the entry values used in the computation. The uncertainty for σ_c was set to the 10% of its value. With this measures we built the anisotropy diagram superimposed

to a line representing the OIR prediction (Fig. 5.1a). In theory, the inclination angle i of our galaxy should be known in order to interpret this diagram. Fortunately, by varying inclination, isotropic models move along a vector that is very close to the sequence defined by the $i = 90°$ models (Illingworth, 1977). Thus if a sperimental point lies significantly off the prediction line, it is inconsistent with the OIR model, irrespective of its inclination. Furthermore, even for anisotropic models, projection effects don't seem to be relevant for the comparison with the OIR prediction for galaxies rounder than E5 (Davies et al., 1983). Therefore, we feel confident about the reliability of this diagram.

From the plot it can be seen that the bulk of the sample lies under the OIR prediction. At low ellipticities, most of the galaxies seems to show a relevant amount of radial anisotropy, while just few lie close to the OIR line. At greater ellipticities there are several galaxies that show an excess of rotation with respect to the isotropic model. All of them, except one, are of type S0, so the extra rotation can be explained considering that the disk component is not included in the OIR model. Only NGC4742 is classified as an elliptical and shows a large amount of $\left(\frac{V_m}{\bar{\sigma}}\right)$. Since the distinction between ellipticals and lenticulars is not quite easy, we think that this is an indication for NGC4742 to be an S0, according to Davies et al. (1983). It can be noted that, at these ellipticities, inclination effects can be relevant so this could be an alternative explanation for the extra rotation.

We computed also the quantity $\left(\frac{V_m}{\bar{\sigma}}\right)^*$, defined as the ratio between $\left(\frac{V_m}{\bar{\sigma}}\right)$ and $\left(\frac{V_m}{\bar{\sigma}}\right)_{OIR}$, and plotted it against the absolute blue magnitude (Fig. 5.1b). The magnitudes M_b are taken from the Hyperleda catalogue (Paturel et al., 2003), for a value of $H_0 = 70 Kms^{-1}Mpc^{-1}$. Again, it can be seen that the only galaxies that show extra rotation are the S0's excepting two ellipticals. We have already commented the case of NGC4742 but the most rotating galaxy respect to the OIR model is NGC4278 with a value of $\left(\frac{V_m}{\bar{\sigma}}\right)^* = 2.26$. We think this is because of the small value of ε we used ($\varepsilon = 0.02$). Near $\varepsilon = 0$, $\left(\frac{V_m}{\bar{\sigma}}\right)_{OIR}$ rises very steeply, so any difference between the adopted ellipticity and the true one may significantly distort the measured $\left(\frac{V_m}{\bar{\sigma}}\right)^*$. Several authors have used values of ε that differ from ours, even importantly (Peletier et al., 1990; van der Marel, Binney, & Davies, 1990). Using $\varepsilon = 0.14$ would imply a value of $\left(\frac{V_m}{\bar{\sigma}}\right)^* = 0.8$, placing NGC4278 well under the isotropy line.

It can be seen from Fig. 5.1b that there is a correlation between the amount of rotation support and the luminosity of the galaxy. Brighter galaxies tend to be more pressure supported while the faintest ones seem to be closer to the isotropic rotator model or even show greater rotation contributions. This can also be interpreted like a correlation between the degree of radial anisotropy and the luminosity for ETGs. We searched also for a correlation with the ellipticity. Even in this case there is a correlation but is weaker and not so clear as that with luminosity. Anyway, it seems that the most flattened galaxy are the same that show the larger amount of rotation while the roundest ones are more likely to be anisotropic.

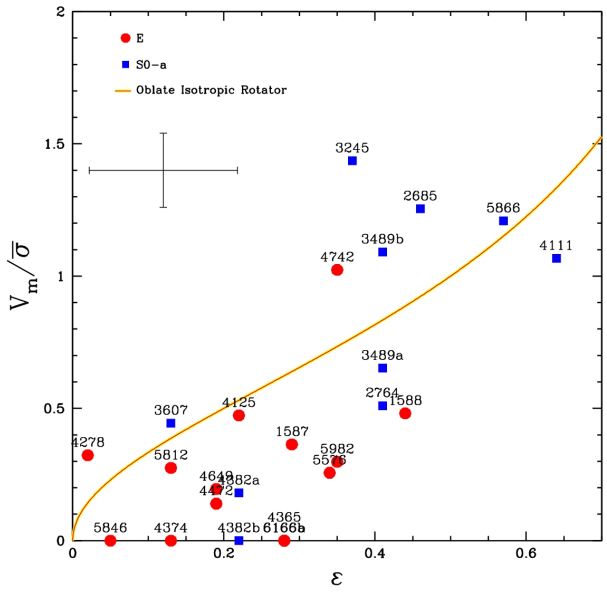

(a)

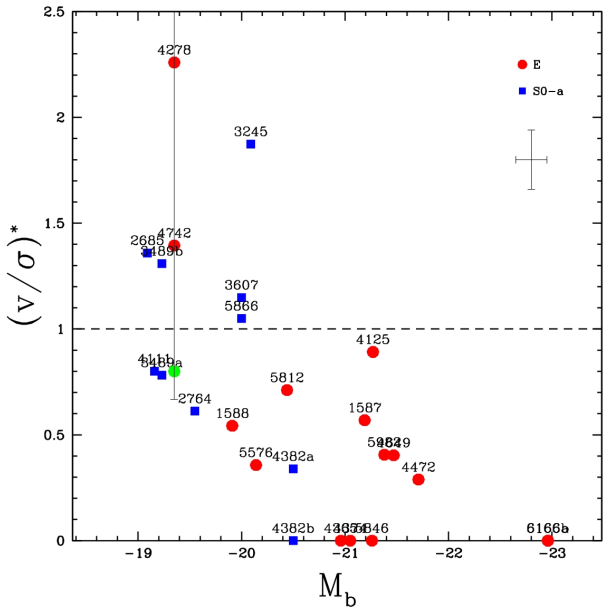

(b)

Figure 5.1 *Amount of rotational support for our sample. Red circles represent the ellipticals while the blue squares are the S0-a: a)* $\left(\frac{V_m}{\bar{\sigma}}\right)$ *versus the ellipticity, the yellow solid line is the prediction for an oblate isotropic rotator; b)* $\left(\frac{V_m}{\bar{\sigma}}\right)^*$*, that is the* $\left(\frac{V_m}{\bar{\sigma}}\right)$ *excess with respect to the OIR case, versus absolute blue magnitude, the dashed line represent* $\left(\frac{V_m}{\bar{\sigma}}\right)^* = 1$*. Though the typical error bar is reported, the uncertainty increases dramatically near* $\varepsilon = 0$*. For this reason we reported the error bar computed for NGC4278. As confirm, the green circle represent the position of NGC4278 if we adopt* $\varepsilon = 0.14$

5.2 Galaxies mass and mass-to-light ratio

A very interesting application of the stellar dynamics theory is the possibility, known the kinematics of the system and under certain hypothesis, to evaluate the mass of a stellar system. The simplest method to retrieve such mass is the virial estimator (Cappellari et al., 2006):

$$M(r) = \beta \frac{r\sigma^2}{G}, \tag{5.2}$$

where $M(r)$ is the mass contained in a sphere of radius r and β is a coefficient that depends on the characteristics of the system. Cappellari et al. (2006) found a good agreement between the eq. (5.2) and the results from more detailed models, considering β as a free parameter. Thus, we thought this method could led to reliable results. To better tune up the parameter β, we followed Michard (1980). Hereafter we report the arguments he followed and the consideration we made in the application to our sample. The starting model is a spherical isotropic galaxy that obeys the De Vaucouleurs law of $r^{1/4}$ in projection. For such a system the Jeans equation is written:

$$\frac{d(\varrho_L \sigma_r^2)}{dr} + \varrho_L \frac{GM(r)}{r^2} = 0 \tag{5.3}$$

and can be transformed into:

$$M(r) = r\frac{\sigma_r^2}{G}\left[-\frac{d\ln \varrho_L}{d\ln r} - \frac{d\ln \sigma_r^2}{d\ln r}\right], \tag{5.4}$$

where σ_r is the radial component of the velocity dispersion and ϱ_L is the density of the tracers of the kinematical information.

The last term can be written as $\varrho_L = \eta\kappa$, being η the luminosity density and κ the local M/L ratio. Shortly, we will note the bracket in the right hand term of eq. (5.4) as $\beta(r)$, and we can note that in this way the relation has the same form of eq. (5.2). If we link the radial component of the velocity dispersion to the observed line of sight velocity dispersion trough $\sigma_r(r) = \Gamma(r)\sigma_{obs}(r)$, eq. (5.4) becomes:

$$M(r) = \beta(r)\Gamma^2(r)\frac{r\sigma_{obs}^2(r)}{G}. \tag{5.5}$$

Thus, to evaluate the mass of the observed galaxy, we need to know β and Γ^2. This requires a further specification of our model. We consider two simple cases:

Case A) The Isothermal Sphere (hereafter IS): This is a power-law model with $\sigma_r = const.$ and characterized by a density distribution of the form $\varrho = \varrho_e(r/R_e)^{-2}$. For this model $\beta(r) = 2$ and $\Gamma(r) = 1$. Clearly this model presents a central singularity and an infinite total mass so is not reliable at very small or very large values of r.

Case B) A model with $\kappa = const.$: Many of the properties of this model have been tabulated by Poveda, Iturriaga, & Orozco (1960) and Young (1976), so hereafter it is called PY model. For this model, the values of β and Γ aren't constant with radius, so we must

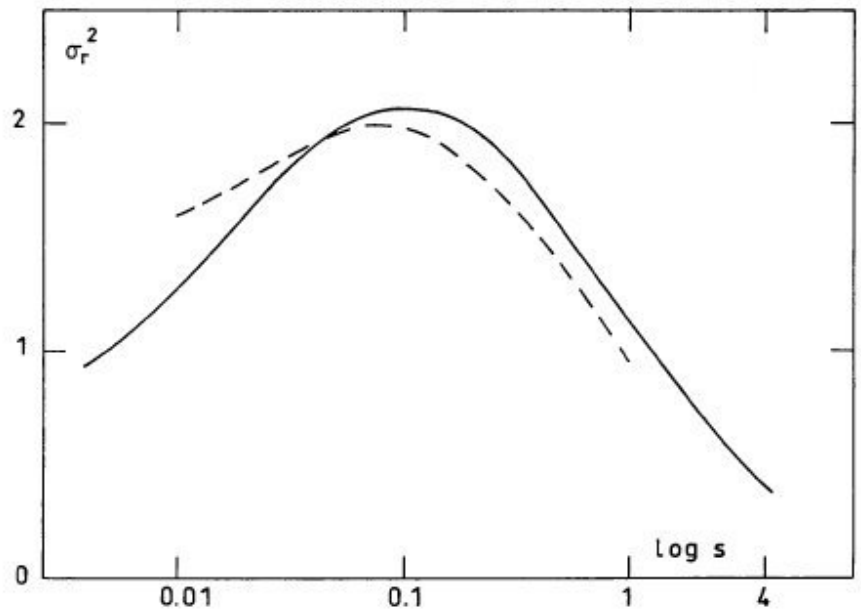

Figure 5.2 *The trends of velocity dispersion with radius for the case B of our discussion. The solid line represent the σ_r^2, while the dashed line is the σ_{obs}^2. The radius is in unit of R_e and the velocity dispersion is in unit of σ_0. Taken from Michard (1980).*

evaluate them point by point. For the sake of simplicity, from now on we restrict our analysis only to the value of $M(R_e)$, i.e. the mass enclosed in the sphere traced by the half light radius. At this radius $\beta(R_e) = 3.33$ and we can rewrite eq. (5.5) as:

$$M(r) = 3.33\Gamma^2(R_e)\frac{r_e\sigma_{obs}^2(R_e)}{G} = 3.33\gamma^2(r)\frac{R_e\sigma_{obs}^2(r)}{G}, \tag{5.6}$$

where $\gamma(r)$ is a factor that links the value of σ_r at R_e with the value of the σ_{obs} observed at an arbitrary radius. Since observations of σ_{obs} at R_e aren't always available, this rewriting is more useful.

For the evaluation of $\gamma^2(r)$, Michard (1980) traces the trends of σ_r and σ_{obs} with radius for the PY model. This is shown in Fig. 5.2. The velocity dispersion and the radius are normalized using R_e for the length and, for the velocity dispersion, a σ_0 such that $\sqrt{3}\sigma_0$ is the average velocity defined by the total kinetic energy of the galaxy. In this reduced form, $\sigma_r^2(r_e)$ turns out to be 1.11. We would like to use, as σ_{obs}, the $\bar{\sigma}$ defined in § 5.1. This quantity is defined as the mean in the first $R_e/2$, thus, given the trend of σ_{obs}, $\bar{\sigma}$ is essentially equal to a line of sight velocity dispersion sampled at $s = 0.22$ (where $s = r/R_e$). Adopting this value as σ_{obs}, the quantity $\beta * \gamma^2$ is very close to 2, so for both the models, the formula becomes:

$$M(R_e) = 2\frac{R_e\bar{\sigma}}{G}. \tag{5.7}$$

We now compute a more realistic model where the galaxy, instead of being spherical, is an oblate spheroid supported by rotation. In this case the Jeans equation in the equatorial plane is written:

$$\beta(r)\sigma_r^2 + u_\theta^2 = 4\pi G(1-\varepsilon^2)^{1/2} \int_0^r \frac{\varrho(x)x^2}{(r^2-\varepsilon^2x^2)^{1/2}}\, dx, \tag{5.8}$$

where u_θ is the rotation velocity and e is the eccentricity of the isodensity spheroids. Given the mass within the spheroid of equatorial radius r:

$$M(r) = 4\pi(1-\varepsilon^2)^{1/2} \int_0^r \varrho(x)x^2\, dx, \tag{5.9}$$

we find the following relation:

$$M(r) = \beta(r)\frac{r\sigma_r^2}{G}[1 + u_\theta^2/\beta\sigma_r^2]\varphi(\varepsilon, r), \tag{5.10}$$

where $\varphi(e, r)$ is linked to the two integrals of the previous equations. The assumption that this model has the same volume emissivity of our case B with a scale factor a_e, introduces a further corrective factor, $\alpha(\varepsilon, i)$, which links the observed R_e with the intrinsic a_e of the galaxy. Thus, considering the mass inside an half light radius, the relation becomes:

$$M(R_e) = 2\frac{R_e\bar{\sigma}^2}{G}[1 + u_\theta^2/2\bar{\sigma}^2]\alpha(\varepsilon, i)\varphi(\varepsilon, r_e). \tag{5.11}$$

Further considerations about the lesser amount of rotation with respect to the OIR model and about the presence of anisotropy in the velocity dispersion tensor, adopting the mean features of the elliptical population, lead to an additional correction of value 1.11. Thus, assuming that the V_m can be adopted as the typical rotation velocity of the galaxy, the final relation we find is:

$$M(R_e) = 2.22\frac{R_e\bar{\sigma}^2}{G}[1 + \frac{V_m^2}{2\bar{\sigma}^2}]\alpha(\varepsilon, i)\varphi(\varepsilon, r_e) \tag{5.12}$$

For the application to our sample, we assumed an IS structure (Case A of previous discussion) for all the galaxies that showed a constant profile of velocity dispersion and applied the PY model (Case B)to the other galaxies, that showed a decrease of σ_{obs} with radius. However, since the coefficient is the same at R_e, the choice of the model is irrelevant to the computation of the mass and we keep trace of the two families only to search for eventual differences between them regard some of the physical correlations we investigate in § 5.4. We derive R_e from the distance modulus obtained from the comparison of the apparent and the absolute magnitude. Concerning the two corrective factors in the eq. (5.12), $\alpha(\varepsilon, i)$ varies between 1 for $i = 0°$ to $(1-\varepsilon^2)^{-1/4}$ for $i = 90°$, while $\varphi(\varepsilon, r)$ reduces to $\varepsilon/\arcsin\varepsilon$ for the IS model. This should be a tenable approximation for the other models. Therefore, the true correction can't be estimated without knowing the inclination of the galaxy.

In Fig. 5.3 are shown the values of the correction factor $\alpha\cdot\varphi$ with varying ellipticity. It can be seen that the uncertainty on the inclination is not very critical, implying, for the more

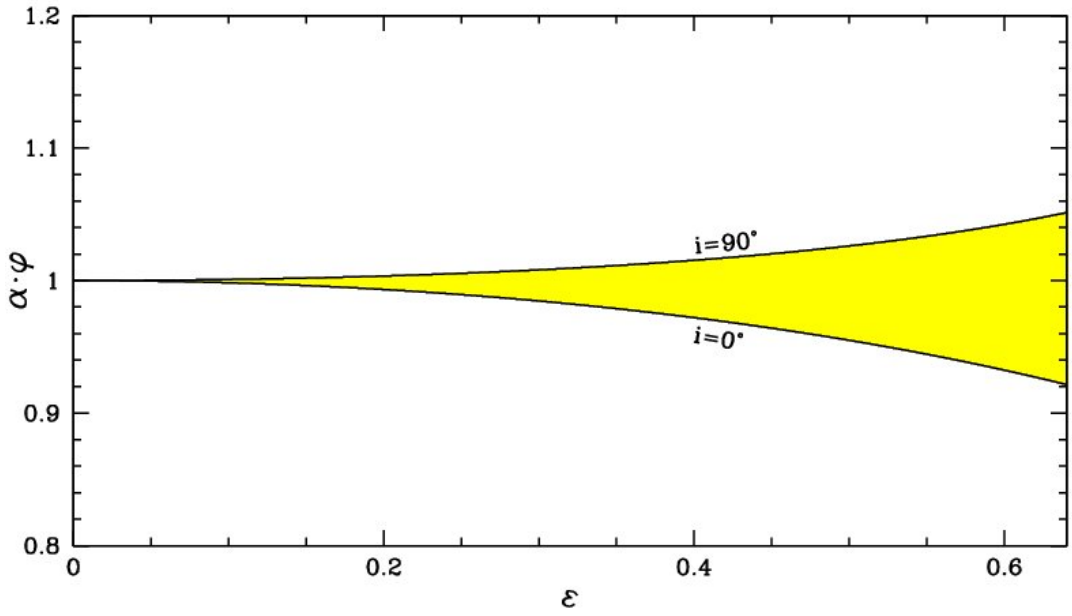

Figure 5.3 *Trend of the corrective factor $\alpha \cdot \varphi$ with the ellipticity. The black solid lines represent the limit cases of an edge-on and a face-on galaxy, while the yellow shading traces the region of the intermediate inclinations. One sees that the maximum expected uncertainty is better than $\pm 5\%$.*

flattened galaxy of our sample, an error of 5%. This error can be further reduced considering that, under the hypothesis of oblateness, the more flattened galaxies can't admit inclinations too low. Concerning the uncertainties on our mass estimation, the major contribute derives from the estimation of R_e, that depends on the value of the cosmological constant H_0 and from the scatter in the velocity dispersion, which we have seen to be of the order of 10%. *Then, because the velocity dispersion is squared in eq. (5.12), we conclude that the value of the mass we find inside R_e can be reliable within a 25% uncertainty and up to a factor $H_0/70 Km\, s^{-1} Mpc^{-1}$.*

Once we know the value of mass and R_e, an easy computable quantity is the escape velocity, defined by the simple relation:

$$V_{esc}^2(R_e) = \frac{2GM(R_e)}{R_e}. \tag{5.13}$$

Being rigorous, the eq. (5.13) holds only for a spherical symmetric system, but it should be a fair approximation for our flattened objects. Successively, we computed also the M/L of the sample. Given the absolute magnitudes, the most immediate thing we did was to evaluate the mass to light ratio in the blue band. Taken a value for the solar blue magnitude of $M_\odot^B = 5.448$ (Portinari, Sommer-Larsen, & Tantalo, 2004), we calculated the total blue luminosity of our galaxies. Since the value of magnitudes we used are the asymptotic extrapolation, we used the luminosity inside R_e, $L(R_e) = 0.415_T$ (Young, 1976). Given the

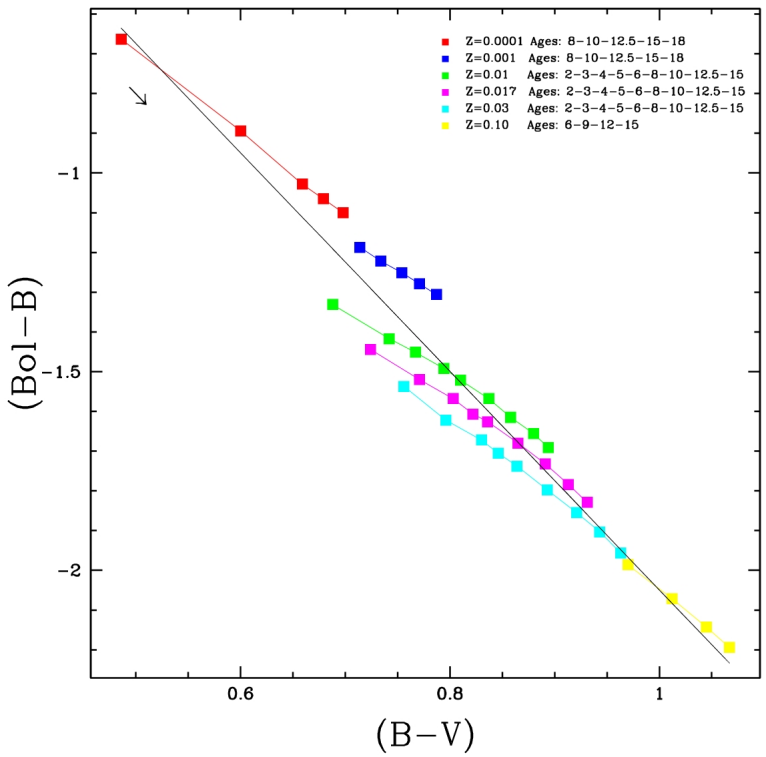

Figure 5.4 *Relation between the (B-V) colour and the (Bol-B) correction for SSP models. All the models are computed for a Salpeter IMF, a value of* $\eta = 0.3$ *and a red horizontal branch. Different colours represent different metallicities. Ages considered span from 2 to 18 Gy, while metallicities range from* $Z = 0.0001$ *to* $Z = 0.10$*. The arrow points in the direction of increasing age. The black solid line represent the fitted relation.*

error of 25% on the masses and assuming a typical uncertainty on the luminosities of the order of $\approx 15\%$, we can estimate an uncertainty on the M/L of $\approx 30\%$.

As the measure of the M/L was done inside one R_e, we expect that these values give poor constraints to the content of dark matter, which dominates at more external radius. The M/L is then fully determined by the nature of the stellar population. Elliptical galaxies are stellar system composed principally of old, small and red stars and the measured M/Ls range from the unity to about 15, being in accord to the values predicted from these population. Being the bulk of the luminosity of these stellar populations emitted at redder frequencies respect to the blue band, we thought a more reliable estimate of the true mass to light ratio was needed. Using the simple stellar population models from Buzzoni (1989), we estimated a relation between the correction, needed to transform the blue magnitude to the bolometric one, and the colour of the stellar system.

Fig. 5.4 shows the relation between the integrated colour of an SSP and the bolometric correction from the B band for several values of age and metallicities. It can be noted that

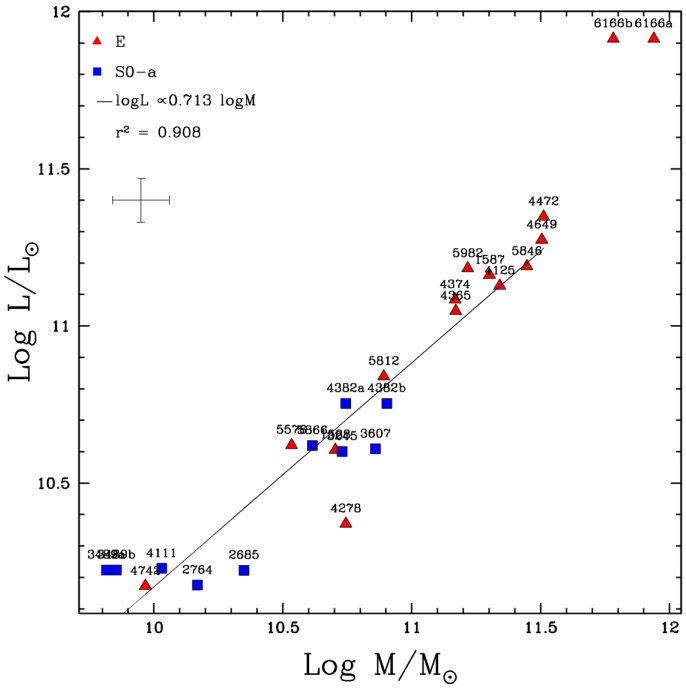

Figure 5.5 *Relations between mass, bolometric luminosity. Red triangles are ellipticals while blue square are S0-a. The black solid line is the fitted relation. The correlation coefficient* r^2 *is given at the top of the diagram.*

the points define a tight sequence and, even if the age or the metallicity of the system is unknown, a reasonable bolometric magnitude can be extracted fitting the points with the relations:

$$(Bol - B) = -2.75(B - V) + 0.70, \tag{5.14a}$$

$$(Bol - V) = (Bol - B) + (B - V) = -1.75(B - V) + 0.70. \tag{5.14b}$$

Thus we could retrieve the bolometric luminosity adopting a $M_{\odot}^{Bol} = 4.72$. Tab. 5.2 report the values found for the mass and the M/L ratio (respect both the blue and the bolometric luminosity). The model of the velocity dispersion profile and the escape velocity are also reported.

To verify if the mass determination was reliable and to investigate for any significant trend we plotted the bolometric luminosities versus the previous found masses (Fig. 5.5). It can be seen that there is a very tight correlation between this two quantities. Remembering that the dynamical mass is linked to the velocity dispersion, this correlation is a reinterpretation of the famous Faber-Jackson relation (Faber & Jackson, 1976). We probed also the distribution of the mass-to-light ratios respect to the bolometric luminosities. Even in this diagram we found a correlation, although it is less defined. The bulk of the galaxies lies in a relatively tight sequence, while few objects lies outside. Among them, the most

Table 5.2 *The mass and mass to light values for the studied sample, together with the escape velocity and the model inferred from the velocity dispersion distribution. The masses are in unit of* $10^{10} M_{\odot}$. *The mass to light ratios are computed both in blue and in bolometric luminosity and are in solar units. The escape velocity is reported in Km/s.*

Name NGC	M $[10^{10} M_{\odot}]$	M/L_B	M/L_{Bol}	V_{esc} [Km/s]	Model
1587	20.0 ± 5.0	10.67 ± 3.20	3.32 ± 1.00	514 ± 77	PY
1588	5.1 ± 1.3	8.74 ± 2.62	3.02 ± 0.91	361 ± 54	IS
2685	2.24 ± 0.56	8.24 ± 2.47	3.22 ± 0.97	273 ± 41	IS
2764	1.48 ± 0.37	3.56 ± 1.07	2.37 ± 0.71	240 ± 36	IS
3245	5.4 ± 1.3	7.88 ± 2.36	3.24 ± 0.97	411 ± 62	PY
3489(32°)	0.65 ± 0.16	2.12 ± 0.64	0.94 ± 0.28	231 ± 35	IS
3489(58°)	0.72 ± 0.18	2.32 ± 0.70	1.03 ± 0.31	242 ± 36	IS
3607	7.2 ± 1.8	11.53 ± 3.46	4.29 ± 1.29	447 ± 67	IS
4111	1.07 ± 0.27	3.71 ± 1.11	1.53 ± 0.46	377 ± 57	PY
4125	22.0 ± 5.5	10.86 ± 3.26	3.94 ± 1.18	533 ± 80	PY
4278	5.6 ± 1.4	16.12 ± 4.84	5.70 ± 1.71	498 ± 75	PY
4365	14.8 ± 3.7	9.75 ± 2.93	3.20 ± 0.96	531 ± 80	IS
4374	14.7 ± 3.7	8.92 ± 2.68	2.92 ± 0.88	562 ± 84	PY
4382(1996)	5.6 ± 1.4	5.58 ± 1.67	2.36 ± 0.71	385 ± 58	IS
4382(1997)	8.0 ± 2.0	8.05 ± 2.42	3.40 ± 1.02	462 ± 69	IS
4472	32.5 ± 8.1	10.71 ± 3.21	3.51 ± 1.05	606 ± 91	PY
4649	31.9 ± 8.0	13.14 ± 3.94	4.09 ± 1.23	686 ± 103	IS
4742	0.93 ± 0.23	2.69 ± 0.81	1.50 ± 0.45	276 ± 41	IS
5576	3.42 ± 0.86	4.79 ± 1.44	1.97 ± 0.59	386 ± 58	PY
5812	7.8 ± 1.9	8.28 ± 2.48	2.72 ± 0.82	409 ± 61	PY
5846	28.0 ± 7.0	13.97 ± 4.19	4.35 ± 1.31	527 ± 79	IS
5866	4.1 ± 1.0	6.56 ± 1.97	2.38 ± 0.71	380 ± 57	PY
5982	16.5 ± 4.1	7.38 ± 2.21	2.61 ± 2.28	526 ± 79	IS
6166a	86.9 ± 21.7	9.06 ± 2.72	2.55 ± 0.77	478 ± 72	PY
6166b	60.5 ± 15.1	6.31 ± 1.89	1.78 ± 0.53	399 ± 60	PY

remarkable is NGC6166. Since this galaxy is a central dominant, it may underwent trough a different evolution respect to standard galaxies. For this reason we kept this galaxy off the fit. Last square fitting for this diagram gives us:

$$L_{Bol} \propto M^{0.71\pm0.049} \qquad r.m.s. = 0.12\,dex, \tag{5.15a}$$

$$\frac{M}{L_{Bol}} \propto L_{Bol}^{0.28\pm0.088} \qquad r.m.s. = 0.16\,dex. \tag{5.15b}$$

Eq.(5.15b) can be compared with Kobayashi & Arimoto (1999), who found a luminosity exponent of 0.35. Accordingly, Jorgensen, Franx, & Kjaergaard (1996) infer a value of 0.31, while the first results from Faber et al. (1987) outlined a trend with $L^{0.24}$. *The confirmed correlation between the mass to light ratio and the galaxy luminosity is a key point in our analysis and will be considered in the context of the next section.*

5.3 The fundamental plane

Since we have acquired, for our sample, a dataset of quite several physical properties, we considered natural to probe how they are interconnected and which relations can be inferred. The most obvious relation we can investigate is the fundamental plane. In the Djorgovski & Davis (1987) formulation it relates the effective radius R_e with the velocity dispersion σ and the mean surface brightness inside R_e, $\langle I \rangle_e$. As we have the total bolometric luminosity, we could compute an estimate of $\langle I \rangle_e$ in a fast and easy way, as:

$$\langle I \rangle_e = \frac{0.42 L_{bol}}{\pi R_e^2}. \tag{5.16}$$

We used the coefficient 0.42 instead of the classical 0.5 for coherence with what already done in the previous section, in accord with Young (1976) tables.

The firsts trails of the fundamental plane were discovered trough its projections, the Faber-Jackson (hereafter FJ) and the Kormendy relations (Kormendy, 1977). Fig. 5.6 shows the plots for for our sample. As already pointed out, NGC 6166 is a cD galaxy and, since these objects lie on different scaling relations (Oegerle & Hoessel, 1991), in the present section we kept it off our fitting procedures. We found good agreement with Kormendy results, while the slope for the FJ is steeper than the canonical $\log \sigma \propto -0.1M$. Analysing the plot we noted a group of several galaxies, among the faintest, that steepens the relations. *A similar steepening was found also by Tonry (1981), and it can be interpreted as an evidence of the so called "Downsizing" mass assembling mechanism (Cowie et al., 1996; Gavazzi, Pierini, & Boselli, 1996).* Smaller galaxies have a higher birthrate with respect to the biggest ones (Buzzoni, 2011), so the younger population provides a higher luminosity (that is a lower M/L ratio) than predicted from the Faber-Jackson standard relation. Excluding these objects from the FJ fit allow us to retrieve a good estimate of the scaling relations:

$$\log \sigma \propto -(0.106 \pm 0.02) M_{bol} \qquad r.m.s. = 0.065\,dex, \tag{5.17a}$$

$$\log R_e \propto -(0.804 \pm 0.091) \log \langle I \rangle_e \qquad r.m.s. = 0.135\,dex. \tag{5.17b}$$

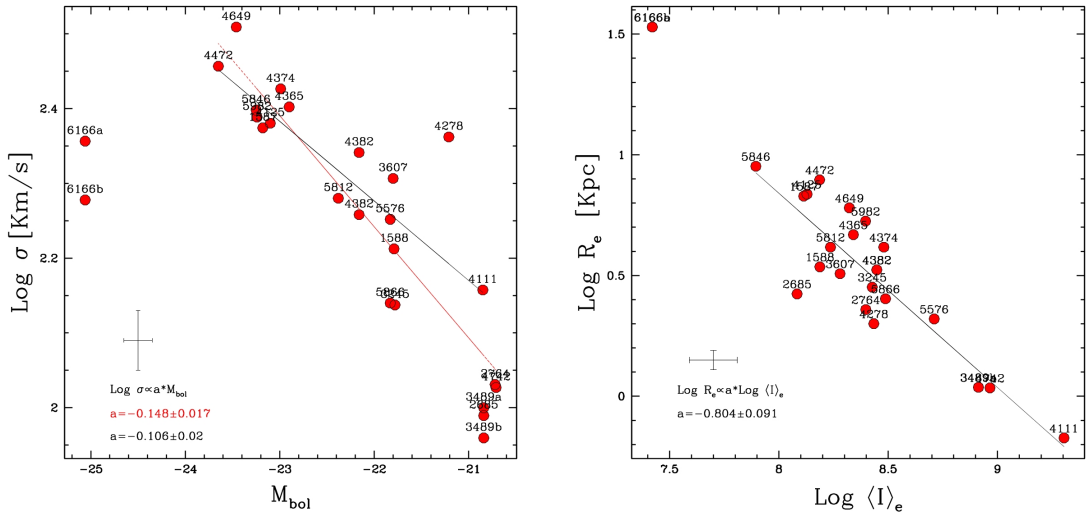

(a) (b)

Figure 5.6 *Projected scaling relations for our sample. The black line represent the least square fit: a) The Faber-Jackson. The red line represent the fit done including also the faintest galaxies; b) The Kormendy relation.*

Moreover, we considered the three dimensional set of $R_e - \sigma - \langle I \rangle_e$. We implemented a routine for the evaluation of the best-fitting plane, based on generalized least-squares approach. If we suppose that these quantity are linked by a relation of the form:

$$y = \alpha \cdot x + \beta \cdot z + \gamma, \tag{5.18}$$

the sum of the residuals between the observed y and the calculated ones can be wrote:

$$\mathcal{R}^2 = \sum_i \mathcal{R}_i^2 = \sum_i (y_i - \alpha \cdot x_i - \beta \cdot z_i - \gamma)^2. \tag{5.19}$$

The best fitting parameter set is the one which minimizes $\mathcal{R}^2$ and can be find by imposing:

$$\frac{\partial \mathcal{R}^2}{\partial \alpha} = 0 \quad ; \quad \frac{\partial \mathcal{R}^2}{\partial \beta} = 0 \quad ; \quad \frac{\partial \mathcal{R}^2}{\partial \gamma} = 0. \tag{5.20}$$

These conditions provide the system of equations to solve in order to find the best fitting plane:

$$\alpha \sum x_i^2 - \sum x_i y_i + \beta \sum x_i z_i + \gamma \sum x_i = 0, \tag{5.21a}$$

$$\beta \sum z_i^2 - \sum y_i z_i + \alpha \sum x_i z_i + \gamma \sum z_i = 0, \tag{5.21b}$$

$$\gamma - \sum y_i + \alpha \sum x_i + \beta \sum z_i = 0. \tag{5.21c}$$

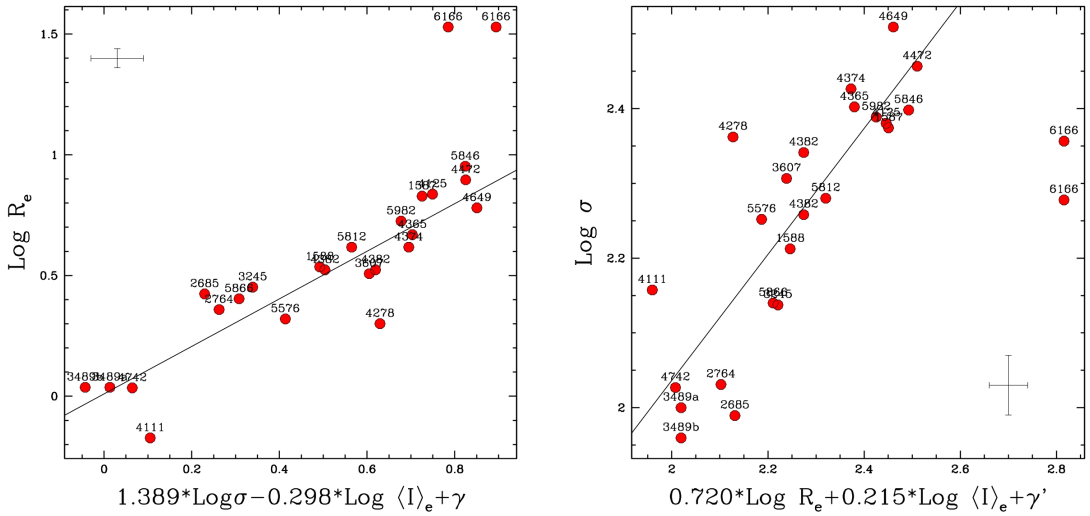

(a) (b)

Figure 5.7 *Fundamental plane projections: a)* $\log R_e$ *vs.* $1.389 \log \sigma - 0.298 \log \langle I \rangle_e$*; b)* $\log \sigma$ *vs.* $0.72 \log R_e + 0.215 \log \langle I \rangle_e$

If we put $y = \log R_e$, $x = \log \sigma$ and $z = \log \langle I \rangle_e$ we find a fundamental plane of the form (Fig. 5.7a):

$$R_e \propto \sigma^{1.39} \langle I \rangle_e^{-0.30}. \tag{5.22}$$

By comparing with reference results, such as Jorgensen, Franx, & Kjaergaard (1996), the slopes of the plane we found are in good agreement as for the dependence on σ, but are significantly shallower respect to $\langle I \rangle_e$. Furthermore, the *r.m.s.* of the residuals about $\log R_e$ is $0.12\, dex$. If we want to convert this value in a percent scatter trough the relation (valid for adequately small r.m.s.):

$$r.m.s.(\%) = \frac{dx}{x} = d \ln x = d \log x \cdot \ln 10 \approx 2.30\, r.m.s.(dex), \tag{5.23}$$

we obtain a scatter of 28%, slightly higher with than usually found ($\approx$ 15%). A tighter correlation can be seen by plotting the corresponding relation, as in Fig. 5.7b:

$$\sigma \propto R_e^{0.72} \langle I \rangle_e^{0.22}. \tag{5.24}$$

In this case the *r.m.s.* is $0.09\, dex$, corresponding to a scatter of 19%. In this form, the comparison with Kobayashi & Arimoto (1999) confirms that the our best-fit plane has a shallower slope in $\log \langle I \rangle_e$. If elliptical galaxies were an homologous family with an M/L we would expect to find a dependence of the order of $R_e \propto \sigma^2 \langle I \rangle_e^{-1}$. Since we observe different

exponents, we have clues on the structure of ETGs. Assuming homology, we can retrieve the variation of the M/L needed to explain the tilt (Jorgensen, Franx, & Kjaergaard, 1996):

$$M/L \propto L^{1/\alpha - 1/2} \simeq L^{0.22}. \tag{5.25}$$

This results seem to be compatible with our previous finding of eq.(5.15b), namely, $M/L \propto L^{0.28}$.

5.4 Lick indices

As a final part of our work, we want to study the link between the dynamical data of our galaxies and the chemical properties of their composing stellar populations. A relation between spectroscopical tracers of metallicity and structural parameters for ETGs has been known since long (Burstein et al., 1988; Bender, Burstein, & Faber, 1993) and contains information about the formation process of these objects. In particular, the correlation with the central velocity dispersion has been interpreted as an evidence of the role of supernovae driven galactic winds in the star formation history of young galaxies (Arimoto & Yoshii, 1987).

In this context, we investigated the dynamical properties of our sample with a wide range of chemical tracers, in order to keep trace not only of the overall metallicity, but also of age, abundance of α elements and so on. We focused our attention on the possible correlation with dynamical mass, velocity dispersion, escape velocity and M/L ratio. For this analysis we relied on the Lick/IDS index set as derived by Buzzoni et al. (2014) for the same galaxy sample. The indices provide informations about the spectral contributions of elements such Magnesium, Iron and Hydrogen, as well as Calcium, Carbon and Oxygen.

Before we can use these measures, a few preparatory operations were needed. First, we had to correct two of the values, $[OIII]_{5007}$ and Fe_{5015}. The former index is not part of the Lik/IDS system, which was built on a stellar observation database, but was formalized by González (1993) to account for possible emission of residual gas in active ellipticals. The correction is due to the overlap of the two bandpasses used for the indices measurement, thus the two indices influences each other, as can be seen in Fig. 5.8. If $[OIII]^{obs}_{5007}$ and Fe^{obs}_{5015} are the observed features, we can infer the intrinsic values, $[OIII]^{clean}_{5007}$ and Fe^{clean}_{5015}, trough the relation (Buzzoni and Bertone, 2014):

$$Fe^{clean}_{5015} = 1.36\Big(Fe^{obs}_{5015} - [OIII]^{obs}_{5007}\Big), \tag{5.26a}$$

$$[OIII]^{clean}_{5007} = [OIII]^{obs}_{5007} - 0.26Fe^{clean}_{5015} = 1.36[OIII]^{obs}_{5007} - 0.36Fe^{obs}_{5015}. \tag{5.26b}$$

Subsequently, we selected the indices to use. We chose Mgb and Mg_2 as tracer of, respectively, atomic and molecular Magnesium and, consequently of the overall metallicity. The $H\beta$ was selected as Hydrogen index. Being related to the emission from hot stellar atmospheres, this index is not a tracer of chemical abundances but is linked to the age of the stellar population. Though we have already kept trace of the metallicity, the Magnesium abundance count principally as a tracer of α elements and is, hence, linked to the contribution of core-collapse supernovae in the metal enrichment process of the ISM. The other

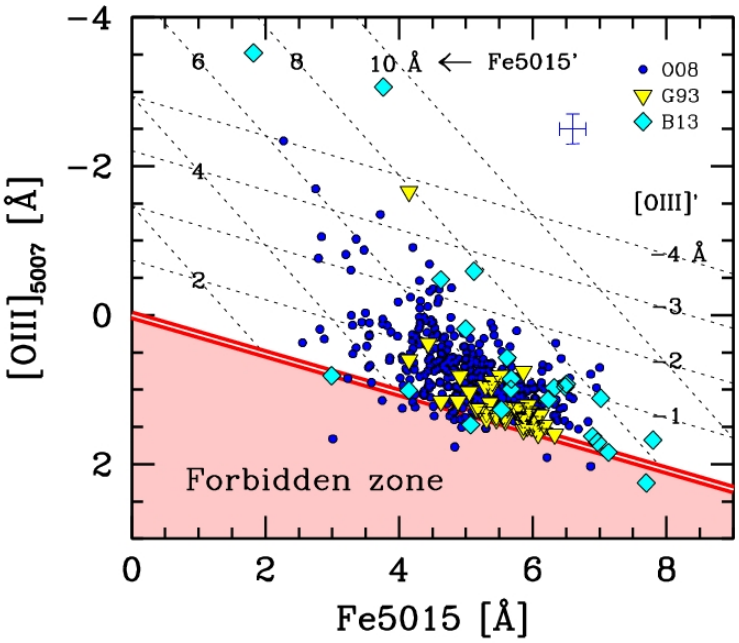

Figure 5.8 *The correlation of* $[OIII]_{5007}$ *and* Fe_{5015} *observed indices. Taken from Buzzoni and Bertone (2014). The dotted lines represent the intrinsic value of the indices while the dot are the observed data from González (1993); Ogando et al. (2008); Buzzoni et al. (2014).*

contribution is played by type-Ia supernovae that, on the other hand, produce principally elements of the Iron-Nickel group. Since the time scales of this two process in a stellar population are quite different, we decided to include in our analysis a feature linked to the Iron content.

The choice of the appropriate indices is a delicate matter since many of the "Fe" labelled indices are actually a blend of several chemical features (Trager et al., 1998). The Fe_{5015} index seems to be an ideal choice, due to its very deep equivalent width, but we excluded it because of the influence of the possible hidden Oxygen emission. Although we made a correction to account for this effect, we used Fe_{5015} only to make possible a comparison with a previous work on escape velocity and, as Iron indicator, we preferred to consider less pronounced but more reliable tracers. Among these other feature, a distinction need to be made about the indices lying in the red part of the spectrum and those lying in the blue one. Despite the fact that the majority of them are blend dominated by the Iron spectral lines, the formers present a contribution principally from Nickel and Chromium (all elements produced in type-Ia supernovae), while the latters are characterized by a strong influence from Titanium and Magnesium (Buzzoni and Bertone, 2014). To keep trace of these two family, we computed two composite indices, defined as:

$$\langle Fe \rangle_{red} = \frac{Fe_{5270} + Fe_{5335}}{2}, \tag{5.27a}$$

$$\langle Fe \rangle_{blue} = \frac{Fe_{4383} + Fe_{4531}}{2}. \tag{5.27b}$$

Table 5.3 *Nuclear absorption indices from Buzzoni et al. (2014).* $[OIII]_{5007}$ *and* Fe_{5015} *are cleaned from their mutual influence. All the indices except from the* Mg_2 *are expressed in Ångstroms.* Mg_2 *is expressed in magnitudes.*

Name NGC	G_{4300} [Å]	$\langle Fe\rangle_{blue}$ [Å]	Ca_{4455} [Å]	Fe_{4668} [Å]	$H\beta$ [Å]	$[OIII]_{5007}$ [Å]	Fe_{5015} [Å]	Mg_2 [mag]	Mgb [Å]	$\langle Fe\rangle_{red}$ [Å]
1587	···	···	···	5.74	2.57	0.15	···	0.299	4.73	2.73
1588	···	···	···	···	···	···	···	···	···	···
2685	6.15	4.16	1.54	5.61	2.11	-1.25	6.87	0.264	3.89	3.16
2764	4.15	0.53	0.24	1.04	-6.57	-5.44	7.26	0.094	2.08	1.68
3245	5.13	3.73	1.56	7.81	0.81	-0.88	6.56	0.292	3.67	2.62
3489a	4.20	4.38	1.44	4.96	2.47	-2.32	6.94	0.204	3.21	2.52
3489b	4.33	3.91	1.99	4.75	2.50	-2.65	7.77	0.216	3.31	2.63
3607	5.89	5.63	1.76	9.14	1.20	-0.96	7.28	0.315	5.08	3.52
4111	5.08	4.41	1.35	8.15	1.93	-1.03	7.52	0.252	4.09	3.12
4125	5.78	5.02	1.83	7.75	1.27	-1.09	7.59	0.287	4.58	3.16
4278	6.34	5.15	1.62	7.44	-1.69	-5.53	9.30	0.331	6.37	2.89
4365	···	4.27	···	7.61	···	-0.06	7.19	0.314	5.01	···
4374	7.67	5.43	1.61	8.85	1.33	-0.71	6.95	0.307	5.15	2.97
4382	5.71	3.72	0.72	4.96	1.83	0.17	4.90	0.229	3.58	2.63
4472	6.14	5.28	1.97	8.48	1.28	-0.27	7.17	0.351	5.38	3.29
4649	5.95	5.07	1.55	8.90	1.32	-0.52	8.32	0.370	5.85	2.98
4742	3.72	3.54	1.52	5.19	3.04	-0.12	4.27	0.212	2.56	2.41
5576	5.30	4.91	1.78	6.61	1.91	-0.69	6.36	0.255	4.18	2.84
5812	5.73	4.98	1.84	9.48	1.25	-0.20	7.17	0.349	5.04	3.01
5846	5.68	4.88	1.73	8.94	1.10	-1.00	8.02	0.335	5.10	3.39
5866	5.62	3.75	1.63	5.84	1.87	-1.56	6.56	0.232	3.77	3.13
5982	5.43	5.18	1.70	8.56	1.25	-0.26	5.78	0.291	4.92	3.37
6166	6.99	5.08	1.76	8.55	1.81	0.03	2.96	0.335	6.19	3.68

Moreover, we decided to monitor a couple of other α elements, Calcium and Carbon, to probe for any anomalous behaviour. We included in our analysis the Ca_{4455} feature, as well as the G_{4300} and the Fe_{4668}. Concerning the last two indices, the first is a measure of the famous G-band, produced principally by the CH, and the latter one, despite the name, is dominated by the absorption of the C_2 (Trager et al., 1998). In addition, we thought it could be useful to have an indicator of the gaseous component so we used the $O[III]_{5007}$. Tab. 5.3 reports the value of the measures for the chosen indices.

Finally, after the selection of the suitable indices, we converted all the values, that, except for the Mg_2, were measured in Å, in magnitude. Following the definition of

Worthey et al. (1994), we obtain:

$$I_{Mag} = -2.5 \log \left(1 - \frac{I_{EW}}{\Delta\lambda}\right), \tag{5.28}$$

where I_{Mag} is the index expressed in magnitudes, I_{EW} is the value in Å and $\Delta\lambda$ is the width of the feature spectral window (as from Worthey et al., 1994, Table 1). We adopted this formulation, instead of take the logarithm of the indices measured in Å, because of its smoother behaviour for values near the zero and because this formulation permits to include also emission features. For the composite indices we set:

$$I_{Mag} = -2.5 \log \left(1 - \left\langle \frac{I_{EW}}{\Delta\lambda} \right\rangle\right). \tag{5.29}$$

The relationship of Lick indices with the galaxy dynamical parameter has been searched relying on a standard least squares fitting procedure in the log-log domain. We kept some galaxies out of the fitting process. NGC2764 has a considerable amount of on-going star formation, so many of the measured indices returned a very low value. The explanation is, rather than a low abundance of metals, that absorption features from cool stars are dumped by the light of hotter and brighter stars. For this reason we excluded this galaxies from every correlation, except for the Mgb, the G_{4300} and the Fe_{5015}. The star formation activity of this galaxy also give rise to a strong $H\beta$ emission. Also NGC 4278 has a strong $H\beta$ emission line, this time due to the intense nuclear activity of this LINER galaxy (Véron-Cetty & Véron, 2006).

The $H\beta$ index is influenced both by the emission component, that trace the presence of ionized gas, and the absorption lines of stellar atmospheres, whose intensities are linked to the age of the system(e.g.). In the case of these two galaxies, the emission component overwhelms the absorption one, and the carried information are uncorrelated with respect to the rest of the sample. Thus, we excluded them from the analysis of the $H\beta$ relations. Their strong emission, led us to exclude them also from the analysis on the $O[III]$. Finally, NGC6166 has shown an anomalous M/L ratio with respect to other objects, due to its cD nature, and we decided to keep it off of the M/L correlations. Our choice is also confirmed by the outlier behaviour of these galaxies in the respective diagrams.

Tab. 5.4 shows the results of the least squares fit on the datasets considered. The angular coefficients, $r.m.s.$ and coefficient determination, R^2 (computed as the product of the angular coefficient of the fit whit that of fitted inverse relation), are listed. *Generally, we found correlation between the dynamical data and all of the considered indices except for the Fe_{5015} and the Ca_{4455}.* The choice of the dynamical parameter seems to be quite irrelevant on the scatter of the data, although the dynamical mass exhibit slightly tighter correlations and the M/L shows less defined trends. The better correlations with the mass are in contrast with the results of Scott et al. (2009), in which the escape velocity is found to be in a tighter relation respect to the mass. The indices considered in that paper are the Mgb, the Fe_{5015} and the $H\beta$. Fig. 5.9 show our plot for those indices.

We found a similar correlation with the Mgb, while our gradient with $H\beta$ is shallower and the correlation with the Fe_{5015} is absent at all. Scott et al. (2009) find also a correlation

Table 5.4 *Correlation parameters for any combination of the indices and the dynamical properties considered. The parameters refers to a relation of the form: $y \propto m \cdot \log x$. The r.m.s. is expressed in dex. Where data aren't present, no correlation was found.*

Index	Dynamical data	m	*r.m.s.*	R^2
G_{4300}	V_{esc}	0.18 ± 0.04	0.03	0.45
	M	0.04 ± 0.01	0.02	0.59
	σ	0.14 ± 0.04	0.03	0.46
	M/L	0.11 ± 0.03	0.02	0.46
$\langle Fe \rangle_{blue}$	V_{esc}	0.08 ± 0.02	0.01	0.35
	M	0.016 ± 0.005	0.01	0.37
	σ	0.07 ± 0.02	0.01	0.43
	M/L	0.04 ± 0.02	0.01	0.23
Ca_{4455}	V_{esc}	...	...	...
	M	...	...	...
	σ	...	...	...
	M/L	...	...	...
Fe_{4668}	V_{esc}	0.12 ± 0.03	0.02	0.44
	M	0.02 ± 0.01	0.02	0.40
	σ	0.09 ± 0.02	0.02	0.41
	M/L	0.06 ± 0.02	0.02	0.29
$H\beta$	V_{esc}	-0.12 ± 0.03	0.02	0.46
	M	-0.02 ± 0.01	0.02	0.31
	σ	-0.09 ± 0.03	0.02	0.37
	M/L	-0.09 ± 0.02	0.02	0.47
$O[III]_{5007}$	V_{esc}	0.18 ± 0.06	0.03	0.36
	M	0.04 ± 0.01	0.03	0.31
	σ	0.15 ± 0.05	0.03	0.36
	M/L	0.11 ± 0.04	0.03	0.27
Fe_{5015}	V_{esc}	...	...	...
	M	...	...	...
	σ	...	...	...
	M/L	...	...	...
Mg_2	V_{esc}	0.31 ± 0.06	0.03	0.58
	M	0.07 ± 0.01	0.03	0.63
	σ	0.24 ± 0.05	0.03	0.56
	M/L	0.19 ± 0.04	0.03	0.57
Mgb	V_{esc}	0.25 ± 0.05	0.03	0.56
	M	0.06 ± 0.01	0.03	0.63
	σ	0.21 ± 0.04	0.03	0.58
	M/L	0.14 ± 0.03	0.03	0.47
$\langle Fe \rangle_{red}$	V_{esc}	0.04 ± 0.02	0.01	0.18
	M	0.012 ± 0.003	0.01	0.43
	σ	0.03 ± 0.01	0.01	0.19
	M/L	0.03 ± 0.01	0.01	0.27

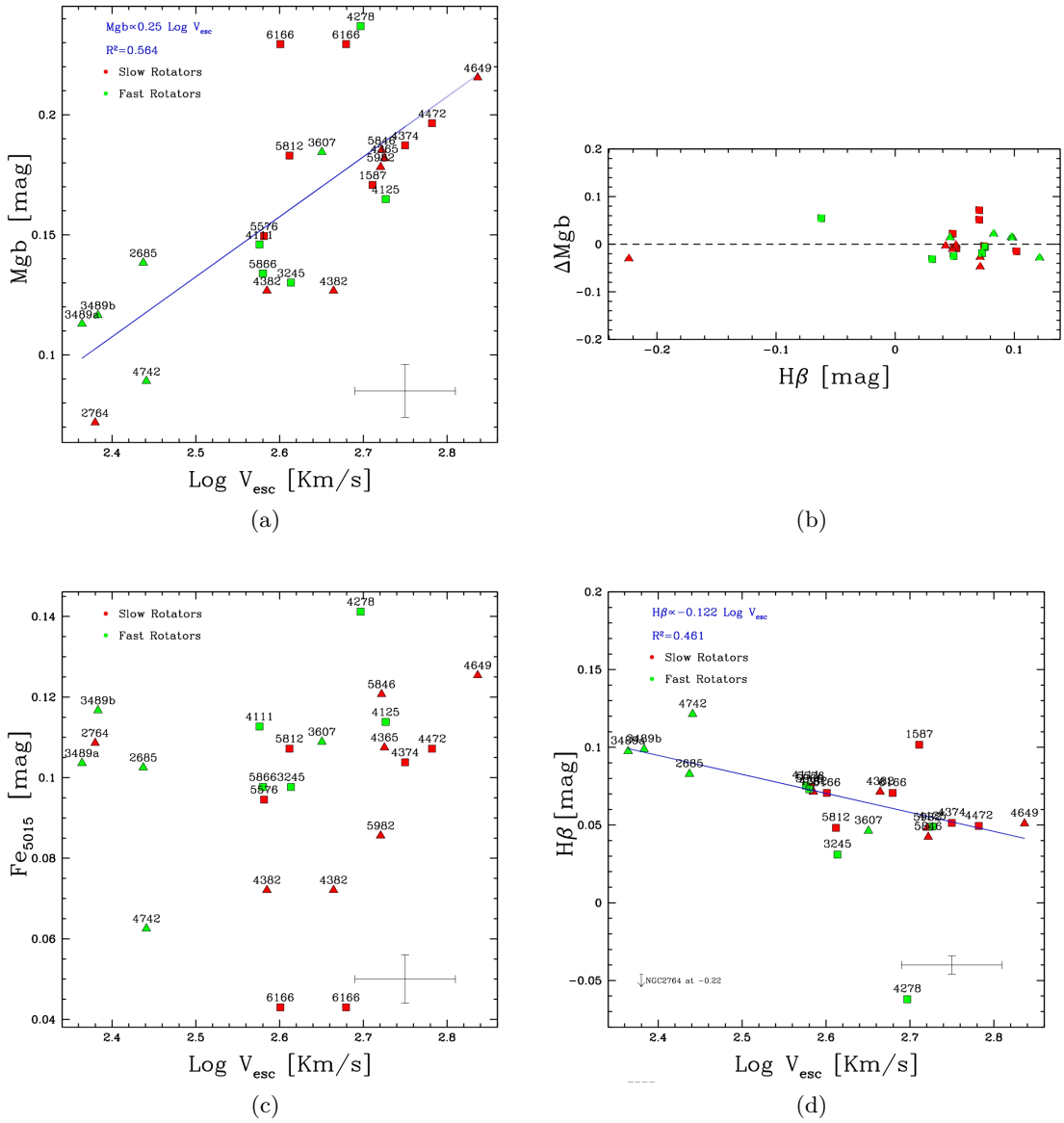

Figure 5.9 *Relation of escape velocities with some of the considered indices: a) Relation with the Mgb; b) Residuals of the $V_{esc} - Mgb$ relation, $\Delta Mgb = Mgb_{obs} - Mgb_{fit}$, plotted against the $H\beta$; c) Relation with the Fe_{5015}; Relation with the $H\beta$. Red points are the galaxies with $(V_m/\bar{\sigma})^* < 0.75$. Green points represent the objects with an higher value. Galaxies modelled with an isothermal sphere are shown as triangles, while squares represent PY like galaxies. The solid blue line, where present, shows the least squares fit. If a relation was found, the angular coefficient and the correlation coefficient are superimposed on the diagrams.*

between the residuals of the $V_{esc} - Mgb$ relation and the $H\beta$, used to explain the behaviour of some outlier galaxies (included one galaxy of our sample: NGC 4382). We also searched for this interesting correlation but we found none. The fact we found correlation between most of the metallic absorption indices and all of the data considered is not unexpected. Mass, velocity dispersion and escape velocity are all linked to the depth of the gravitational potential well. A galaxy with a deeper potential, and so an higher escape velocity, could retain an higher fraction of the gas accelerated by supernovae, and so that gas can be recycled in a new generation of stars with higher metallicity.

On the other hand, the correlation of the mass to light ratio is probably linked to the downsizing scenario. As said before, the M/L we found is connected with only the stellar population properties. If more massive, i.e. more metallic, galaxies have an older stellar population (it can be seen from the anticorrelation of the $H\beta$ with the mass) we can expect the M/L of these stellar system to be higher respect to less massive objects. Lastly, we considered if the scatter and the placement of our galaxies around the relations we found were linked to other dynamical properties. In particular, we focused on the shape of the velocity dispersion profile and on the rotation component. For each pair of parameters, we kept memory of the model used to describe the galaxies (see § 5.2), discriminating between a flat velocity dispersion profile and a decreasing one. We distinguished also those galaxies with a $(V_m/\bar{\sigma})^*$ greater than 0.75 from those with a lower value.

Furthermore, for each correlation we found, we plotted the residuals against both rotation velocity and $(V_m/\bar{\sigma})^*$. Fig. 5.10 shows the correlation between the Mg_2 index and the mass. There are also showed the plot of the residuals. *It can be seen that the placement of the galaxies in the $Mg_2 - M$ diagram is not affected by their amount of rotation nor by the shape of their velocity dispersion profile.* Furthermore, neither the residuals show any correlation with the rotation parameters. We found a similar behaviour for all the indices considered. The full set of correlation diagrams can be found in appendix C.

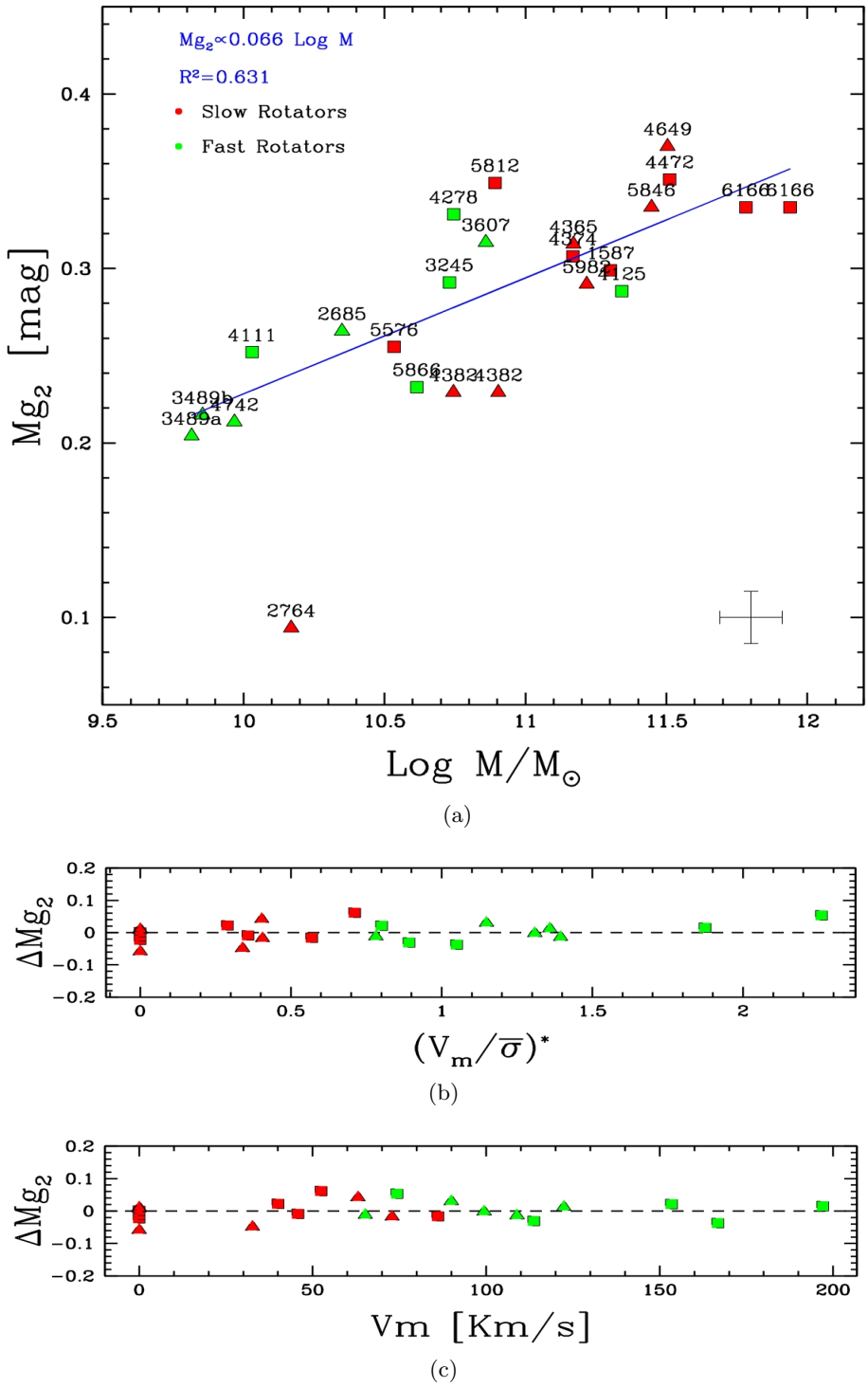

Figure 5.10 *Correlation between the Mg_2 and some dynamical properties: a) Mg_2 versus the dynamical mass; b) Residuals of the $Mg_2 - M$ relation plotted against the $(V_m/\bar{\sigma})^*$; c) The same residuals plotted against the rotation velocity V_m. The symbols and colours meanings are the same of Fig. 5.9.*

Chapter 6

Discussion and conclusions

We analysed a sample of 22 early type galaxies, containing both ellipticals and lenticular galaxies, spanning in a range of ellipticity from 0 to 0.6 and of absolute B magnitude from -19 to -23. The galaxies mainly belong to cluster (Virgo) and group environments, with a few field objects. Using a cross-correlation technique we retrieved rotation curves and velocity dispersion profiles. All the galaxies, except four, were found to have an appreciable amount of rotation along the observed direction, with velocities ranging from few tenth of kilometers per second to more than $200\,km/s$. Gas rotation, where detected, was found to be always concordant with stellar streaming but its amplitude was found to be systematically higher with respect to stellar velocities. This seems to exclude that both gas and stars are in virial equilibrium. Velocity dispersion profiles were found to be separable in two classes, depending on whether they have a flat or a radially decreasing profile, though this distinction seems to be irrelevant to both the galaxies placement in the scaling laws and in their mass computation.

With the rotation velocity and the velocity dispersion of our galaxies we investigated their rotational support. The roundest galaxies were found to need an amount of radial anisotropy in the velocity dispersion tensor in order to explain their shapes, while the more flattened ones seems to be isotropic, though inclination effects could play an important role at such high ellipticities. The ratio of rotation to dispersion compared with an isotropic model seems to be correlated with both the galaxies ellipticity and luminosity. Using a simple model, we calculated the mass and the mass to light ratio inside one effective radius. Masses found ranges from 10^{10} to almost $10^{12} M_{\odot}$, with a mean value of $1.55 \cdot 10^{11} M_{\odot}$(from the log distribution). The most massive galaxy resulted to be NGC6166, while the least massive is NGC3489. By comparing our values with the literature (Poveda, 1961; Fish, 1964; Aizu, 1980) we note that our masses are underestimated by a factor typically of $\approx 2-4$, except for the case of NGC4278 mass, which is in accord with Poveda (1961). *It should be noted that most of the values in literature refer to the total mass of the galaxy, while we measured the mass enclosed inside one* R_e. Part of this discrepancy, thus, is justified.

The mass to light ratios we measured refer to a region where the dark matter contribution is negligible, thus, they are a proxy of only the stellar population properties. We found M/L values that are compatible with an old stellar population, as can be seen in Fig. 6.1. We plotted the bolometric M/L versus the integrated (B-V) colour of our galaxies,

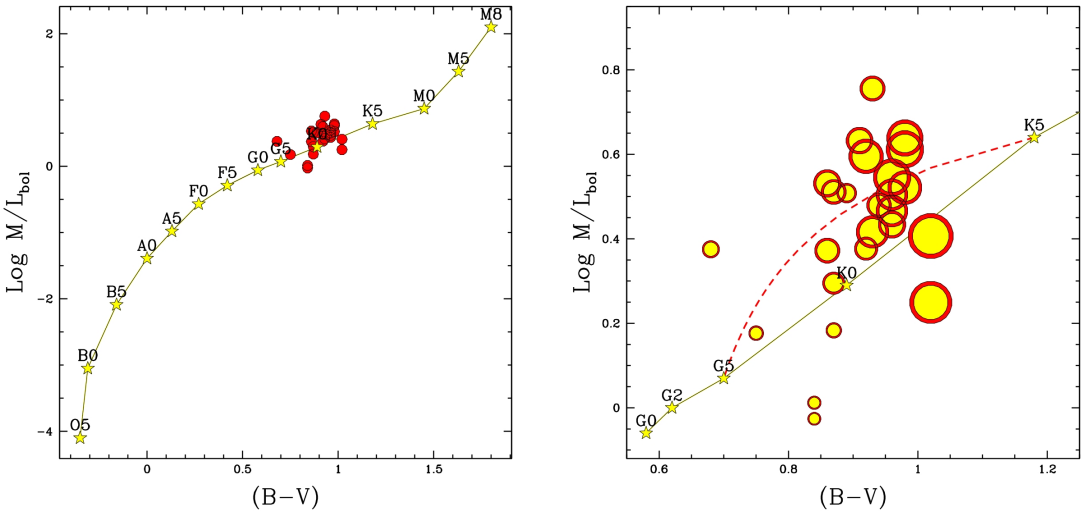

(a) (b)

Figure 6.1 *Mass-to-light ratios and integrated colour of our sample. Galaxies are marked with red circles. The stars represent the position of a main sequence star of the labelled spectral class. The second panel shows a zoom on our sample. The dimension of the points is related to the mass of the galaxy. The red dashed line marks the positions of a stellar population with a variable composition of G5 dwarfs and K5 giants.*

together with the values of typical main sequence stars (reported in Tab. 6.1), taken from Allen (1973). It can be seen that the galaxies take place near the sequence traced by the stars. In particular they have values of colour and mass-to-light ratio compatible with late-G and early-K stars. This result is in accord with the model, generally accepted, of ETGs viewed as red and old nearly-SSPs. The bulk of galaxies, effectively, is very close to the K0-K3 spectral types. Main sequence stars of these classes have masses of about $0.7 - 0.8 M_{\odot}$, thus, if we admit that the (B-V) and the M/L are representative of the main sequence turn-off, we find ages greater of $10\,Gyr$.

Actually, the integrated colour of an old SSP better compare with the K-type stars due the contribution of the RGB population. The galaxies integrated colour is, consequently, redder than the colour of their turn-off stars, for which we can estimate a G5-8 spectral type affinity (O'Connell, 1980; Buzzoni, 1995). This effect could explain the smaller spread of the colour distribution with respect to that of the M/L, *which might also be influenced by the presence of a central massive object (see the case of NGC4278).* To include the presence of the RGB population we built a simple model of stellar population, composed by a variable percentage of G5 main sequence dwarves and K5 giants, and computed its values for the (B-V) and the M/L ratio. As we can see from Fig. 6.1b, the sequence traced by varying the stellar composition better reproduces the values of the sample with respect to the stars values. Furthermore, we can see that less massive galaxies tend to correspond to stars of earlier class, typically G5-G8, while the most massive lie beyond K2 stars. This could be an indication that the former objects are younger and can be seen as an evidence

Table 6.1 *Main sequence stars M/L and (B-V). Taken from Allen (1973).*

Spectral Class	M/L_{bol}	(B-V)
O5V	0.00008	-0.35
B0V	0.0009	-0.31
B5V	0.008	-0.16
A0V	0.04	0
A5V	0.10	0.13
F0V	0.27	0.27
F5V	0.51	0.42
G0V	0.87	0.58
G2V	1.00	0.62
G5V	1.18	0.70
K0V	1.95	0.89
K5V	4.37	1.18
M0V	7.41	1.45
M5V	26.9	1.63
M8V	126	1.8

of downsizing. A word of caution is needed, however, since the metallicity of the stellar population influences both its colour and mass-to-light ratio, and, since the overall metal abundance is related to the stellar mass, it plays, in principle, a role in this trend.

We found, indeed, a correlation between the depth of the potential well (expressed by the velocity dispersion, the dynamical mass and the escape velocity) and many of the Lick/IDS indices tracing the age, the metallicity, the α elements abundance and the warm gas component. These quantities correlate as well with the mass-to-light ratio and this could be explained in the downsizing scenario. We probed also the well known scaling relations between velocity dispersion, effective radius and luminosity (or surface brightness). Though we have been able to consistently match both the Kormendy and the Faber Jackson relations, we found a fundamental plane in the $R_e - \sigma - \langle I \rangle_e$ space with a shallower slope in the surface brightness direction.

Among the several correlations we found, it could be interesting to consider the $Mg_2 - \sigma$ relation. This is also known as the Burstein relation and tightly links the potential in which a galaxies form with the overall metallicity of its stellar population. *In this framework, the Mg_2 index can be seen as a tracer of the mass, as well.* We thought we could replace the velocity dispersion with this index in the fundamental plane. We excluded from the fit NGC6166, because it is a cD, and NGC2764, because of the too low value of the Mg_2 index. The least squares routine we used in § 5.3 give us a best fitting plane of the form:

$$\log R_e \propto 4.04 Mg_2 - 0.27 \log \langle I \rangle_e. \tag{6.1}$$

Fig. 6.2 shows this plane on its edge view. The scatter of the relation is quite high ($\approx 40\%$), but it is fully comparable, if not smaller, with that found by Jorgensen, Franx, & Kjaergaard (1996).

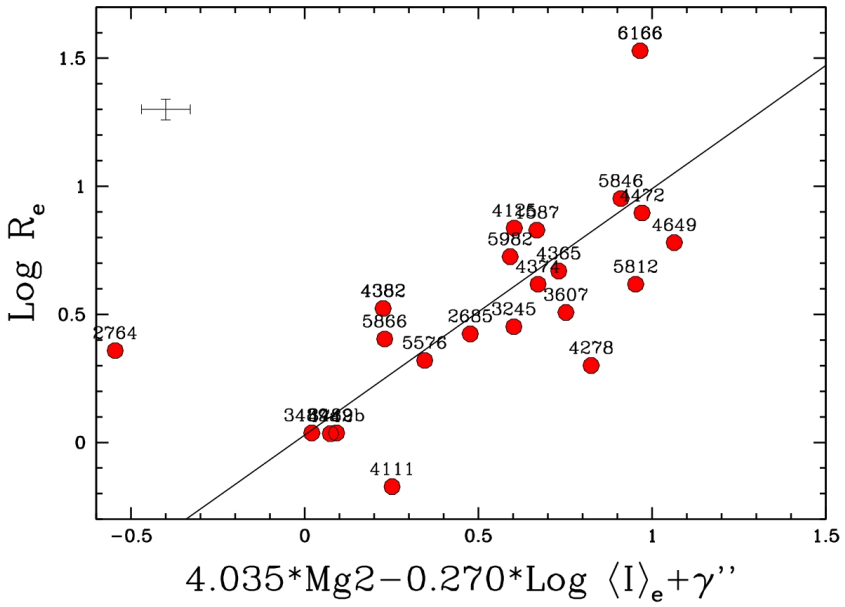

Figure 6.2 *The fundamental plane we found substituting the velocity dispersion with the* Mg_2.

As a final part of our considerations, we contemplate the relation that exists between the mass of ETGs and their X-ray luminosities (Kim & Fabbiano, 2013). Fig. 6.3 shows the mass and the velocity dispersion of our galaxies against their X-ray luminosity. We take the X-ray data from O'Sullivan, Forbes, & Ponman (2001). Due to the sensibility of the least squares procedure to the position of external points in the diagram, we excluded any strong outlier such as NGC4742 and NGC2685. The presence of outliers is expected since the emission from the hot halo isn't the only source of the X-ray luminosity. Other strong contributors are the compact stellar sources and the nuclear activity, where present (Pellegrini, 2011a). Linear fitting gives us the following relations:

$$L_X \propto M^{1.27\pm0.21}, \tag{6.2a}$$

$$L_X \propto \sigma^{4.66\pm1.0}. \tag{6.2b}$$

The existing correlation between the potential of the galaxies and their X-ray luminosity can be explained noting that more massive objects can retain an higher amount of hot gas in their halo, due to their higher escape velocities, with respect to smaller ones. *In addition, is reasonable that the depth of the potential well in which the gas resides influences its temperature.* In fact, if we assume that the halo is in equilibrium, its pressure must satisfy:

$$\nabla P_{gas} = -\rho_{gas} g_{gal} = -\rho_{gas} \frac{GM_{gal}}{R^2}. \tag{6.3}$$

Due to the nature of the gas we are considering (plasma), is reasonable that it must satisfy

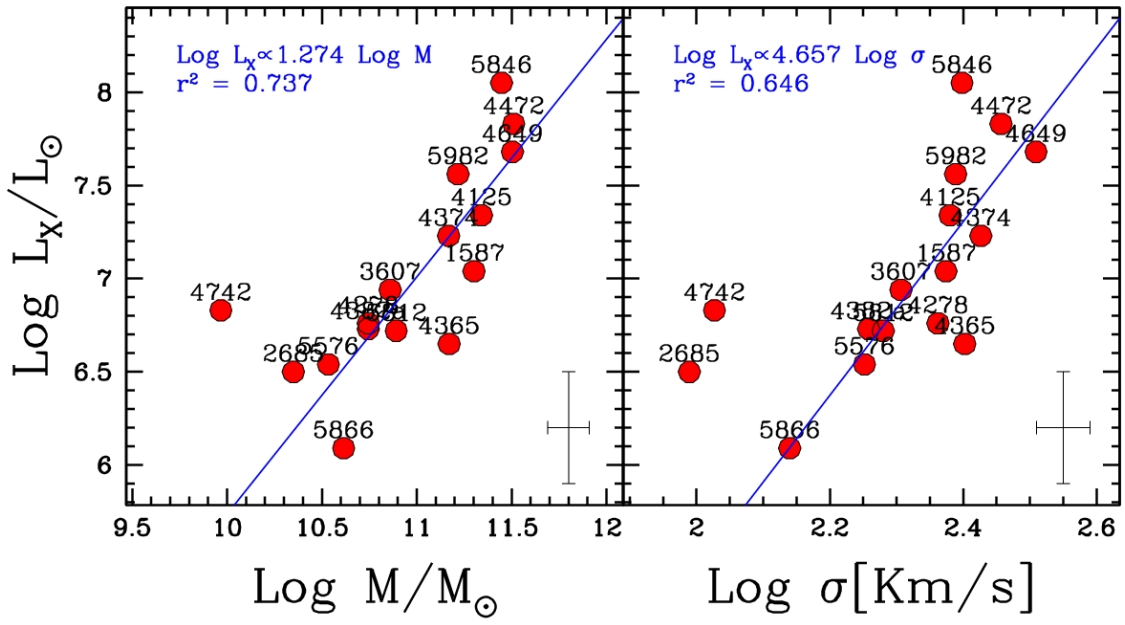

Figure 6.3 *Relations between X-ray luminosity and some dynamical properties. The solid blue line is the least squares fitted relation: The left panel shows* $\log M$ *vs.* $\log L_X$*, while the right one represents* $\log \sigma$ *vs.* $\log L_X$*.*

the equation of state of perfect gases, too:

$$P_{gas} = \frac{\rho_{gas} k T_{gas}}{\mu H}. \tag{6.4}$$

Combining eq.(6.3) and (6.4), we can approximate the temperature of the gas with:

$$T_{gas} \simeq \frac{G M_{gal} \mu H}{kR} \approx 4.57 \cdot 10^7 \frac{M_{11}}{R_{Kpc}} K, \tag{6.5}$$

where M_{11} is the galaxy mass expressed in $10^{11} M_\odot$ and R_{Kpc} is the radius expressed in Kpc. Adopting the values of a typical elliptical galaxy we retrieve a temperature of the order of $\approx 5 \cdot 10^6 K$. This value is coherent with the frequency of emission found applying the Wien law, that is of the order of $10^{18} Hz$ (X-ray).

Actually, the gas temperature observed in ETGs is systematically higher with respect to the equilibrium prediction. Additional heating mechanisms have been invoked to justify this discrepancy. Among them, the gravitational heating from gas infall toward the galaxy centre and the thermalization of the stellar velocity dispersion on the material lost by the stellar population (Pellegrini, 2011b). Both of them depends on the depth of the potential well of the galaxy. Given this context, and since the depth of the potential well is also linked to the chemical properties of the galactic stellar population, we wondered if a correlation could be found between metallicity and X-ray emission.

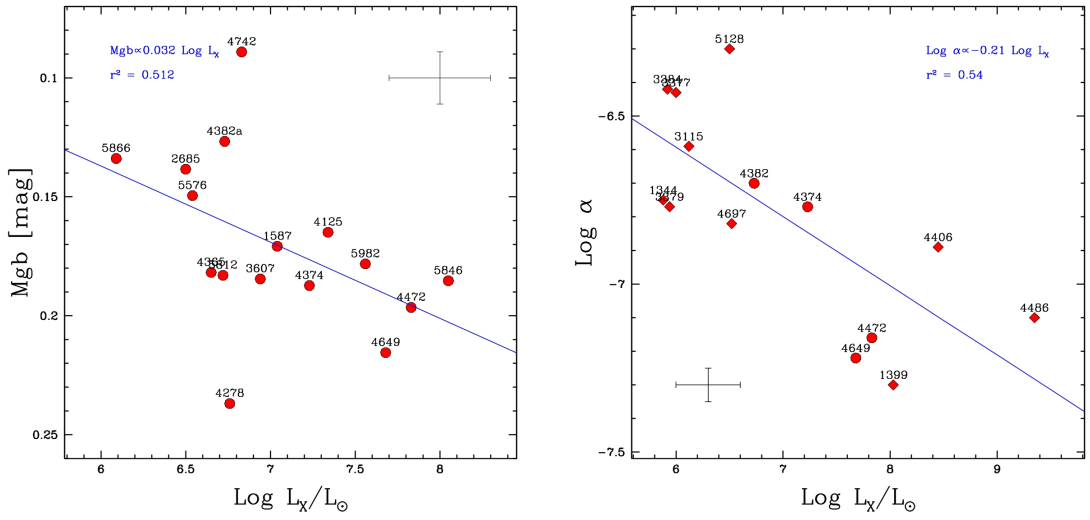

(a) (b)

Figure 6.4 *Dependence of the X-ray luminosity with some of the galaxy properties. The solid blue line is the least squared fitted relation: a)* $\log L_X$ *vs. Mgb index; b)* $\log L_X$ *vs.* $\log \alpha$*. Data taken form Buzzoni, Arnaboldi, & Corradi (2006) and O'Sullivan, Forbes, & Ponman (2001). The galaxies contained in our sample are marked by circles.*

Fig. 6.4a shows the Mgb strengths and the X-ray luminosities of our sample. We kept NGC6166 off our analysis for the already exposed reasons. The plot shows a trend between the X-ray emission of our galaxies and the metallicity of their stellar population. Excluding NGC4742 and NGC4278, we obtain a relation of the form:

$$Mgb \propto (0.03 \pm 0.01)\ \log L_X. \tag{6.6}$$

Is interesting to note that, among the other properties that correlate with the mass of ETGs, there is the number of planetary nebulae detected. The number of detection drastically drops for massive objects, although this behaviour isn't predictable from stellar evolutionary theory alone. In order to probe this problematic, we took the α parameter, defined as the number of detected planetary nebulae per unit of optical luminosity, for a set of galaxies from Buzzoni, Arnaboldi, & Corradi (2006) and plotted it against their X-ray luminosity (Fig. 6.4b). We found a correlation of the kind:

$$\log \alpha \propto -(0.21 \pm 0.06) \log L_X. \tag{6.7}$$

If we assume that the X-ray luminosity is linked with the potential in which the halo is embedded and, then, relates to its typical energetic, *we wonder if the gas dynamics might play a role in the lifetime of the planetary nebulae through phenomenon of ram stripping and ablation (Villaver, García-Segura, & Manchado, 2003; Villaver & Stanghellini, 2005).*

Appendix A

Supermongo routines

This appendix contains the code of some of the supermongo macro utilized in the execution of this study. Since most of the code we implemented was just composed of basic plotting command and simple mathematical operations, we thought its attachment was unnecessary, and here we presents only the three most complex macros. These routines were conceived to execute more elaborated operations and we thought that the view of the relative code could be useful to better understand how these procedures were carried out. Inside the code, supermongo keywords are emphasized with the bold type, while the strings are coloured in red and the comments in blue.

A.1 The computation of the kinematic profiles

The routine presented in this section was utilized to extract and manage the output data from the cross-correlation procedure, as explained in § 3.3.3. The lists, containing respectively the bins of the considered galaxy and the templates, were inputted to the XCSAO task. The output file, named "xcsao.log" contains the cross-correlation informations about all the bin-template couples. Once specified the number of bins in which the galaxy has been subdivided and the number of templates, the macro can extract the informations pertaining to each bin and, after the computation of a mean redshift, report all the velocities to the galactic rest frame. All the values are corrected for the earth motion at the time of the observation. The mean radial velocity of each bin is averaged, using the errors as weights, over all the templates, and a mean uncertainty is computed . The correlation peak width is averaged over all the values and the error on it is taken as the standard deviation of the widths distribution. Using the value of the instrumental broadening, the routine obtain the value of the velocity dispersion and its error as stated in eq.(3.22) and (3.27).

Listing A.1 Profiles extractor

```
1 #Sets the input file for the cross-correlation data
2 data xcsao.log
3
4 #Defines the number of template stars
5 define n_t ('Template number')
```

```
6
7 #Defines the number of bins for each side
8 define right ('Galaxy right bins number')
9 define left ('Galaxy left bins number')
10 define n_b ($right+$left+1)
11
12 #Sets the heliocentric correction for the templates
13 set corrt = 1,$n_t
14 set corrt[0] = -23.49
15 set corrt[1] = -23.49
16 set corrt[2] = -28.75
17 set corrt[3] = -28.76
18 set corrt[4] = -28.78
19 set corrt[5] = -20.89
20 set corrt[6] = -21.16
21 set corrt[7] = -21.45
22 set corrt[8] = -1.67
23 set corrt[9] = -3.39
24 set corrt[10] = 8.85
25 set corrt[11] = 6.92
26 set corrt[12] = 28.72
27 set corrt[13] = 25.97
28
29 #Set the heliocentric correction for the galaxy
30 define corrg ('Galaxy heliocentric correction')
31
32 #Computes the mean redshift
33 define lo (($right*$n_t)+1)
34 define up (($right+1)*$n_t)
35 lines $lo $up
36 read {vc 4 dvc 5}
37 set vc = vc-corrt+$corrg
38 set cz = sum(vc/dvc**2)/sum(1/dvc**2)
39 set dcz = sqrt(1/sum(1/dvc**2))
40 print redshift.dat {cz dcz}
41
42 #Creates the vectors for the kynematical data
43 set vm = 1,$n_f
44 set vm = vm-vm
45 set dvm = vm
46 set um = vm
47 set dum = vm
48 set sigma = vm
49 set dsigma = vm
50
51 #Finds the mean radial velocities and correlation peak widths
52 do j = 1, $n_f {
53         define lo ($n_t*($j-1)+1)
54         define up ($n_t*$j)
55         lines  $lo $up
```

```
56          read {v 4 dv 5 u 7}
57          set v = v-corrt+$corrg
58          #Sets the velocities to the rest frame
59          set v = v-vc
60          set vm[$j-1] = sum(v/dv**2)/sum(1/dv**2)
61          set dvm[$j-1] = sqrt(1/sum(1/dv**2))
62          set um[$j-1] = sum(u)/$n_t
63          set dum[$j-1] = sqrt(sum((u-um[$j-1])**2)/($n_t-1))
64 }
65
66 #Defines the instrumental broadening
67 define t ('Instrumental broadening value')
68 define dt ('Instrumental broadening error')
69
70 #Computes the velocity dispersions and the relative uncertainties
71 set sigma = sqrt((um**2)-2*($t**2))
72 set dsigma = 2*sqrt((u**2*du**2+4*$t**2*$dt**2+sig**4))-2*sig**2
73
74 #Prints the results
75 print 'Output File'.dat {vm dvm um dum sigma dsigma}
```

A.2 The folding of the rotation curve

The present macro implements the folding procedure utilized in § 4.3. Taking in input the radial velocity profile, the code does a preliminary interpolation. Subsequently, it searches for the best turning point. This operation id done by a fold of the profile around a set of points progressively farther from the zero. For each point, the routine shifts the profile to the new centre, then executes the folding. The goodness of the fold is established computing a merit value. This factor is defined as the square root of the sums of the square residuals between each velocity measure and the previous one. In this way, since we are considering the absolute value of the radius, an asymmetric profile will return an high value for the merit factor. The best folding point is defined as the one corresponding to the minimum value of the merit factor. The last piece of the code outputs a graphical plot of the merit factor profile and display the value of the best folding point. The code we report refers to a dataset comprehensive of a gas rotation profile. If this data aren't available, the code has to be considered deprived of the relative commands.

Listing A.2 Folding procedure

```
1 #Acquires the data about radii, star velocities
2 #and gas velocities if present
3 data bar.dat
4 read {r 4 dr 7}
5 data star.dat
6 read {vr 1 dvr 2}
7 data emiss.dat
8 read {vgas 2 dvgas 3 rgas 4 drgas 5}
```

```
9
10 #Interpolates the stellar and gaseous profiles
11 vecminmax r rmin rmax
12 set rspline = $rmin,$rmax,0.01
13 spline r vr rspline vspline
14 spline rgas vgas rspline vgasspline
15
16 #Sets the offset vector
17 set jj=0,49,1
18 set offr = 0.01*jj-0.25
19
20 #Creates the merit vector
21 set merit = jj-jj
22
23 do j=0,49,1 {
24         #Chooses an horizontal offset value
25         define off (offr[$j])
26
27         define voff (0)
28         define vgoff (0)
29
30         #Searches for vertical offset values
31         do i=0,dimen(rspline)-1 {
32                 if(abs(rspline[$i]-$off)<=0.01) {
33                         define voff (vspline[$i])
34                         define vgoff (vgasspline[$i])
35                 }
36         }
37
38         #Shifts the profiles
39         set ro = r-$off
40         set vro = vr-$voff
41         set vgaso = vgas-$vgoff
42         set rgo = rgas-$off
43
44         set rs = rspline-$off
45         set vrs = vspline-$voff
46         set vgs = vgasspline-$vgoff
47
48         #Folds the velocities
49         set rr = abs(ro)
50         set signr = ro/rr
51         set rgr = abs(rgo)
52         set sigg = rgo/rgr
53         set vrr = vro*signr
54         set vgass = vgaso*sigg
55
56         set rso = abs(rs)
57         set signrs = rs/rso
58         set vrsp = vrs*signrs
```

```
59          set vgsp = vgs*signrs
60
61          #Computes the merit factor
62          sort {rso vrsp}
63          set xrs = 0 concat rso
64          set yvrsp = 0 concat vrsp
65
66          define res (0)
67          do k=1,dimen(xrs)-1 {
68                  define res ($res+(yvrsp[$k]-yvrsp[$k-1])**2)
69          }
70          set merit[$j] = sqrt($res)
71          }
72
73 #Creates the graphical output
74 vecminmax merit mmin mmax
75 define mmax ($mmax*1.1)
76 set xx = (jj*0.01-0.25)
77 set xxsec = xx*('Effective radius value [arcsec]')
78
79 ticksize 0 0 0 0
80 location 5000 18000 8000 21000
81 ctype 0 lweight 3 expand 1.1
82 limits xxsec 0 1000
83 box
84 xlabel dR  [arcsec]
85 ylabel Merit factor
86
87
88 lweight 8 ctype 3
89 connect xxsec merit
90 lweight 2 ctype 5
91 connect xxsec merit
92
93 limits 0 1 0 1  ctype 0 lweight 3
94 relocate 0.15 0.90  expand 1.4 putlabel 6 'Galaxy name'
95
96 #Searches for the best turning point
97 sort {merit xx xxsec}
98 define best (xx[0])
99 define bestsec (xxsec[0])
100 define mbest (merit[0])
101
102 #Outputs the result
103 echo $best $bestsec $mbest
```

A.3 The fitting of the fundamental plane

The last routine we attach was conceived for the search of the best fitting plane for a three dimensional set of data. We used it to search the parameters of the fundamental plane in § 5.3. Given a set of data which obey to a relation of the kind $y = \alpha x + \beta z + \gamma$, the best fitting coefficients are those minimizing the square residuals. Imposing these conditions we retrieve the eq.(5.21). This routine resolves the equations system for a chosen set of three parameters. First, all the points selected to be excluded from the fit are removed. Then, the code resolves the equations for the coefficients determination. Once the best fitting plane is found, the scatter is computed transforming the variables to an edge on view and executing a linear fit procedure. Finally, a graphical plot of the edge on plane and an output of the fitting parameters are produced.

Listing A.3 Fundamental plane fitting

```
#Sets the three parameters to fit
set XX = lg(sigma)
set YY = lg(Re)
set ZZ = lg(0.41*Lbol/(3.14*Re**2))

#Excludes the chosen galaxies from the fit
set Y = YY if(lab!='6166a'&&lab!='6166b')
set X = XX if(lab!='6166a'&&lab!='6166b')
set Z = ZZ if(lab!='6166a'&&lab!='6166b')

#Computes some useful values
set sx2 = sum(X**2)
set sxy = sum(X*Y)
set sxz = sum(X*Z)
set sx = sum(X)
set sz2 = sum(Z**2)
set syz = sum(Z*Y)
set sxz = sum(X*Z)
set sz = sum(Z)
set sy = sum(Y)
set dx = sx2-sx**2

#Resolves the equation for the second coefficient
set coeff_b = (sz2-(sxz*(sxz-sx*sz)/dx)-sz**2+(sx*sz*(sxz-sx*sz)/dx))
set term_b = syz-(sxz*(sxy-sx*sy)/dx)-sz*sy+(sz*sx*(sxy-sx*sy)/dx)
define B (term_b/coeff_b)

#Resolves equations for the first coefficient and the constant term
define A ((sxy-sx*sy-$B*(sxz-sx*sz))/dx)
define C (sy-$A*sx-$B*sz)

#Cuts off the coefficients
define A1 (1000*$A)
if ($A1-int($A1)<0.5) {define A1 (int($A1)/1000)} else {
```

```
35          define A1 ((int($A1)+1)/1000)
36  }
37  define B1 (1000*$B)
38  if ($B1-int($B1)<0.5) {define B1 (int($B1)/1000)} else {
39          define B1 ((int($B1)+1)/1000)
40  }
41  define C1 (1000*$C)
42  if ($C1-int($C1)<0.5) {define C1 (int($C1)/1000)} else {
43          define C1 ((int($C1)+1)/1000)
44  }
45
46  #Computes the edge on variables
47  set x = ($A*X+$B*Z+$C)
48  set y = Y
49  set xx = ($A*XX+$B*ZZ+$C)
50  set yy = YY
51
52  #Creates the graphical output
53  limits xx yy
54  ctype black
55  lweight 3
56  box
57  expand 1.5
58  xlabel $A1*\sigma+$B1*Log \langle I\rangle_e+\gamma
59  ylabel Log R_e
60  ptype 10 3 ctype red points xx yy
61  expand 1.01
62  ctype black
63  set yl = yy+0.03
64  expand 0.7
65  lweight 1
66  ptype lab points xx yl
67
68  #Computes the scatter
69  lsq x y x yt rms
70  define perc (230*$rms)
71
72  #Outputs the results
73  echo  A=$A1 B=$B1 C=$C1
74  echo rms(dex)=$rms  $rms(%)=$perc
```

Appendix B

Folded profiles and comparison diagrams

This appendix contains the full list of diagrams outcome from the folding process and from the comparison we made with the kinematical results in literature. The procedures followed to obtain this graphs are well explained in § 4.

B.1 Folding and interpolation

The following diagrams comes from the folding process described in § 4.3. The folded curves of the stellar component are represented by circles of different colours for the two sides of the profiles. Where present, the gaseous component is plotted using the diamonds. The coloured shading enclose the area delimited by the error bars. Together with the folded curve there is a graph showing the respective merit factor curve. The merit factor diagrams are all plotted with the same scale (0 to 1000). This is done to permit a direct confrontation between the galaxies that show a "true" minimum and others that show a more complex structure a low merit value. The only exception is represented by NGC4278, whose merit function is also everywhere greater than 1000.

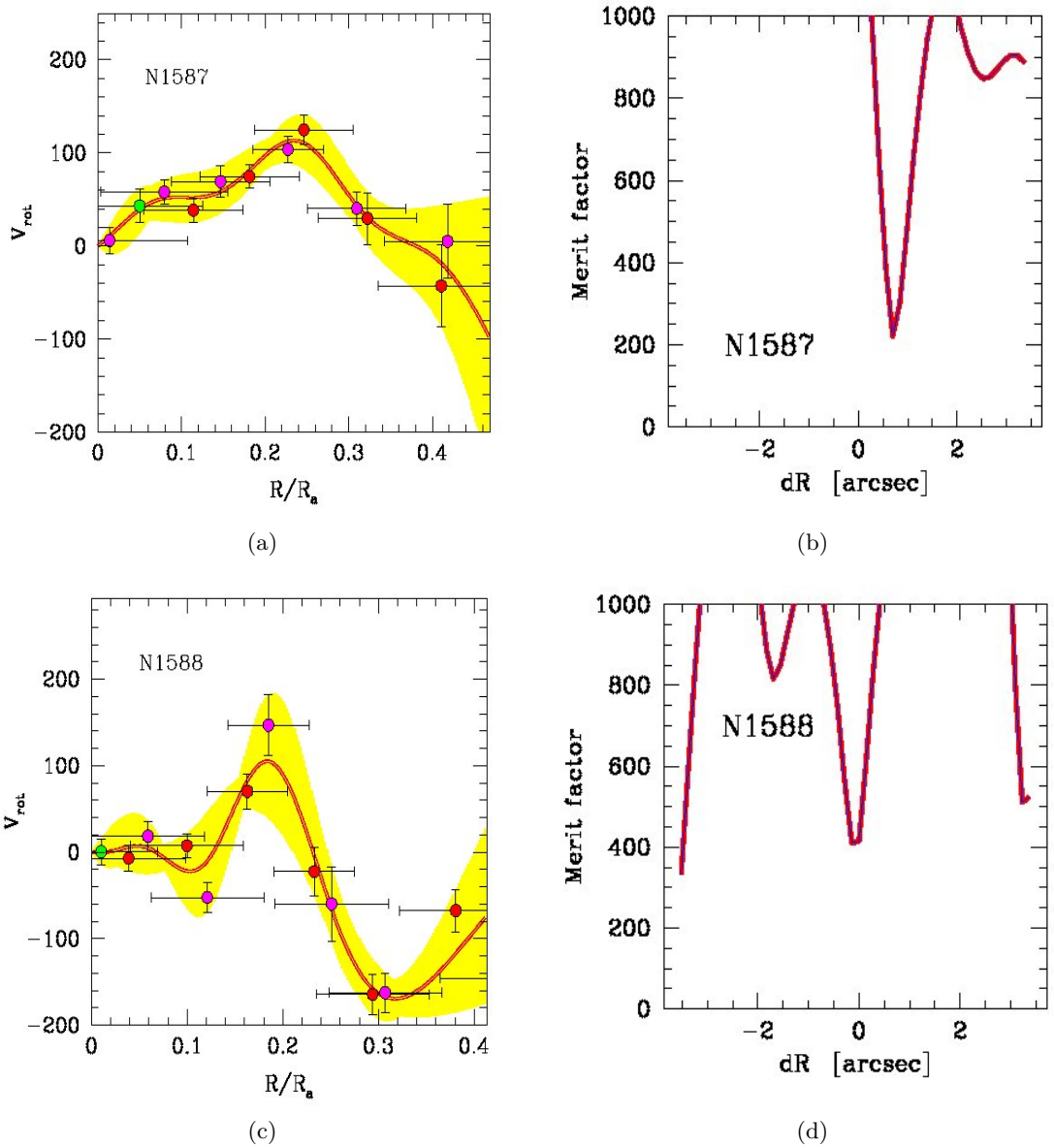

(a) (b)

(c) (d)

Figure B.1 *Folded profile and merit factor for NGC1587 (a, b) and NGC1588 (c, d).*

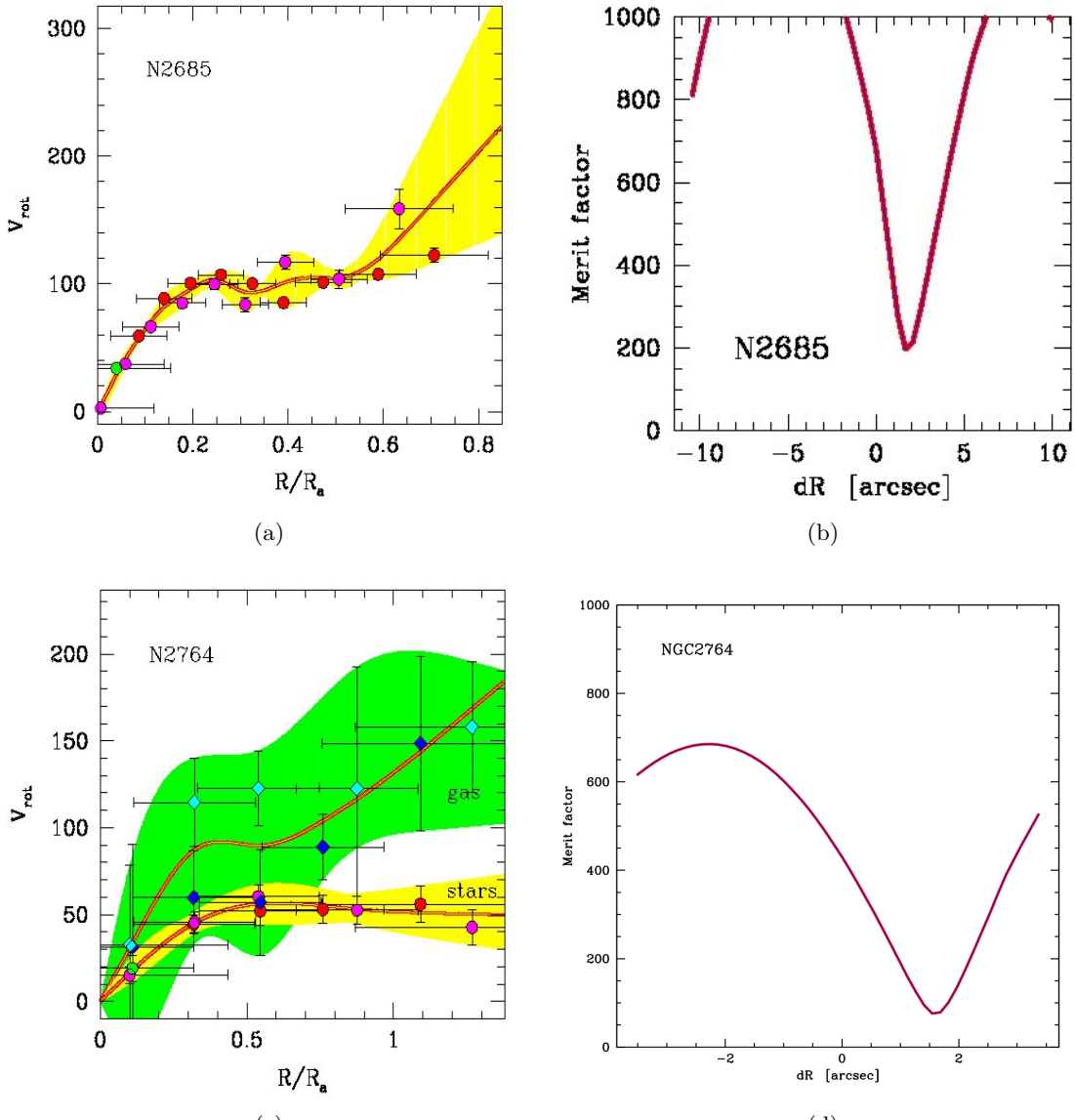

(a) (b)

(c) (d)

Figure B.2 *Folded profile and merit factor for NGC2685 (a, b) and NGC2764 (c, d).*

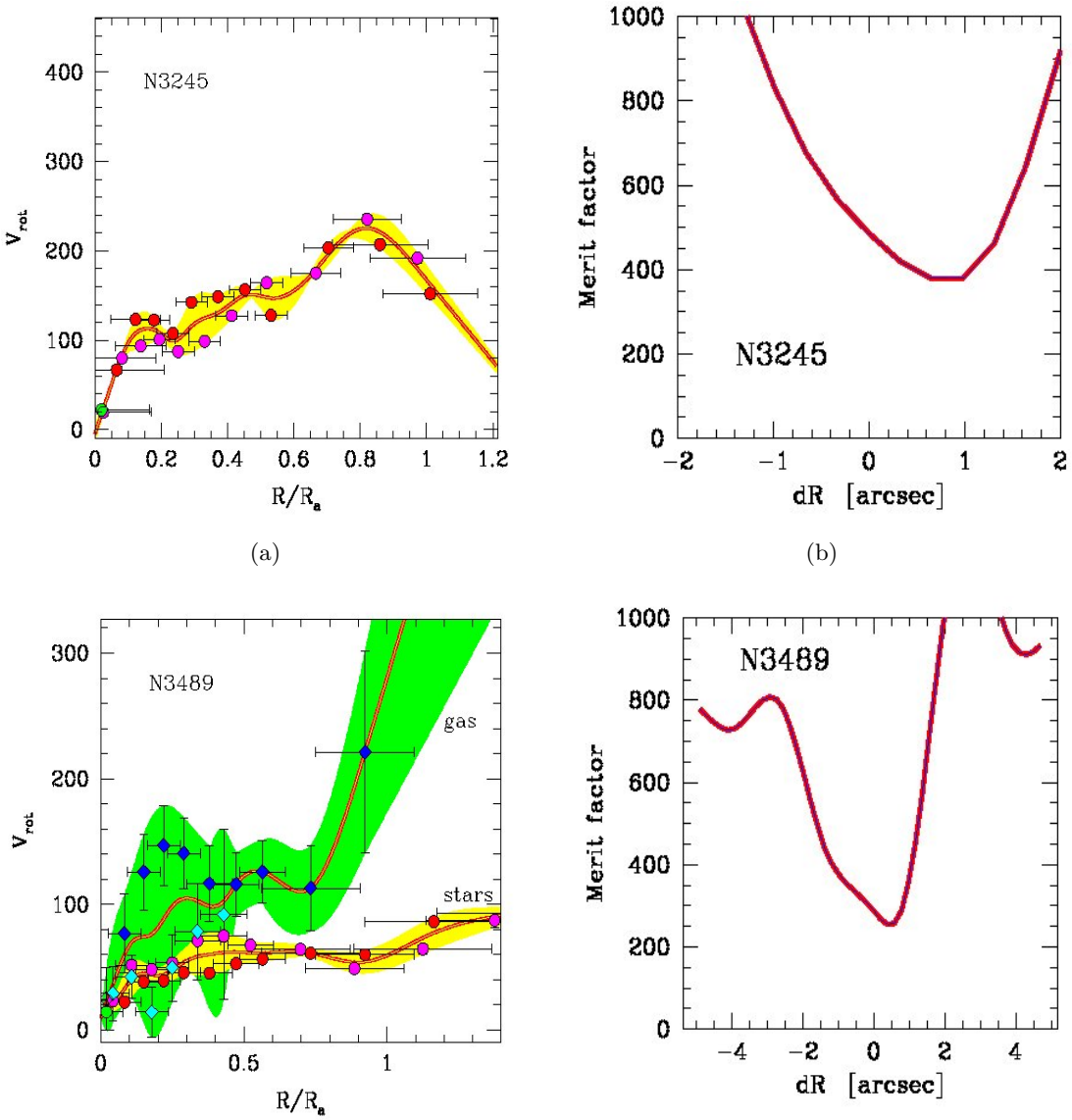

(a) (b)

(c) (d)

Figure B.3 *Folded profile and merit factor for NGC3245 (a, b) and NGC3489 (32°) (c, d).*

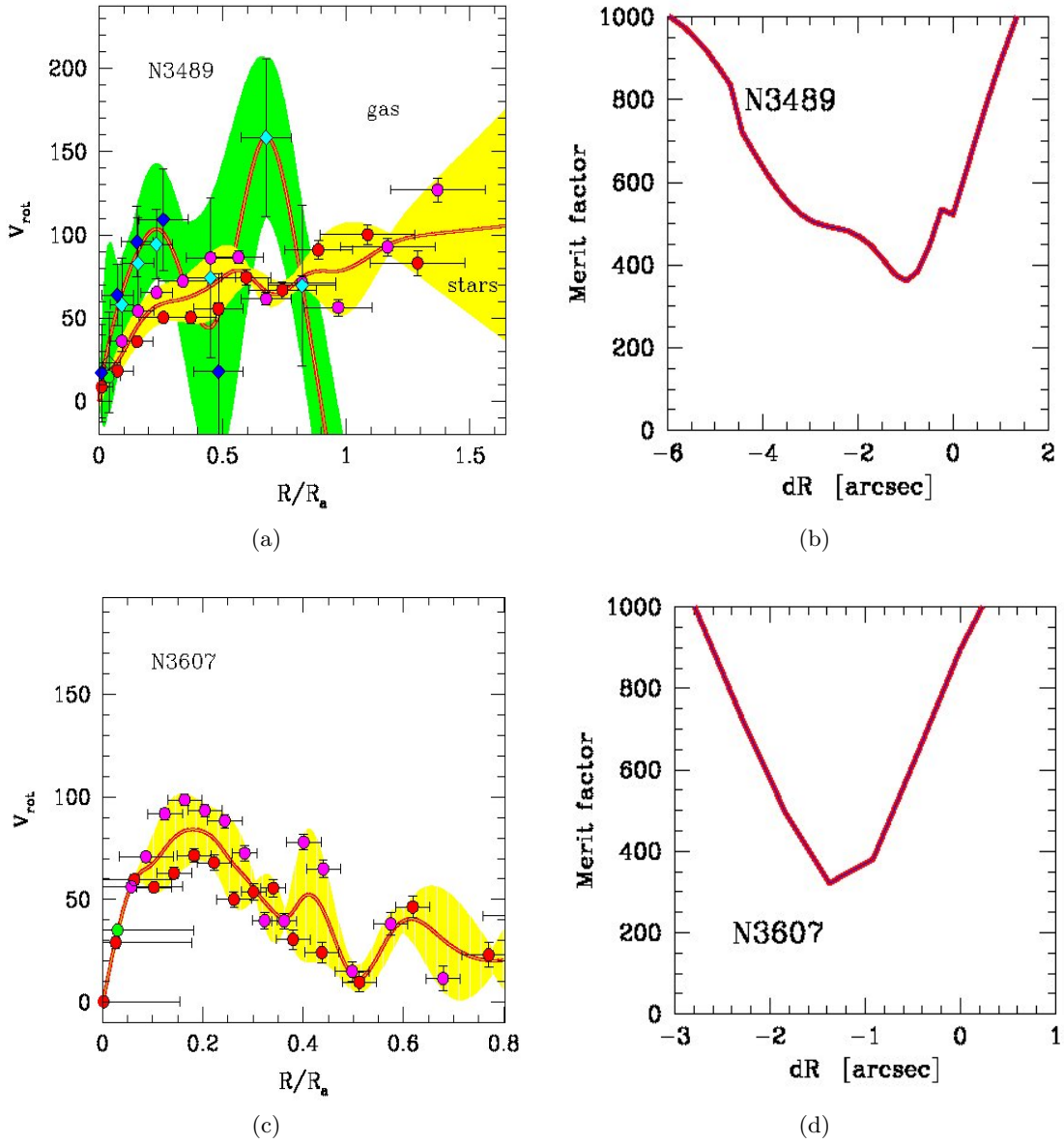

(a) (b)

(c) (d)

Figure B.4 *Folded profile and merit factor for NGC3489 (58°) (a, b) and NGC3607 (c, d).*

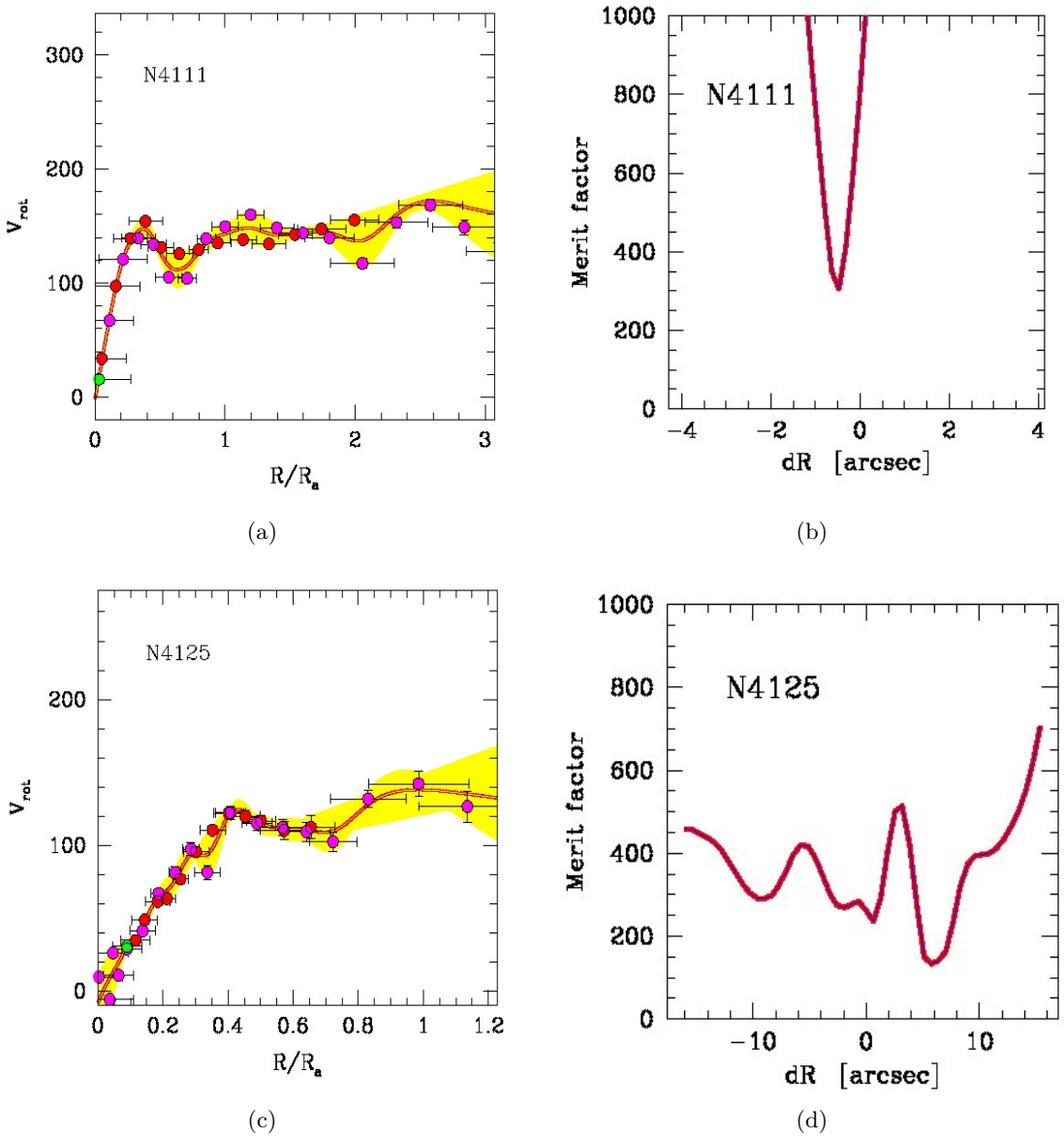

(a) (b)

(c) (d)

Figure B.5 *Folded profile and merit factor for NGC4111 (a, b) and NGC4125 (c, d).*

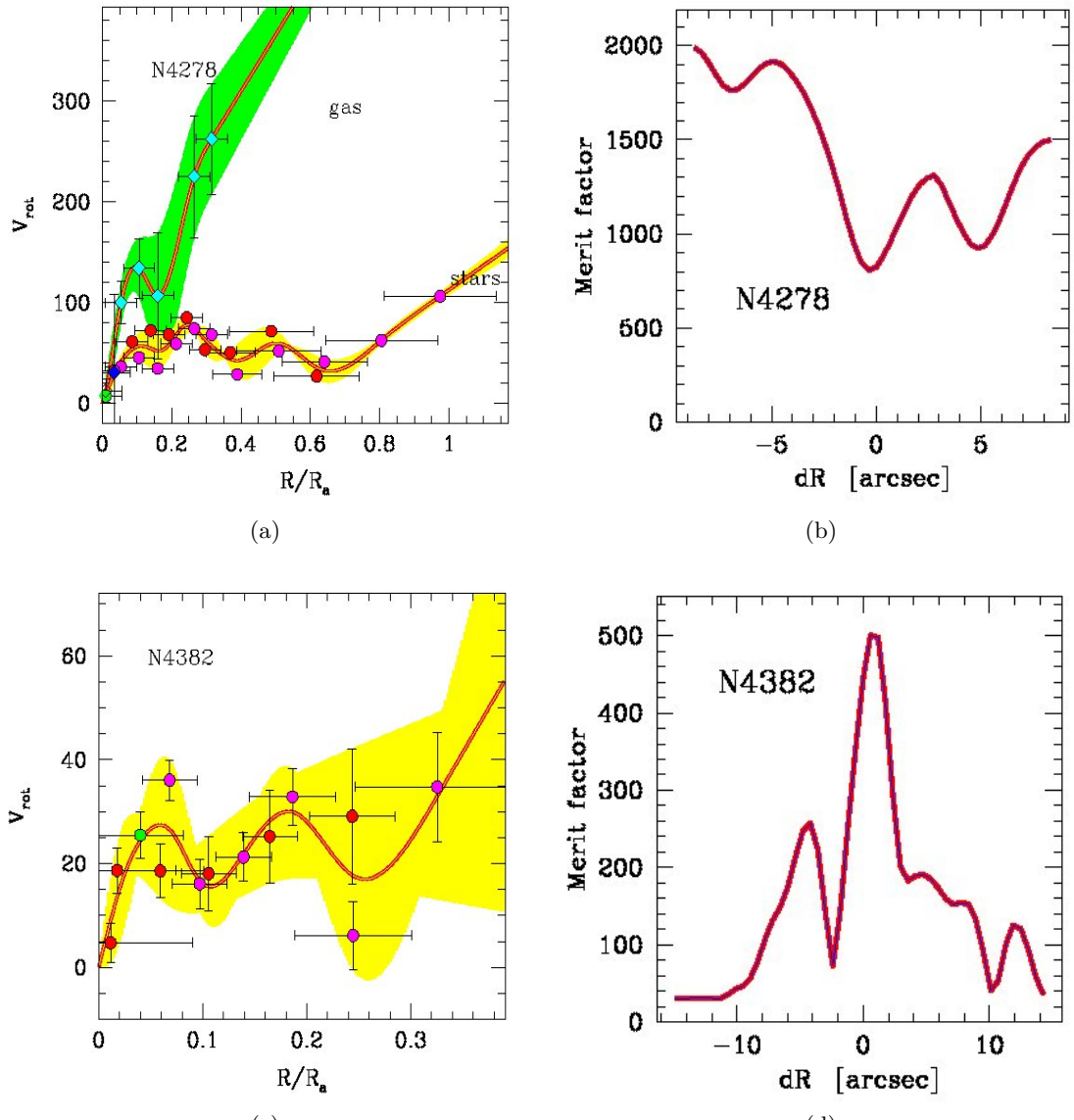

(a) (b)

(c) (d)

Figure B.6 *Folded profile and merit factor for NGC4278 (a, b) and NGC4382 (1996) (c, d).*

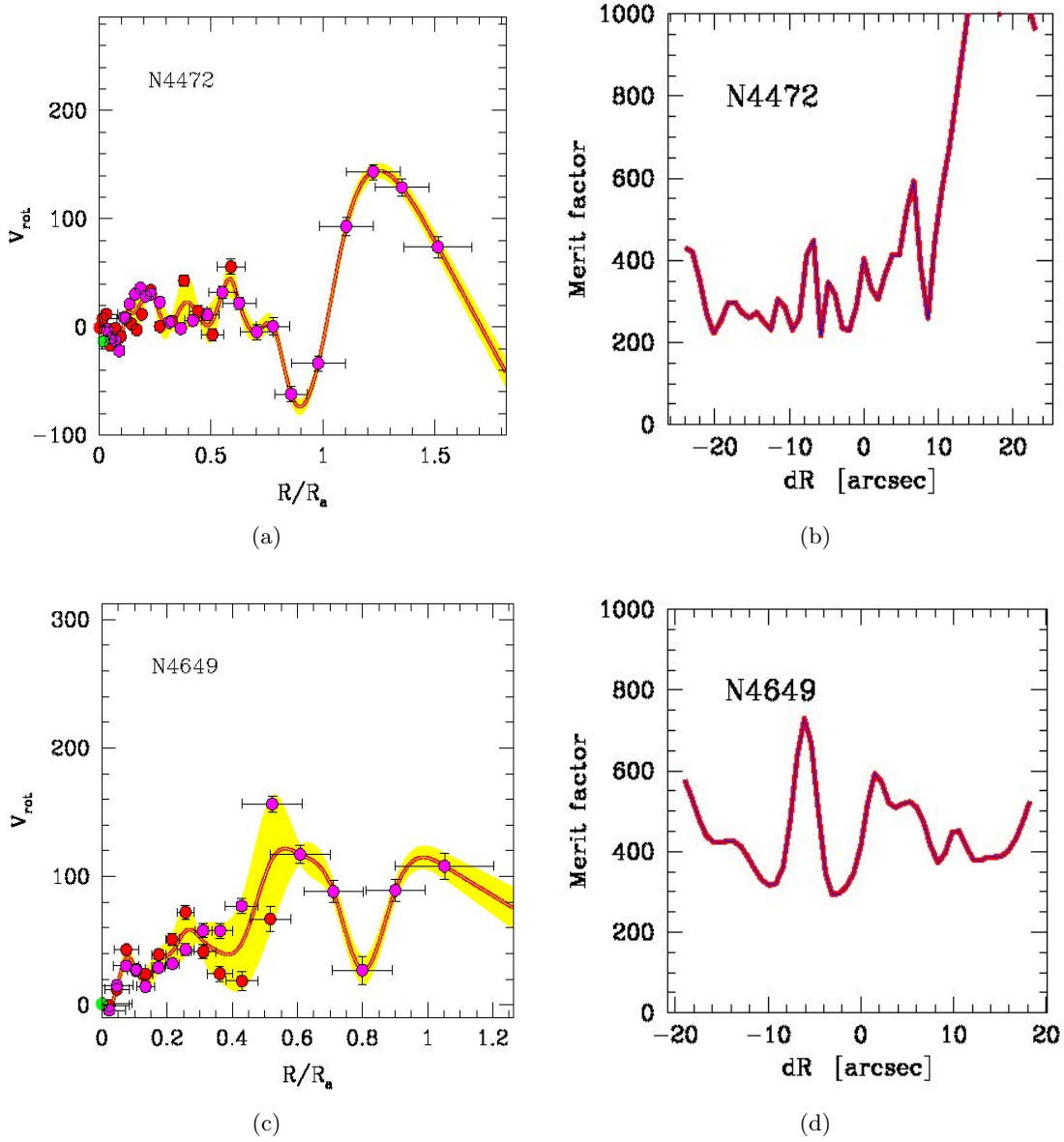

(a) (b)

(c) (d)

Figure B.7 *Folded profile and merit factor for NGC4472 (a, b) and NGC4649 (c, d).*

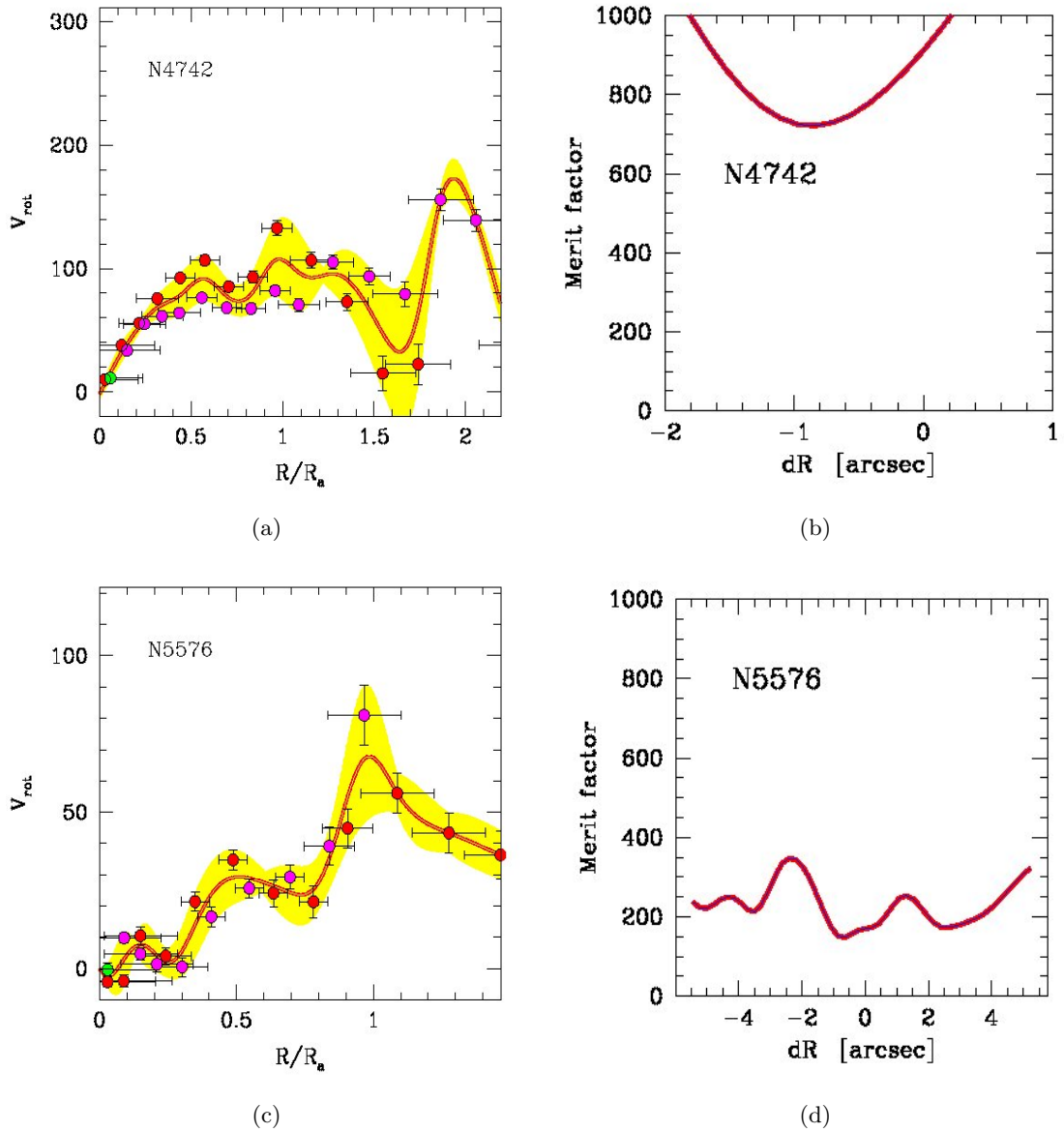

(a) (b)

(c) (d)

Figure B.8 *Folded profile and merit factor for NGC4742 (a, b) and NGC5576 (c, d).*

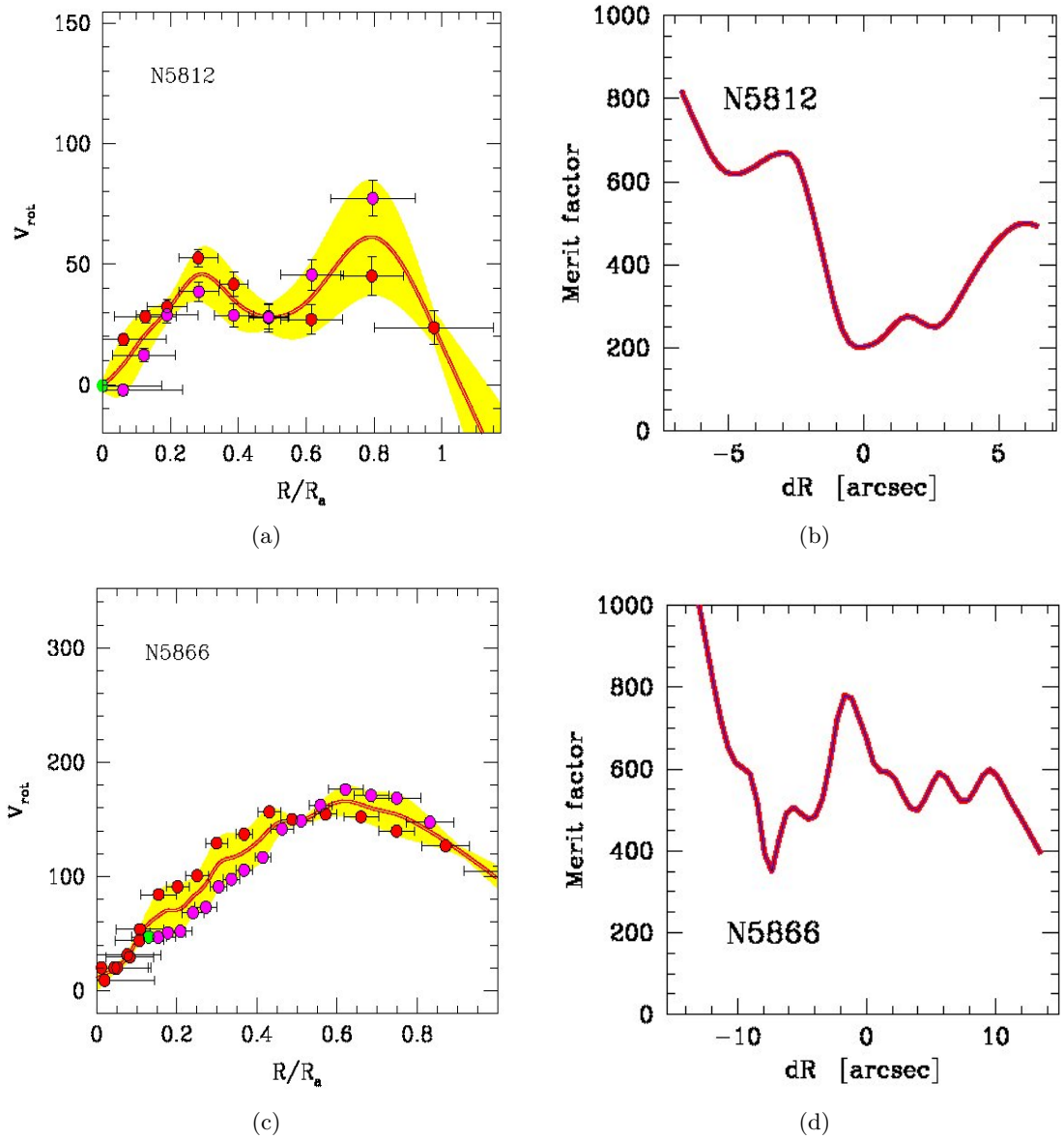

(a) (b)

(c) (d)

Figure B.9 *Folded profile and merit factor for NGC5812 (a, b) and NGC5866 (c, d).*

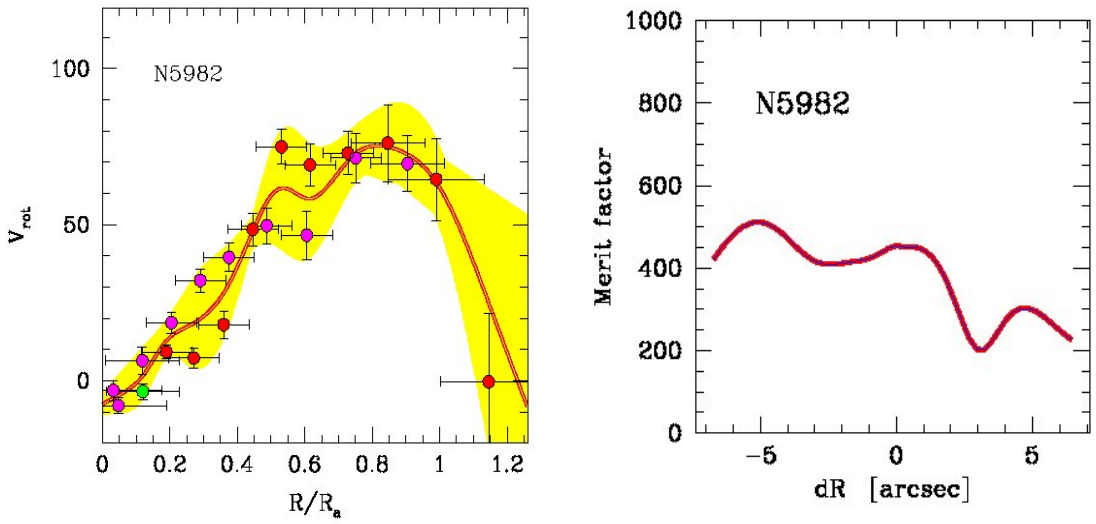

(a) (b)

Figure B.10 *Folded profile and merit factor for NGC5982.*

B.2 Comparison diagrams

Here are presented the confrontations between our data and the beforehand found results from the previous works. The articles taken in consideration are: Peterson (1978), Schechter and Gunn (1979), Efstathiou et al. (1980), Davies (1981), Kormendy and Illingworth (1982), Davies et al. (1983), Larsen et al. (1983), Bertola et al. (1984), Tonry (1984), Heckman et al. (1985), Davies and Birkinshaw (1988), Bender (1988), Borne and Hoessel (1988), Franx et al. (1989), Wagner (1990), Saglia et al. (1993), Bertin et al. (1994), Borne et al. (1994), Bender et al. (1994), Fried and Illingworth (1994), Oosterloo, Balcells, & Carter (1994),Bonfanti et al. (1995), Bertola et al. (1995), Surma and Bender (1995),Seifert and Scorza (1996), Fisher (1997), Simien and Prugniel (1997), Simien and Prugniel (1998), Loyer et al. (1998), Caon et al. (2000), De Bruyne et al. (2001), Pinkney et al. (2003), Pu et al. (2010).

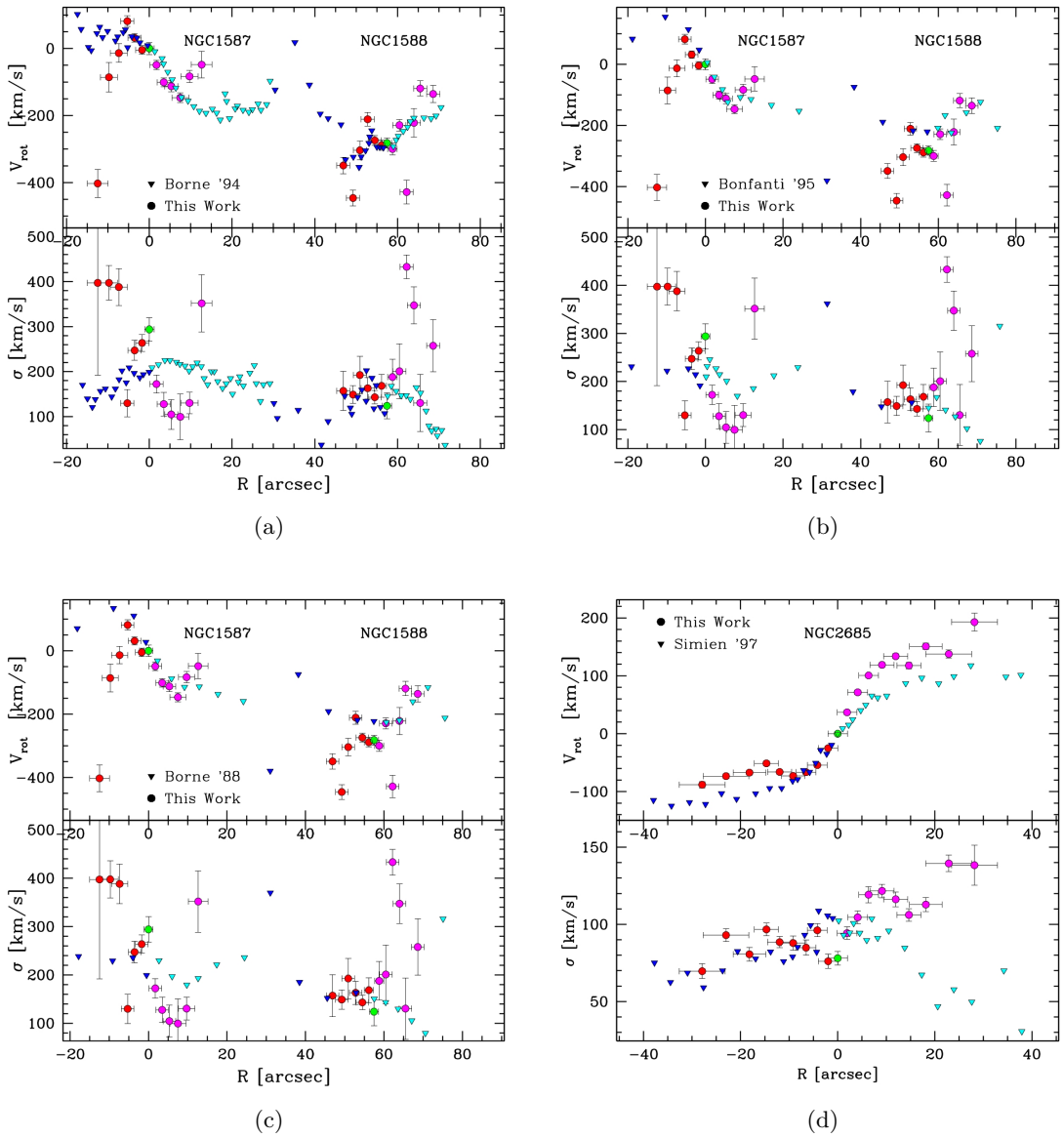

Figure B.11 *Comparison diagrams made from the previous published data. The upper panel is the rotation curve while the lower one is the velocity dispersion profile. Different colour account for the two side of the galaxy. The centre is the green point. a) NGC1587/1588, data taken from Borne et al. (1994); b) NGC1587/1588, data taken from Bonfanti et al. (1995); c) NGC1587/1588, data taken from Borne and Hoessel (1988); d) NGC2685, data taken from Simien and Prugniel (1997)*

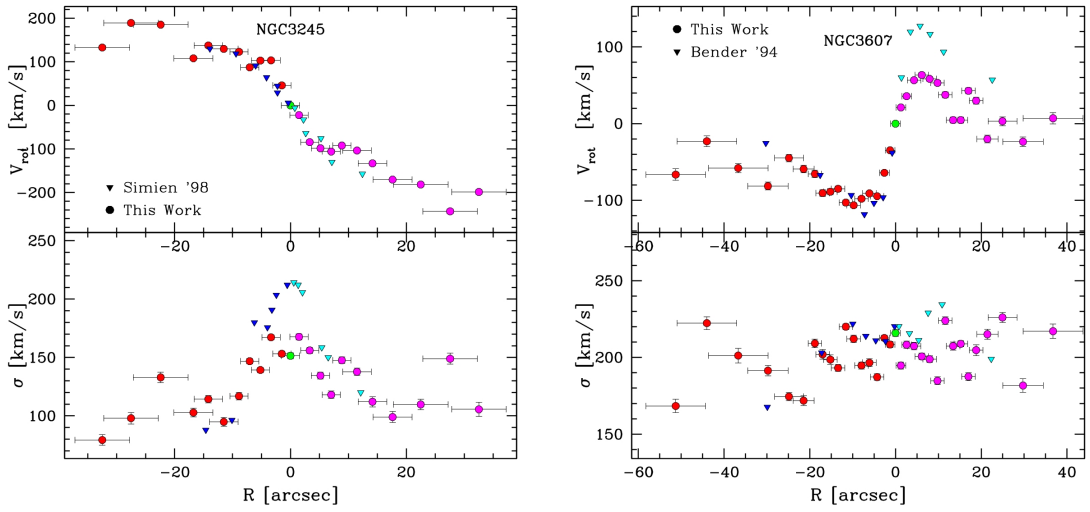

(a)

(b)

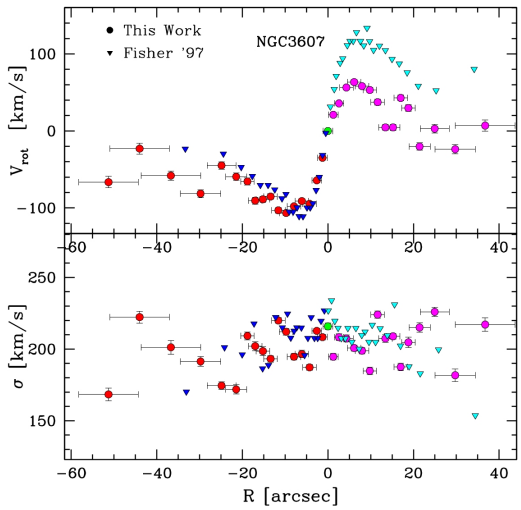

(c)

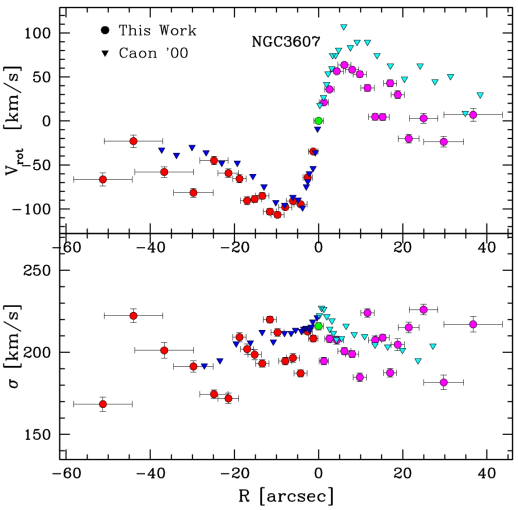

(d)

Figure B.12 *Same of fig. B.11: a) NGC3245, data taken from Simien and Prugniel (1998); b) NGC3607, data taken from Bender et al. (1994); c) NGC3607, data taken from Fisher (1997); d) NGC3607, data taken from Caon et al. (2000)*

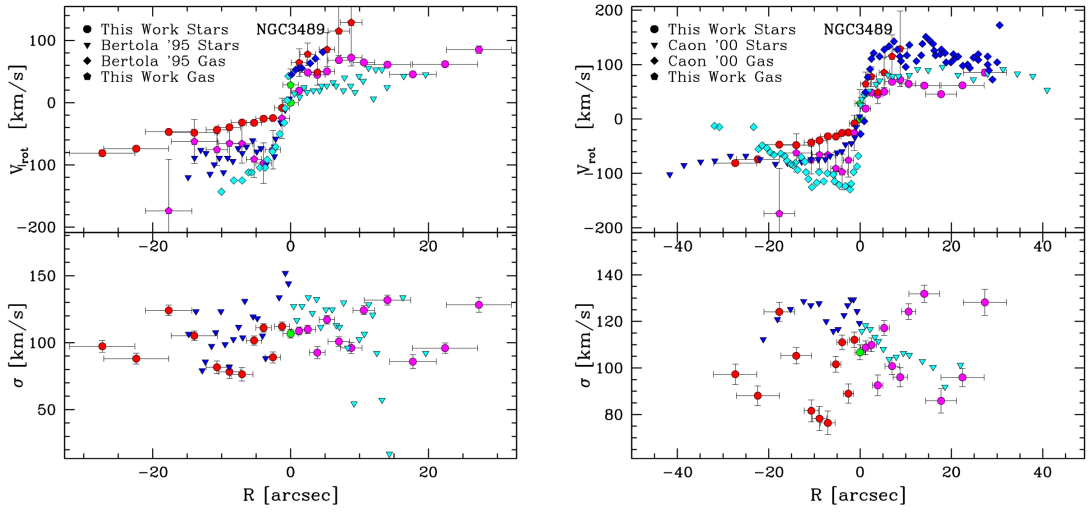

(a)

(b)

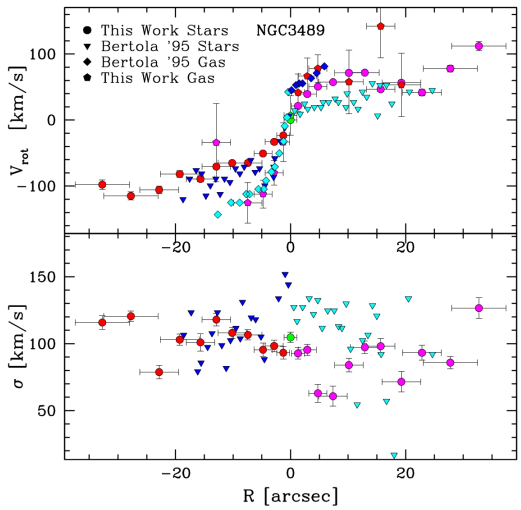

(c)

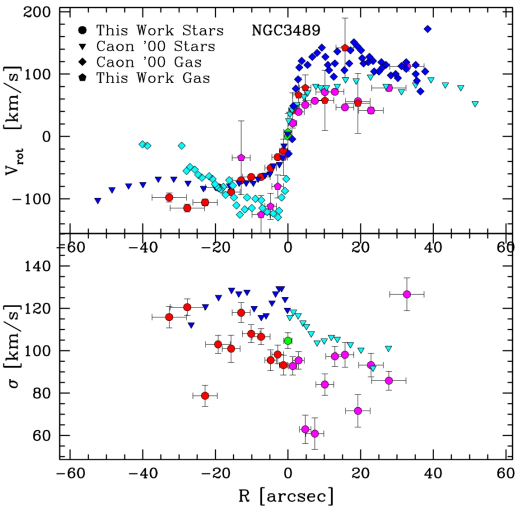

(d)

Figure B.13 *Same of fig. B.11: a) NGC3489 (32°), data taken from Bertola et al. (1995); b) NGC3489 (32°), data taken from Caon et al. (2000); c) NGC3489 (58°), data taken from Bertola et al. (1995); d) NGC3489 (58°), data taken from Caon et al. (2000)*

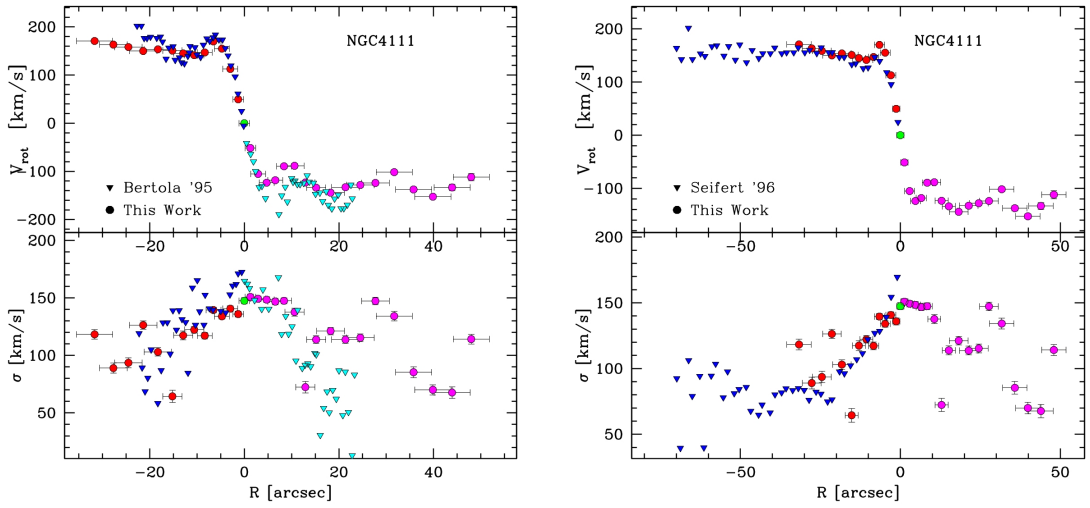

(a)

(b)

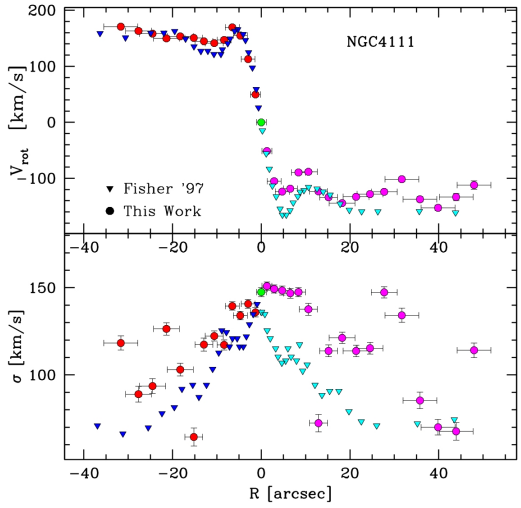

(c)

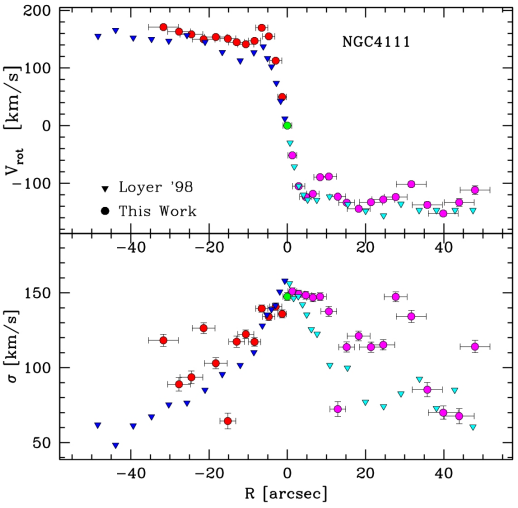

(d)

Figure B.14 *Same of fig. B.11: a) NGC4111, data taken from Bertola et al. (1995); b) NGC4111, data taken from Seifert and Scorza (1996); c) NGC4111, data taken from Fisher (1997); d) NGC4111, data taken from Loyer et al. (1998)*

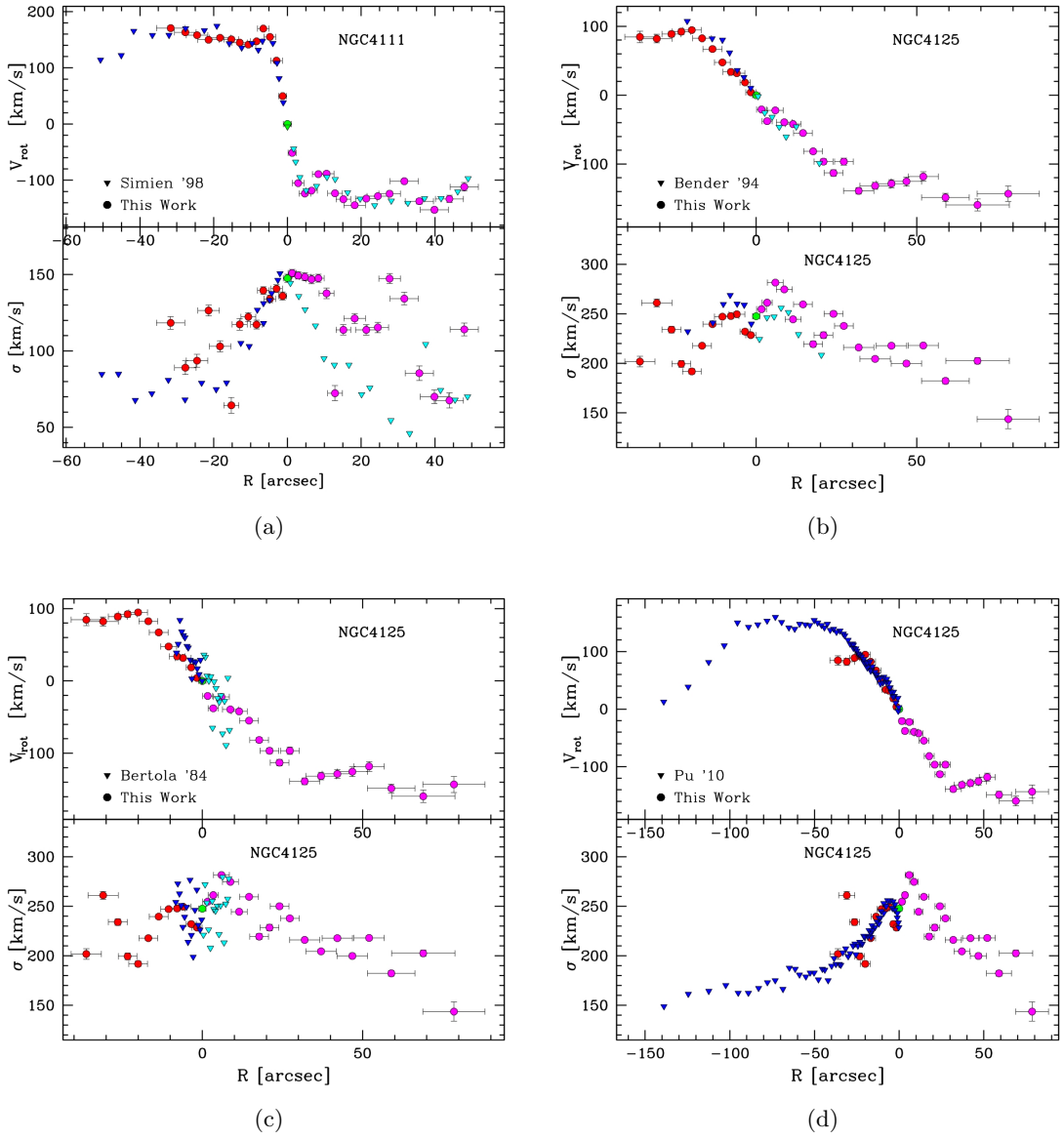

Figure B.15 *Same of fig. B.11: a) NGC4111, data taken from Simien and Prugniel (1998); b) NGC4125, data taken from Bender et al. (1994); c) NGC4125, data taken from Bertola et al. (1984); d) NGC4125, data taken from Pu et al. (2010)*

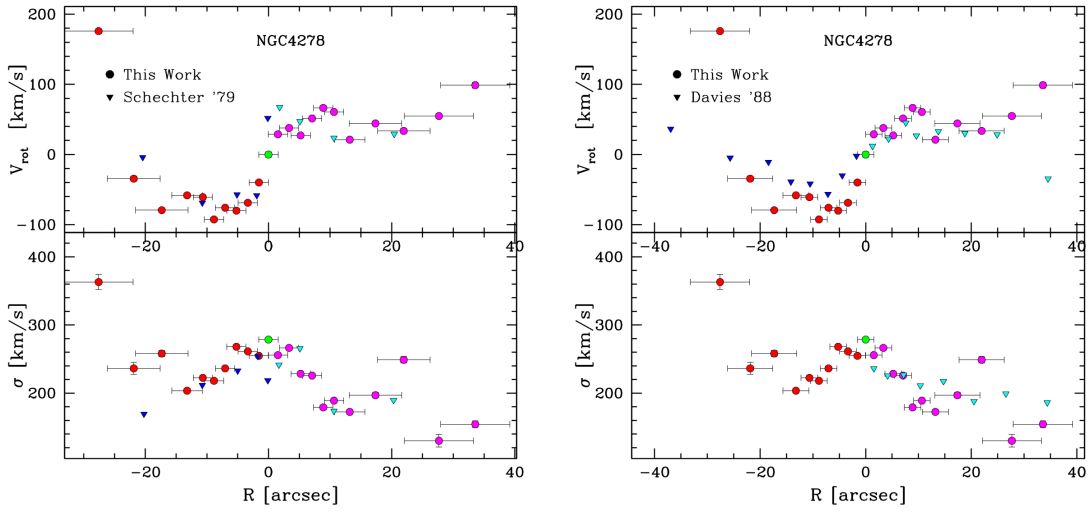

(a)

(b)

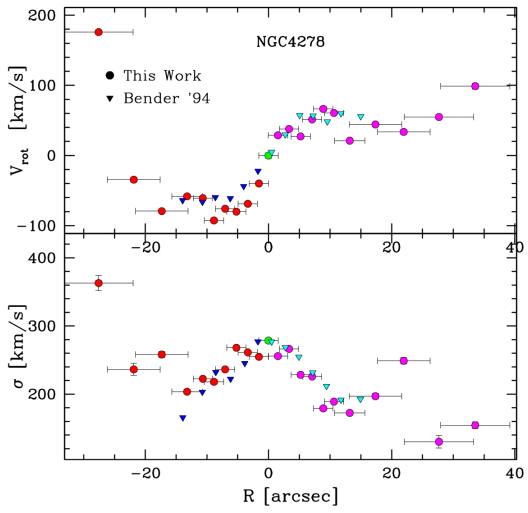

(c)

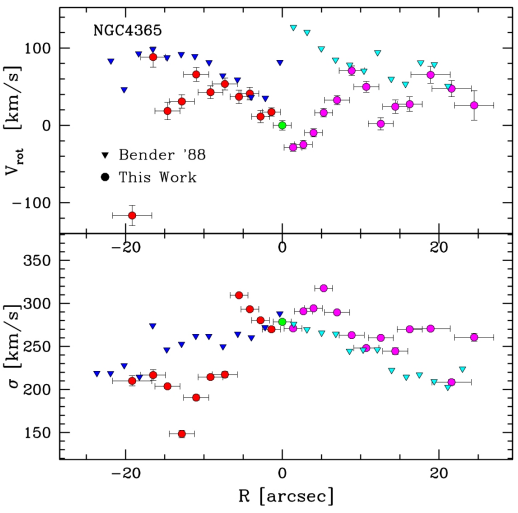

(d)

Figure B.16 *Same of fig. B.11: a) NGC4278, data taken from Schechter and Gunn (1979); b) NGC4278, data taken from Davies and Birkinshaw (1988); c) NGC4278, data taken from Bender et al. (1994); d) NGC4365, data taken from Bender (1988)*

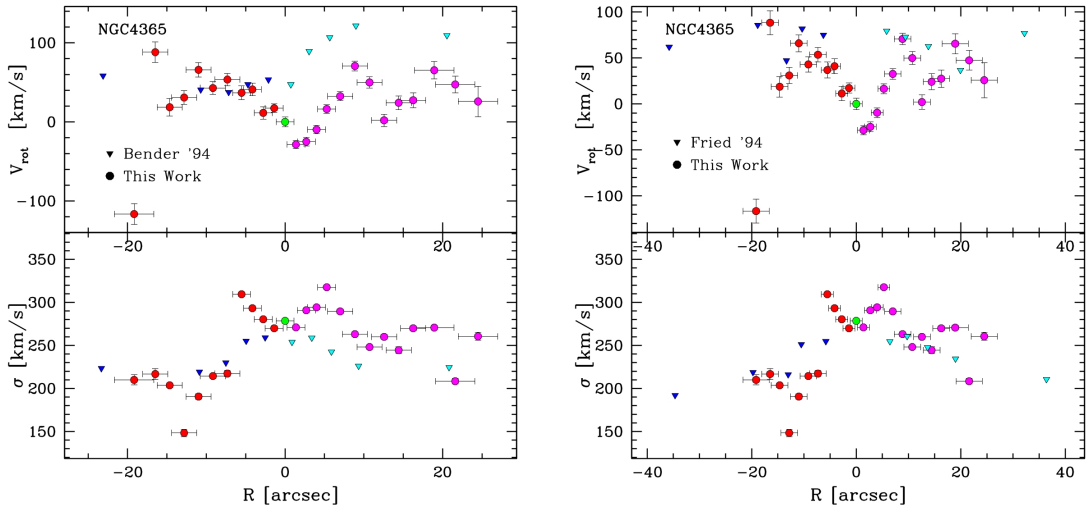

(a)

(b)

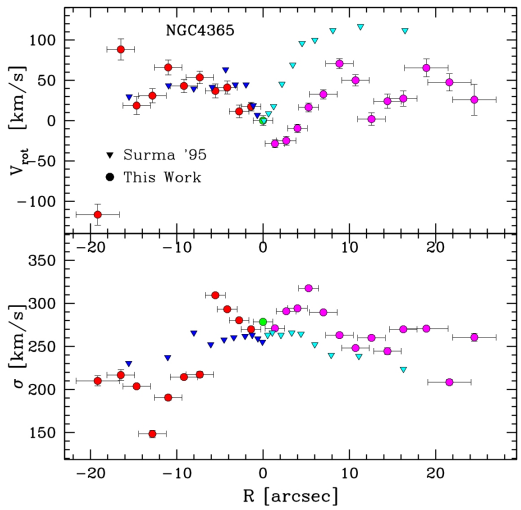

(c)

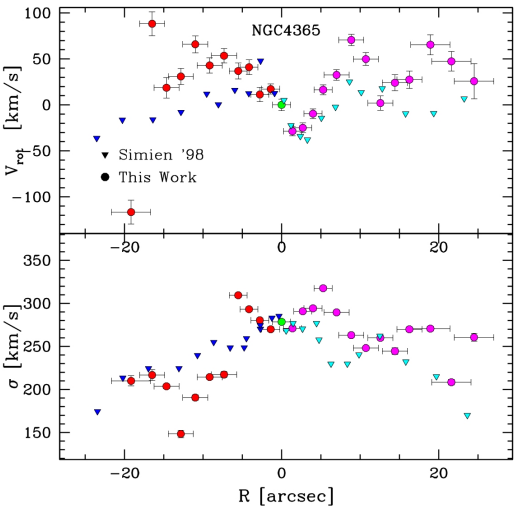

(d)

Figure B.17 *Same of fig. B.11: a) NGC4365, data taken from Bender et al. (1994); b) NGC4365, data taken from Fried and Illingworth (1994); c) NGC4365, data taken from Surma and Bender (1995); d) NGC4365, data taken from Simien and Prugniel (1998)*

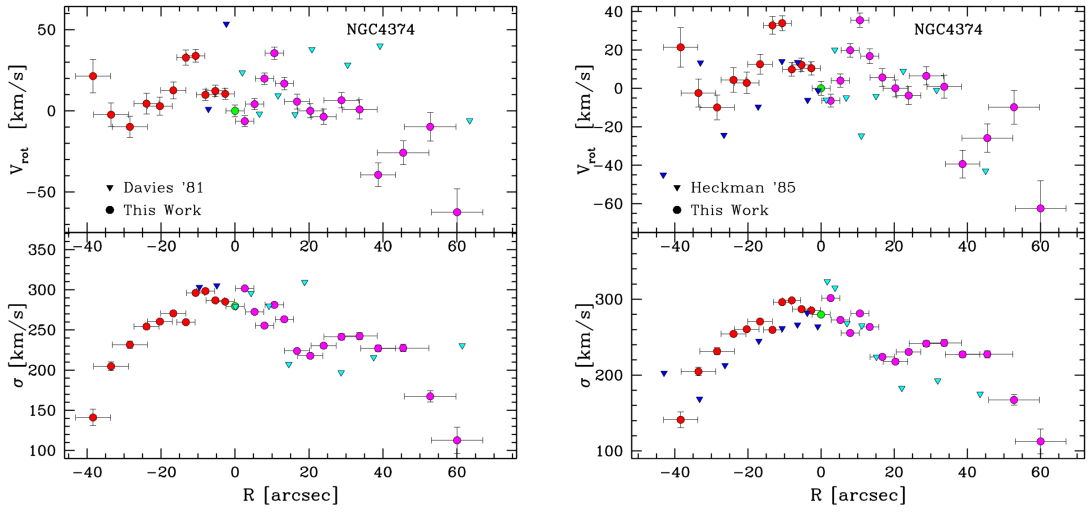

(a)

(b)

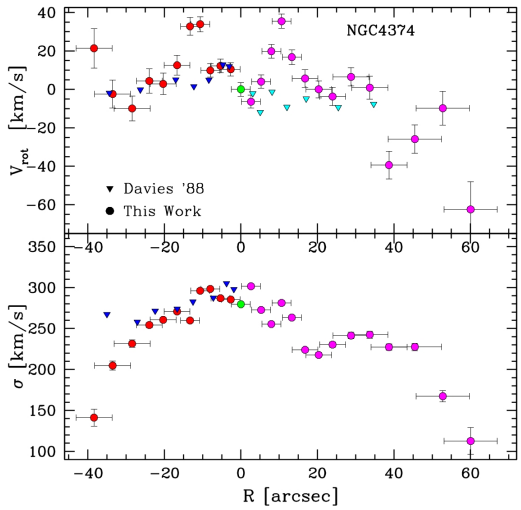

(c)

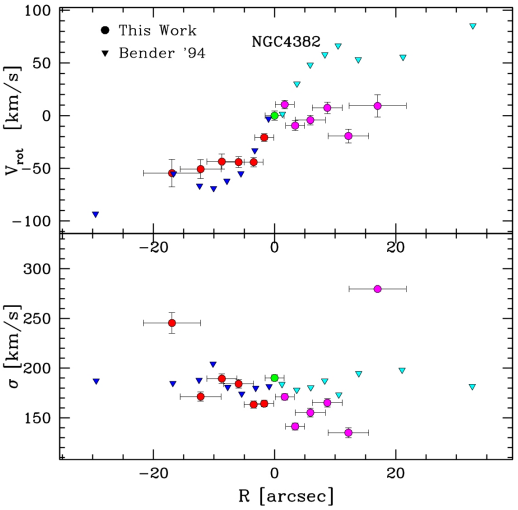

(d)

Figure B.18 *Same of fig. B.11: a) NGC4374, data taken from Davies (1981); b) NGC4374, data taken from Heckman et al. (1985); c) NGC4374, data taken from Davies and Birkinshaw (1988); d) NGC4382 (1996), data taken from Bender et al. (1994)*

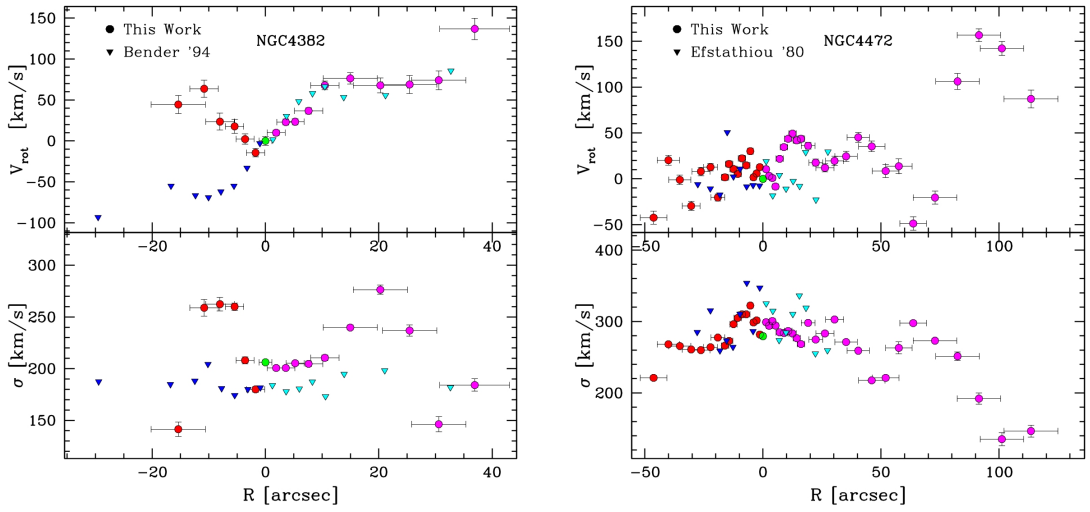

(a)

(b)

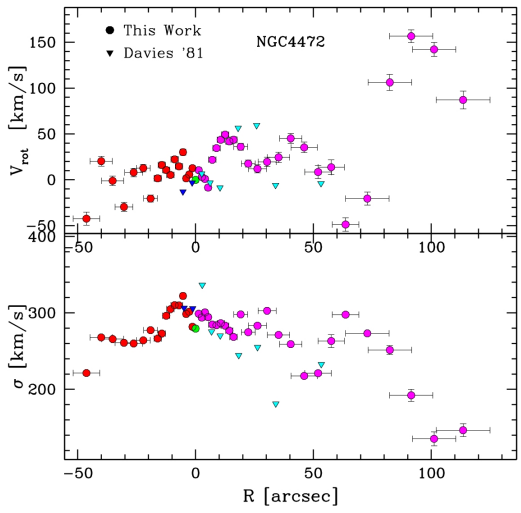

(c)

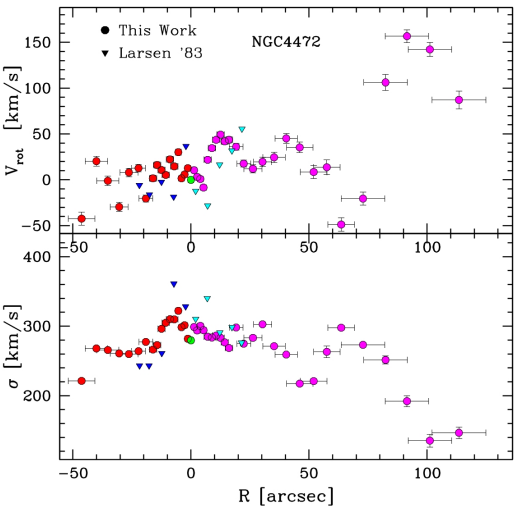

(d)

Figure B.19 *Same of fig. B.11: a) NGC4382 (1997), data taken from Bender et al. (1994); b) NGC4472, data taken from Efstathiou et al. (1980); c) NGC4472, data taken from Davies (1981); d) NGC4472, data taken from Larsen et al. (1983)*

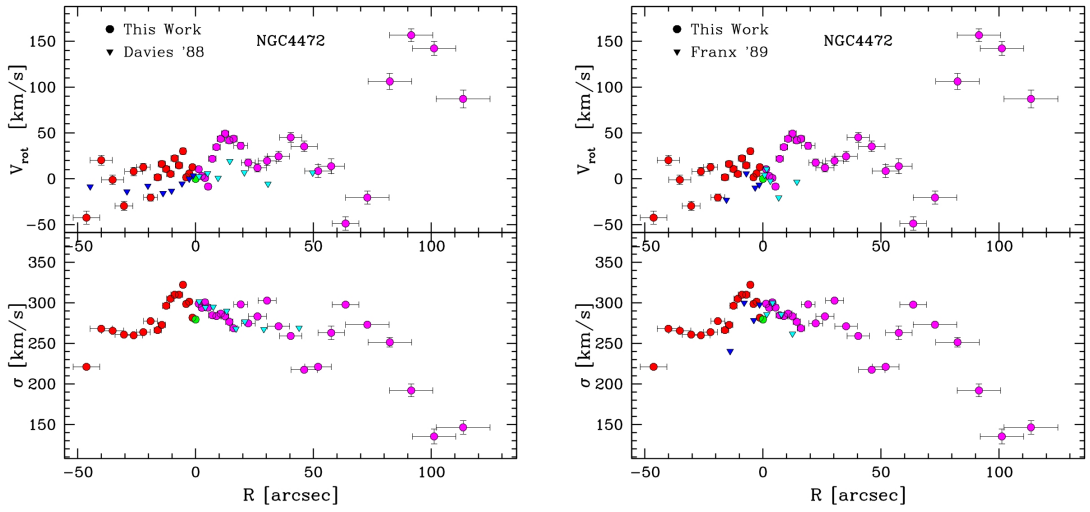

(a)

(b)

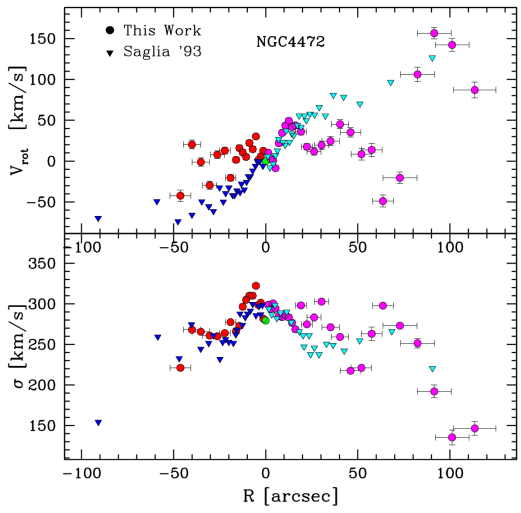

(c)

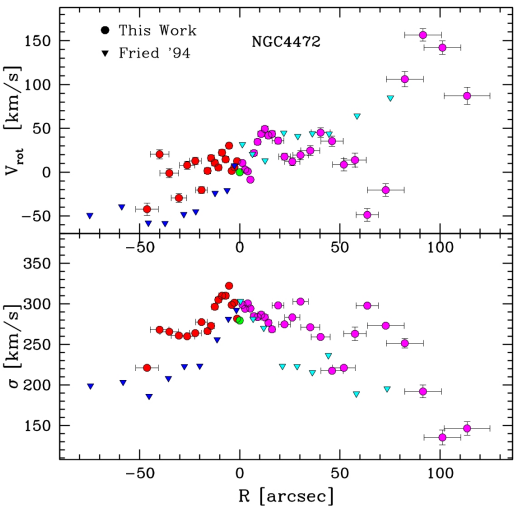

(d)

Figure B.20 *Same of fig. B.11: a) NGC4472, data taken from Davies and Birkinshaw (1988); b) NGC4472, data taken from Franx et al. (1989); c) NGC4472, data taken from Saglia et al. (1993); d) NGC4472, data taken from Fried and Illingworth (1994)*

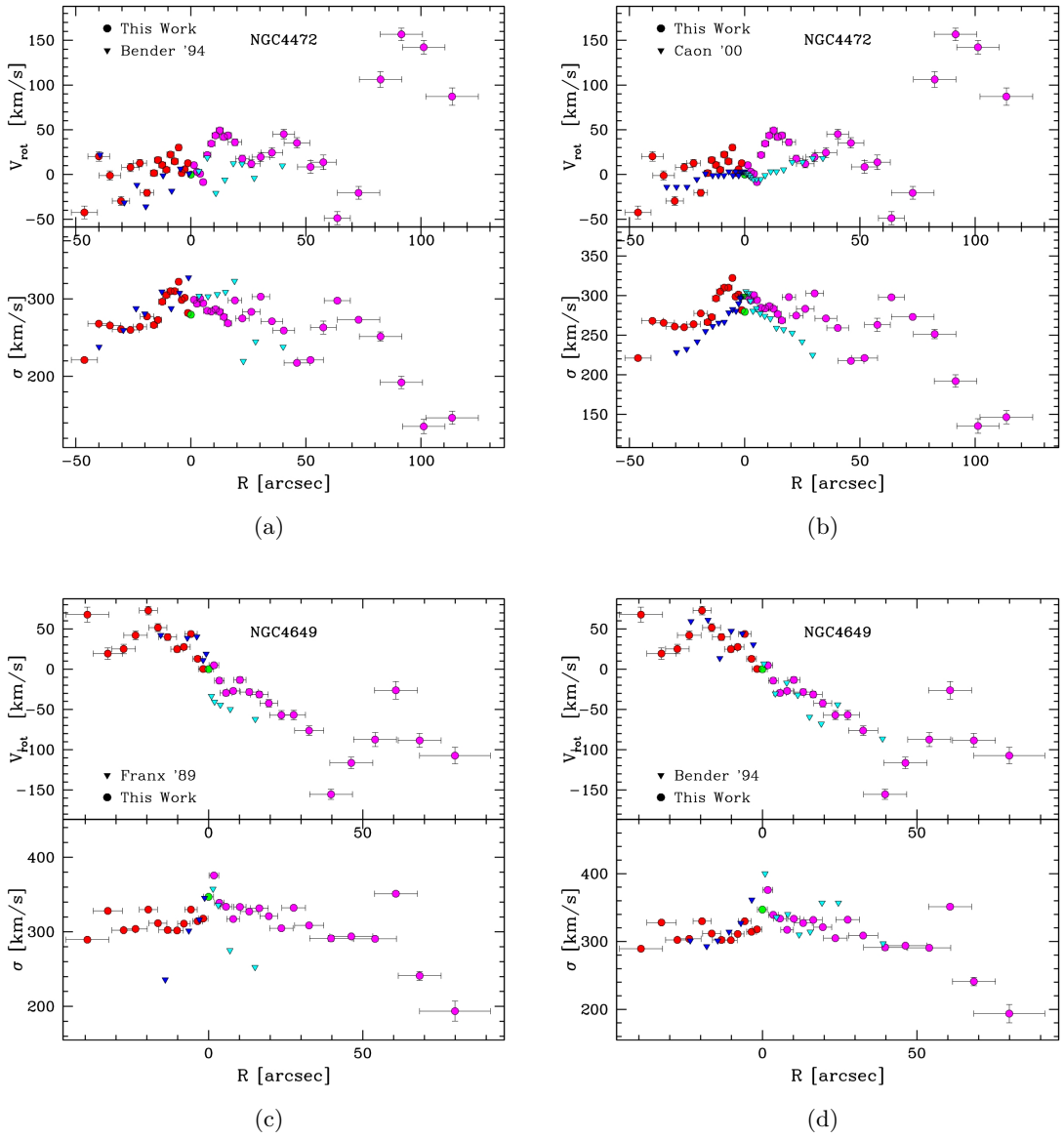

Figure B.21 *Same of fig. B.11: a) NGC4472, data taken from Bender et al. (1994); b) NGC4472, data taken from Caon et al. (2000); c) NGC4649, data taken from Franx et al. (1989); d) NGC4649, data taken from Bender et al. (1994)*

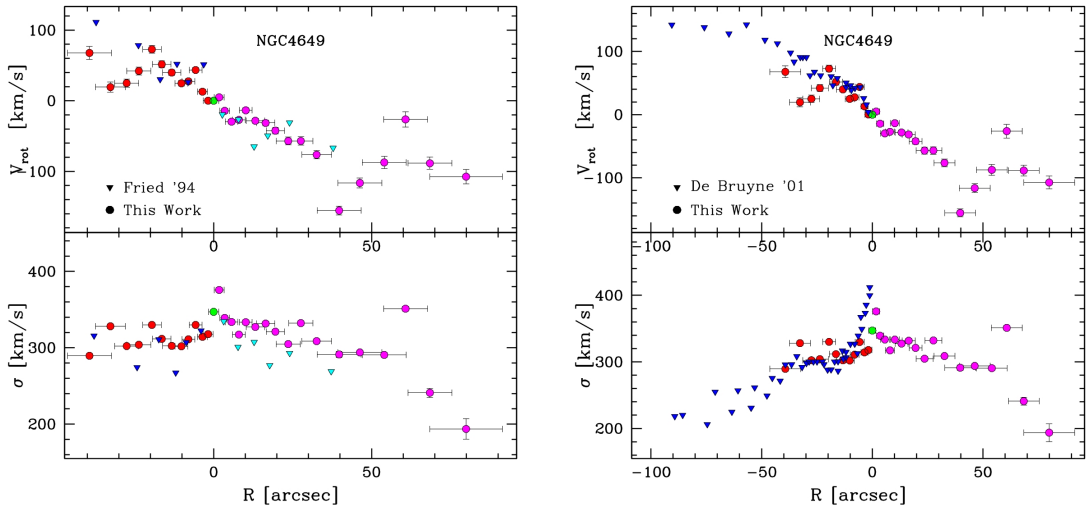

(a)

(b)

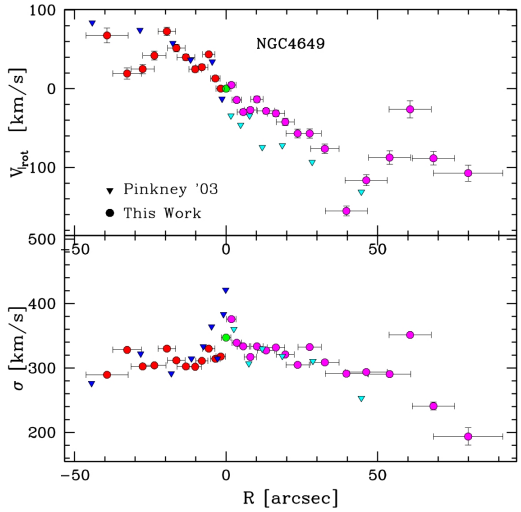

(c)

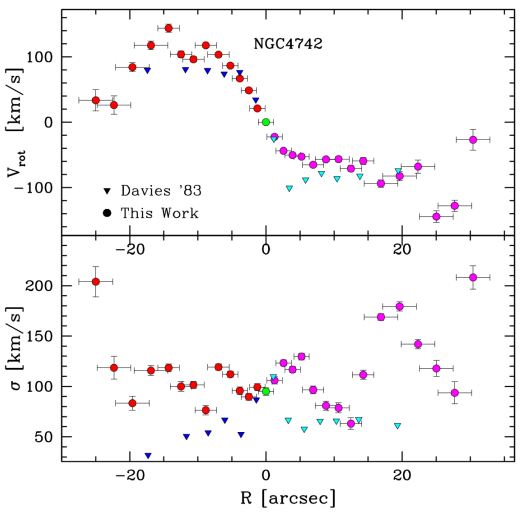

(d)

Figure B.22 *Same of fig. B.11: a) NGC4649, data taken from Fried and Illingworth (1994); b) NGC4649, data taken from De Bruyne et al. (2001); c) NGC4649, data taken from Pinkney et al. (2003); d) NGC4742, data taken from Davies et al. (1983)*

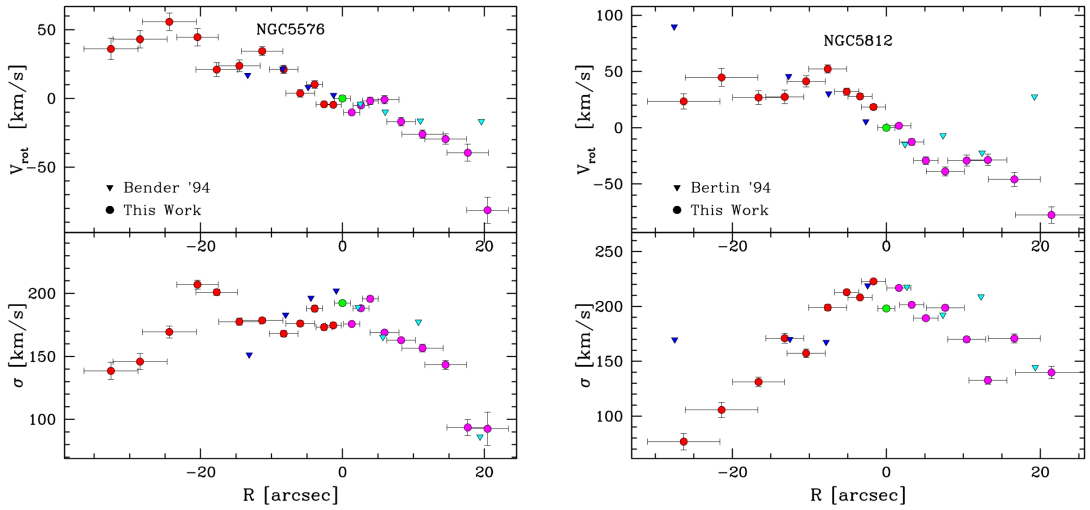

(a)

(b)

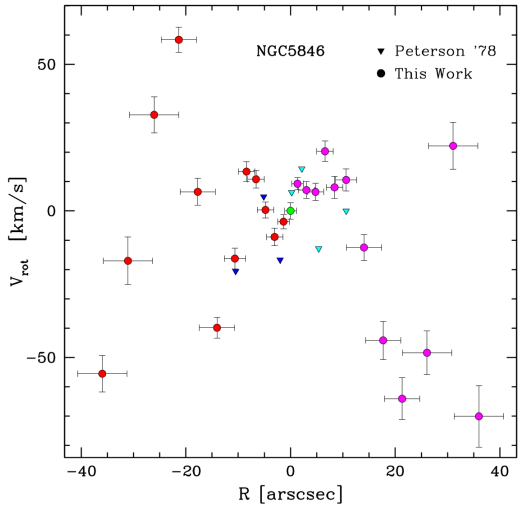

(c)

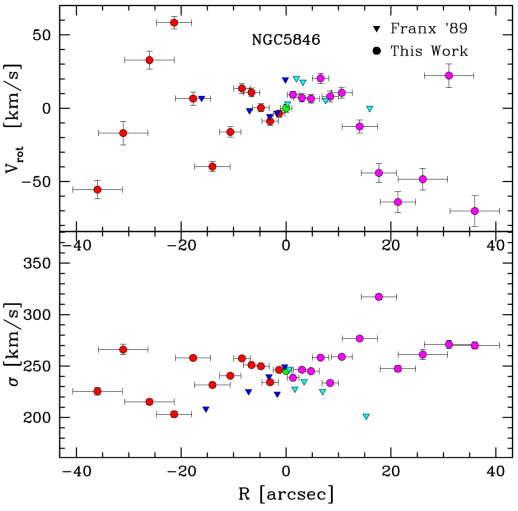

(d)

Figure B.23 *Same of fig. B.11: a) NGC5576, data taken from Bender et al. (1994); b) NGC5812, data taken from Bertin et al. (1994); c) NGC5846, data taken from Peterson (1978), from this work, only the rotation data are available; d) NGC5846, data taken from Franx et al. (1989)*

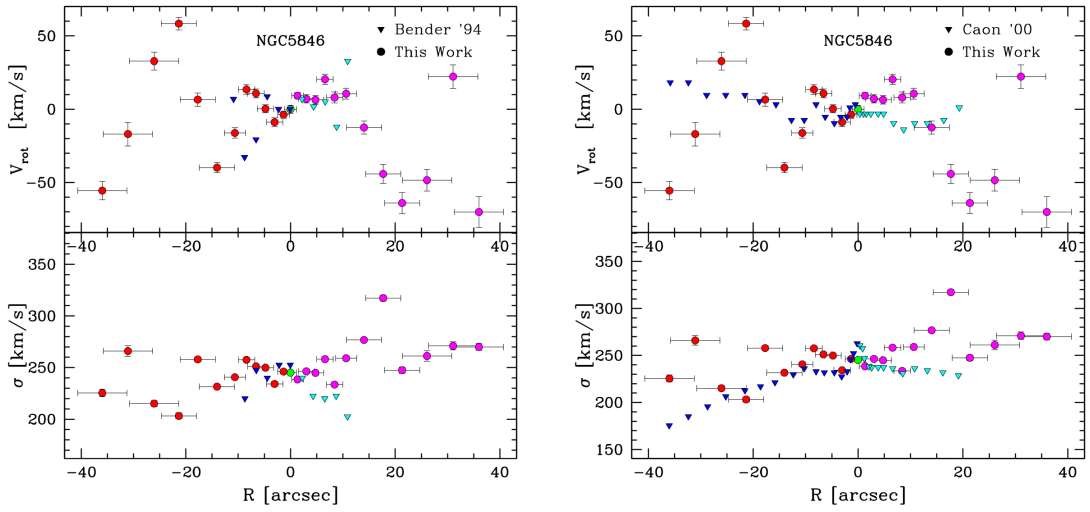

(a)

(b)

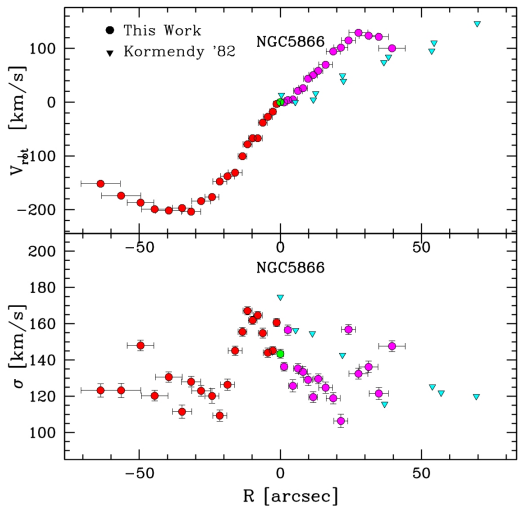

(c)

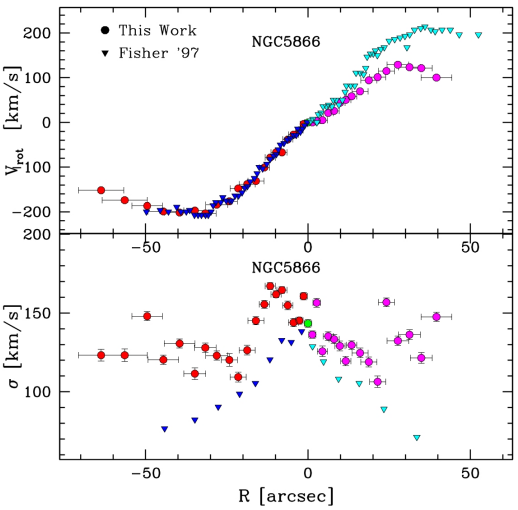

(d)

Figure B.24 *Same of fig. B.11: a) NGC5846, data taken from Bender et al. (1994); b) NGC5846, data taken from Caon et al. (2000); c) NGC5866, data taken from Kormendy and Illingworth (1982); d) NGC5866, data taken from Fisher (1997)*

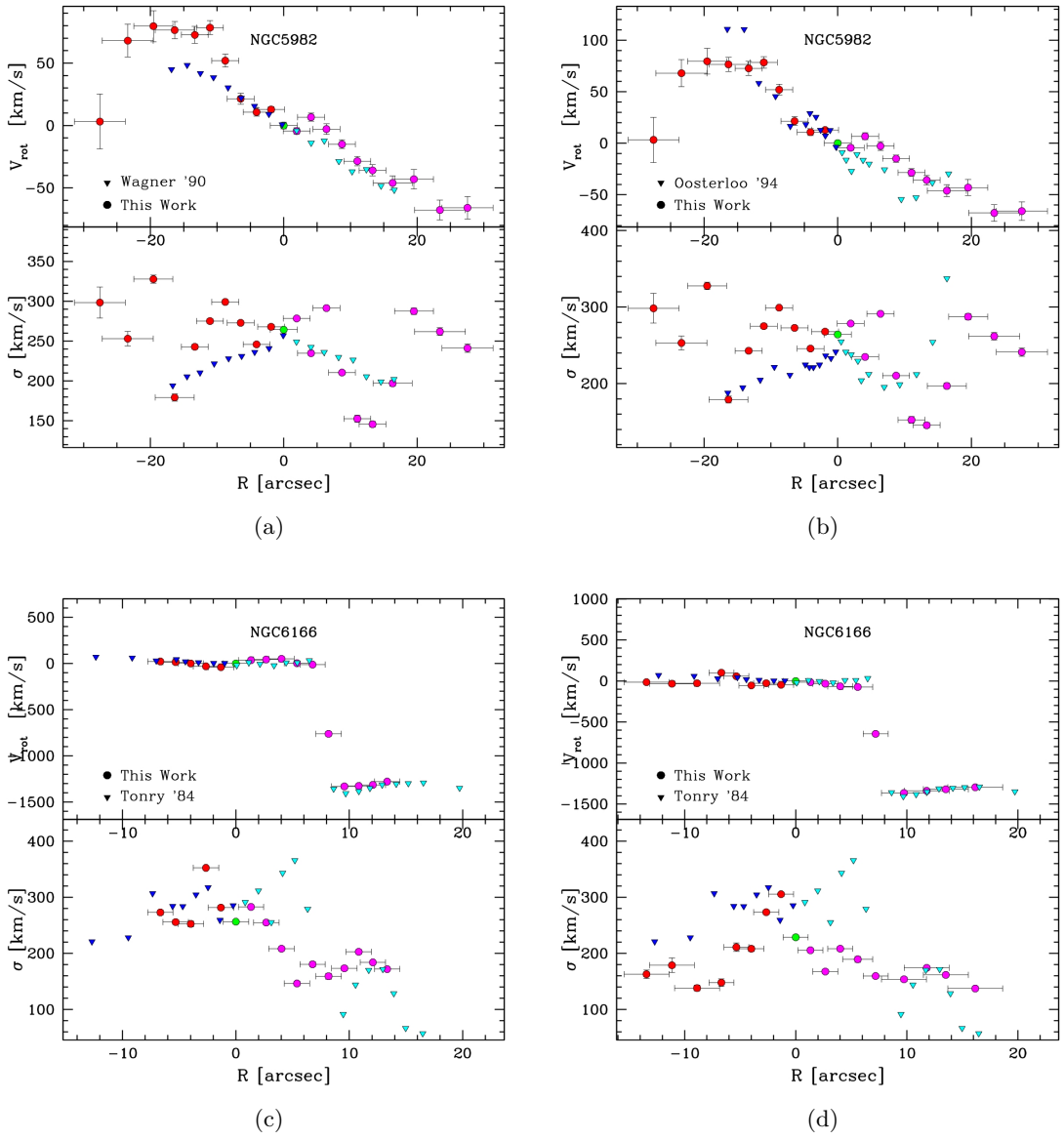

Figure B.25 *Same of fig. B.11: a) NGC5982, data taken from Wagner (1990); b) NGC5982, data taken from Oosterloo, Balcells, & Carter (1994); c) NGC6166 (first observation), data taken from Tonry (1984); d) NGC6166 (second observation), data taken from Tonry (1984)*

Appendix C

Correlation diagrams between Lick indices and dynamical properties

This appendix contains the set of diagrams pertinent to the analysis on Lick indices explained in § 5.4. The indices considered are the G_{4300}, the $\langle Fe \rangle_{blue}$, the Ca_{4455}, the Fe_{4668}, the $H\beta$, the $[OIII]_{5007}$, the Fe_{5015}, the Mg_2, the Mgb and the $\langle Fe \rangle_{red}$. For each index we show the diagrams relative to the velocity dispersion, the escape velocity, the dynamical mass and the mass to light ratio. In each diagram, galaxies with a flat velocity dispersion profile are represented by triangles, while galaxies with a radially decreasing profile are plotted as squares. Red points are the galaxies with $(V_m/\bar{\sigma})^* < 0.75$. Green points represent the objects with an higher value. Where we found a correlation, the solid blue line show the least squares fit, and angular coefficient, as well as correlation coefficient are showed in a corner.

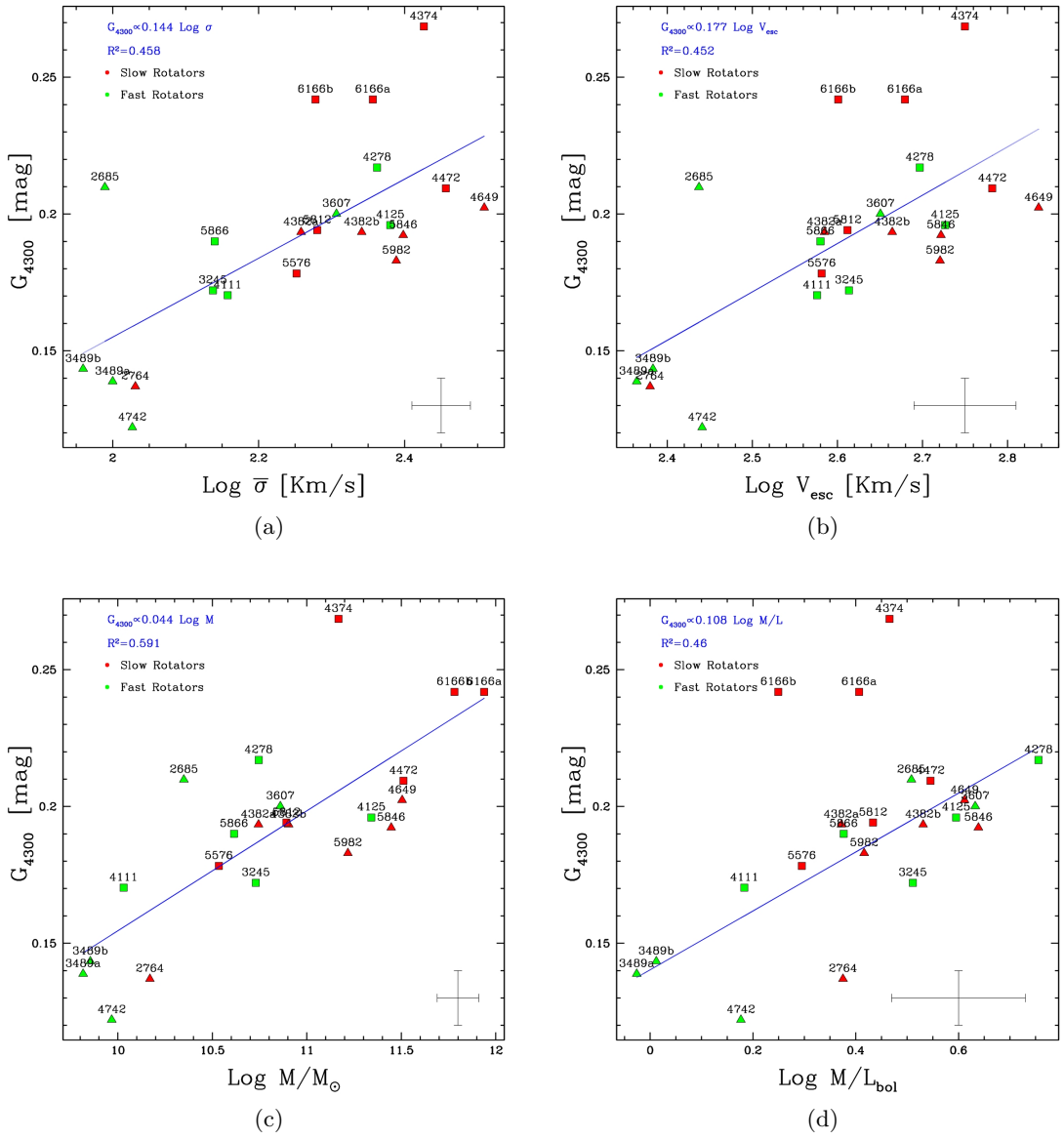

Figure C.1 *Correlation diagrams for the G_{4300}: a) Velocity dispersion; b) Escape velocity; c) Dynamical mass; d) Mass to light ratio.*

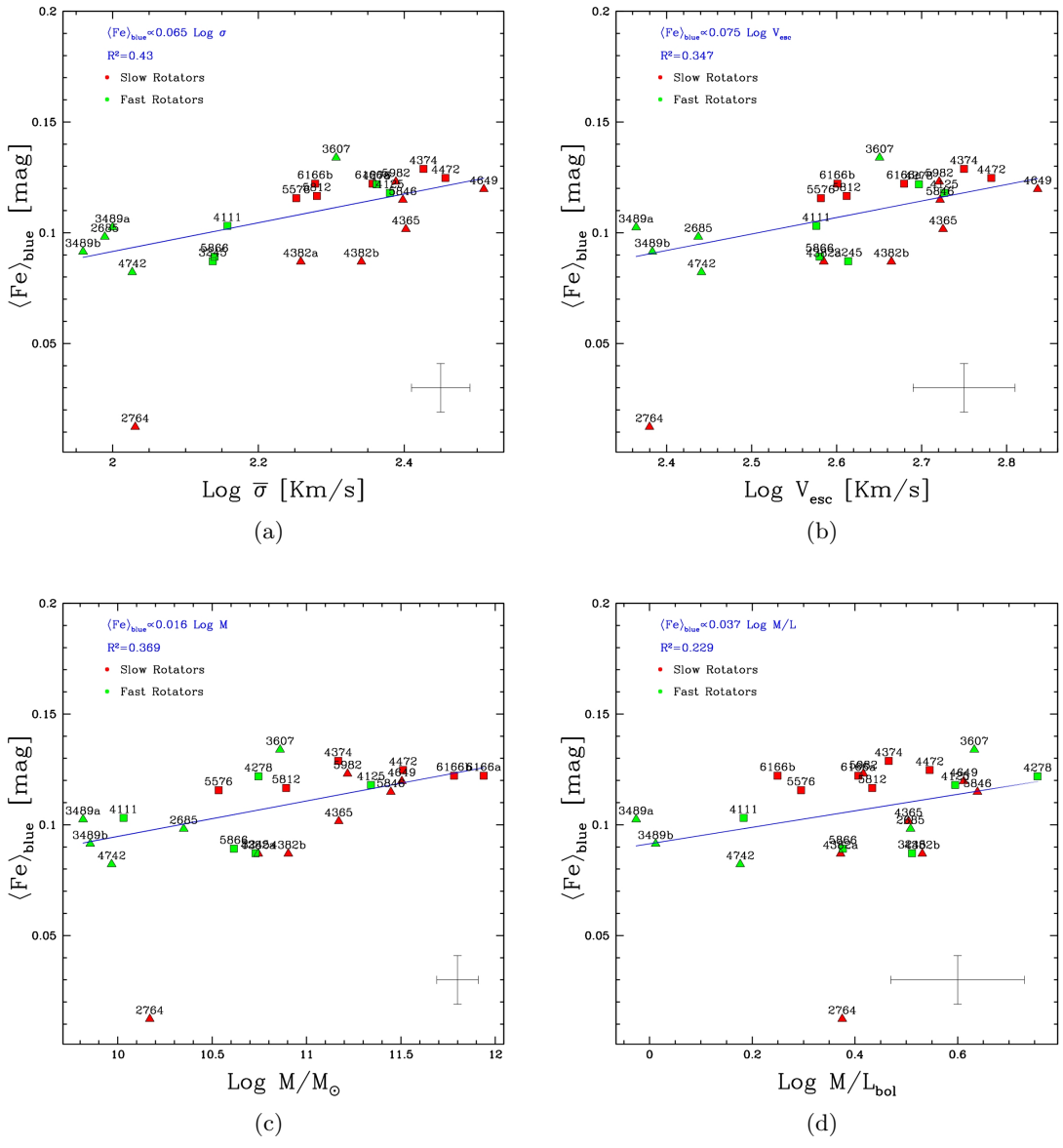

Figure C.2 *Correlation diagrams for the* $\langle Fe \rangle_{blue}$*: a) Velocity dispersion; b) Escape velocity; c) Dynamical mass; d) Mass to light ratio.*

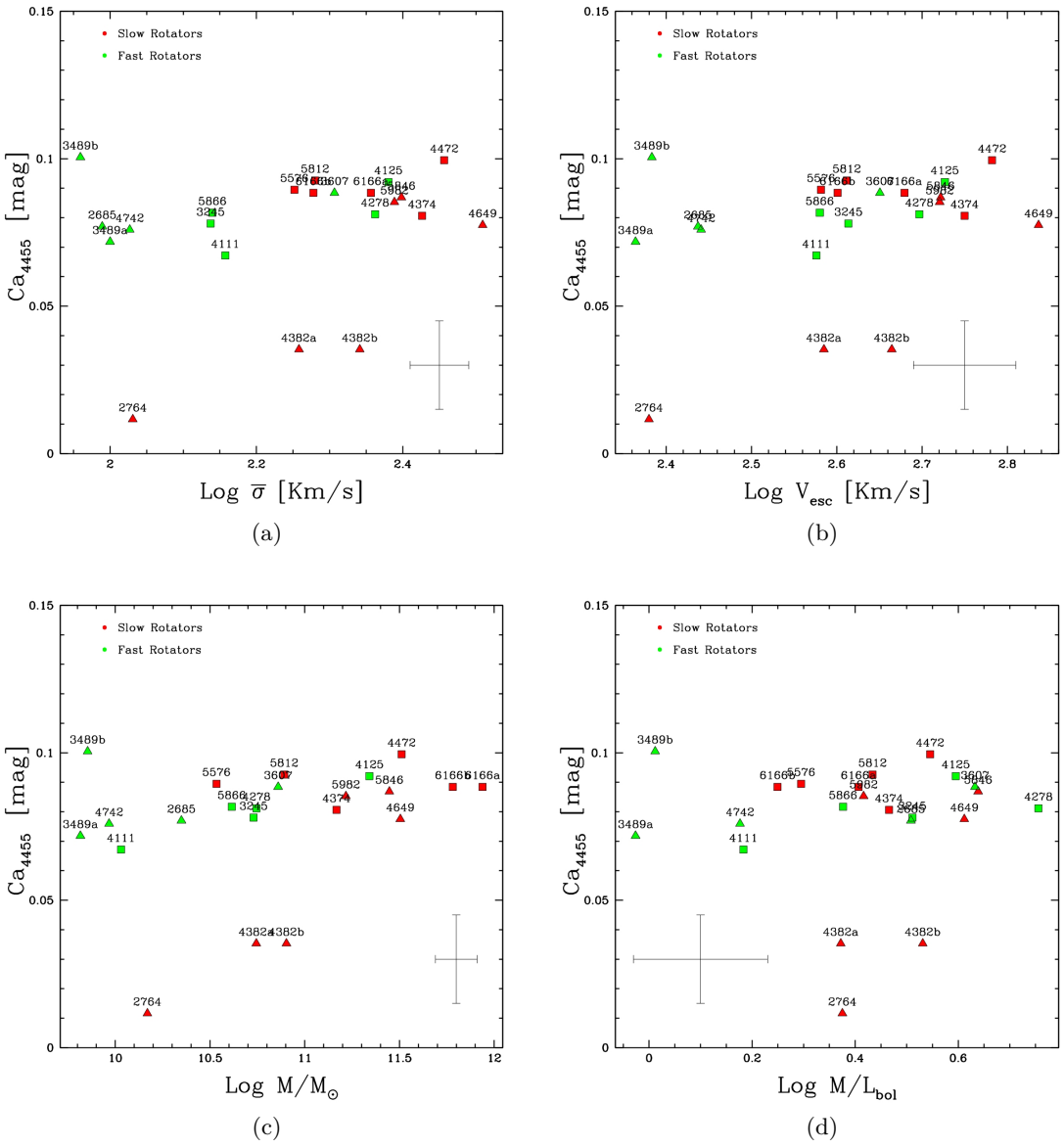

Figure C.3 *Correlation diagrams for the Ca_{4455}: a) Velocity dispersion; b) Escape velocity; c) Dynamical mass; d) Mass to light ratio.*

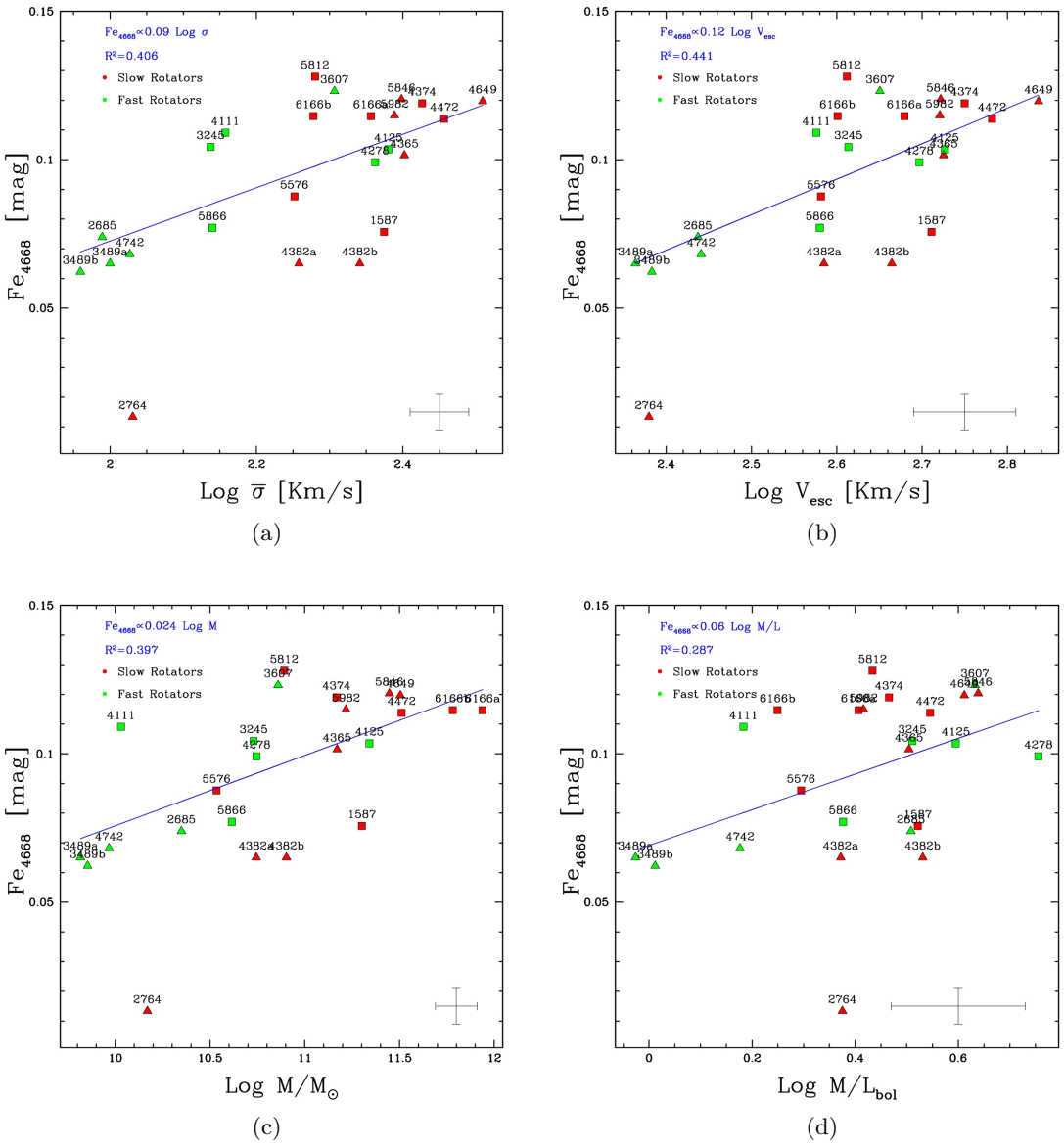

Figure C.4 *Correlation diagrams for the Fe_{4668}: a) Velocity dispersion; b) Escape velocity; c) Dynamical mass; d) Mass to light ratio.*

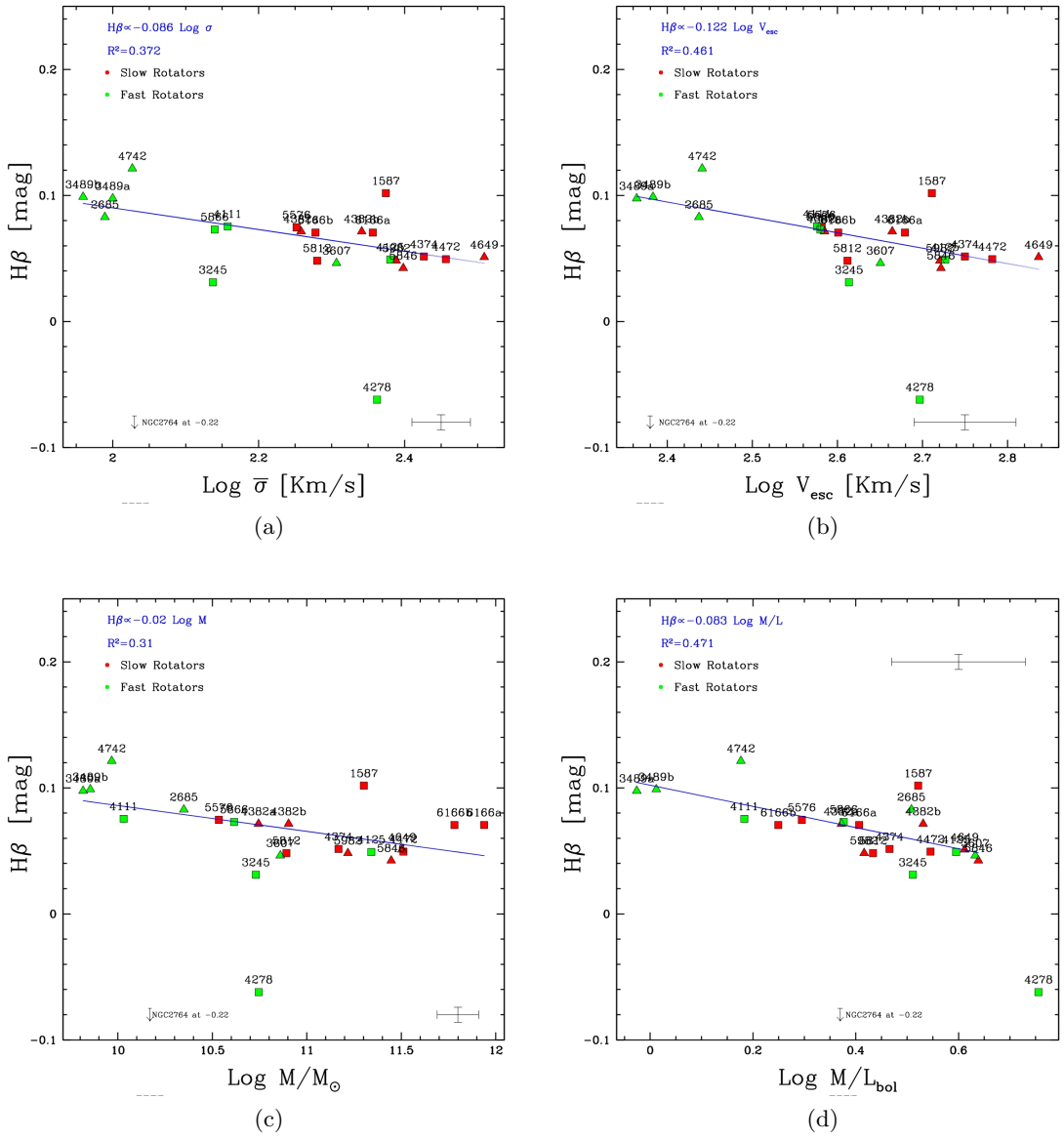

Figure C.5 *Correlation diagrams for the Hβ: a) Velocity dispersion; b) Escape velocity; c) Dynamical mass; d) Mass to light ratio.*

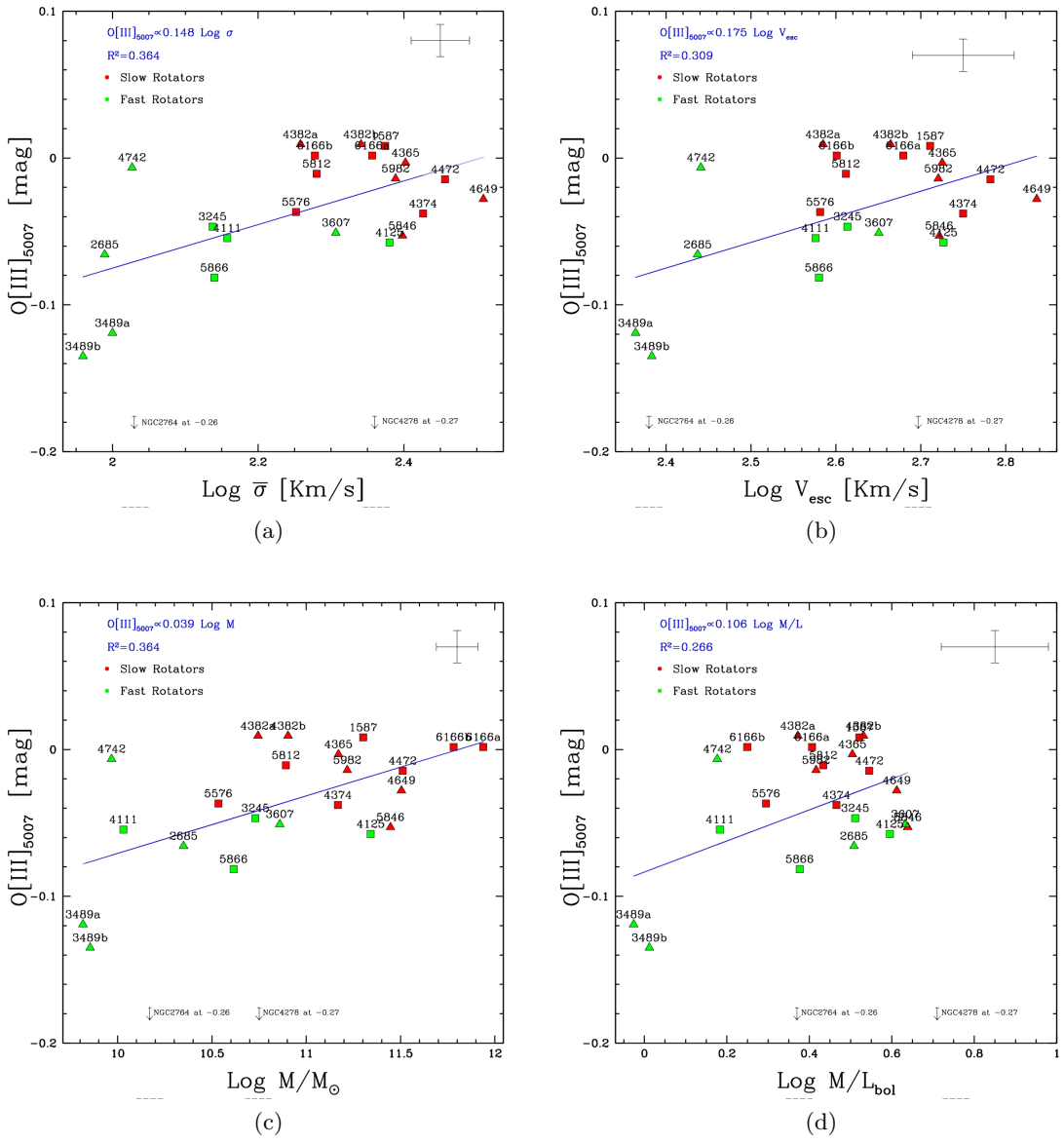

Figure C.6 *Correlation diagrams for the* $O[III]_{5007}$*: a) Velocity dispersion; b) Escape velocity; c) Dynamical mass; d) Mass to light ratio.*

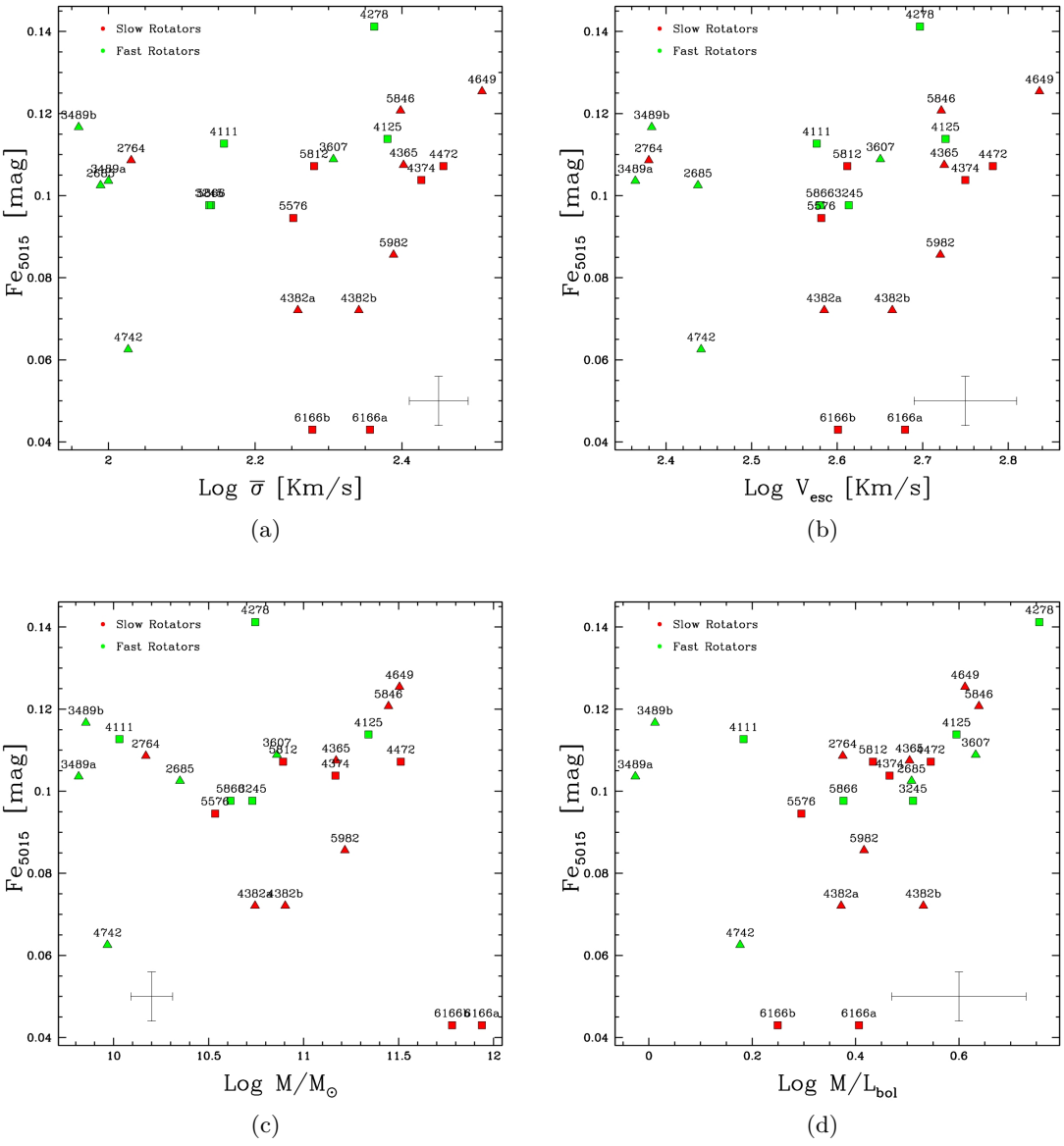

Figure C.7 *Correlation diagrams for the Fe_{5015}: a) Velocity dispersion; b) Escape velocity; c) Dynamical mass; d) Mass to light ratio.*

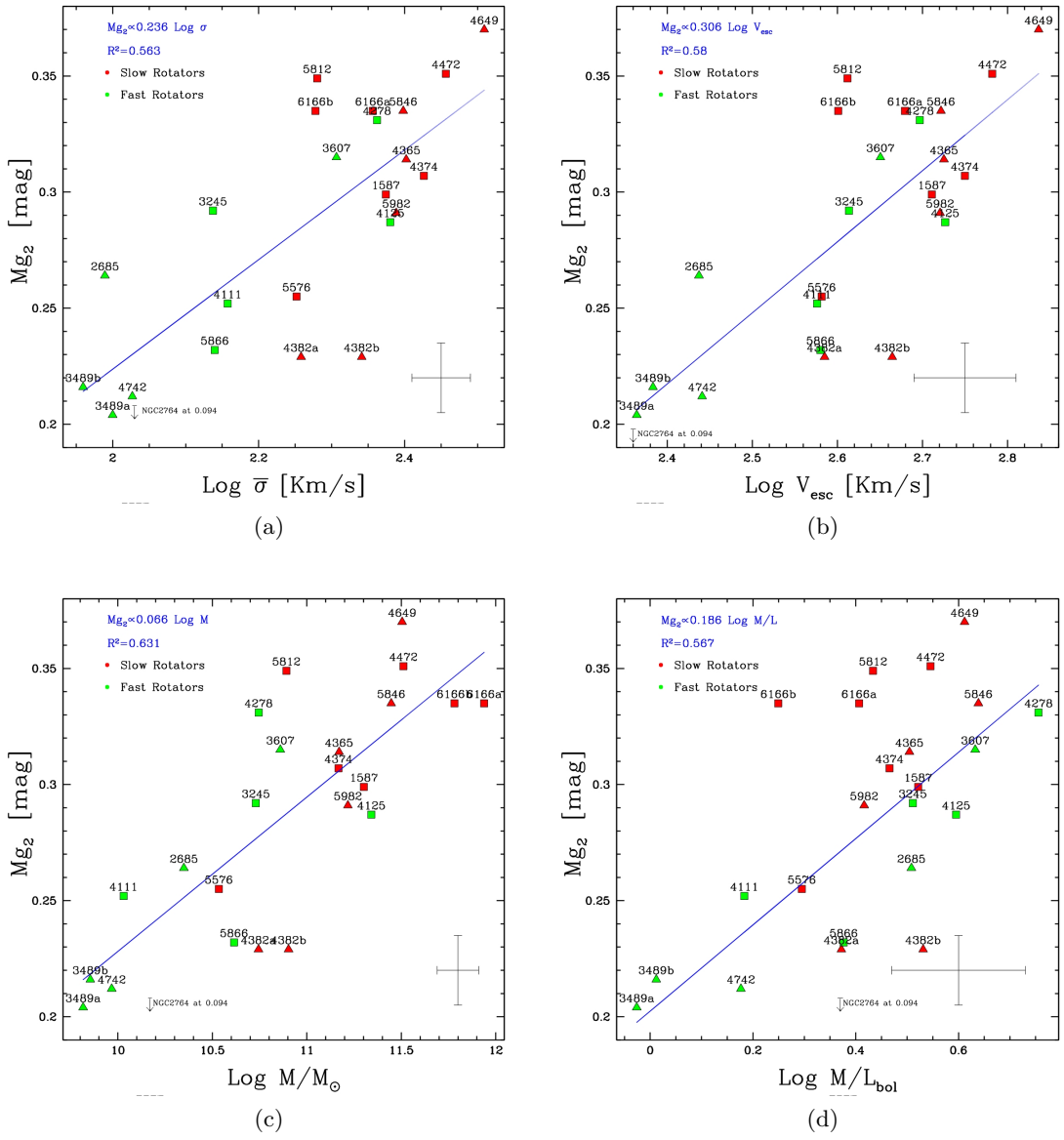

Figure C.8 *Correlation diagrams for the Mg_2: a) Velocity dispersion; b) Escape velocity; c) Dynamical mass; d) Mass to light ratio.*

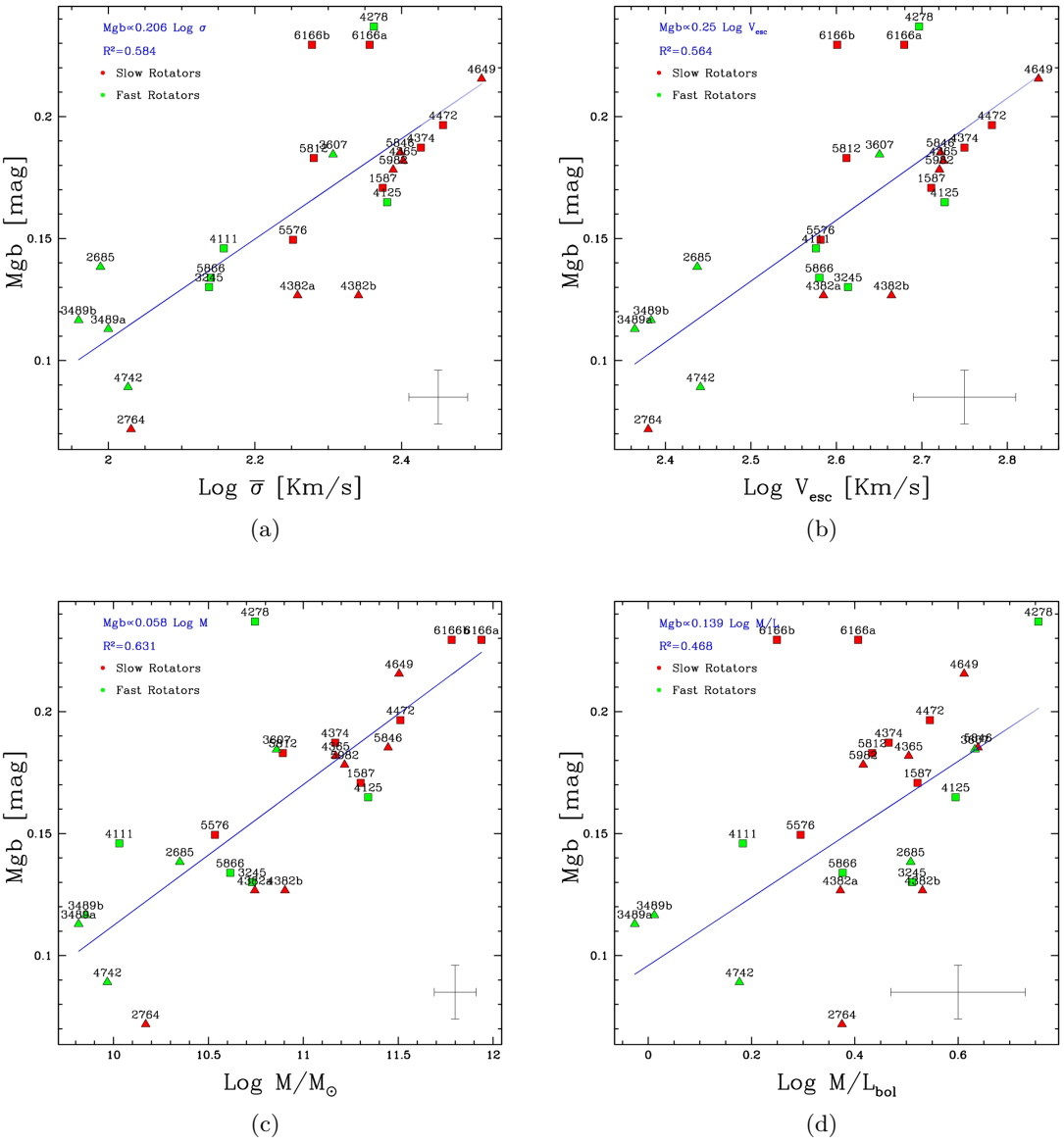

Figure C.9 *Correlation diagrams for the Mgb: a) Velocity dispersion; b) Escape velocity; c) Dynamical mass; d) Mass to light ratio.*

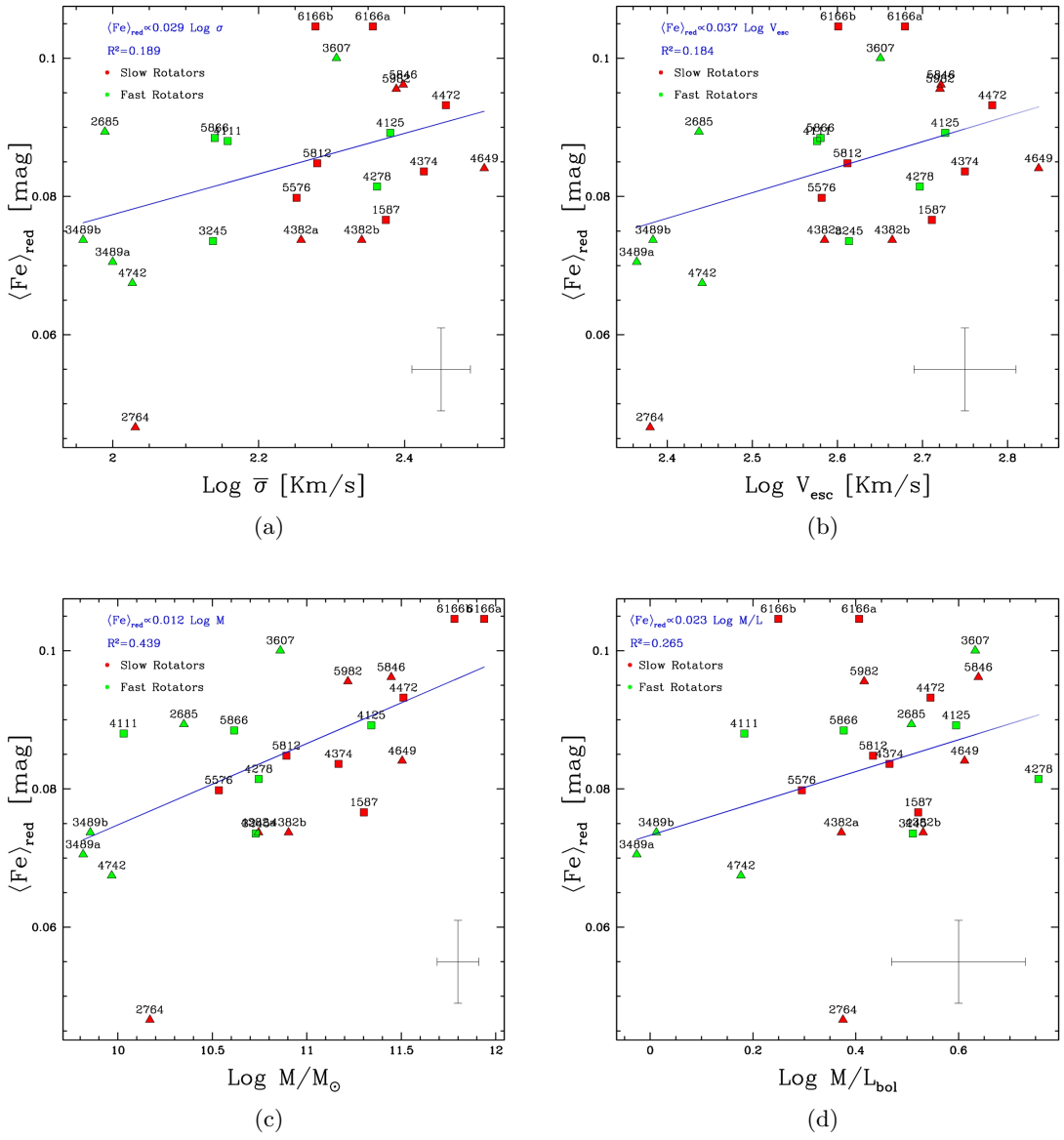

Figure C.10 *Correlation diagrams for the* $\langle Fe \rangle_{red}$*: a) Velocity dispersion; b) Escape velocity; c) Dynamical mass; d) Mass to light ratio.*

Bibliography

Aizu K., 1980, PThPh, 63, 415

Allen C. W., 1973, *Astrophysical Quantities*, The Athlone Press

Arimoto N., Yoshii Y., 1987, A&A, 173, 23

Bender R., 1988, A&A, 202, L5

Bender R., Doebereiner S., Moellenhoff C., 1988, A&AS, 74, 385

Bender R., Burstein D., Faber S. M., 1993, ApJ, 411, 153

Bender R., Saglia R. P., Gerhard O. E., 1994, MNRAS, 269, 785

Bertin, G., Bertola, F., Buson, L. M., et al., 1994, A&A, 292, 381

Bertola F., Capaccioli M., 1975, ApJ, 200, 439

Bertola F., Bettoni D., Rusconi L., Sedmak G., 1984, AJ, 89, 356

Bertola F., Cinzano P., Corsini E. M., Rix H.-W., Zeilinger W. W., 1995, ApJ, 448, L13

Bevington P., Robinson D. K., 2003, *Data Reduction and Error Analysis*, McGraw-Hill

Binney J., 1978, MNRAS, 183, 501

Binney J., Tremaine S., 1987, *Galactic Dynamics*, Princeton University Press

Bonfanti P., Rampazzo R., Combes F., Prugniel P., Sulentic J. W., 1995, A&A, 297, 28

Borne K. D., Hoessel J. G., 1988, ApJ, 330, 51

Borne K. D., Balcells M., Hoessel J. G., McMaster M., 1994, ApJ, 435, 79

Burbidge E. M., Burbidge G. R., Fish R. A., 1961, ApJ, 133, 393

Burstein D., Davies R. L., Dressler A., Faber S. M., Lynden-Bell D., 1988, ASSL, 141, 17

Buzzoni A., 1989, ApJS, 71, 817

Buzzoni A., Mantegazza L., Gariboldi G., 1994, AJ, 107, 513

Buzzoni A., 1995, ApJS, 98, 69

Buzzoni A., Arnaboldi M., Corradi R. L. M., 2006, MNRAS, 368, 877

Buzzoni A., 2011, MNRAS, 415, 1155

Buzzoni A., Cellone S. A., Saracco P., Zucca E., 2012, MNRAS, 420, 3427

Buzzoni A., Bertone E., 2014, MNRAS, submitted

Buzzoni A., Salsa M., Battistini C., Carrasco L., Recillas-Cruz E., 2014, ApJ, submitted

Caon N., Macchetto D., Pastoriza M., 2000, ApJS, 127, 39

Cappellari M., et al., 2006, MNRAS, 366, 1126

Cowie L. L., Songaila A., Hu E. M., Cohen J. G., 1996, AJ, 112, 839

Davies R. L., 1981, MNRAS, 194, 879

Davies R. L., Efstathiou G., Fall S. M., Illingworth G., Schechter P. L., 1983, ApJ, 266, 41

Davies R. L., Birkinshaw M., 1988, ApJS, 68, 409

De Bruyne V., Dejonghe H., Pizzella A., Bernardi M., Zeilinger W. W., 2001, ApJ, 546, 903

de Vaucouleurs G., de Vaucouleurs A., Corwin H. G., Jr., Buta R. J., Paturel G., Fouqué P., 1991, rc3..book,

Djorgovski S., Davis M., 1987, ApJ, 313, 59

Dressler A., Lynden-Bell D., Burstein D., Davies R. L., Faber S. M., Terlevich R., Wegner G., 1987, ApJ, 313, 42

Efstathiou G., Ellis R. S., Carter D., 1980, MNRAS, 193, 931

Emsellem E., et al., 2004, MNRAS, 352, 721

Faber S. M., Jackson R. E., 1976, ApJ, 204, 668

Faber S. M., Dressler A., Davies R. L., Burstein D., Lynden-Bell D., 1987, nngp.proc, 175

Fish R. A., 1964, ApJ, 139, 284

Fisher D., 1997, AJ, 113, 950

Franx M., Illingworth G., Heckman T., 1989, ApJ, 344, 613

Fried J. W., Illingworth G. D., 1994, AJ, 107, 992

Gavazzi G., Pierini D., Boselli A., 1996, A&A, 312, 397

González J. J., 1993, PhDT

Graham A., Colless M., 1997, MNRAS, 287, 221

Heckman T. M., Illingworth G. D., Miley G. K., van Breugel W. J. M., 1985, ApJ, 299, 41

Hoffleit D., Jaschek C. V., 1991, *The Bright star catalogue*

Hubble E. P., 1930, ApJ, 71, 231

Illingworth G., 1977, ApJ, 218, L43

Illingworth G. D., Franx M., 1989, ddse.work, 13

Jorgensen I., Franx M., Kjaergaard P., 1996, MNRAS, 280, 167

Kim D.-W., Fabbiano G., 2013, ApJ, 776, 116

Kobayashi C., Arimoto N., 1999, ApJ, 527, 573

Kormendy J., 1977, ApJ, 218, 333

Kormendy J., Illingworth G., 1982, ApJ, 256, 460

Kormendy J., 1982, in Martinet L., Major M., eds. *Morphology and Dynamics of Galaxies*, Geneva Observatory, p.113

Kormendy J., Djorgovski S., 1989, ARA&A, 27, 235

Kormendy J., Bender R., 1996, ApJ, 464, L119

Krajnović D., et al., 2011, MNRAS, 414, 2923

Larsen N., Norgaard-Nielsen H. U., Kjaergaard P., Dickens R. J., 1983, A&A, 117, 257

Lauer T. R., 1985, MNRAS, 216, 429

Loyer E., Simien F., Michard R., Prugniel P., 1998, A&A, 334, 805

Lynden-Bell D., 1967, MNRAS, 136, 101

Malin D. F., Carter D., 1980, Natur, 285, 643

Michard R., 1980, A&A, 91, 122

O'Connell R. W., 1980, ApJ, 236, 430

Oegerle W. R., Hoessel J. G., 1991, ApJ, 375, 15

Ogando R. L. C., Maia M. A. G., Pellegrini P. S., da Costa L. N., 2008, AJ, 135, 2424

Oort J. H., 1940, ApJ, 91, 273

Oosterloo T., Balcells M., Carter D., 1994, MNRAS, 266,L10

O'Sullivan E., Forbes D. A., Ponman T. J., 2001, MNRAS, 328, 461

Paturel G., Petit C., Prugniel P., Theureau G., Rousseau J., Brouty M., Dubois P., Cambrésy L., 2003, A&A, 412, 45

Peletier R. F., Davies R. L., Illingworth G. D., Davis L. E., Cawson M., 1990, AJ, 100, 1091

Pellegrini S., 2011a, MSAIS, 17, 128

Pellegrini S., 2011b, ApJ, 738, 57

Peterson C. J., 1978, ApJ, 222, 84

Pinkney, J., Gebhardt, K., Bender, R., et al., 2003, ApJ, 596, 903

Portinari L., Sommer-Larsen J., Tantalo R., 2004, MNRAS, 347, 691

Poveda A., Iturriaga R., Orozco I., 1960, BOTT, 2, 3

Poveda A., 1961, ApJ, 134, 910

Pu S. B., Saglia R. P., Fabricius M. H., Thomas J., Bender R., Han Z., 2010, A&A, 516, A4

Richstone D., Sargent W. L. W., 1972, ApJ, 176, 91

Rix H.-W., White S. D. M., 1992, MNRAS, 254, 389

Saglia, R. P., Bertin, G., Bertola, F., et al., 1993, ApJ, 403, 567

Sargent W. L. W., Schechter P. L., Boksenberg A., Shortridge K., 1977, ApJ, 212, 326

Sargent W. L. W., Young P. J., Lynds C. R., Boksenberg A., Shortridge K., Hartwick F. D. A., 1978, ApJ, 221, 731

Schechter P. L., Gunn J. E., 1979, ApJ, 229, 472

Schlafly E. F., Finkbeiner D. P., 2011, ApJ, 737, 103

Scott N., et al., 2009, MNRAS, 398, 1835

Seifert W., Scorza C., 1996, A&A, 310, 75

Simien F., Prugniel P., 1997, A&AS, 122, 521

Simien F., Prugniel P., 1998, A&AS, 131, 287

Simkin S. M., 1974, A&A, 31, 129

Surma P., Bender R., 1995, A&A, 298, 405

Tonry J., Davis M., 1979, AJ, 84, 151

Tonry J. L., 1981, ApJ, 251, L1

Tonry J. L., 1984, ApJ, 279, 13

Trager S. C., Worthey G., Faber S. M., Burstein D., Gonzalez J. J., 1998, ApJS, 116, 1

Trujillo I., Burkert A., Bell E. F., 2004, ApJ, 600, L39

van Albada T. S., Bertin G., Stiavelli M., 1995, MNRAS, 276, 1255

van der Marel R. P., Binney J., Davies R. L., 1990, MNRAS, 245, 582

van Gorkom J., 1992, ASSL, 178, 233

Véron-Cetty M.-P., Véron P., 2006, A&A, 455, 773

Villaver E., García-Segura G., Manchado A., 2003, ApJ, 585, L49

Villaver E., Stanghellini L., 2005, ApJ, 632, 854

Wagner S. J., 1990, dig..book, 244

Wilson C. P., 1976, BAAS, 8, 313

Worthey G., Faber S. M., Gonzalez J. J., Burstein D., 1994, ApJS, 94, 687

York D. G., et al., 2000, AJ, 120, 1579

Young P. J., 1976, AJ, 81, 807

Young P., Lynds C. R., Sargent W. L. W., Boksenberg A., Hartwick F. D. A., 1978, ApJ, 222, 450